Enhancement of Heat Transfer Performance on Nacelle Lip-skin for Swirl Anti-Icing

Kingston University London

School of Aerospace Engineering

Thesis submitted for the Degree of Doctor of Philosophy

Mohd Azmi bin Ismail, MSc

January 2014

ABSTRACT

Ice accretion on the wing and nacelle leading edges diminishes aerodynamic performance and increases fuel consumption and chances of aircraft crash. For these reasons, the Federal Aviation Administration mandates aircraft manufacturers to demonstrate that their aircraft can fly safely in icing conditions. This study has investigated the thermal performance and measures for improvement of Swirl Anti-Icing (SAI) systems in preventing ice accretion on nacelle leading edges.

A Piccolo Tube Anti-Icing (PTAI) system with experimental data was used as the benchmark of this study. PTAI consists of perforated pipe and is installed inside the wing and/or nacelle leading edge. The hot air from the compressor is directed onto inner skin through the holes/nozzles in a perforated pipe. As a result, the inner skin is warmed up and free from icing. In this study, numerical simulations have been performed to analyse the thermal performance of PTAI at 4 different altitudes/scenarios namely Ground Run, Climb, Hold and Descent. The FLUENT CFD results demonstrated excellent agreements with the experimental data obtained by Bombardier Aerospace. Based on the results, the gradient coefficients of the empirical equations proposed by colleagues have been modified to take into account the ambient air temperature in order to make the correlations suitable for all the 4 conditions analysed.

In future, Bias flow Acoustic Liner (BAL) is expected to be employed in engine nacelle and to form part of the inner skin of nacelle lip. The hotspots produced by PTAI would possibly destroy BAL. Thus, an old and mature technology, SAI, was further investigated in the present study with a hope to get rid of hotspot phenomenon on the inner skin and to increase the efficiency of the system. SAI has better temperature distribution along nacelle lip-skin than that of PTAI. In addition, SAI contains fewer components, requires simple plumbing, and is light and inexpensive both for the system itself and for maintenance of the system compared to PTAI. Some potential modifications of nozzle including sloped nozzle, altered nozzle length and nozzle outlet, rotated nozzle towards inner skin, decreased exhaust area and increased nozzle diameter have been proposed and investigated in order to improve thermal performance of SAI. According to the results, only nozzle directions and nozzle diameters had significant effects on the thermal performance of SAI although all the modifications would have certain effects on anti icing performances of SAI. Thermal performance of SAI was inversely related to nozzle diameter. The hotspot temperature decreased by 18.53°C and cold spot temperature increased by 2.30°C respectively as the nozzle rotated 13° towards inner skin at hot air mass flow rate of 0.0118kg/s. For hot air mass flow rate of 0.04536 kg/s, the cold spot temperature decreased from 28.78 to 6.37°C as nozzle diameter increased from 0.0127m to

0.0254m. In addition, the temperature distribution on the nacelle lip-skin has improved as the angle of nozzle direction towards inner skin increased. Based on the results, novel empirical correlations for SAI system have been developed and presented.

The augmentor was employed in SAI system in order to enhance momentum and heat exchanges between hot air and cold air in the D-chamber. As a result, the uniformity of temperature distribution and thermal performance of SAI on the nacelle lip-skin were improved. The results showed that the thermal performance of SAI with augmentor increased with the increase of hot air mass flow rate. Although SAI with Augmentor 3 at 2° rotation showed poor thermal performance than SAI without augmentor but nozzle rotating at 13° with hot air mass flow rate above 0.028kg/s, the former showed better thermal performance than latter for hot air mass flow rate equal to or lower than 0.028kg/s. The performance of the Final nozzle was also tested and compared with the performances of Circle nozzle and ellipse nozzle 1. The final design of the nozzle has demonstrated the best performance at any given hot air mass flow rate, especially at 0.04356 kg/s. At this mass flow rate, $C_{tem\ deviation}$, hotspot temperature and cold spot temperature were 13.19%, 371.42K and 322.02K respectively.

The hotspot temperature, temperature difference between hotspot and cold spot, standard temperature deviation and coefficient of temperature deviation produced by SAI were lower, while anti-icing efficiency and cold-spot temperature of SAI were higher than PTAI despite PTAI having higher average inner skin temperature than SAI. In other words, SAI showed better uniform temperature distribution on the nacelle lip-skin compared to PTAI.

Keywords: *Piccolo Tube Anti-Icing, Swirl Anti-Icing, Augmentor, Hotspot, Cold spot, Anti-Icing Efficiency, Standard Temperature Deviation, Coefficient of Temperature Deviation.*

Acknowledgement

I would like to take this opportunity to thank my son, daugther, mother and sisters for being a constant source of support and encouragement during four and half years. Particularly, thanks to my wife, Shuhairiah Daud, for her love, support, encouragement and sacrifice.

I would like to thank my supervisor Dr Jian Wang for providing guidance, discussion, correcting thesis and support during these years. I wish to thank my ex supervisors, Dr John Watterson and Dr Richard Copper for their suggestions and discussion during my early research stage. I would like to thank Michael and Richard from Bombardier Aerospace Belfast for providing information of nacelle lip.

Many thanks go to Hafiz, Tri, Patna, Sarjito, Hilmi, Ainor, Marwan and Joko for their friendship in Kingston University.

Financial support from Malaysian Government, University Science of Malaysia and Kingston University are gratefully acknowledged.

Contents

List of Figures

List of Tables

Nomenclature

3-D	Three dimensional
2-D	Two dimensional
A	Cross sectional area
$A_{D\text{-}C}$	Cross sectional area of D-chamber
A_{nozzle}	Cross sectional area of nozzle
$A_{sur\ lip\text{-}skin}$	Total area of internal lip-skin surface
A_{imp}	Effective-impingement-surface area
$C_{tem\ deviation}$	Coefficient of temperature deviation
C_p	Specific heat at a constant pressure
Cx	Jet spacing
d	Nozzle diameter
D_h	Hydraulic diameter
$\check{D}$	Ratio of Cross sectional area of nozzle to Cross sectional area of D-chamber
f	Wall friction
g	Gravity
G	Hot air mass flow rate per unit area of impingement surface
$\hat{G}$	Ratio of hot air mass flow rate to cross sectional area of D-chamber
h	Heat transfer coefficient
h_{sw}	Average heat transfer coefficient for SAI
h_{PTAI}	Average heat transfer coefficient for PTAI
k_f	Thermal conductivity of fluid
m	Mass flow rate
$m_{hot\ air}$	Hot air mass flow rate
m_{sw}	Mass flow rate of swirling air in D-chamber
Mn	Mach number
Nu	Nusselt number

Nu_{PTAI}	Average Nusselt number for PTAI
Nu_d	Nusselt number for circular tube
Nu_{sw}	Average Nusselt number for SAI
P	Air pressure
P_w	Wetted perimeter
Pr	Prandtl number
q	Heat flux
q_{ave}	Average heat flux of lip-skin surface
Q	Heat transfer through lip-skin
Q_{inlet}	Heat entering D-chamber
Q_{outlet}	Heat exiting from the exhausts
R	Air constant
R_f	Recovery factor
Re	Reynolds number
Re_d	Reynolds number for circular tube
Re_G	Reynolds number based on the area of impingement surface
Re_{PTAI}	Reynolds number for PTAI
Re_{sw}	Reynolds number for SAI
Si	Swirl intensity
St	Stanton number
Sw	Swirl number
T	Temperature
T_s	Local static temperature
T_{hi}	Temperature of hotspot
T_{lo}	Temperature of cold spot
T_{ave}	Average lip-skin temperature
T_{imp}	Average temperature of effective-impingement-surface

T_m	Mean air temperature
T_{tsw}	Mean total temperature of swirling air inside D-chamber
T_{nozzle}	Total temperature of hot air inside nozzle
T_{exh}	Exhaust temperature
$T_{adiabatic\ wall}$	Adiabatic temperature of lip-skin
$T_{piccolo}$	Temperature of hot air inside piccolo pipe
T_j	Jet temperature
T_w	Wall temperature
T_y	Local static temperature
T_∞	Ambient temperature
$\dot{T}$	Dimensionless temperature
$\widehat{T}$	Dimensionless average lip-skin temperature
$\check{T}$	Dimensionless air temperature
$\check{T}_{tsw}$	Dimensionless total temperature of swirling air in D-chamber
T_0	Total temperature
$T_{inner\ ave}$	Average inner skin temperature
u	Air velocity
u_{ave}	Average velocity of swirling air in D-chamber
u_m	Mean velocity of air
u_j	Jet velocity
u_y	Local air Mach number
u_∞	Free stream velocity of air
$V_{D\text{-}C}$	Air volume inside D-chamber
W	Work done
z	Distance from local point to the nozzle
Z	Distance from nozzle outlet to impinging point
$\dot{z}$	Elevation head

Abbreviation

AI	Anti-icing
AL	Acoustic liner
BAL	Bias acoustic liner
CFD	Computational fluid dynamic
DI	De-icing
DCU	De-icing control unit
DWAI	Double-walled anti-icing
EFF	Anti-icing efficiency
EIDI	Electro impulse de-icing
EMEDS	Electromagnetic expulsion de-icing system
ESB	Energy storage bank
ETH	Electric thermal heater
FAI	Fluid anti-icing
LPED	Low power electro-thermal de-icing
LPDI	Low power de-icing
LWC	Liquid water content
MVD	Mean volumetric diameter
NRA	Nozzle rotation angle
PIB	Pneumatic inflatable boot
PIIP	Pneumatic impulse ice protection
PTAI	Piccolo Tube Anti-Icing
RANS	Reynolds Averaged Navier Stokes
SAI	Swirl anti-icing
SST	Shear stress transport
SWDs	Super-cooled water droplets
SQC	Statistical quality control

TMEDS	Thermo-mechanical expulsion de-icing system

Greek Letter

ρ	Density
ω	Dimensionless air velocity
μ	Dynamic viscosity
γ	The ratio of specific heats (1.41)
σ	Temperature deviation
σ_{hi}	Dimensionless hotspot temperature
σ_{lo}	Dimensionless cold spot temperature
θ	Impingement angle
τ	Shear stress
δ	Boundary layer thickness
α	Angle of attack
K	Kelvin

CHAPTER ONE: Introduction

1.1 Background and Motivation

Ice accretion on the critical surface of the aircraft, leading edges of tail, wing and nacelle, contributes to a lot of problems. The ice accumulation on the wing leading edge impacts the aerodynamic performance, i.e. it reduces lift force and increases drag force which in turn causes increase in the fuel consumption [1]. In the worst case scenario, the aircraft could also crash on account of the ice accretion deforming the design of the wing [2]. Between 2000 and 2008, at least eight aircraft crashes were reported because of icing problems. Most commercial aviation accidents occur during take-off or landing. Table 1.1.1 provides a summary of aircraft crashes from 1982 to 2008 in which ice accretion on an aerodynamic surface was considered among one of the primary causes [3].

Table 1.1.1: Summary of aircraft crash from 1982 to 2008 [2]

Year	Site	Air Carrier	Aircraft	Phase
1982	U.S.A.	Air Florida	Boeing 737–222	Takeoff
1985	Canada	Arrow Air	McDonnell-Douglas DC-8-63CF	Takeoff
1985	Russia	Aeroflot	Tupolev TU-134A	Landing
1987	U.S.A.	Continental Airlines	McDonnell-Douglas DC-9-14	Takeoff
1989	Canada	Air Ontario	Fokker F-28	Takeoff
1991	U.S.A.	Ryan Airlines	McDonnell-Douglas DC-9-15RC	Takeoff
1991	Russia	Aeroflot	Antonov AN-12B	Landing
1991	Russia	Tartarstan Airlines	Antonov AN-24	Landing
1992	U.S.A.	USAir	Fokker F-28	Takeoff
1993	Macedonia	Palair Macedonian	Fokker 100	Takeoff
1994	U.S.A.	American Eagle	ATR 72-212	Landing
1994	Russia	North Western Air Transport	Antonov AN-12B	Landing
1995	Italy	Romanian Banat Air	Antonov AN-24B	Takeoff
1997	U.S.A.	Comair Airlines	Embraer EMB120-Brasilia	Landing
1998	Canada	Private	CRJ-200LR	Takeoff
1999	Turkey	Turkish Airlines	Boeing 737-400	Takeoff
2000	Russia	Vologodskiye Airlines	Yakovlev YAK-40	Takeoff
2002	U.K.	Private	Bombardier CL-600-2B16	Takeoff
2004	U.S.A.	Private	Bombardier CL-600-2A12	Takeoff
2004	China	China Eastern Airlines	Bombardier CRJ-200LR	Takeoff
2005	U.S.A.	Private	Cessna Citation 560	Landing
2006	China	China PLA Air Force	KJ-200	Landing
2007	Russia	Private	Bombardier CL-600-2B16	Takeoff
2008	Armenia	Belavia	Bombardier CL-600-2B19	Takeoff

The probable causes of the last aircraft crash in the United States, in February 2005, were documented by the National Transport Safety Board (NTSB). The report suggested that the most probable reason for Cessna Citation 560 crashing was the formation of rime ice on the wing leading

edge during descent. As a result, the left wing suddenly stalled, causing the aircraft to roll towards the left resulting in the crashed [4]. Besides the wing leading edge, ice accumulation on the nacelle lip-skin surface restricts the air flow through the engine, and can lead to loss in performance and possible engine malfunction. Moreover, the ice may shed and be ingested into the engine or hit the blades and the acoustic lining in the nacelle cowl zone, resulting in severe damage to the engine and noise abatement devices [5].

In terms of noise pollution, aircraft noise is the second highest after road traffic and is increasing yearly. The Federal Aviation Administration (FAA) has therefore introduced a certification scheme requiring all aircraft to limit their noise. Therefore, a noise abatement device is implanted in the nacelle cowl zone in order to reduce noise from the engine. The acoustic liner (AL) has been introduced and implanted in the nacelle cowl zone in order to reduce noise generated by the engine. Recently, researchers have tried to incorporate Bias Flow Acoustic Liner (BAL) into the inner skin of nacelle lip to overcome the limited space and deficiency of heat transfer when implanting AL in the nacelle nose cowl zone. The heat transfer characteristic of BAL was studied by Ives at Queen's University Belfast (QUB) [6].

1.2 Disadvantages of Piccolo Tube Anti-Icing system

Since the ice accumulation is one of probable reasons of aircraft crash, the Federal Aviation Administration (FAA) therefore necessitates that aircraft manufacturers to demonstrate that their aircraft can fly safely in icing conditions, as defined in the Federal Airworthiness Regulations (FAR/JAR) Part 23 and 25, Appendix C. Currently, Piccolo Tube Anti-Icing (PTAI, Figure 1.3.1) is one of the most popular hot air anti-icing systems and widely used in commercial passenger aircraft. This anti-icing system is implemented on the wing leading edge, nacelle lip and leading edge of aircraft tail.

PTAI utilizes the high temperature and velocity of the impinging jet to keep the inner skin warm and free from icing. The hot jet from the nozzle impinges on the inner skin. As a result, the hotspots occur on the inner skin along the nacelle lip-skin. The high temperature of the hotspots along the inner skin of the nacelle lip may cause problems and even destroy BAL. Besides, PTAI produces non-uniform temperature distribution and low temperature cold spot, which causes runback ice accretion on the downstream of outer skin [44]. In addition, PTAI requires complex plumbing and is made from high density material, resulting in high manufacturing costs and weight penalties.

1.3 Advantages of Swirl Anti-Icing

In swirl anti-icing (SAI, Figure 1.3.1) system, the hot air with high velocity from the nozzle mixes with cooler stagnation air in D-chamber. Subsequently, this mixed air swirls around annular D-chamber and transfers uniform heat to nacelle lip-skin (convection process). Since BAL may possibly be installed on the inner skin of the nacelle lip, SAI system has the potential to be used together with BAL since it does not produce hotspots with the same level of temperature as the hotspots of PTAI system along the inner skin. Moreover, SAI system is an effective anti-icing system [42] and capable of providing uniform temperature distributions along the nacelle lip-skin and causing no runback of ice accretion on the downstream area [44]. In addition, SAI has fewer components, simple plumbing, is light and inexpensive compared to PTAI.

PTAI SAI

Figure 1.3.1: Photo of PTAI and SAI [100]

1.4 Importance of SAI study

The development and demand on low noise emission in aircraft industry necessitate BAL in the inner skin of nacelle lip. In the meantime, aircraft manufacturer needs to provide anti-icing system inside the D-chamber as ruled by FAA. The hot air impinging method (PTAI system) as anti-icing on the critical aircraft surface is very effective [39]. However, the hotspots along nacelle inner skin would potentially destroy BAL if BAL is installed in the inner skin of nacelle lip. Besides, this method causes cold spot with relatively lower temperature in the outer skin, resulting in runback ice accretion on the downstream of nacelle lip. This method also produces non-uniform temperature distribution along the nacelle lip, resulting in low average lip-skin temperature and anti-icing efficiency. Consequently, the need of alternative technique to reduce hotspot temperature and increase cold spot temperature is obvious. An old technology (SAI system) has a potential to solve hotspot problem along inner skin of nacelle. Also, SAI can provide uniform temperature along nacelle lip-

skin. Moreover, SAI only produces one hotspot on the outer skin, which is at very low temperature level compared to hotspots of PTAI.

Although SAI system has been adopted in the aircraft industry for many years, there is no systematic and comprehensive study ever conducted in the literature. The following paragraphs will discuss the most important factors which affect the performance of SAI system.

The distance from nozzle to impinging point (Z) is a key factor in SAI thermal performance improvement. As Z increases, the momentum and heat exchange between hot air and cold air increases. Consequently, the mixing process is enhanced, which leads to lower velocity gradient on the hotspot vicinity and higher swirling air velocity inside the D-chamber. As a result, the average lip-skin temperature and cold spot temperature increases, and hotspot temperature decreases. The alteration of nozzle direction towards inner skin and nozzle length are the ways to increase Z in SAI thermal performance study.

The nozzle diameter is expected to have tremendous effect on SAI thermal performance. As nozzle diameter increases, the velocity of jet from the nozzle decreases, contributing to low velocity gradient on the impinging spot. Moreover, the air mixing activity in the D-chamber is inversely related to nozzle diameter, resulting in low swirling air velocity in the D-chamber. Therefore, increase in nozzle diameter is expected to decrease average temperature, hotspot temperature and cold spot temperature of nacelle lip-skin.

The nozzle outlet shapes; including sloped nozzle and ellipse nozzle, influence air mixing process in the D-chamber and SAI thermal performance. The earlier air mixing process is expected to result in better SAI thermal performance and temperature distribution on the nacelle lip-skin. As the hot air mixes with cold air in earlier stage, the hot air transfers higher momentum and heat to the cold air. Thus, the velocity gradient on the impinging-surface decreases leading to lower hotspot temperature on the outer skin. Moreover, as the cold air receives higher momentum and heat from the nozzle, it increases average heat transfer capability of swirling air in the D-chamber, resulting in better average heat transfer coefficient, average lip-skin temperature and cold spot temperature.

The application of augmentor in SAI enhances air mixing process in the D-chamber, and then improves uniformity of temperature on the nacelle lip-skin. Since the jet from the nozzle creates low air pressure in augmentor throat, the momentum and heat exchange between hot air and cold air robustly increased, which in turn contributes to a significant improvement in the uniformity of swirling air velocity and temperature distribution in D-chamber. This phenomenon enhances uniformity of temperature distribution on the nacelle lip-skin.

From 1985 till now, only few researchers [42-45] studied the SAI thermal performance. None of studies utilized CFD to predict SAI thermal performance. Therefore, the present study employs CFD to understand the parameters associated with swirl anti-icing. Furthermore, some alterations have been made on design and arrangement of nozzle orientation in order to enhance SAI thermal performance i.e. nozzle rotation angle, nozzle diameter, nozzle length and nozzle outlet surface. Moreover, the effect of augmentor on the SAI thermal performance is investigated in the present study. Besides, a new parameter has been introduced and utilized to measure the uniformity of temperature distribution on nacelle lip-skin. In addition, a new empirical correlation for SAI has been developed and presented in the study. Therefore, the present study is unique in nacelle lip-skin anti-icing study.

1.5 Aim and Objectives

The primary goal of this work is to improve the SAI thermal performance and this is carried out by:

- increasing the cold spot and average temperatures
- reducing the hot spot temperature and
- enhancing uniformity of lip-skin temperature

The air mixing process in the D-chamber affects the SAI thermal performance. Consequently, the characteristics of air mixing process that takes place between the hot air from nozzle and cold air in the D-chamber requires further assessment. Moreover, the study also investigates the effects of nozzle rotation angle, nozzle length, nozzle diameter and nozzle outlet surface on air mixing process and the functionality in improving the heat transfer performance and uniformity of temperature distribution in the nacelle lip-skin. In addition, the empirical correlation for SAI system has been developed and plotted in the present study. This study also investigates the effects of augmentor/ejector employed in the SAI system on the air mixing process and heat transfer characteristics of the Falcon 20g nacelle lip. Finally, the comparison of thermal performance between SAI and PTAI for BR 710 nacelle lip-skin is elaborated at the end of the thesis in order to demonstrate the effectiveness of SAI as an ice protection system.

The objectives of the study are as follows:

1. To conduct critical literature review and understand the state-of-the-art ice accretion phenomenon and ice protection system, fundamentals of internal and external flows, and basics of augmentor and acoustic liner.
2. To carry out numerical simulation for PTAI system and validated with experimental data obtained by Bombardier Aerospace Belfast at various altitudes and to compare the average Nusselt number for PTAI at four different altitudes with the experimental correlation developed by Jeffry Brown [41].
3. To carry out numerical simulation for SAI system at the ground level and laboratory condition and study the performance of various nozzle types and diameter in SAI system on Falcon 20g nacelle lip.
4. To develop a correlation between several thermal performance characteristics of SAI such as dimensionless cold spot temperature, dimensionless hotspot temperature, average Nusselt number of SAI and coefficient of temperature deviation on the nacelle lip-skin, for different nozzle types and diameter at the operating condition.
5. To carry out numerical simulation for the SAI system with augmentor to study the effects of the augmentor on the thermal performance of the SAI system for Falcon 20g nacelle lip.
6. To compare the thermal performance between PTAI and SAI systems on the BR 710 nacelle lip at several hot air mass flow rates at the climb operating condition.

Upon understanding the aim and objectives of this investigation, the thesis is organised as follows:

Chapter 2 critically reviews the literature on ice formation, exiting ice protection, impinging jet study, application of CFD in ice protection study, augmentor system and design of AL and BAL.

Chapter 3 discusses the simulation of the thermal performance for PTAI on BR710, validates simulation results with experimental results from the Bombardier report [100], and elaborates the comparison between the empirical correlations based on the simulation outcomes in this study and the experimental empirical correlation developed by Brown [41]. A modified Brown empirical correlation is presented in the end of this chapter.

Chapter 4 concentrates on the thermal performance of a small nozzle in the SAI system on the Falcon 20g nacelle. Some design features related to small nozzle designs and arrangements of SAI system have been discussed in this chapter.

Then, the effects of nozzle diameters and exhaust areas on the thermal performance of SAI are elaborated in Chapter 5. The empirical correlations based on simulation results for various nozzle diameters are developed and presented in the end of Chapter 5.

Chapter 6 explores the effect of augmentor in the SAI system on the thermal performance for Falcon 20g nacelle lip. Some design features of augmentor and its arrangement with nozzle are discussed in this chapter.

Chapter 7 emphasises on the comparison of thermal performances of PTAI and SAI for BR710 nacelle lip at climb operating condition.

Chapter 8 presents the conclusions of the SAI and PTAI studies with some suggestions for future work.

CHAPTER TWO: Literature Review

In this chapter, an overview of the basics of ice accretion phenomenon on the surface is presented in the beginning. Then, it is directly followed by a survey of de-icing and anti-icing devices. The fundamental of impinging jet is reviewed in the third section. The fourth section reviews the application of Computational Fluid Dynamics (CFD) in anti-icing study and other related areas. The fundamentals of heat transfer for external and internal flow are described in fifth section. In addition to this, research and application of augmentor system is explained in sixth section. In the final section, the basic mechanism of AL and BAL are discussed. This review demonstrates the state-of-the-art hot air ice protection system and relevant subjects, which are the foundation of the proposed study. Studying the fundaments of ice accretion on the aircraft surface may help researchers to design the appropriate ice protection devices required for the aircraft. The ice accretion on the aircraft surface generally depends on the type of ice protection devices used [8].

2.1 Ice Accretion Phenomenon and Potential Harm

The ice accretion on the nacelle or wing surface occurs mostly when the aircraft is on the ground or under cruise conditions. On the ground, the icing on aircraft surface occurs on account of slush, snow and clear ice or a combination of them after the snow and freezing ice pours over the aircraft surface. Besides, the icing can build up on the aircraft surface when the ambient temperature is above freezing point as a result of below-freezing fuel in the wing [7].

The ice also accumulates on the aircraft surface when the aircraft is cruising through clouds containing super-cooled water droplets (SWDs) at a temperature below 0°C. Normally, the diameter of SWDs in the clouds range from 5–50 microns. In fact, SWDs in the cloud with temperature under 0°C are under metastable conditions. Therefore, SWDs freeze upon impinging on the aircraft skin, forming a non-aerodynamic shape, especially on the leading edge of the nacelle and wings [5]. The ice build-up rate or icing intensity strongly depends on meteorological and aircraft-specific factors, such as ambient temperature, liquid water content (LWC), SWD size, air speed and ice protection devices [8].

The ice structure can be categorized into three forms, rime, glaze and mixed. The rime form is developed at the cloud temperature in the range of -40°C to -20°C. In this temperature range, SWDs freeze immediately on contact with the surface after impinging on the aircraft skin. The rime ice usually occurs when the small droplets collide with the aircraft surface. Research shows that the air is trapped inside the rime ice, which renders the rime ice appear milky white and opaque. Rime ice has lower density (approximately 880kg/m^3) than glaze ice, which has a density of 917kg/m^3. In

general, the feature of rime ice accumulating on the leading edge follows a streamline shape (essentially an extension of the airfoil) as shown in Figure 2.1.1. In this ice form, drag force occurs due to surface roughness of the rime ice surface [12].

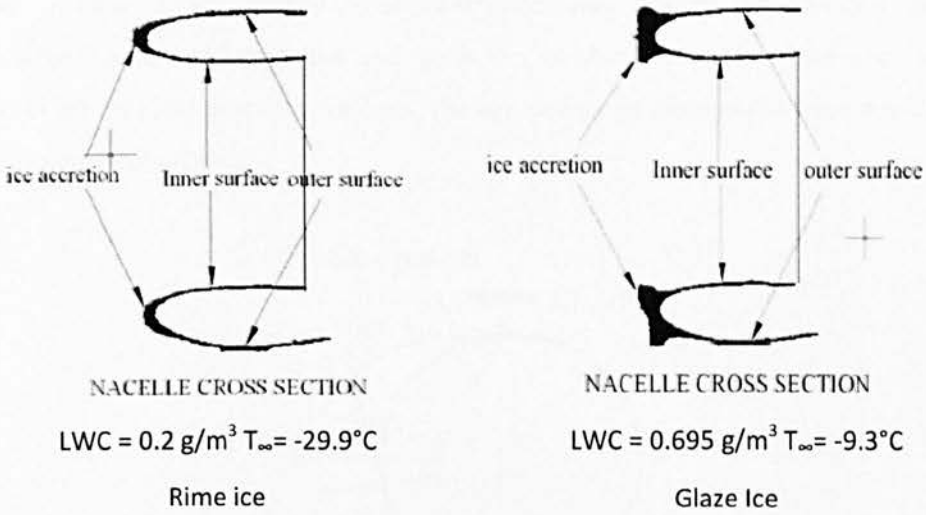

Figure 2.1.1: Ice accretion on the nacelle inlet section [17]

The glaze formed at the centre of the ice is followed by the formation of rime ice, which further results in the mixed ice. The mixed ice form is the combination of rime and glaze ice forms. Rime ice in mixed ice form is also known as rime feathers since it is thin, feather-like shaped and delicate in nature [9, 10, and 13]. Normally, glaze ice appears in the cloud temperature range of -18°C to 0°C. This ice form is translucent due to less or no air being entrapped inside the ice particle. Glaze ice forms in a non-aerodynamic shape due to laminar-turbulent transition occurring within the boundary layer. The unfrozen water and the ice substrate in the glaze ice boundary layer becomes a complex air-water-ice multi-phase fluid flow [11]. The glaze ice is hard, dense and has good adhesive qualities. The bond between the ice and the surface is stronger than the bond between particles of the ice. Therefore, it becomes extremely difficult to be removed, except by melting [14]. The drag force on the aircraft increases in glaze ice primarily due to flow separation occurring at the aft of the ice horn [12].

Many researchers have studied ice accretion in laboratories instead of real flight due to non availability of requisite instruments, measuring devices and recording difficulties [12]. According to observations made by a previous study on the cylinder, the glaze ice can be characterized into three major zones, as shown in Figure 2.1.2. In Zone 1, the icing is smooth and translucent with very low roughness. On the slight downstream surface (or Zone 2), the rough and horn-shape zone appears

before the run back, whereas the rime feature zone (Zone 3) emerges in the aft of Zone 2. As SWDs impinge on the surface, they will freeze, and then ice formation further enhances the convective heat transfer and collection efficiency characteristics. As a result, the ice accretion process is enhanced and the double-horn ice shape begins to build in Zone 2. Then, the rate of freezing decreases as the heat transfer coefficient decreases during double-horn development. Consequently, the run back continues and forces the ice shape away from stagnation point. As this reduction of the freezing process continues, the appearance of glaze shape becomes clearer until it is virtually transparent [13-15].

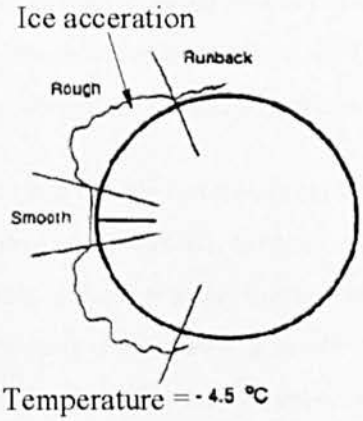

Figure 2.1.2: Ice accretion zones on the cylinder [15]

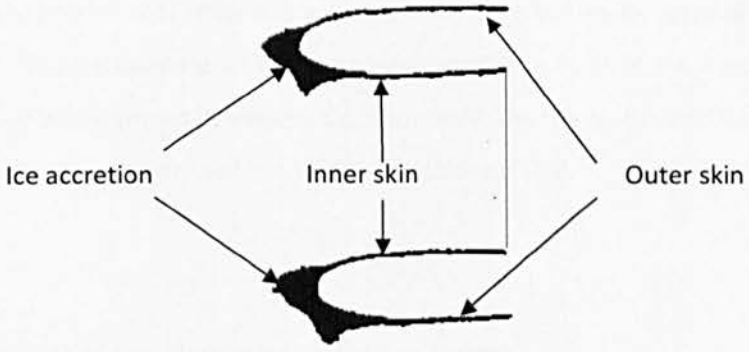

Figure 2.1.3: Ice accretion on the underside of nacelle lip-skin [17]

The angle of attack (α), mean volumetric diameter (MVD), inlet mass flow, LWC and nacelle geometry have been identified as characteristics affecting ice accretion features on the leading edge [16]. For instance, the ice accretion thickness for LWC of 0.695g/m^3 (glaze) is thicker than that for the LWC of 0.2 g/m^3 (rime) is, as shown in Figure 2.1.1. The result also shows that the ice shape moves towards the outer skin as the mass flow rate of free stream increases. Moreover, the ice

accretion seems to be more towards the underside of the nacelle geometry since α increases from 0° to 15°, as shown in Figure 2.1.3 [17].

Besides ice accretion layout, the knowledge of the condition in the clouds might be helpful in designing anti-icing system. Basically, the clouds have been divided into three regions: supercooled, mixed-phased cloud and glaciated cloud. The droplets start as SWDs when the temperature is 0°C or below. The pure liquid supercooled cloud (consisting of SWDs) occurs when its temperature is in the range of 0°C to -4°C. As the temperature decreases, the ice particles are formed in the cloud, since active freezing nuclei are more numerous at lower temperatures. The phenomenon of both SWD and ice particles existing in the clouds is called mixed-phase cloud. This phenomenon usually happens at a cloud temperature range between -4°C and -20°C. As the temperature drops further, i.e. -20°C and below, the mixed-phase cloud changes to glaciated cloud [18].

Ice accumulation on the wing, tail and nacelle can be dangerous to the aircraft. Icing on the aircraft tail reduces the stability and control of the aircraft, especially when the aircraft is climbing, cruising and landing at low Mach number [19]. Furthermore, the aircraft will lose control because of the ice accumulating on the surface. The icing on the wing skin will cause lift force to decline, increasing drag and altering moment characteristics [19]. Aircraft fuel consumption will therefore increase and aviation operating costs will escalate.

In the worst-case scenario, some plane crash incidents occur because of icing. For instance, air crash investigators identified that icing was a factor in the McDonnell Douglas MD-81 twin jet transport aircraft crash. The ice build-up on the wing leading edge in front of the nacelle intake broke during the takeoff and was ingested by engine. Consequently, the fan blades and compressor failed causing the aircraft to go down after four minutes during take-off [20].

2.2 Commercial Wing and Nacelle Ice Protection System

Ice protection is an important consideration in aviation and its significance has increased after it was discovered that some aircraft crashes occurred because of ice accumulation on the aviation critical surface [2-6]. Currently, there are two types of ice protection system widely employed in commercial aviation: the anti-icing system (AI) and de-icing system (DI). The DI system is used in the periodic removal or breakage of ice accumulation, whereas the AI system prevents the ice accumulation on the aircraft components at all times. Thus, the knowledge of the ice protection is very essential in deciding the most appropriate ice protection device suitable for different icing conditions.

2.2.1 De-Icing System

DI is the type of ice protection system which advocates removal of ice accumulation periodically on the outer surface of aviation critical components, i.e. the nacelle and wing leading edges. The mechanical deformations, thermal and chemical fluid methods, are utilized in the de-icing system. Although this system is unable to keep the surface 100% free from ice, its main advantage is that it requires low power consumption. One to three minutes is the regular interval time for the DI device to activate and thus remove the ice accumulation on the surface. The DI device is usually suitable for small aircraft applications due to low energy requirements [5 and 24].

Figure 2.2.1: Construction and operation of pneumatic inflatable boots [21]

The pneumatic inflatable boot (PIB) is a mechanical deformation de-icing device widely used in light airplanes. The advantages of PIBs are light, low operational costs and adaptable to many aircrafts. The development of the inflatable boot dates back to 1928, since then PIBs have been used in over 30,000 aircrafts around the world [21]. Basically, a PIB device contains inflatable strips of rubber and is located on the external surface. The idea is that the ducts inside the rubber strips function as an air conduit. These ducts become inflated when they receive pumped air from the engine/compressor, as shown in Figure 2.2.1. As a result, the surface distorts which will break ice down due to a combination of shear, bending and peel forces. The broken ice is then carried away from the surface by aerodynamic forces [21]. In order to avoid weathering and erosion, the PIB has been made from a special compound material, stretchable fabric-reinforced elastomer.

However, the commercial PIB has low efficiency for shedding ice with thickness lower than 0.762mm. The average lifespan of commercial PIB is only around six years for business aviation due to rain erosion longevity and prolonged resistance. Moreover, PIB is not an aerodynamic-friendly device due to the deformation of surface feature when it has been activated [22]. To overcome such disadvantages of PIB, BF Goodrich developed Pneumatic Impulse Ice Protection (PIIP). The aviation surface, i.e. the wing surface, can distort quickly to about 0.762mm in 50 microns, when the PIIP is planted underneath it. The PIIP is built from titanium alloy overlaying a flexiblized, and a thermoset plastic matrix to enhance PIIP lifespan. The flat fabric-reinforced tubes expand periodically with a

rapid movement when pressurized air is activated in the PIIP system [22]. However, PIIP is unable to keep the aviation surface consistently clean from icing. Besides, both PIBs and PIIP are expensive and must be replaced regularly. The ice that remains on the surface is hard to remove by pneumatic boot, making further ice removal more difficult. In addition, any ice formed on the wing aft of the active portion will not be removed, especially at high angle of attack [23].

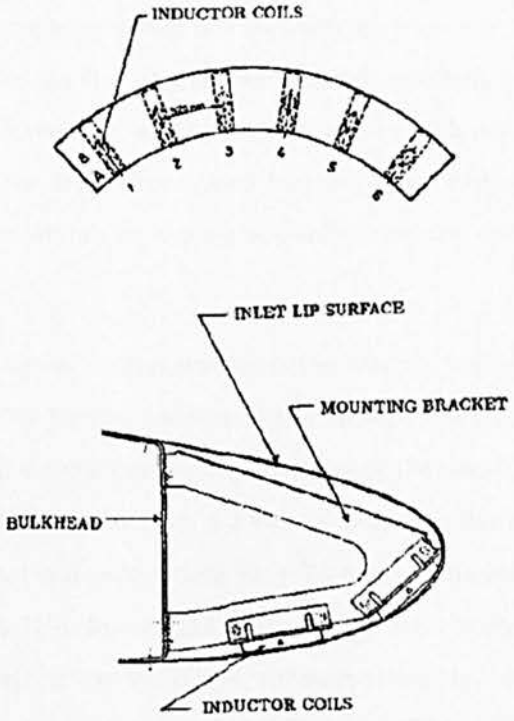

Figure 2.2.2: A310 Inlet Lip EIDI Installation [27]

Besides PIB, the other mechanical deformation DI systems are Electro Impulse De-icing (EIDI) and Electro Magnetic Expulsion De-icing (EMEDS). All of these de-icing devices are also known as Low Power De-icing (LPDI) devices. LPDI systems have been developed in order to overcome energy constraint in ice protection devices. LPDI devices have low power requirement for activation, one hundred times lower than thermal anti-icing, i.e. electrical heater or hot air anti-icing [24]. Therefore, LPDI devices are suitable for small aircrafts with a limited power source. Furthermore, LPDI devices are lighter when compared to other de-icing devices [25].

In chronological order, the EIDI device was suggested by Goldschmidt (1937) and had been explored by Soviet researchers in 1960s. The device became popular in Europe and the USA during the 1970s as an aviation de-icing device [26]. Nowadays, EIDI capacitors are discharged through an electric coil. When the EIDI is activated, it produces a huge magnetic field, and thus a large amplitude and impulse, which act on a nearby electrical conductive plate, as shown in Figure 2.2.2. The impulse force exerting on the aluminium nacelle surface results in the surface slightly expanding, then

contracting, and finally generating mechanical vibrations on the leading edge. As a result, ice accumulated on the surface is shed due to mechanical vibration from impulse forces of EIDI [26 and 27]. Unfortunately, there are two issues regarding the suitability of EIDI as nacelle anti icing applications. First concern is the ability of EIDI to shatter ice particles small enough to be ingested through turbofan blades. Zumwalt [24] conducted two experiments to address this issue. In the first experiment, he installed 11 EIDIs at 9 different locations on a nacelle nose. He claimed that this system could be applied on the engine inlet of a business jet. However, ice accretion thickness lower than 0.508mm still remained on the nacelle inlet surface resulting in high drag force. Secondly, Labeas et al. [25] mentioned that the leading edge structures with radius of curvature smaller than 10mm were difficult to install EIDI. They added that structural fatigue problems would probably appear due to the repetitive impulsive loading applied during the operation of the LPDI, EIDI and EMEDS systems [25].

Currently, the EMEDS is used in conjunction with the electric thermal heaters (ETH), which are known as hybrid systems. The EMEDS consists of low current and voltage actuators which include conductive strips fabricated on the flexible dielectric sheet [26 and 27]. The EMEDS is capable of removing ice accretion with thickness from 1.27mm to 50.8mm. Besides low power consumption, this system is able to control and vary cycling time. As a result, de-ice thickness can be controlled and maintained indefinitely [27]. In addition, the de-icing control unit (DCU) and Energy Storage Bank (ESB) have been added to the system to enhance reliability, impart force, fire sequence of actuator, de-ice timing and heat power output of LPDI in both EIDI and EMEDS systems [28].

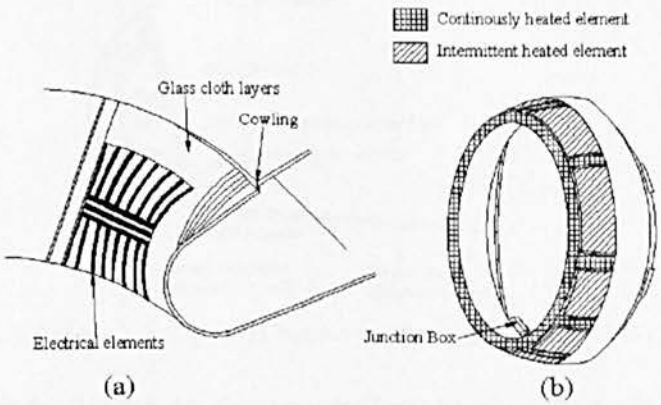

Figures 2.2.3: Electrical elements arrangement layout [5]

The electric thermal heater (ETH) system has been used in small aircrafts where available power for ice protection is limited. In nacelle application, ETH is widely applied in turbo-propeller engines, and in small items such as pitot tubes, scoops and radio masts [20]. Sometimes, ETH systems are also utilized on the nacelle lip-skin. The ETH uses resistive heaters (main part) and has been installed on

the outer skin of the nacelle intake. It consists of strip conductors sandwiched between layers of neoprene, or glass cloth impregnated with epoxy (Figure 2.2.3). In order to protect the pads against rain erosion, the electrical heater elements are coated with polyurethane-based paint. The electric power is used to produce heat and has been supplied by a generator. To reduce the size and weight of the generator, the engine, propeller and airframe are also used as electrical sources.

Usually, the ETH is planted on the underside of the aft of the leading edge skin. The cycling time of the intermittent heated elements needs to be arranged properly in order to ensure that the engine can safely ingest the amount of ice that will be collected during both the heat-off and heat-on periods. This method will be sufficient for ice to shed without causing any run-back icing occurring behind the heated areas [5]. The disadvantage of ETH is that it contains low thermal conductivity of polyurethane (0.02 W/mK). The poor thermal conductivity degrades the thermal efficiency of conventional ETH systems. In order to overcome this problem, the Low Power Electro-thermal De-icing (LPED) system was introduced in 2005. The main difference is that the LPED heating element is installed directly on leading edge. Galdemir et al. [30] claims that LPED only needs low power to operate, 20–50% lower than that the ETH system requires. They also claim that LPED is more capable in reducing potential of runback ice. However, the potential of LPDI on the nacelle lip-skin is still unknown due to lack of research related to its performance on the nacelle leading edge.

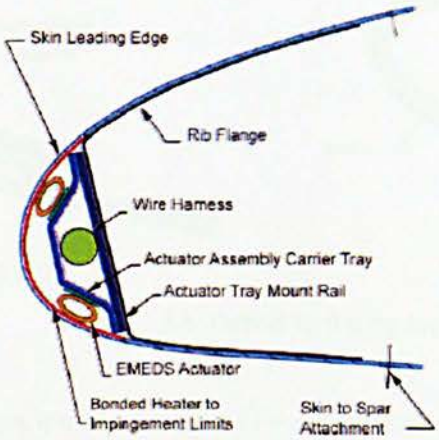

Figure 2.2.4: TMEDS hybrid system configuration [31]

The thermo-mechanical expulsion de-icing system (TMEDS) applies a similar concept to the hybrid anti-icing system. Since the TMEDS is a DI device, it allows thin ice to form in the SWD impingement zone and removes it by co-ordinated sequencing of the thermal and EMEDS sub-system. In contrast, the hybrid anti-icing system keeps the aviation surface warm and free from ice accumulation at all times. Therefore, the heater needs to be switched on for the whole time. Although the TMEDS requires lower power than other anti-icing systems, its capability to remove ice is greater than

conventional expulsive systems. The system is suitable in cases where the ice accumulation thickness is 1.27mm or thinner. The schematic diagram of the TMEDS is shown in Figure 2.2.4 [31].

2.2.2 Anti-icing System

The AI system is an ice protection means of preventing ice accretion at all times. Nowadays, methods regularly used include thermal (hot air and electric heater), and chemical fluid. The thermal anti-icing system is widely used on the nacelle leading edge due to the importance of this area to be kept free from ice accumulation at all times.

The concept of electric AI systems is similar to that of electric DI systems. The electric AI is installed on the leading edge and needs to be permanently switched on to keep the nacelle lip-skin free from ice accumulation, thus avoiding ice shedding and ice ingestion by the engine [28]. Besides aircrafts, this ice protection is also used on helicopter rotors in order to protect tail and main rotor blades from ice damage [33]. Currently, electric heaters have been combined with LPDI in order to reduce energy consumption in the AI system, which is called a hybrid anti-icing system [32].

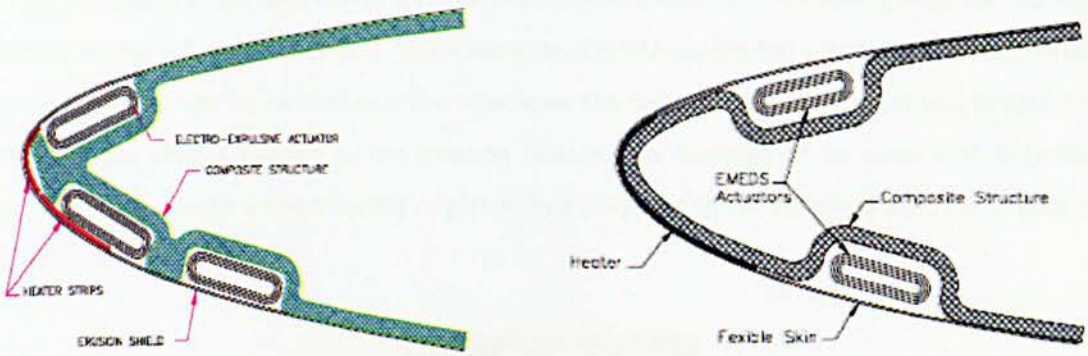

(a) EIDI (b) EMEDS

Figure 2.2.5: Hybrid anti-icing layout [32]

The hybrid anti-icing system is a combination of the ETH anti-icing and LPDI systems, either EIDI or EMEDS. It is an economic alternative for ice protection instead of hot air which requires a lot of energy to bleed hot air from compressor to leading edge. The heaters on the leading edge are permanently kept warm to ensure there is no ice built-up in this area. At the same time, EIDIs or EMEDSs are placed on the runback region to break up ice periodically. Figure 2.2.5 shows the schematic diagram of the hybrid anti-icing system [32].

A special liquid, glycol, which has a low freezing temperature, is used in the fluid anti-icing (FAI) system. A mixture of ethylene/propylene/diethylene glycol additives and de-ionized fluids/water is

pumped through porous panels. Among three types of glycol, propylene glycol is the most popular and widely used in aircraft anti-icing due to its having the lowest toxic glycol level compared to the other two [33]. A typical concentration of glycol in an FAI system varies from 50% to 80% [34]. Liquid is then impregnated with impacting water droplets resulting in a lower freezing temperature of SWD than the local/ambient temperature [33]. However, the freezing temperature increases with the amount of SWD or LWC. An FAI system consists of porous leading edges, a reservoir (usually holding 27.25 litres of liquid), and a pump. The system can usually last for 3.5 hours [36]. Laser-drilled titanium panels are used instead of stainless steel due to higher performance and lighter weight. These panels have thousands of tiny holes and are bonded/riveted into place over the wing's leading edge to keep this area free from ice. The glycol is capable of de-icing by dissolving the bonds between the accreted ice and the panel skin. Within a few seconds to several minutes, the dynamic force will carry the broken ice accretion to downstream. This build-shed cycle is then repeated, without allowing any permanent ice accretion to form on the surface. The laser-drilled holes and locations for porous panels are shown in Figures 2.2.6 to 2.2.8 respectively. The ambient temperature, LWC in the air, velocity and droplet size are characteristics influencing minimum glycol flow rate (consumption). In addition, the ice shedding time is affected by incident angle α, glycol mass flow rate, type of ice and size of ice. The FAI system is capable of removing large ice cap from the surface within a few minutes [23]. Unfortunately, the FAI system has several drawbacks. Firstly, the glycol solution must be carried onboard whenever the need of ice protection is anticipated. This will increase the weight burden of the aviation system. The duration of ice protection is limited, around 3.5 hours, due to a finite supply of glycol fluid [35]. So the FAI system is risky for long-range aviation.

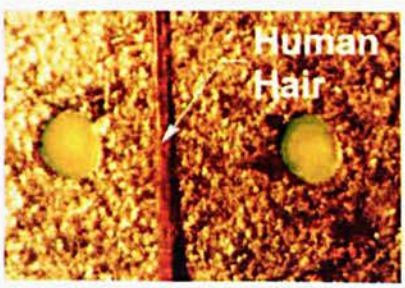

Figure 2.2.6: View of laser-drilled holes [www.weepingwings.com]

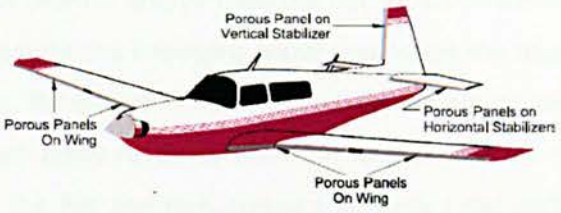

Figure 2.2.7: Fluid anti-icing system [www.weepingwings.com]

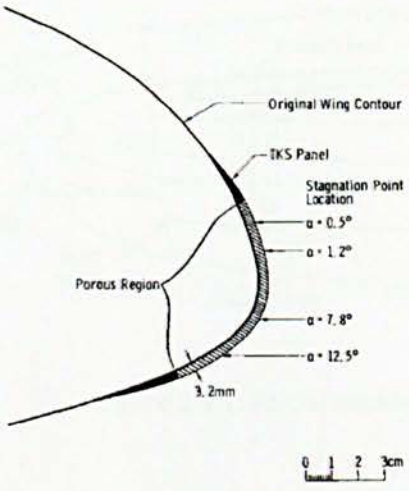

Figure 2.2.8: Cross section of porous panel fluid anti-icing system [23]

2.3 Hot Air Anti-icing System

The hot air anti-icing system, particularly the PTAI is one of the most popular thermal anti-icing systems. This method has been employed as nacelle and wing ice protection mechanism in modern commercial aviation [37]. Thermal anti-icing systems are classified as either evaporative or running wet. In evaporative mode, the surface is heated sufficiently to evaporate the impinging ice and then prevent runback beyond the heated zone. In running wet mode, the surface is heated to prevent the impinging ice from freezing within the heat zone [38]. This mode requires heat at a much lower temperature than the evaporative mode. A hot air anti-icing system is generally used in evaporative mode to keep the nacelle lip-skin free from ice accretion during cruising. Although this system requires a lot of energy to supply hot air to the nacelle leading edge, it is the most effective and reliable ice protection device in avoiding ice accumulation on the surface. The advantage of hot air anti-icing system is that it can also prevent very thin ice formation on the surface. This high level performance is not observed for any other ice protection systems [39].

In the hot air AI system, the thermal energy from the hot air is transferred to the nacelle lip-skin. This energy is used to evaporate the impinging water and keeps the nacelle lip-skin temperature above freezing point. In fact, the engine compressors supply the hot air with high temperature and pressure. This hot and high pressure air is then introduced to PTAI, for example, through a conduit/supply pipe. Then, the hot and high pressure air enters the perforated/piccolo tube and runs circumferentially around the D-chamber. The schematic drawing of a hot air anti-icing system is shown in Figure 2.3.1.

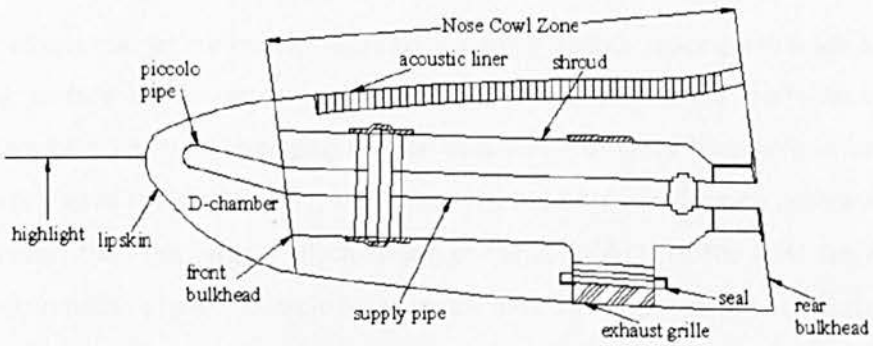

Figure 2.3.1: Part of nacelle intake [41]

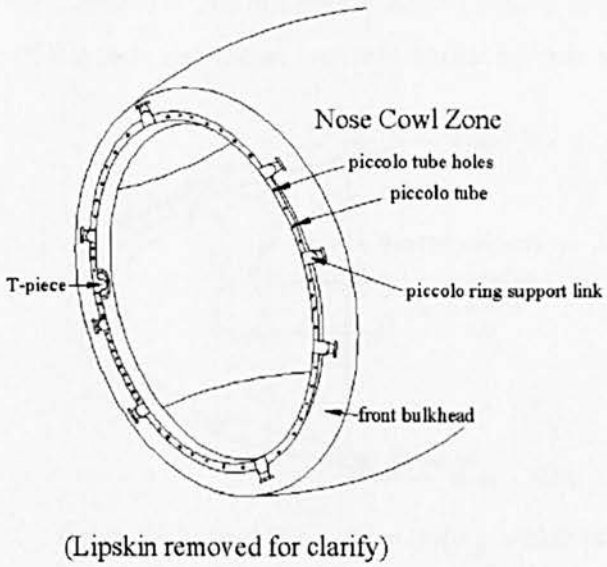

Figure 2.3.2: Piccolo tube anti-icing system [41]

PTAI uses the hot air anti-icing, in which the hot and high pressure air from the supply pipe is directed towards the internal surface through discrete holes in the perforated piccolo tube, shown in Figures 2.3.2. After impinging on the internal surface, this exhausted air flows around the D-chamber

and exits through the exhaust grill. Pneumatic operation valves are used to control the PTAI system. The control valves are the simple ON/OFF type valves and can be controlled from the flight deck [41]. Conditions, such as the mass flow rate, temperature drop between the engine compressors and piccolo pipe, the amount of water caught or impinged, impingement limits on the nacelle surface and conditions for thermal equilibrium at the nose cowl are the characteristics influencing the performance of PTAI system [39 and 40]. However, according to the experiment conducted at QUB, the correlation has shown a strong dependence on the mass flow per unit area and, to a certain extent, the weak influence of jet (nozzle) spacing [39].

William [37] pointed out that jet curvature, nozzle-to-impinging-surface spacing and angle between jet and impinging surface as the other parameters affecting PTAI thermal performance. The maximum heat transfer from jet to impinging surface occurs at a distance from hole to impinging surface of 5-7 times that of the jet diameter. Unfortunately, the heat transfer rate decreases when the distance is greater than this length, which is one of the drawbacks of the PTAI system [39]. Moreover, the concentration of the maximum heat transfer rate on hotspot locations results in non-uniform temperature distribution on the nacelle lip-skin. As a result, the ice accretion moves downstream to the outer skin area. In addition, Rosenthal [42] has claimed that the jet impingement system is not fully effective since the hot air which has been introduced is relatively small compared to the mass of air in the D-chamber. The effective impinging area is limited to the hotspot vicinity. The complexity of the PTAI system also causes high manufacturing costs and a weight penalty [43].

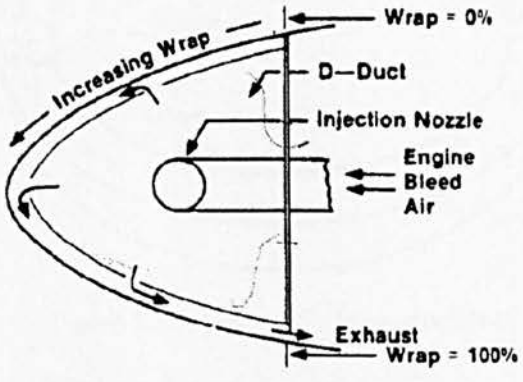

Figure 2.3.3: Double-walled anti-icing system [44]

The double-walled anti-icing (DWAI) system is another alternative ice protection system, shown in Figure 2.3.3. However, this hot air anti-icing system is unpopular and rarely employed in aircraft. The hot air from the D-chamber is forced into a channel between two walls. Consequently, the heat from hot air transfers to the walls by convection [44]. This method provides more uniform temperature distribution and avoids hotspots occurring on the nacelle lip-skin. However, it produces a high

pressure drop inside the channel, since the spacing between the two walls is small. Furthermore, this method disrupts the installation of noise abatement material, i.e. acoustic liner, to reduce noise from the engine. This system also requires complex construction resulting to higher cost of installation and maintenance [45].

The exhausted air flows out from the D-chamber through AI exhausts. The temperature of exhausted hot air has the potential to reattach on the surface of composite fan cowl doors, thereby blistering the paint. In order to reduce the temperature of exhausted hot air, thereby avoiding paint damage, the thermal AI exhausted grills are employed to enhance the mixing process between exhausted hot air and cold air outside. By applying blended central tapered bar, or church-window, together with 3/4 inch high-faired fence, the temperature of exhausted air drops to the range of 80°C to 130°C, which is within the imposed composites and paint temperature tolerance [46]. For safety reasons, some protections have been installed inside the nose cowl zone to protect nearby structures or components which are sensitive to heat, or in case pressured hot air leaks or bursts [47]. One protective method is spraying a coating of thermally insulating foam or paint onto temperature-sensitive structures. Besides the coating, the leakage detection devices are installed in the cowl in order to detect the hot air leakages.

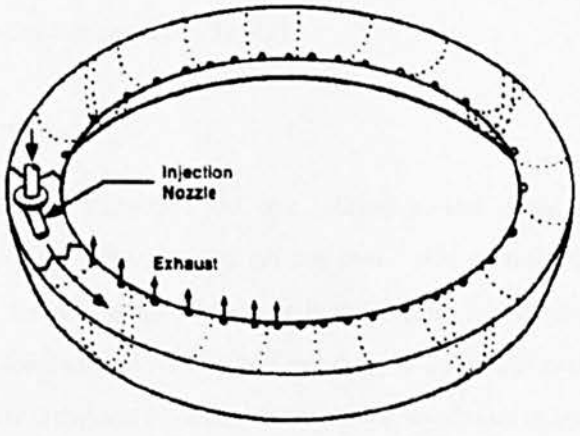

Figure 2.3.4: Swirl anti-icing system [44]

The SAI system was introduced a long time ago. Unfortunately, not many researchers have published their study regarding the effectiveness of this system in preventing ice accumulation on the nacelle lip-skin. Although the system requires a huge amount of hot air, it has the potential to provide uniform temperature distribution on the nacelle lip-skin and prevent the runback ice accretion on the downstream area. SAI is also more simply constructed compared to other hot air anti-icing systems. The air with high pressure and temperature from the jet engine is directed to the D-chamber by a supply pipe. The nozzle is positioned at the end of the supply pipe and is bent 90° in

order to direct the high pressure and hot air to swirl inside the D-chamber. The nozzle direction is usually parallel to the bulkhead and tangent to the middle circle of the D-chamber. The air with high temperature and velocity exits from the nozzle and thus encounters the cooler air in the D-chamber, which causes a relative large amount of cold air entrained by hot air. Thus, the mixed air swirls circularly around the annular D-chamber. As a result, the heat transferred from hot air to the nacelle lip-skin in SAI system is more uniform compared to other anti-icing systems.

The high pressure hot air from the nozzle mixes with a large and cooler stationary air (cold air) inside the D-chamber. Thus, the heat from hot air is transferred to the cold air, which brings down the temperature of the hot air to an intermediate but still relatively high temperature. The small stream of hot air with high velocity begins to entrain the stagnation air having larger amount of mass, bringing the velocity of mixed air to intermediate level. The exhausted air exits through the exhaust holes provided on the bulkhead, as shown in Figure 2.3.4 [42]. Vest [43] believed that an elliptically shaped nozzle enhances the mixing process between hot air and cold air inside the D-chamber. However, there is no data or other evidence provided on the performance of the ellipse nozzle. In addition, plurality of nozzles and arrangements also enhance heat transfer and temperature distribution in stationary air due to turbulent enhancement, thus increasing the mixing process between hot air and stationary air. As a result, the duration of heat transfer from hot air to the nacelle lip-skin has been reduced significantly [43].

2.4 Study of Jet Impingement

Hot air anti-icing systems, i.e. PTAI and SAI, are related to the study of jet impingement. PTAI produces high velocity hot jet impingement on the inner skin of nacelle in order to prevent ice accretion on the nacelle lip-skin. Meanwhile, the high velocity hot air from the nozzle of the SAI system impinges on the outer skin of nacelle and resulting in a hotspot on the outer skin. In general, the impingement of hot air is divided into four major zones, as shown in Figure 2.4.1. Zone I contains potential core flow, within which the exit velocity is retained. This flow is shrinking as the hot air moves downstream towards the impingement surface. Downstream of Zone I is the free jet section (Zone II). This zone has non-uniform air velocity, and the highest velocity of the hot air occurs in the centre of the jet. The hot air velocity decreases and the free jet widened in this zone as the hot air moves downstream. It happens due to the mixing and inherent momentum exchange between hot air and stagnation cold air. The hot air then impinges on the surface in Zone III, which is called the impingement zone or deflection area. The presence of the surface in this zone results in massive deceleration in the original direction of the hot air flow from the nozzle [48]. Therefore, Zone IV emerges as the hot air reflected into the directions parallel to the impinging surface. The hot air in

this zone accelerates and at the same time, entrains stagnation air, while the inner flow (adjacent to the impingement surface) is affected by shear friction between boundary layer and surface. Thus, the hot air in Zone IV presented the velocity profile is shown in Figure 2.4.1.

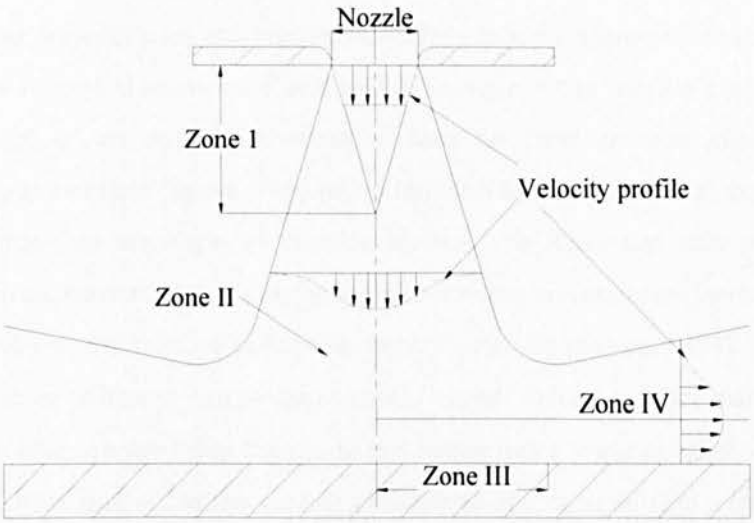

Figure 2.4.1: Flow structure of impinging jet [41]

The heat transfer in PTAI occurs in Zone III and Zone IV. As the high velocity hot air exits from the nozzle, the boundary layer in Zone III is very thin and the highest heat transfer coefficient occurs on the impingement spot on the surface. Therefore, the hotspot occurs in Zone III. Thereafter, the heat transfer coefficient decreases in Zone IV due to the boundary layer thickness becoming thicker as the hot air flows downstream from the impingement zone, or Zone III [41].

The geometry and angles of the impingement surface have an effect on the heat transfer from hot air to the impingement surface. The effect of heat transfer by convection with high velocity and temperature jet on the incline flat plate was studied by Perry [49]. It was observed that the heat transfer coefficient decreased when the jet impingement angle varied from being normal to the heater surface to parallel orientation. Roy and Patel [50] have predicted the heat transfer of rectangular jet impingement for a low Reynolds number on the incline flat plate. They studied heat transfer of jet impingement for two different cases: open to ambient and confined/closed conditions. They found that the Nusselt number of confined conditions was higher compared to the Nusselt number of open to ambient condition [50]. However, the heat transfer characteristics for short nozzle-to-plate spacing show contrasting results with long nozzle-to-plate spacing. It was found that the average Nusselt number increased with inclination angle for short nozzle-to-plate spacing. Choo et al. have claimed this phenomenon happens due to increase in the pumping power with inclination angle [51].

The heat transfer coefficient on the concave and convex geometry surface for incompressible flow was higher than the heat transfer coefficient on the flat surface. According to an experiment conducted by Souris et al. [52], the total heat transfer to the concave surface was higher than the total heat transfer to the flat surface. This is because the former having a larger effective impinging area than the latter, especially for short nozzle-to-surface spacing. Moreover, the vortex occurring in the flow structure enhanced momentum and energy transfer to the concave surface. Lee et al. [53] studied the effect of an inclined concave surface on heat transfer characteristics in an incompressible turbulent flow regime. They found the local Nusselt number at stagnation point was inversely proportional to the angle of concave surface. The maximum heat transfer coefficient occurred further from stagnation point as the inclined concave surface angle increased. The effect of slot nozzle geometry on the concave surface has been studied by Yang et al. [54]. They conducted an experiment for three different nozzle geometries, round shaped, rectangular shaped and 2-D contoured. Their results showed that the round slot nozzle had a lower average Nusselt number for short nozzle-to-surface spacing. As the spacing of nozzle to impinging surface increased, the average Nusselt number for the round slot nozzle also increased and exceeded the average Nusselt number for both rectangular and 2-D contoured slot nozzles.

The heat transfer characteristics of jet impingement on a convex surface have been studied by Chan et al. [55]. They found that the heat transfer coefficient for flat plate could be used for convex plate at a low Reynolds number and short nozzle-to-surface spacing. They also found that the average circumferential Nusselt number decreases faster than that does laterally along a flat surface. Lee et al. [56] conducted the experiment to study heat transfer characteristics on a convex surface. They claimed that the stagnation point Nusselt number on the convex surface was higher than that observed on the flat surface. They revealed that for long nozzle-to-surface spacing, the stagnation point Nusselt number strongly depended on Reynolds number. The effect of the impinging jet on the inclined convex surface has been studied by Lim et al. [57]. They reported that for the best spacing between nozzle and surface, the stagnation Nusselt number decreased with jet angle. The results obtained by Lim et al. also showed that the ratio of the maximum Nusselt number to the stagnation Nusselt number increased as the jet angle increased.

The turbulent flow structure of impinging jet on the flat, concave and convex surfaces at a low Reynolds number was studied by Cornaro et al. using visualization methods [58]. The nozzle to impinging surface spacing was four times lower than the nozzle diameter (short spacing between nozzle and surface). They claimed that the concave surface produced the largest vortex in the jet flow structure, followed by the flat surface and convex surface. The jet flow tends to be more

laminar in the convex surface due to the larger stabilizing effect on the flow with the increasing centrifugal force. However, the flow on concave surface was unstable and turbulent, especially flow upstream of the concave surface, which was strongly affected by flow exiting the surface into recirculation. This exhaust flow became entrained in the primary jet flow, reducing the likelihood of stable ring vortices.

The impingement effect of rectangular slot jets on the flat surface for laminar flow regime has been studied by El-Maghlany et al. [59]. They investigated the effect of the number of jet impingements from single to five jets on the heat transfer characteristics at the given hot air mass flow rate. It was found that the peak local Nusselt number decreases with the number of impinging jets. However, the maximum differences between the maximum local Nusselt number and the minimum local Nusselt number became smaller as the number of jet impingements increased. The result obtained by El-Maghlany et al. also showed that the average Nusselt number increased with the number of impinging jets. Several different turbulent models have been tested by Badra et al. [60] in order to find a suitable turbulent model for predicting heat transfer characteristics of impinging jets. According to their results, the turbulent model SST k-omega showed excellent agreement with experimental results obtained by Lee and Lee [61].

Chougule et al. [62] studied the heat transfer characteristics of multi-jet air impingement numerically and experimentally. Similar to Badra [60], they tested different turbulent models for their predictions. The SST k-omega model was demonstrated again to be the most suitable turbulent model in the jet impingement study. The empirical correlation of heat transfer for a single array of impinging jets on the concave surface has been developed by Freqeau et al. [63]. They employed the CANICE-3D code to predict thermal performance of the impinging jets. Freqeau et al. claimed that their results were in satisfactory agreement with the result of the empirical correlation obtained by Gardon and Cobonpue [64], who showed that the average Nusselt number was proportional to the Reynolds number.

The techniques of flow visualization have been employed to investigate heat transfer characteristics of the swirling impinging jet by Nuntadusit et al. [110]. They employed a dye visualization technique to visualize the flow pattern of swirling impinging surface at five different swirl numbers (Sw), from 0 to 0.94 using conventional impinging nozzle. As shown in Figure 2.4.2, the flow pattern of impinging jets were diverged as the swirl number increases, which might be caused by the reason that the turbulent level increases as the swirl number increases. Thus, the momentum exchanges between impinging jet and stagnation medium increase. The impinging jet velocity reduces rapidly and widens as the swirl number increases from 0 to 0.94, as shown in Figure 2.4.2.

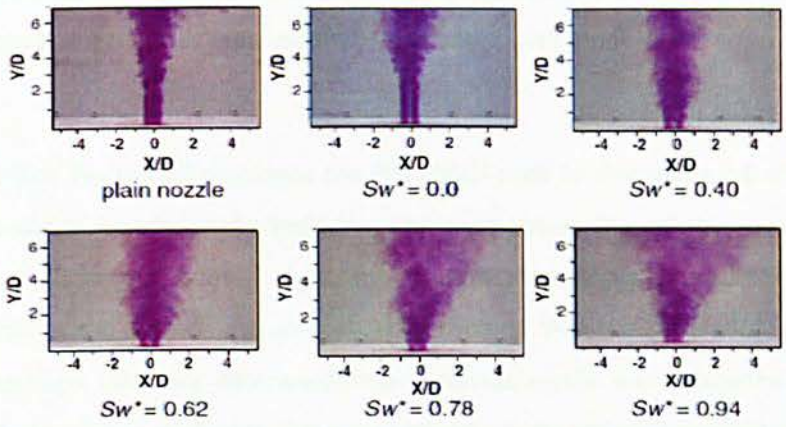

Figure 2.4.2: Dye visualization of swirling impinging jets [110]

Ortega-Casanova [111] studied the effect of impinging swirling jet on the heat transfer characteristics. He used the FLUENT CFD code to predict the average Nusselt number and the local Nusselt number at four different swirl intensity (Si) ranging from 0.02 to 0.45, and three different nozzle-to-wall spacings, 5d, 10d and 30d. The results revealed that the effect of the swirling impinging jet on the local Nusselt number diminishes as the nozzle-to-wall spacing increases from 5d to 30d. In addition, the effect of swirl intensity on the average Nusselt number was intensified with the decrease of nozzle–to-wall spacing. In other words, the application of swirling flow potentially reduces temperature concentration on the impinging surface, while at the same time enhancing the average temperature on the surface. This phenomenon occurs because turbulent intensity of impinging jet increases and diverges as the swirl intensity increases.

2.5 CFD Application in Anti-icing Study

Nowadays, the commercial CFD packages are widely used in AI studies. Many researchers use CFD due to the complexity of anti-icing experiments and flight tests. Moreover, the cost of experimental study is extremely high, especially for cases involving wet conditions. The CFD has been popular among researchers since the early 1990s. At that time, researchers employed CFD to optimize the performance of hot air anti-icing systems, especially PTAI. In early 1990, Khalil et al. analysed the performance of hot air anti-icing as a means of engine inlet ice protection [65]. The authors utilised trajectory code to estimate local water-impingement rates on the nacelle inlet surface. The temperature distribution on the nacelle lip-skin was determined by solving the energy balance on both surface runback water and nacelle lip-skin. According to the results, the authors recommended that a large amount of heat should be concentrated on the stagnation point of water droplet impingement in order to evaporate these water droplets. The results also showed that the runback

water might reach freezing temperature at the downstream of nacelle lip-skin. Therefore, the authors also suggested that this area should be protected with moderate thermal anti-icing systems, such as ETH.

Later on, Smith and Taylor [66] employed the PHEONICS code to simulate a 2-D anti-icing system on the nacelle lip-skin in dry and wet conditions. The code solved the energy equation to determine cooling effects of water impingement. As a simplification, the authors ignored heat transfer between water impinging on the surface and airflow. They claimed that the simulation result was in good agreement with flight test data. Afterwards, the predicted results were obtained from the FENSAP-ICE code, studied by Croce et al. [67]. The code utilised a finite element method to solve the Navier-Stokes equation for determining ice accretion, droplet impingement and conjugate heat transfer. They employed standard k-epsilon model to resolve turbulent flows inside the wing leading edge. They claimed their results were satisfactory. However, no validation experimental results were provided.

Subsequently, a simple mathematical model has been introduced by Morency et al. [68] to analyse the heat transfer phenomenon on the airfoil surface. This mathematical model was used to simulate temperature changes in the runback water film and conduction in airfoil skin. The authors also utilised internal convection coefficients from other research to determine the heat transfer from impinging jet to airfoil surface. They claimed that their simulation result was quite good when compared with the results from other numerical modelling. Furthermore, the numerical simulation using the FLUENT CFD code to investigate conjugate heat transfer on a wing slat in an anti-icing system was studied by Mattos and Olivera [69]. They employed the Spalart-Allmaras turbulent equation to resolve turbulent flow jet impingement. The results showed that heat transfer characteristics were proportional to hot air mass flow rate.

In another study, Morency et al. [70] developed a numerical code and implemented it into a CANICE CFD code in order to design ice protection system on wing leading edges. The authors used two different methods, integral method and finite difference method, to solve boundary layer equations. The results obtained by the finite difference method were closer to the experimental results than those obtained by integral method. Five years later, Hua and Liu [71] employed the FLUENT CFD code to predict temperature distribution along a wing leading edge. They focused on two dimensional bay slice approximations to obtain predicted results. A low number of meshes are required for this method. Therefore, shorter time is needed for the computational results to converge. The authors compared the results from the flow field of 2-D bay slice with the results from the flow field of the 3-D simulation. The comparison concluded that the results of the 2-D bay slice

had overestimated the vortex area inside the wing leading edge and the wing leading edge temperature, which is confirmed by experimental results.

At the same period, Planquart et al. [72] carried out 3-D simulation to map heat transfer coefficients in multi-impinging jets anti-icing system using a FLUENT CFD code. The authors reported that their simulation results showed excellent agreement with the experimental results for the surface heat transfer coefficients, which had been measured by infrared thermography. Later on, the numerical study of diamond arrangement of holes of PTAI was conducted by Ridgy [73]. He used a GLENN-HT code to predict anti-icing performance, which employed standard k-epsilon model to resolve turbulent flow of jet impingement. The author reported that a significant improvement was determined also for small amount of total heat supplied to PTAI in their design. Afterwards, Papadakis and Wong [74] studied the effect of piccolo tube configuration on the temperature distribution of the wing leading edge. They were utilising a FLUENT CFD code to obtain predicted results and compared them with experimental results obtained by other researchers. They reported that the predicted results showed good agreement with experimental findings. According to their investigation, the best configuration of piccolo tube occurred when piccolo pipe centre was of 0.75 inch and 0.193 inch behind and under the wing highlight respectively.

Saeed and Al-Garni [75] studied the effects of different nozzle arrays on thermal performance of the PTAI. They revealed that the single array and arrays with 20° stagger yield have better surface heat transfer than the 10° stagger yield. 3-D unsteady thermodynamic models were developed by Hua et al. [76] in order to describe the dynamic response of an aircraft wing anti-icing operation. The results obtained by the authors showed that the 3-D CFD unsteady simulation produced excellent agreement with flight test. However, 2-D unsteady simulation underestimated the increment of skin temperature at initial time period and suddenly overestimated the temperature increment of skin surface when the flow was well set up.

In 2007, FENSAP-ICE CFD code was employed by Wang et al. [77] to study PTAI performance on the wing slat in wet conditions. They developed a model with a single array of holes which were directed towards the upper skin of the wing leading edge in their model. The altitude, ambient temperature and SWDs in this study were 3048m, -20°C and 20 micron respectively. The result showed that the single array of holes was not enough to prevent ice occurrence on the lower skin of the wing leading edge. Therefore, they recommended double wall anti-icing to be utilized on the lower slat surface in order to prevent icing on the whole wing leading edge surface. Soon after, a new code was developed by Elangovan and Hung [78] using C++ in order to predict the temperature distribution on the wing leading edge in both wet and dry conditions. This code had the ability to determine the

minimum heat requirement of PTAI to protect the wing from icing. The skin temperature prediction was achieved by using alternating direction implicit methods. They also utilised thermodynamic energy transfer rate to resolve thermodynamic energy and boundary conditions later on the external wing skin. The simulation result showed that the wing skin temperature under dry conditions was higher than wing skin temperature under wet conditions.

In 2009, a comprehensive experimental and numerical study of PTAI was conducted by Wong et al. [79]. The authors used a FLUENT CFD code to predict temperature distribution on a wing leading edge. Then, the simulation results were validated with experimental results obtained from NASA Glenn Icing Research Tunnel (IRT). The second order upwind with SST k-omega turbulent model was used in the study to resolve turbulent and compressible flow of impinging jet. They claimed that the parameters of study including computed leading edge skin temperature, piccolo centreline total temperature and pressure were in excellent agreement with experimental data.

Later, Domingos et al. [80] developed a 2-D computational method in order to analyse hot air anti-icing system. The authors claimed that their method was able to predict the temperature of the wing leading edge for both dry and wet conditions. Moreover, this method enabled them to predict runback ice phenomenon. The external and internal flow was decoupled before being used to provide boundary conditions to the steady state thermal dynamic model. For external flow, they utilised 2-D RANS equation with SST k-ω turbulent model to compute gaseous phase flow. The isothermal boundary condition was then used in order to enhance accuracy of the modelling. A Nusselt number correlation was also used to solve the heat transfer problem in the internal flow module. They claimed that the simulation results showed good agreement with experimental data for both dry and wet conditions.

2.6 Fundamentals on Boundary Layer of Internal and External Flows

When a fluid flows on a surface, i.e. flat plate, the fluid particles makes contact with the surface which is assumed has zero velocity (no slip condition). These particles seem to slow down the particle in the adjacent fluid layer, which act to retard the particle movement in the next layer, and so on until at a certain distance from the surface [48]. This flow retardation zone in the fluid appears due to shear stress between fluid layers. On the flat plate, this stress is assumed to be proportional with normal velocity gradient, thus the shear stress is described as:

$$\tau = \mu \frac{du}{dy} \tag{2.1}$$

Where: τ = shear stress

μ = dynamic viscosity

$\frac{du}{dy}$ = velocity gradient

This retardation flow zone is also known as the boundary layer. The boundary layer of air is very thin due to the dynamic viscosity of air being low. The boundary layer thickness (δ) is the distance from flow velocity (u) of 99% free stream velocity (u_∞) to the surface, as shown in figure 2.6.1:

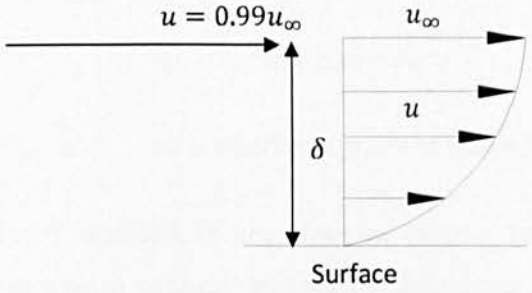

Figure 2.6.1: Laminar velocity profile on the flat plate [115]

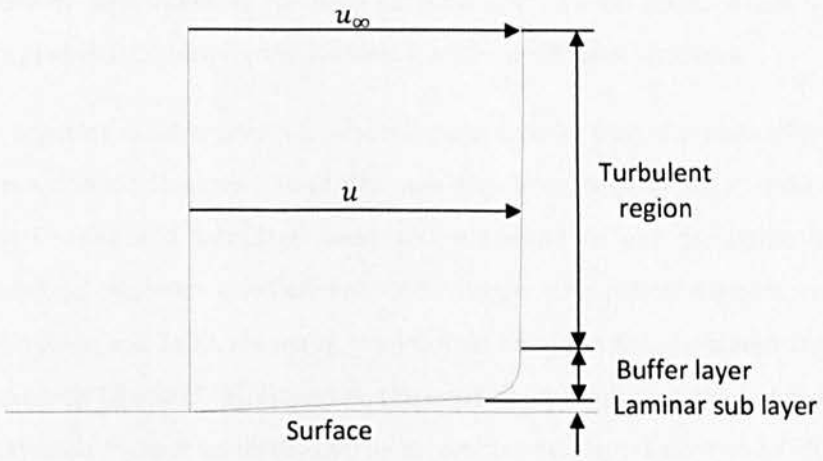

Figure 2.6.2: Velocity profile in turbulent boundary layer [48]

For external flow, the critical Reynolds number varies from 10^5 to 3 x 10^6. It depends on surface roughness and turbulent level of the free stream. In the turbulent boundary layer, three different regions are delineated: laminar sub-layer, buffer layer and turbulent region. As shown in Figure 2.6.2, the laminar sub-layer is very thin and close to the wall. The particle transport in this region is dominated by diffusion and the velocity profile is nearly linear. The particle transport in the

adjoining buffer is controlled by turbulent mixing and diffusion. Finally, the particle transport in the turbulent zone is dominated by turbulent mixing [115].

In the laminar sub-layer, the heat transfers from layer to layer by conduction. Meanwhile, in the turbulent region, the heat and momentum exchange mechanism is one involving a macroscopic lump of fluid moving in the flow. Some molecular viscous action appears in the buffer layer. However, heat conduction is still important. The heat transfer in the laminar sub-layer zone is defined as:

$$q = -k_f \frac{dT}{dy} \tag{2.2}$$

Where q = heat flux

k_f = fluid thermal conductivity

$\frac{dT}{dy}$ = air temperature gradient within boundary layer zone

As shown in the above equation, at any given air thermal conductivity, the heat transfer from surface to fluid or vice versa strongly depends on the temperature gradient inside the boundary layer. Consequently, the thinner boundary layer results in a higher temperature gradient, thus higher enhancing rate of heat flux from surface to fluid or vice versa. The boundary layer thickness decreases as the velocity of flow increases for both external and internal flows, which leads to increase of temperature gradient. Consequently, the heat transfer coefficient increases.

In fluid mechanics, the Reynolds number (*Re*) is a dimensionless number that represent the ratio of inertial forces to viscous forces. However, Reynolds was the first to propose a criterion for differentiation between laminar and turbulent flows and suggested to use the upper limit of Reynolds number, the critical Reynolds number. For internal flow, the critical Reynolds number naturally occurs between 2100 and 2300. Normally, the internal flow is in fully turbulent regime as the Reynolds number exceeds 10,000 [115]. However, the laminar pipe/tube regime has the ability to maintain flow with Reynolds number up to 100,000 by minimising ambient disturbances [107].

In turbulent regime, the flow structure is divided into laminar sub-layer and turbulent core as shown in Figure 2.6.3. The local heat transfer from the fluid to the wall may be expressed by:

$$q = h(T_m - T_w) \tag{2.3}$$

Where q = heat flux

h = heat transfer coefficient

T_m = mean temperature

T_w = wall temperature

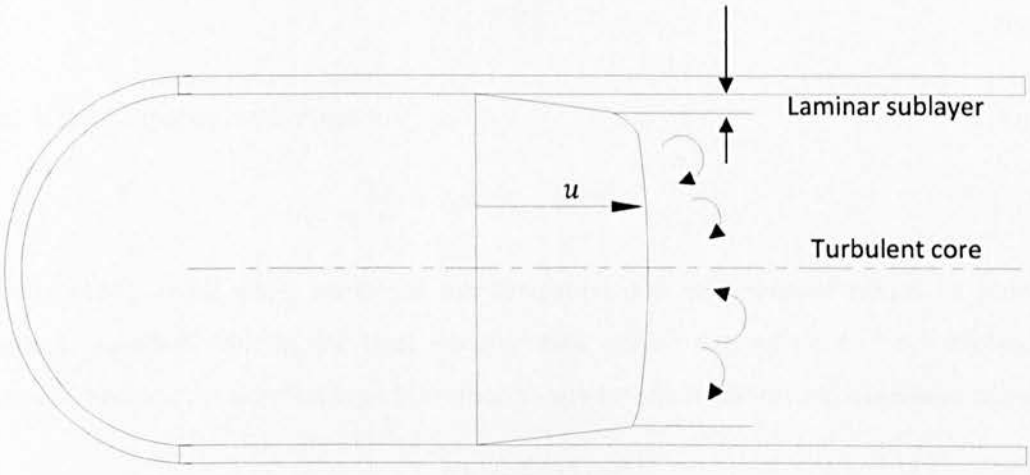

Figure 2.6.3: Velocity profile in turbulent tube flow [115]

Then Stanton number (St) is a dimensionless parameter relating heat transfer coefficient to heat capacity of the fluid stream per unit cross-sectional area per unit time, which is defined as:

$$St = \frac{h}{\rho c_p u_m} \tag{2.4}$$

It also can be expressed in terms of the fluid's Nusselt, Reynolds, and Prandtl numbers, which established the links for fundamental physical characteristics and made mathematics alive in Physics. The Nusselt number represents the ratio of convective to conductive heat transfer perpendicularly across the boundary within the fluid at the boundary. The Prandtl number is a dimensionless number of energy conversion, the ratio of momentum diffusivity (kinematic viscosity) to thermal diffusivity. For internal laminar flow is expressed as:

$$St = \frac{Nu_d}{Re_d Pr} = \frac{f}{8} \tag{2.5}$$

Where Nu_d = local Nusselt number for tube

C_p = specific heat at constant pressure

u_m = mean velocity

Re_d = Reynolds number for tube

Pr = Prandtl number

f = wall friction

In the smooth pipe for turbulent-friction up to Re_d of about 2 x 10^5

$$f = \frac{0.316}{Re_d^{0.25}} \tag{2.6}$$

Thus Stanton number is rearrange as:

$$\frac{Nu_d}{Re_d Pr} = 0.0395\, Re_d^{-0.25} \tag{2.7}$$

Holman [114], in his book, combined the simulation and experimental results to arrive at one empirical equation. Mostly, the heat transfer data will be dependent on Reynolds and Prandtl numbers. Perhaps the simplest type of relation to use for all simulation and experimental data is:

$$Nu = ARe_d^B Pr^C \tag{2.12}$$

Where *A*, *B* and *C* are constants to be determined from either simulation or experimental data

Nu_d is expressed as:

$$Nu_d = 0.0395 Re_d^{3/4} Pr^{1/3} \tag{2.8}$$

This equation is valid for Re_d lower than 2 x 10^5

For larger Reynolds number, Petukhoz developed a new correlation for friction:

$$f = (0.790\, ln\, Re_d - 1.64)^{-2} \tag{2.9}$$

Thus, the Colburn equation is then:

$$Nu_d = 0.023 Re_d^{4/5} Pr^n \tag{2.10}$$

Where n = 0.4 for heating

n = 0.3 for cooling

valid from $Re_d \geq 10{,}000$.

Gnielinski suggests that a better result for turbulent flow in smooth tubes may be obtained from the

following equation:

$$Nu = 0.0214(Re^{0.8} - 100)Pr^{0.4} \quad (2.11)$$

Valid for $0.5 < Pr < 1.5$; $10^4 < Re < 5\,x\,10^6$

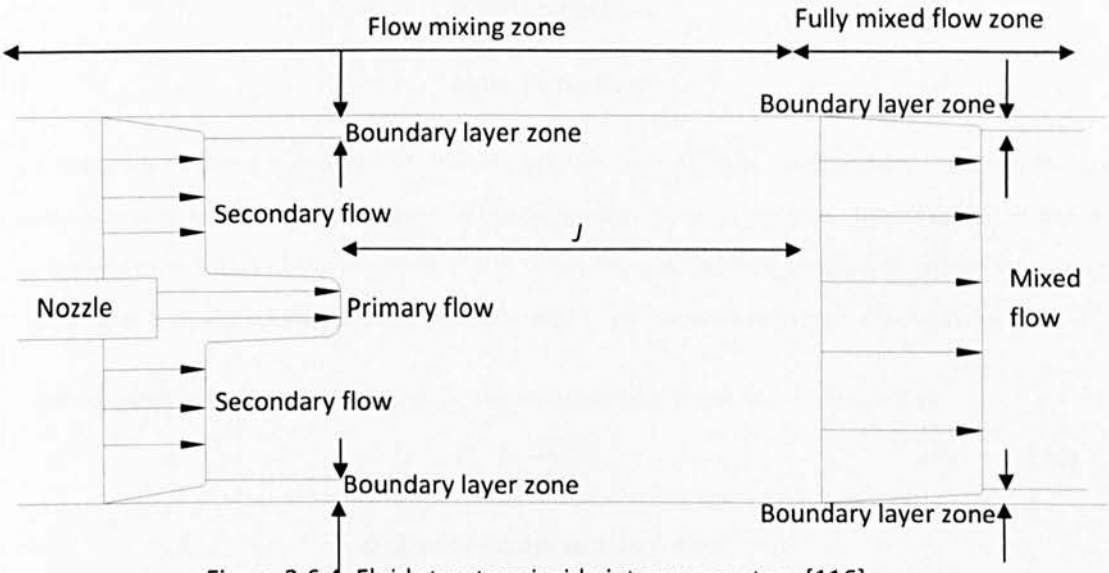

Figure 2.6.4: Fluid structure inside jet pump system [116]

Figure 2.6.4 shows the fluid structure in a jet pump system [116]. The jet flow exits from the nozzle outlet with high velocity. Thus, this jet will entrain and mix with the secondary flow at surroundings. At certain distance (*J*), the primary flow mixes fully with the secondary flow which becomes a mixed flow. Assume the flow is air or compressible flow, the mixed flow velocity *u3* in Figure 2.6.4 is given by:

$$u3 = \frac{\rho 1 A 1 u 1 + \rho 2 A 2 u 2}{\rho 3 A 3} \quad (2.13)$$

And the density of mixed flow is as follows:

$$\rho 3 = \frac{\rho 1 A 1 u 1 + \rho 2 A 2 u 2}{A 1 u 1 + A 2 u 2} \quad (2.14)$$

The temperature for the mixed flow is then determined by:

$$T_0 3 = \frac{m 1 T_0 1 + m 2 T_0 2}{m 1 + m 2} \quad (2.15)$$

Where 1, 2 and 3 are denoted as primary, secondary and mixed flows respectively

m = air mass flow rate

ρ = fluid density

u = Air velocity

T_0 = total temperature

A = cross sectional area

Since the mixed flow is a mixture of primary and secondary flow, the boundary layer of the mixed flow is thinner than the boundary layer of the secondary flow. In addition, temperature of the mixed flow is higher than that of the secondary flow. Thus the pipe surface in the fully mixed flow zone has a higher heat transfer coefficient and heat transfer than the surface in flow mixing zone.

For non-circular tube, i.e. the D-chamber, the hydraulic diameter (D_h) is defined as:

$$D_h \equiv \frac{4A_{D-C}}{P_w} \tag{2.16}$$

Where $A_{D\text{-}C}$ = D-chamber cross sectional area

P_w = wetted perimeter

For asymmetric velocity profile inside D-chamber, heat flux can be described as:

$$q_{ave} = h_{sw}(T_m - T_{ave}) \tag{2.17}$$

Rearrange the equation, average heat transfer coefficient is determined by:

$$h_{sw} = \frac{q_{ave}}{T_m - T_{ave}} \tag{2.18}$$

Where:

$$q_{ave} = \frac{Q}{A_{sur\ lip-skin}} \tag{2.19}$$

$$T_m = \frac{\int_{V_{D-C}} \rho u c_p T_{air}\, dV_{D-C}}{\int_{V_{D-C}} \rho u c_p dV_{D-C}} \tag{2.20}$$

$$T_{ave} = \frac{\sum A_{lip-skin} T_{lip-skin}}{\sum A_{sur\ lip-skin}} \tag{2.21}$$

Where h_{sw} = average heat transfer coefficient of SAI

q_{ave} = average heat flux of lip-skin surface

T_{ave} = average lip-skin temperature

$V_{D\text{-}C}$ = volume of D-chamber

$A_{sur\ lip\text{-}skin}$ = total internal surface area of the lip-skin

Q = heat transfer from air to lip-skin

$A_{lip\text{-}skin}$ = distinct lip-skin area [102]

$T_{lip\text{-}skin}$ = average temperature of a distinct lip-skin area $A_{lip\text{-}skin}$

The SAI Nusselt number is then estimated using the following equation:

$$Nu_{sw} = \frac{h_{sw} D_h}{k_f} \tag{2.22}$$

Where Nu_{sw} = SAI Nusselt number

Reynolds number (Re_{sw}) of SAI for asymmetric flow is described in equation 2.23:

$$Re_{sw} = \frac{\rho\, u_{ave} D_h}{\mu} \tag{2.23}$$

Where: μ = air dynamic viscosity

u_{ave} = average velocity of swirling air in D-chamber

ρ = air density

Since mass flow rate of swirling air (m_{sw}) can be described as:

$$m_{sw} = \rho A_{D-C} u_{ave} \tag{2.24}$$

Thus, SAI Reynolds number is rearrange becomes:

$$Re_{sw} = \frac{m_{sw} . D_h}{A_{D-C} . \mu} \tag{2.25}$$

2.7 Fundamentals of Augmentor System

An augmentor system is widely used in the exhaust of a pulse engine, turbojet engine and rocket in order to enhance the amount of thrust produced by engine jet [81]. The ejector in an augmentor system is capable of decreasing the jet noise from the aircraft by mixing cool ambient air with the high velocity engine gas before they are exhausted to ambient [82]. The ejector system is also used in refrigeration systems to improve the overall absorption system [83-85]. Currently, the pulsejet has been introduced to micro-air vehicles (MAVs) instead of a turbo-machinery component due to the complexity of miniaturising the latter. Therefore, the augmentor system has been used together with the pulsejet in MAVs in order to enhance their thrust [86].

An augmentor system consists of two major components: primary sources and an ejector (Figure 2.7.1). Primary sources including turbines, engine jets and nozzles are used to produce high temperature and velocity flow of air. The ejector functions to energise a secondary flow with a primary source. As the primary jet enters the ejector, it enhances energy and momentum exchange from primary jet to secondary flow by turbulent mixing of two streams. Consequently, the thrust which has been produced by the augmentor system is much better than the thrust produced by the primary source alone. This is because the outlet ejector produces higher momentum using higher mass flow rate and lower velocity than the original primary source alone would be able to achieve [87 and 88].

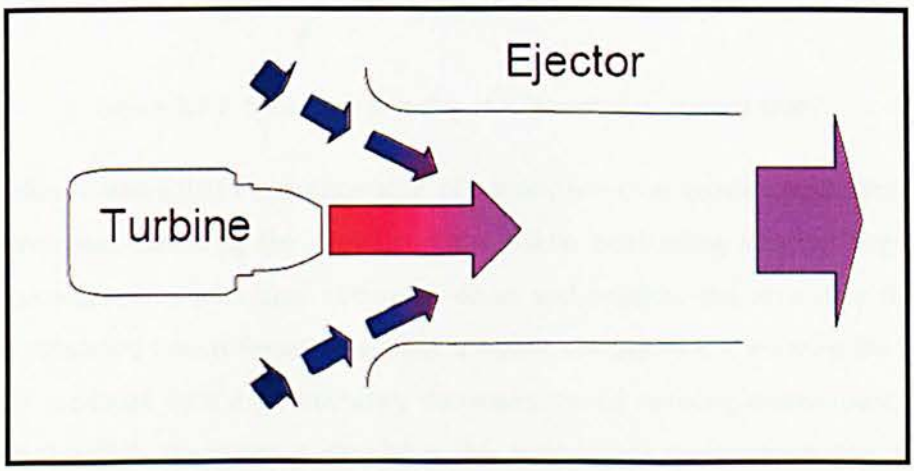

Figure 2.7.1: Basic concept of augmentor system [88]

The application of the augmentor dates as far back as World War II [89]. The primary source generates air with high velocity and temperature flowing through the augmentor. As a result, a low air pressure occurs in the mixing section, or augmentor throat [90], and the secondary flow outside

the augmentor with higher static air pressure flows through the augmentor. Thereafter, the pressure of the mixed air increases slowly in the diffuser section as the mixed air approaches the augmentor outlet due to cross-sectional area increasing towards outlet.

In general, the ejector in this study consists of two sections: entry section and diffuser section (Figure 2.7.2). The design of the augmentor in this study has follows the design of the ejector in the refrigeration system [83], which is different from augmentor design of an engine jet. The augmentor in this study has a very large inlet area compared to outlet area. The large inlet is used to entrain the cold air in the D-chamber flowing through the augmentor. The increment angle of the diffuser section is very critical in the augmentor design. The diffuser section is used to increase augmentor thrust. However, if the increment angle in the diffuser area is too large, the flow separation will probably occur inside the diffuser section. The vortex inside the diffuser section would degrade the performance of the augmentor [91].

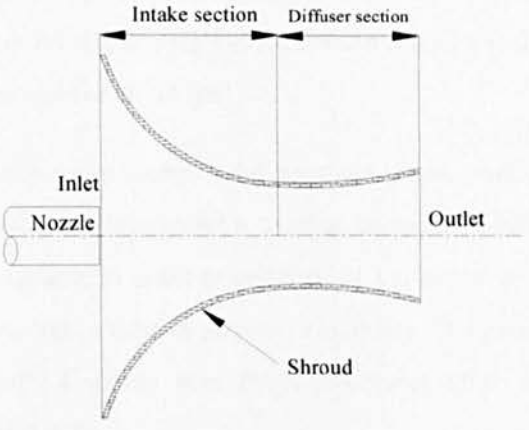

Figure 2.7.2: Schematic drawing of augmentor in present study

Previous studies revealed that the configuration of primary source or nozzle would affect augmentor thrust performance. Increasing the distance of the nozzle penetrating into the augmentor inlet results in the augmentor inlet area narrowing down and restricts the secondary flow entering shroud. The secondary flow is forced to achieve a higher velocity as it is entering the shroud. The rate of shear produced by the jet boundary decreases, hence reducing entrainment as the inlet velocity increases [92]. Therefore, it diminishes the augmentor's performance. The shape of the primary sources could potentially enhance the performance of augmentor. For example, a lobed nozzle was used as a primary source to increase performance of augmentor. This nozzle generates streamwise vortices that enhances mixing, increases secondary flow pumping and decreases the ejector mixing length required [93]. Moreover, the lobed nozzle alone has the potential to increase

mixing between hot air and stagnation air. This mixing enhancement occurs due to the presence and strength of stream-wise vortices that are generated due to nozzle geometry [94].

2.8 Basics of Acoustic Liner

The main function of the acoustic liner (AL) is to reduce noise produced by the turbo jet engine. In commercial aircraft, AL is planted at the nacelle cowl zone. The AL has been developed both to reduce noise and allow cooling of the combustion chamber. In fact, the concept of noise abatement has been around since Greek civilisation. The ancient Greeks used this concept to absorb and amplify sound, and their acoustic absorption coefficient was at its highest value when fluid trapped inside was resonating [95]. Porous material has been introduced in order to enhance the acoustic resistance of the AL. In fact, the porous material is a good acoustic energy absorber over a wide range of frequency, as contrasted to the air cavity of Helmholtz type. Although porous materials are good in energy absorption and widely used, including in air-conditioning and motorbike exhausts, this material is unsuitable for aircraft application for certain reasons such as a tendency to migrate, fracture and blind due to ash, dust or liquid [96].

The AL consists of three major components: solid backface sheet, honeycomb and perforated face sheet (Figure 2.8.1). The perforated face sheet is used as an exterior surface. This type of AL is also known as a perforated face system. In order to enhance AL performance, the linear liner system has been introduced, which enhances sound absorption capability. The linear liner system includes an additional component, namely a woven wire mesh structure, which is attached to the exterior perforated face sheet (Figure 2.8.2).

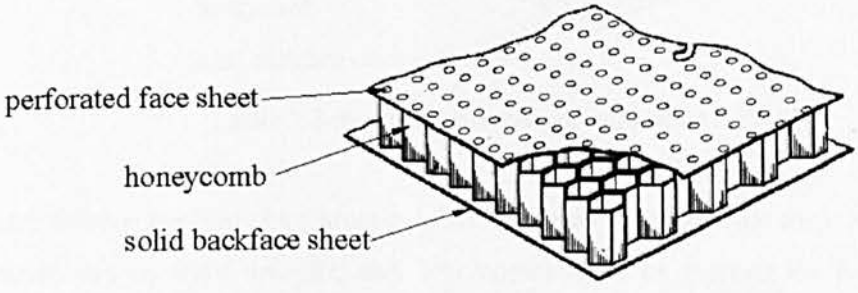

Figure 2.8.1: Perforated face system [98]

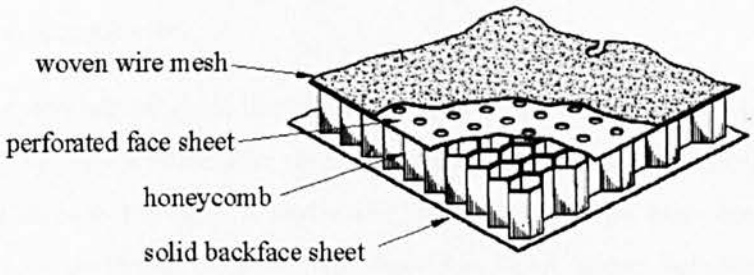

Figure 2.8.2: Linear liner system [119]

The modified linear liner system has been developed in order to meet the same performance as that of the linear liner system and the same durability as the perforated face system. In the modified AL, the woven wire is placed between the perforated face sheet and the honeycomb, as shown in Figure 2.8.3, in order to enhance durability. As an example, the thickness and holes diameter of the aluminium perforated face sheet are 0.025 inch and 0.0257 inch respectively. The 0.006-inch thickness of the woven wire mesh, with porosity between 30% and 38%, has been used in the modified linear liner system. A special adhesive has been used to attach the woven wire mesh to the honeycomb in order to prevent wicking of the adhesive into the mesh structure. The backface sheet has been fabricated by 0.063-inch aluminium thickness.

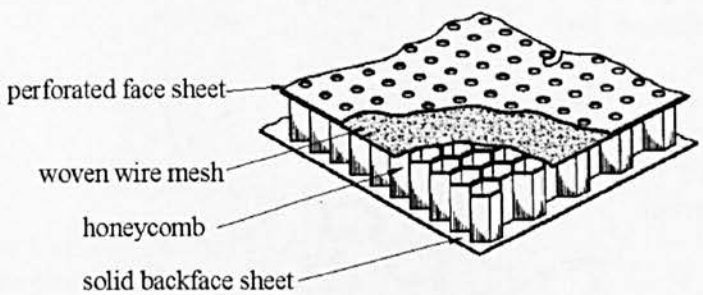

Figure 2.8.3: Linear liner system modification [119]

An electro thermal method of ice protection with isolated solid backface sheet for acoustic liner has been developed by Rohr, Inc [97, 98]. This combination of thermal ice protection and noise abatement design has been introduced to maximize heating power from leading edge to aft nacelle. Besides, the space occupied by heating system at the nacelle inlet region can be reduced and replaced by AL with the benefit of reducing noise from the jet engine as well. The electrical conductor perforated face converts current into heat which prevents ice from forming and resulting in reduction of nacelle intake size, hence reducing drag and saving fuel. In additional, insolate backface sheet prevent heat loss via inner region, thus increase efficiency of heater and save power.

Temperature for this design concept is being kept below 140°C to maintain the shape and structure properties of the acoustic liner.

The Boeing Company had patented the BAL, which uses hot air from the compressor [6]. As shown in Figure 2.8.4 [97, 99], the acoustic liner consists of a multi-layer structure of porous plates that allow hot air to flow through the liner. A perforated backface sheet has been used instead of a solid backface sheet. A perforated intermediate layer has been added between the inner portion honeycomb and outer portion honeycomb. The figure shows that the face sheet has a much higher percentage of porosity compared to the backface sheet. The perforated backface has been applied in the system due to excess bleed hot air from the conduit to honeycomb. In addition, it prevents overheating occurring inside the honeycomb. The perforated intermediate layer has been used in order to enhance sound attenuation of the forward liner by increasing the frequency bandwidth over which the cells of the honeycomb core dissipate noise. In addition, the intermediate perforated layer can add strength and rigidity to the forward liner, which is important near the lip-skin to protect the lip-skin from foreign object damage. Furthermore, the application of an inner portion honeycomb and outer portion, instead of one deep honeycomb, reduces the many risks during honeycomb fabrication and forming.

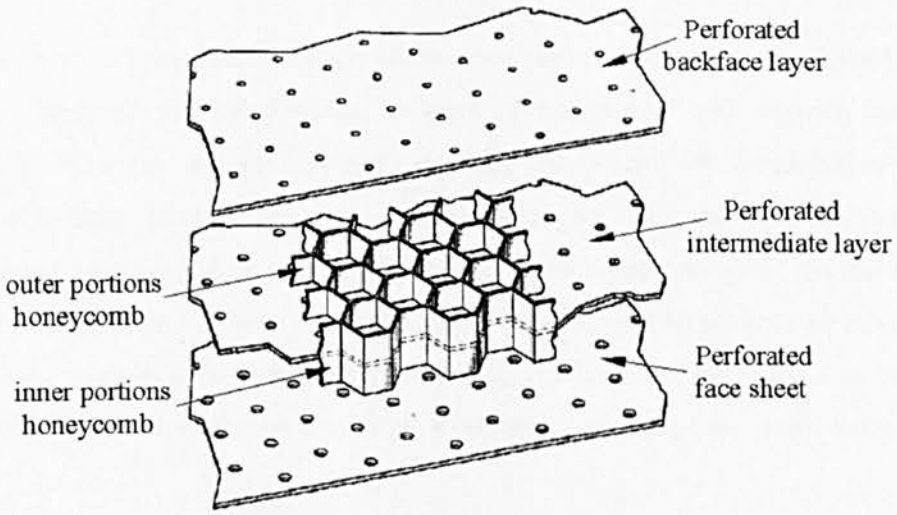

Figure 2.8.4: Configuration of bias acoustic liner for hot air anti-icing [99]

2.9 Summary

Many researchers have studied the ice protection systems i.e. de-icing and anti-icing systems, which are required by aircraft. Several ice protection systems are available to protect critical areas of aircraft skin from icing. Among them, the most effective one is the hot air anti-icing. The hot air from the compressor is supplied to D-chamber through supply pipe. Then, the heat from hot air is transferred to lip-skin. The most popular hot air anti-icing system is PTAI. Many researchers such as William [37], Raghunathan [39], and Brown [40 and 41] have studied the PTAI and its optimisation.

In early 1990, researchers employed CFD to carry out anti-icing studies. They employed CFD to optimise anti-icing design. This is because the cost of experimental work is extremely high especially in wet conditions. Many of them used CFD to predict and enhance PTAI performance, but none of them used CFD to study and improve SAI performance. Indeed, only few researchers [42-45] conducted experimental work of SAI.

Augmentor is widely used in exhaust of pulse engine, turbo jet engine and rocket, and refrigeration systems. The augmentor is used for enhancing the amount of thrust, decrease the noise level and improve the absorption systems, by means of speed up mixing process between high velocity of air from nozzle and cool ambient air. No research addressed the application of augmentor in neither SAI nor PTAI.

In the present work CFD was used to study SAI thermal performance and improve the SAI thermal performance. Besides, the relationship between dimensionless SAI thermal performance characteristics; including average Nusselt number, coefficient of temperature deviation, dimensionless hotspot temperature and dimensionless cold spot temperature, and average Reynolds number have been evaluated and presented in the study. Moreover, the combination of augmentor and SAI system has been simulated in this work in order to enhance air mixing process, which results in increases of SAI thermal performance. Furthermore, the thermal performance of SAI is compared with thermal performance of PTAI, which has not been done before by other researchers.

CHAPTER 3: Piccolo Tube Anti-Icing System

This study has investigated the performance of SAI system. As the experimental data of SAI were very limited, the investigation was started with the thermal performance of PTAI for BR710 nacelle lip-skin. Unlike the previous researches in which the experiments and simulations were performed at laboratory conditions, the present simulations were performed at four different flight conditions, Taxi, Climb, Hold and Descent, at several $m_{hot\ air}$ and dry condition. Then, the simulation results were validated by the experimental results obtained from Bombardier Aerospace Belfast (Bombardier) [100] and Brown et al. [41]. At the end of the chapter, a modified Brown empirical correlation is also presented and proved that it is suitable for a wider range of ambient temperature (T_∞). The comparison of thermal performances between PTAI and SAI on BR710 nacelle lip-skin will be discussed in Chapter 7.

As shown in Figure 3.0.1, the hot air jets exit from the nozzles/holes of the PTAI system and impinge on the targeted surface (inner skin area). Consequently, these surfaces receive adequate amount of heat to prevent the ice accumulation on the critical surfaces of the aircraft.

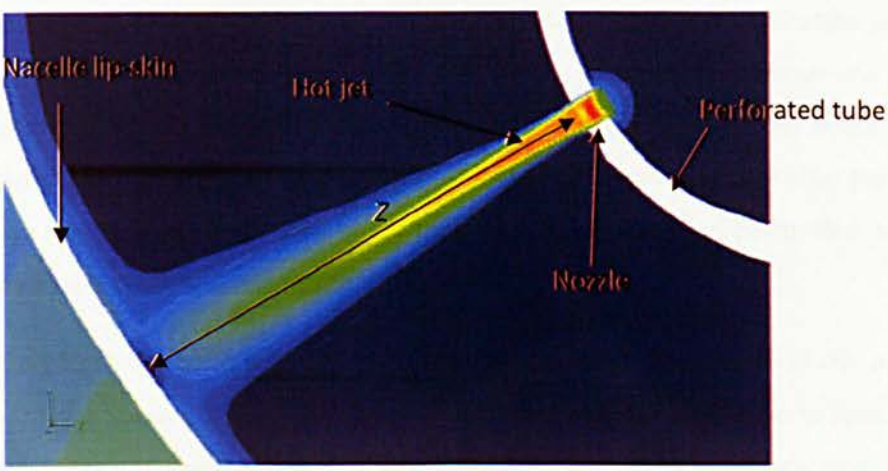

Figure 3.0.1: Piccolo Tube Anti-Icing system

3.1 Model Description

The information of PTAI in BR710 nacelle application, including nacelle lip-skin profile, PTAI design, operating conditions and experimental results at four different altitudes were obtained from Nacelle anti-icing system dry air flight test report [100]. Figure 3.1.1 shows the nacelle lip and PTAI arrangement; black and blue lines represent nacelle lip-skin and PTAI respectively. In this study, due to periodic nature of nozzle arrangement, out of 136 nozzles, only a slot with 2 nozzles or 1 slot/jet spacing was included in the PTAI simulation. This simplification is made in order to minimize number of mesh, thereby reducing computational time. The air pressure inside the perforated tube is assumed to be very similar along the circular perforated tube. Therefore, the results of one slot/jet spacing of nacelle lip are expected to be same as those of other slots along nacelle lip. Moreover, the circular shape of perforated tube and double curvature nacelle lip-skin were replaced with a straight perforated tube and a simplified straight section of nacelle lip-skin with a single curvature as shown in Figure 3.1.2. The simulation results of this simplified geometry were expected to have a little deviation from that of the actual design. Some previous research works have concurred with this assumption (for instance, Brown et al. [41]). Nozzle 1 and Nozzle 2 are shown in Figure 3.1.4, represented by row 1 and row 2 respectively.

The schematic drawings of the D-chamber and PTAI design in BR710 nacelle application are shown in Figures 3.1.3 and 3.1.4 respectively. Brown et al. [41] also used similar D-chamber and nacelle lip-skin in their study. According to Figure 3.1.3, the bulkhead height and D-chamber length were $100d$ and $76.2d$ respectively, where d is nozzle diameter. Nacelle lip-skin was $0.08128d$ thick, and the perforated tube was located $50d$ in front of the bulkhead. The materials of perforated tube, nacelle lip and bulkhead were steel, aluminium and titanium respectively.

The design of perforated tube in the PTAI study has diameter and thickness of $19.05d$ and $0.8128d$ respectively. The jet spacing (Cx) of PTAI was $34.8d$. The nozzles at the perforated tube were arranged in two staggered rows named as Nozzle 1 and Nozzle 2, which were located at 30° and 84° respectively towards the inner skin (Figure 3.1.2). The distance from local nozzle outlet to impinging point (Z) (Figure 3.0.1) for Nozzle 1 and 2 were $15.87d$ and $18.66d$ respectively. The schematic of perforated tube of PTAI design is shown in Figure 3.1.4.

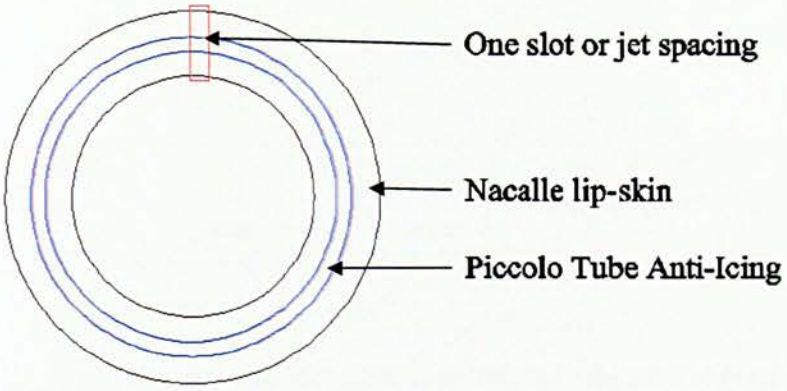

Figure 3.1.1: Piccolo Tube and nacelle lip arrangement

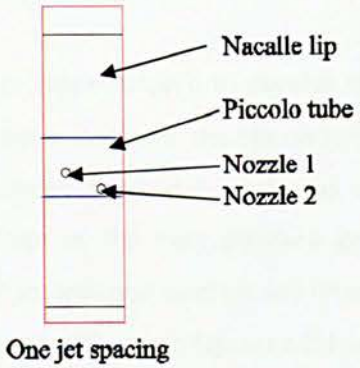

Figure 3.1.2: Simplification of PTAI modelling

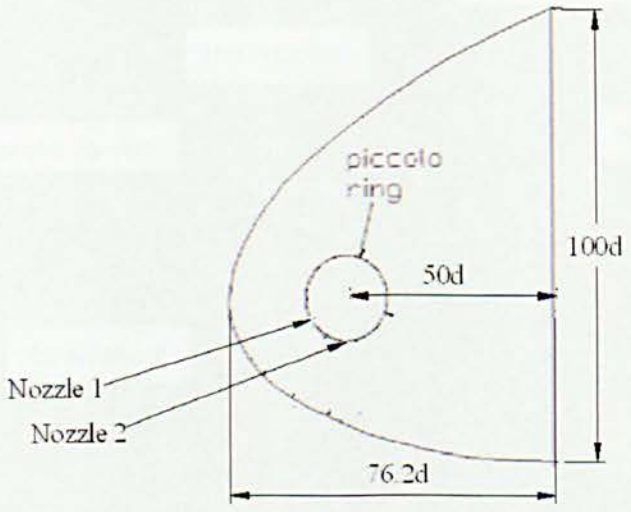

Figure 3.1.3: Schematic drawing of nacelle D-chamber

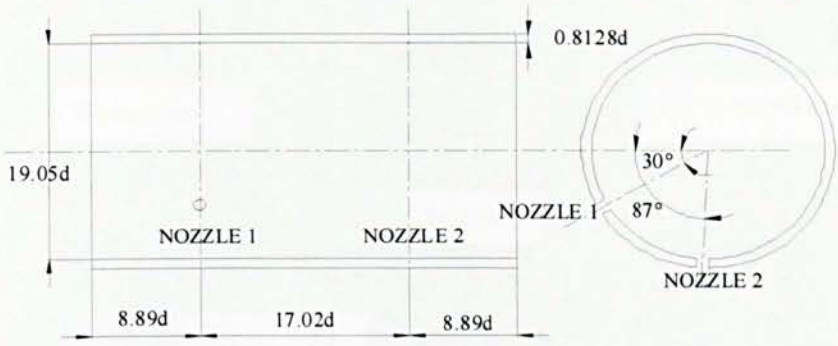

Figure 3.1.4: Schematic of perforated tube of *PTAI* design

3.2 Modelling Setup

GAMBIT [105] pre-processor was employed to develop the models and meshes of PTAI. The study utilized hexagonal non-uniform mesh for the simulation models of PTAI. For better results with higher accuracy, the structured hexagonal mesh was used in all the domains. High density of hexagonal mesh was utilized in the high pressure gradient domains, such as inside nozzles, impinging-surface area, hot jet area and external and internal lip-skin surfaces vicinities. The fine and structured hexagonal meshes are shown in Figures 3.2.1 and 3.2.2.

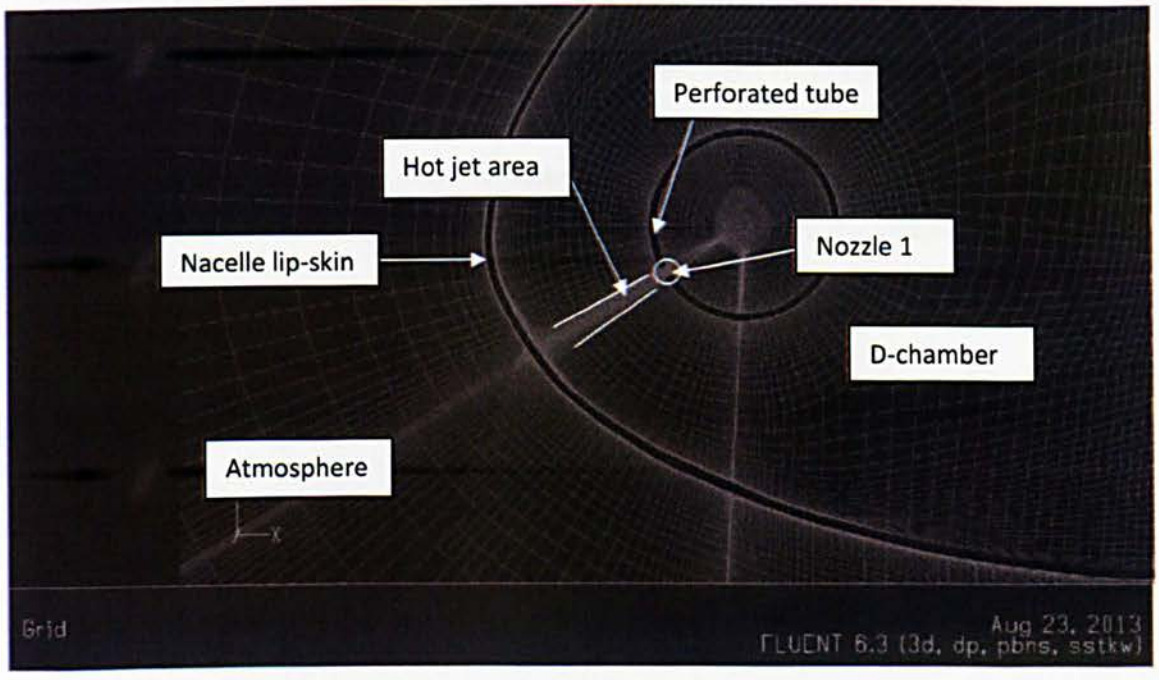

Figure 3.2.1: Structured mesh inside and outside nacelle

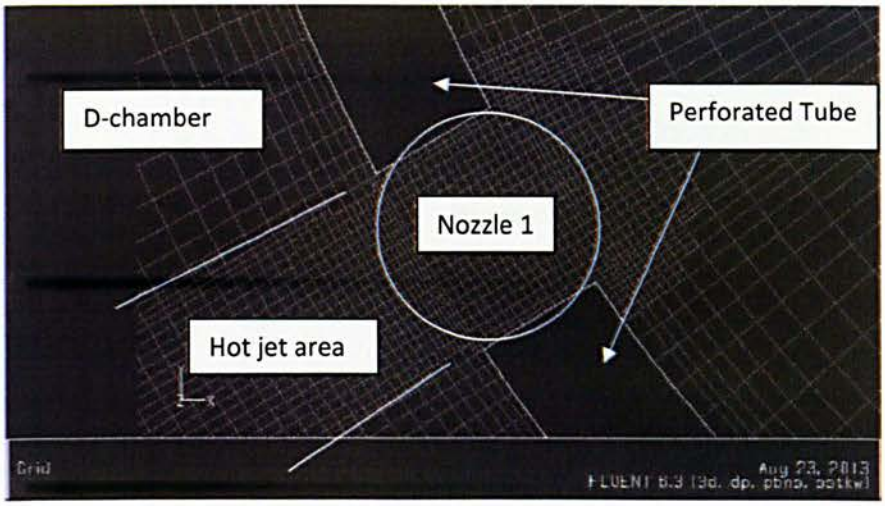

Figure 3.2.2: Structured mesh inside nozzle 1

As for boundary condition inside D-chamber (Figure 3.2.3), a mass flow inlet boundary condition was employed at the piccolo tube entrance and exit surfaces in order to control the mass of hot air entering and exiting piccolo tube. Pressure outlet boundary condition was utilized at the exhaust surface where the air was released to the atmosphere. The nacelle lip-skin and perforated tube were declared as solid domain, while the hot air inside D-chamber as fluid domain. As illustrated in Figure 3.2.3, Bulkhead at the rear D-chamber was set as wall. Periodic boundary conditon was applied on both right and left side surfaces of D-chamber and nacelle lip-skin.

Outside the D-chamber, pressure-far-field was applied at the front curve ambient surface, and used to manage Mach number of the approach free stream. In order to account for the free stream velocity from the ambient domain, pressure outlet was chosen at the rear ambient surface. Periodic boundary condition was set at right and left side ambient surfaces, and the ambient was set as fluid domain.

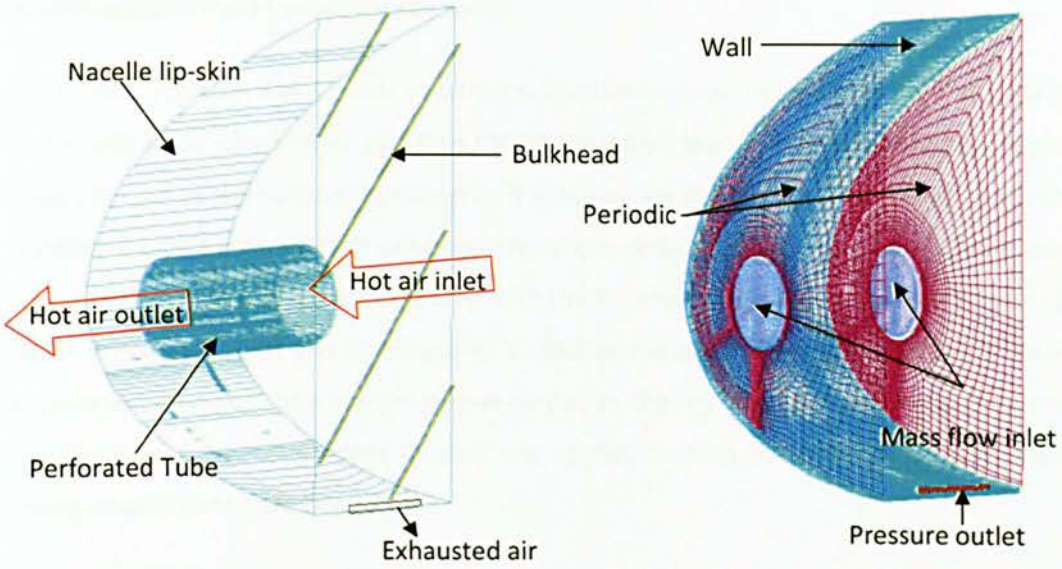

3.2.3: Boundary conditions for PTAI inside D-chamber

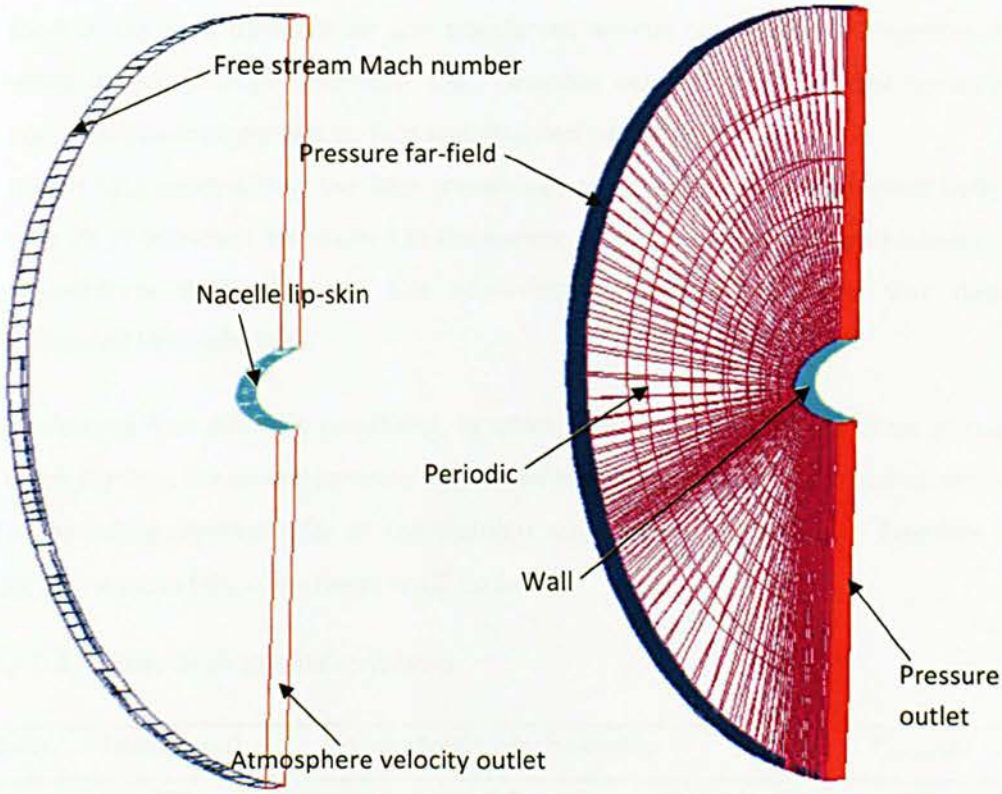

3.2.4: Boundary conditions for PTAI outside D-chamber

3.3 Computational Fluid Dynamic (CFD) Setup

The CFD code 'FLUENT' was utilized to perform the simulations. The lowest PTAI Reynolds number (Re_{PTAI}) in this study was 13'600, and thus the impinging jet was in fully turbulent flow regime. K-ω SST was selected as the turbulence model as it accounts for the transport of turbulent shear stress. In addition, K-ω SST offers better prediction results especially under complex boundary layer with adverse pressure gradients when compared with the k-ε and Spalart-Allmaras models [112-114]. For instance, Wong et al. [79] and Domingos et al. [80] employed this turbulent model in their study. Ideal gas was assumed in the computational model, as the jet Mach number within the simulation was higher than 0.3. Second upper upwind was applied to help obtain more precise results. The following assumptions have been made:

1. The turbulent intensity of free stream air was assumed as a constant for all test conditions (intensity of 2%).
2. α was constant (0°)for all the cases analyzed
3. Most of the heat from hot air was transferred directly to effective-impingent-surface on which the jets impinge. Therefore, the interaction between the exhausted hot air and the non-effective-impingement-surface was assumed negligible.
4. Brown [41] claimed that the heat transferred to non-effective-impingement-surface was only 3% of total heat transferred to the nacelle lip-skin. Therefore, it was believed that the temperature distribution on the non-effective-impingement-surface was dominantly influenced by conduction.

The study covered four different conditions, in which every condition had different altitude, free stream Mach number, hot air temperature ($T_{piccolo}$), ambient temperature (T_∞) and ambient pressure (P_∞). The operating conditions for all the altitudes are shown in Table 3.3.1. Reynolds number (Re_{PTAI}) for all the cases falls in the range of 10^4 to 6×10^4.

Table 3.3.1: Summary of all altitude conditions

Condition	Altitude (m)	Free stream Mach number	T_∞ (K)	$T_{piccolo}$ (K)	P_∞(Pa)
Taxi	396	0.1	290	383	96526
Climb	3200	0.42	276	545	68051
Hold	3048	0.32	279	458	69774
Descent	2438	0.44	282	403	75153

Re_{PTAI} was defined as:

$$Re_{PTAI} = \frac{m_{hot\ air} d}{N_{nozzle} A_{Nozzle} \mu} \quad (3.1)$$

$m_{hot\ air}$ = hot air mass flow rate

A_{nozzle} = nozzle cross sectional area

μ = air dynamic viscosity

d = diameter of nozzle

N_{nozzle} = number of nozzles

The local dimensionless temperature ($\dot{T}$) was defined as:

$$\dot{T} = \frac{T_y - T_\infty}{T_{piccolo} - T_\infty} \quad (3.2)$$

where T_y = local temperature

$T_{piccolo}$ = temperature of hot air within piccolo tube

T_∞ = ambient temperature

The coarse mesh normally produces inaccurate result, but very fine mesh results in longer computation time. Therefore, grid independence test has been conducted to arrive at the optimum mesh size. The dimensionless temperature contour of the nacelle lip-skin obtained with very coarse mesh, coarse mesh, current mesh, fine mesh and very fine mesh, for five different mesh intensities, are illustrated in Figure 3.3.1. There are no significant differences in nacelle lip-skin temperatures obtained by current, fine and very fine meshes, as evidenced by Figure 3.3.1. However the coarse mesh has lower temperature than current mesh especially at point B. It is also observed that the very coarse mesh has produced the lowest temperature in all cases.

Figure 3.3.2 shows the comparison of $\dot{T}$ on the nacelle lip-skin for the very coarse (1.5 x 10^6 grid elements) , coarse (2.0 x 10^6 grid elements), current (2.9 x 10^6 grid elements), fine (4.0 x 10^6 grid elements) and very fine (10 x 10^6 grid elements) meshes. It is obvious from the plot that the $\dot{T}$ profiles for current, fine and very fine meshes are similar. The temperatures of very coarse mesh and coarse mesh are significantly lower than current mesh. Then, Mach number contour plots of the hot air exiting from the nozzles for the coarse, current, fine and very fine meshes are shown in Figure 3.3.3. It can be seen from these plots that the contours for current, fine and very fine meshes are

again very similar. However, Mach number of the coarse mesh seems lower than the other meshes. The current mesh took 3 days for one case to converge. However, finer mesh and very fine mesh took 7 and 21 days respectively for one case to converge, while very coarse and coarse meshes were out of choice. Therefore, the current mesh was chosen for all computational models in the PTAI study.

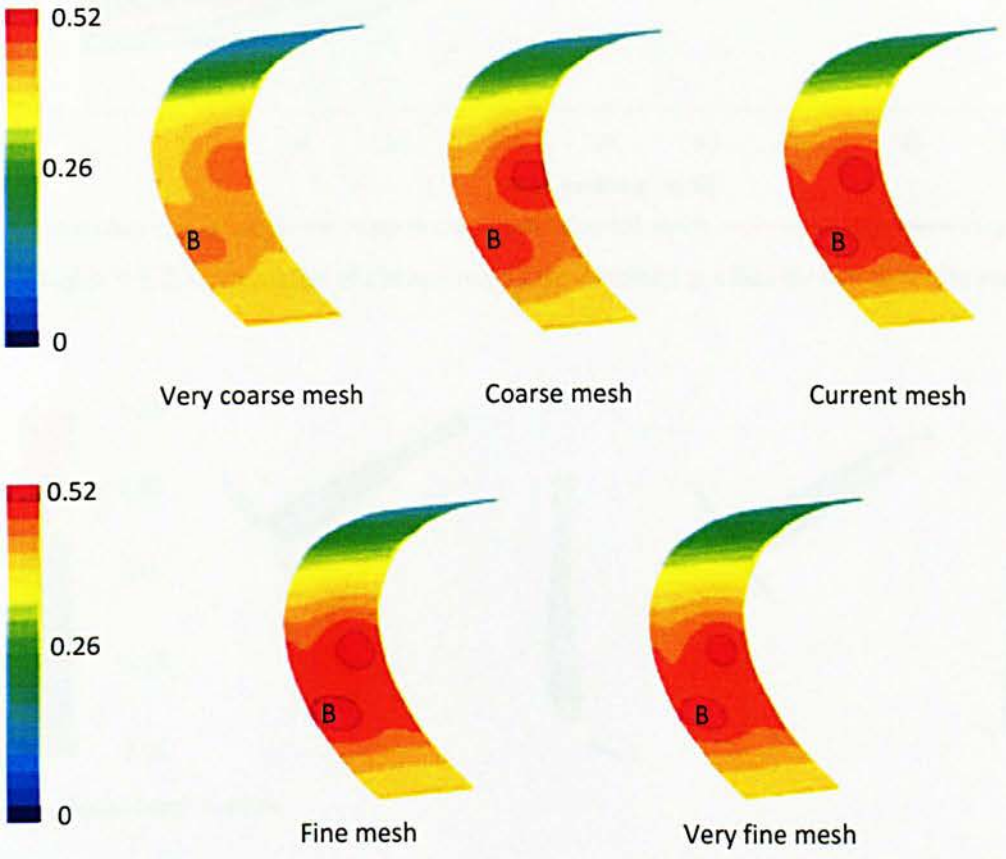

Figure 3.3.1: Lip-skin dimensionless temperature contour of various mesh intensity

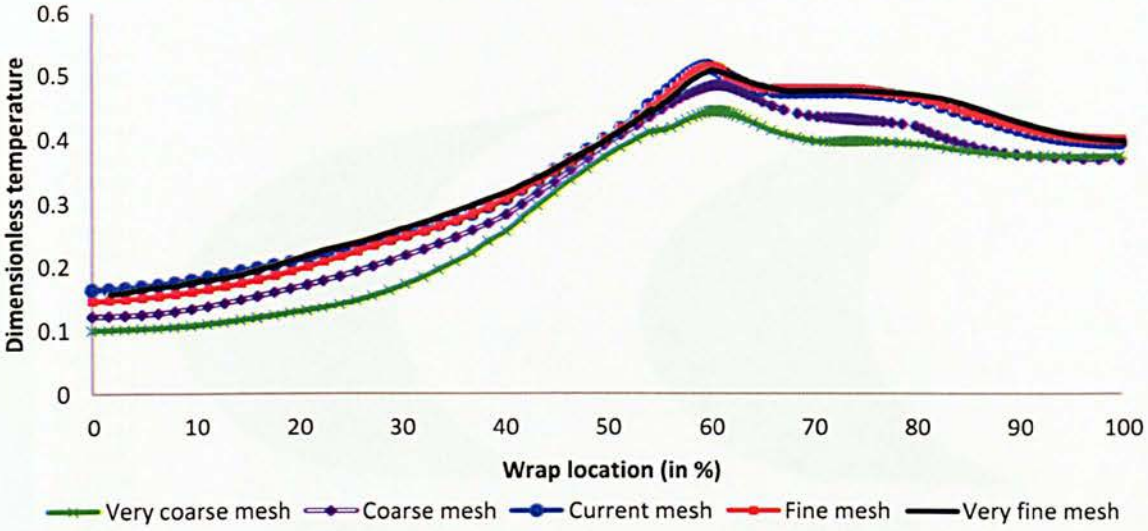

Figure 3.3.2: Comparison of dimensionless temperature profiles for five different mesh densities.

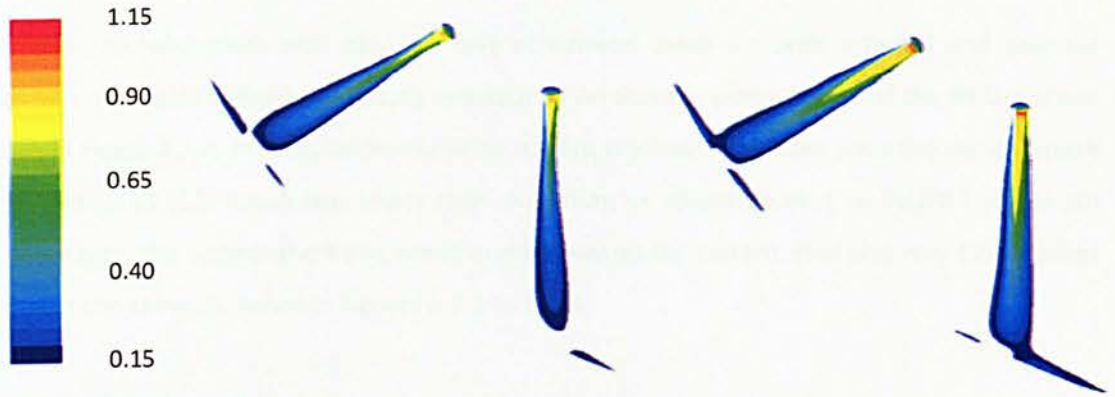

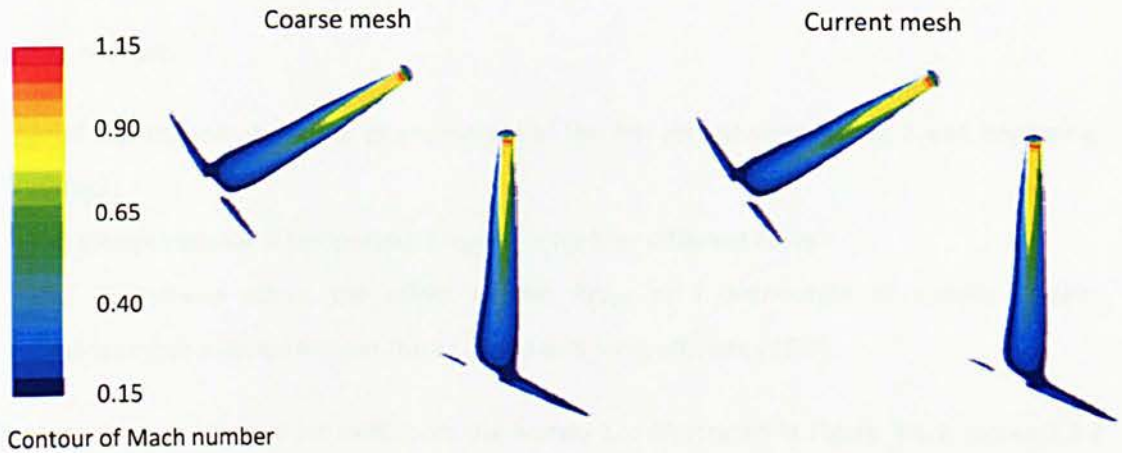

Figure 3.3.3: Jet Mach number contours

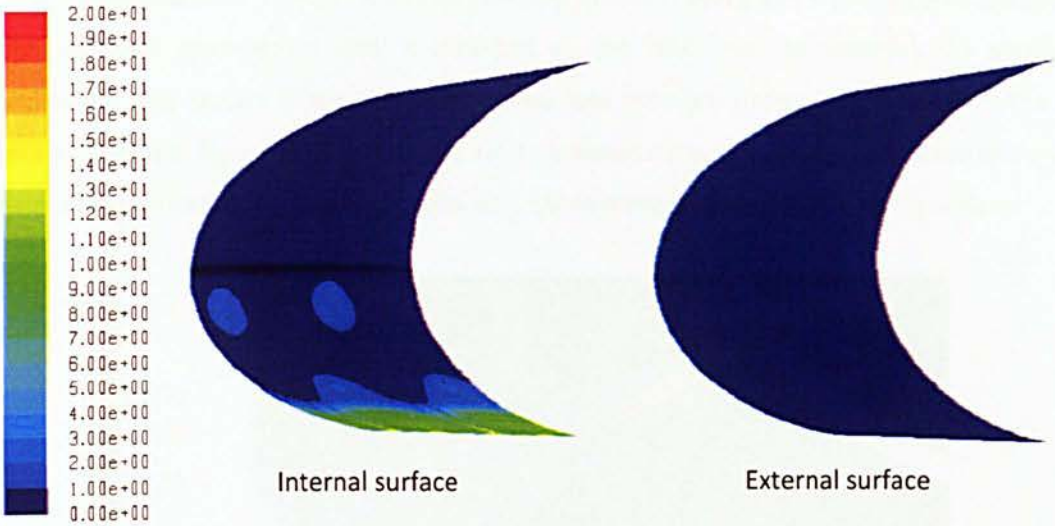

Figure 3.3.4: Dimensionless wall distance contours on internal and external surfaces of nacelle lip-skin

Furthermore, dimensionless wall distance (y+) of current mesh on both internal and external surfaces was examined before conducting simulations on thermal performance of the PTAI system. As shown in Figure 3.3.4, the results produced by current mesh were reliable since the current mesh had the highest y+ (13) which was lower than maximum y+ recommended by FLUENT (y+ of 30) [103]. Moreover, the temperature and Mach number values for current, fine and very fine meshes were almost the same as shown in Figures 3.3.1 to 3.3.3.

3.4 Results and Discussion

This section presents

- Brief explanation about the phenomenon of the hot jet between Nozzle 1 and impinging-surface;
- The interpretations of temperature contours for four different cases;
- The illustrations about the effect of the Re_{PTAI} on $\dot{T}$ distribution of nacelle lip-skin, dimensionless average temperature ($\hat{T}$) and anti-icing efficiency (*EFF*).

The Mach number contour of jet exits from the Nozzle 1 is illustrated in Figure 3.4.1. Figure 3.4.2 shows the local Mach number (u_y) profile of the jet from Nozzle 1 to the inner skin against *z/d*. *z* is the distance from the local point to the nozzle. The high value of u_y inside the nozzle is due to the high air pressure difference between the air inside perforated tube and D-chamber. Just after the jet

exiting the nozzle, u_y fluctuates excessively vs. z/d from point 1 to 6 (Figure 3.4.2) due to shock wave since u_y exceeds Mach 1. Then, u_y is almost constant before it decreases moderately at z/d about 7.5 as the jet flows downstream until it impinges on the inner skin. In addition, the shock wave phenomenon also results in the intermittent absolute pressure (from point 1 to 7) in the nozzle vicinity as shown in Figure 3.4.3 and Figure 3.4.4. Subsequently, the absolute pressure of the hot jet remains constant before it increases slowly with z/d as it approaches the impinging surface.

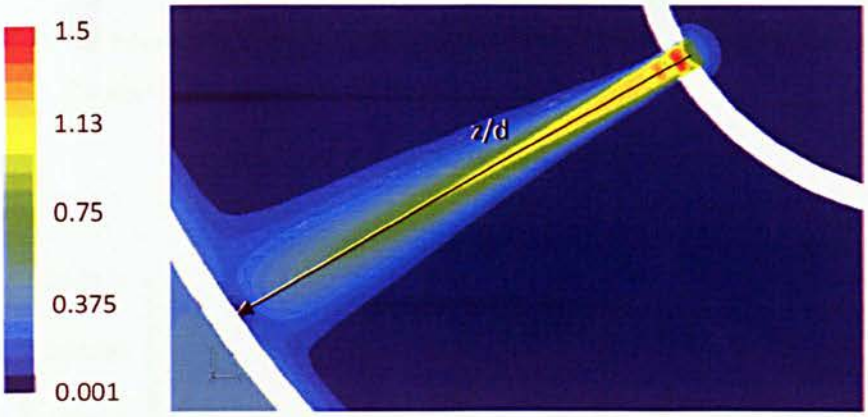

Contour of Mach number

Figure 3.4.1: Contour of Mach number of hot air exit from Nozzle 1.

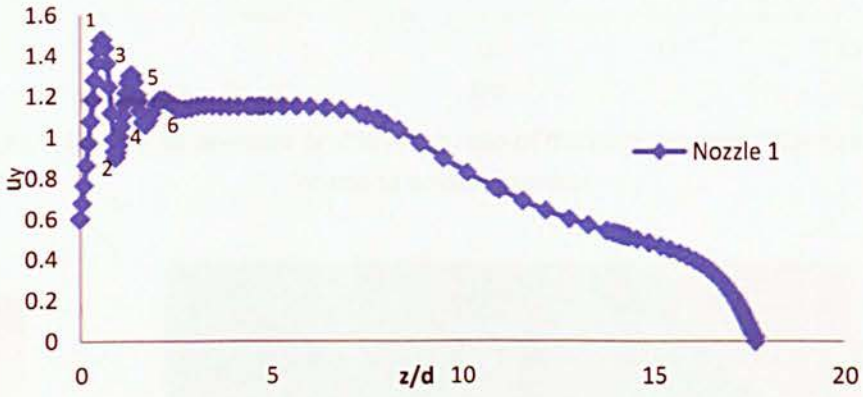

Figure 3.4.2: Hot air Mach number profile along ratio of distance between local point and nozzle to nozzle diameter (z/d) for Nozzle 1

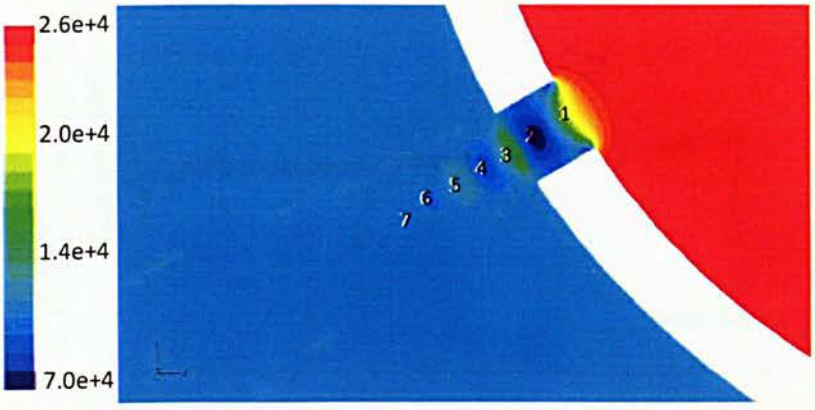

Figure 3.4.3: Pressure contour in Nozzle 1 vicinity

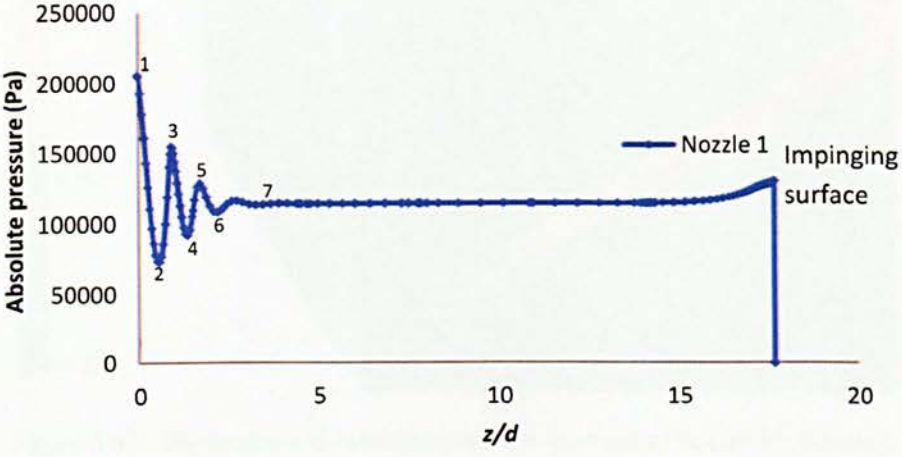

Figure 3.4.4: Hot air pressure profile along ratio of distance between local point and nozzle to nozzle diameter

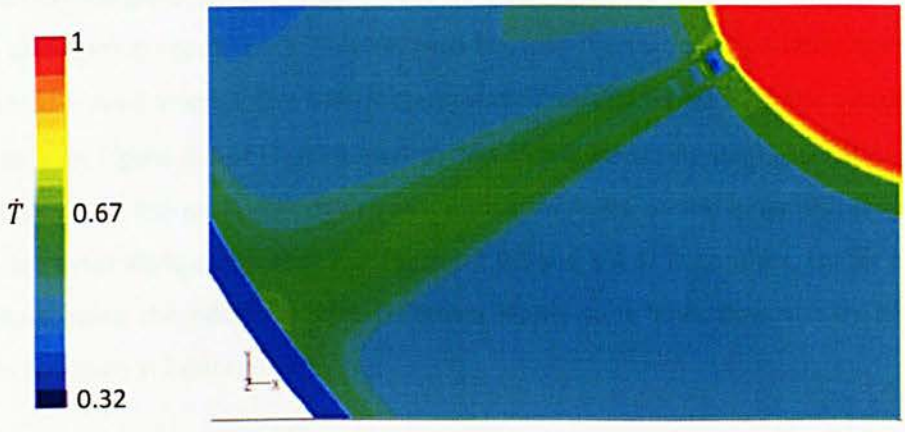

Figure 3.4.5: Dimensionless static temperature contour of hot air for Nozzle 1

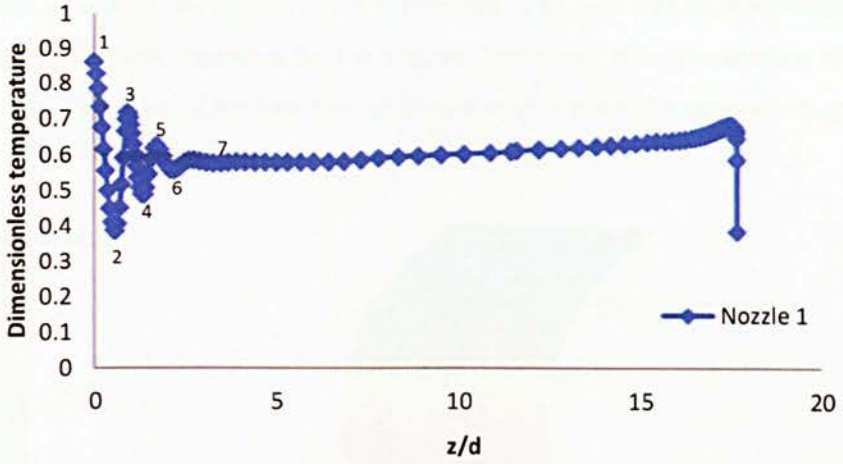

Figure 3.4.6: Static $\dot{T}$ profile of hot air from nozzle 1

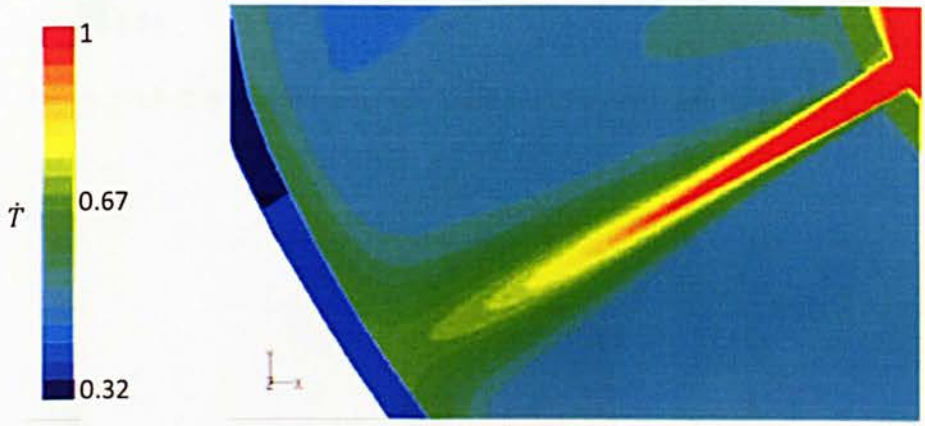

Figure 3.4.7: Dimensionless total temperature contour of hot air for Nozzle 1

The static $\dot{T}$ contour and profile of jet are shown in Figures 3.4.5 and 3.4.6 respectively. Since the hot air flow is compressible, the low static $\dot{T}$ appears inside Nozzle 1 because of the jet with high Mach number, as shown in Figure 3.4.5. This happens because the static temperature from the tube has converted to kinetic energy. The intermittent static $\dot{T}$ at downstream of the nozzle outlet (from point 1 to 6 in Figure 3.4.6) is attributed to the shock wave phenomenon. Afterwards, static $\dot{T}$ increased slowly as the jet flows downstream until it impinges on the inner skin since the jet Mach number decreases along *z/d* as shown in Figures 3.4.5 and 3.4.6. In contrast, the jet has a high total temperature inside the nozzle. It then decreases slowly as it flows downstream until it impinges inner skin as shown in Figure 3.4.7.

Figures 3.4.8 to 3.4.11 illustrate $\dot{T}$ contours of the nacelle lip-skin for Taxi, Climb, Hold and Descent conditions respectively, for $m_{hot\ air}$ of 0.159kg/s. All the figures show that the hotspots occurred on the inner skin, which coincides with the area that the piccolo jets are directly impinged on. In the

real flight, it is that portion of the lip-skin which is required to be kept free from ice in order to avoid ice shedding and subsequent ingestion by the engine. Therefore, the temperature profile of the inner lip-skin should always be higher than that of the outer skin when the system is in operation.

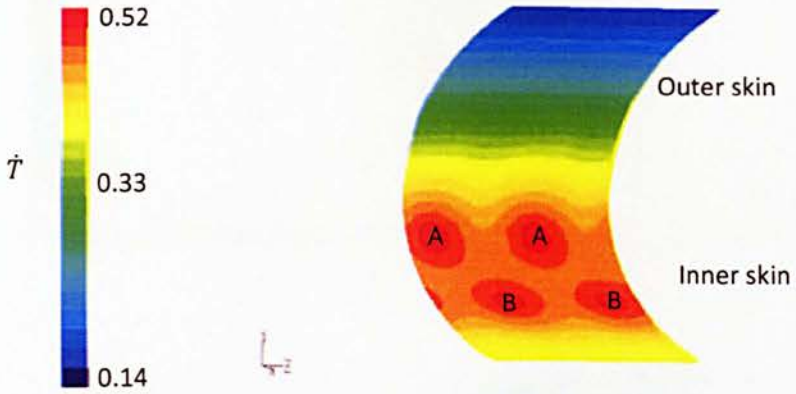

Figure 3.4.8: Dimensionless temperature contour of nacelle lip-skin in Taxi case

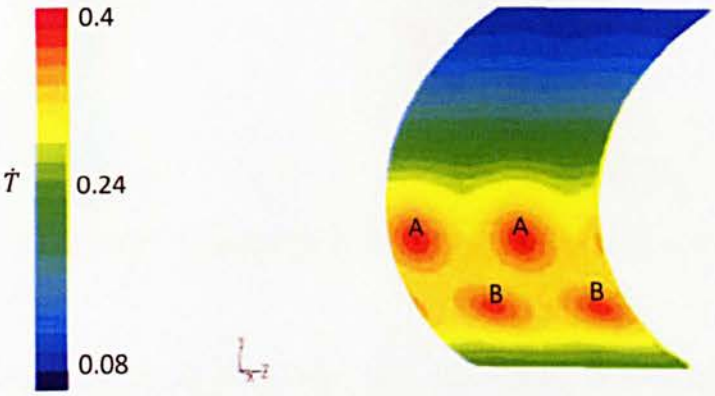

Figure 3.4.9: Dimensionless temperature contour of nacelle lip-skin in Climb

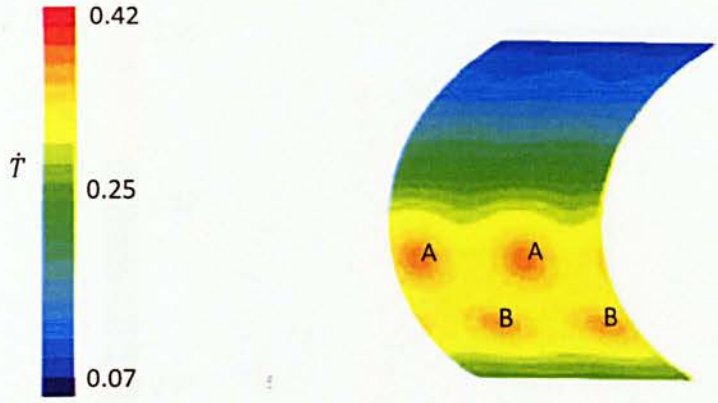

Figure 3.4.10: Dimensionless temperature contour of nacelle lip-skin in Hold

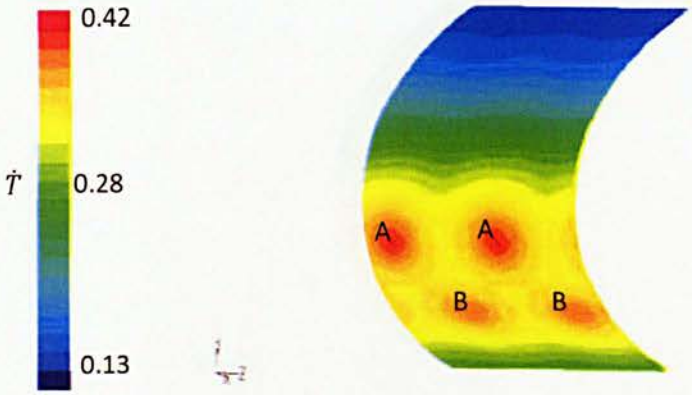

Figure 3.4.11: Dimensionless temperature contour of nacelle lip-skin in Descent

Figures 3.4.8 to 3.4.11 also show that points A and points B have higher temperatures than their surrounding regions. These points are the locations of the highest intensity of the impinging jets for Nozzle arrays 1 and 2 respectively. The figures also reveal that $\dot{T}$ at Point A is slightly higher than that at Point B. This is because z is slightly shorter from Point A to nozzle than from Point B to nozzle. In fact, $\dot{T}$ is inversely related to $T_{piccolo} - T_{\infty}$, while it increases with $T_y - T_{\infty}$ as shown in Equation 3.2. Out of the four cases analysed, the taxi provides the highest $\dot{T}$ because it has the lowest $T_{piccolo} - T_{\infty}$ and intermediate $T_y - T_{\infty}$. From Figures 3.4.8 to 3.4.11, it is evident that the hold produces the lowest lip-skin temperature since it has high $T_{piccolo} - T_{\infty}$ and low $T_y - T_{\infty}$.

The effect of Re_{PTAI} in the range of 25'000 to 50'000 on $\dot{T}$ for climb condition is illustrated in Figures 3.4.12 to 3.4.14. The figures show that $\dot{T}$ of both hotspots; point A and point B, increases with Re_{PTAI}. In addition, the low $\dot{T}$ area (blue colour zone) on the outer skin shrinks as the Re_{PTAI} increases from 25'000 to 50'000. Overall, the whole lip-skin $\dot{T}$ increases with Re_{PTAI}.

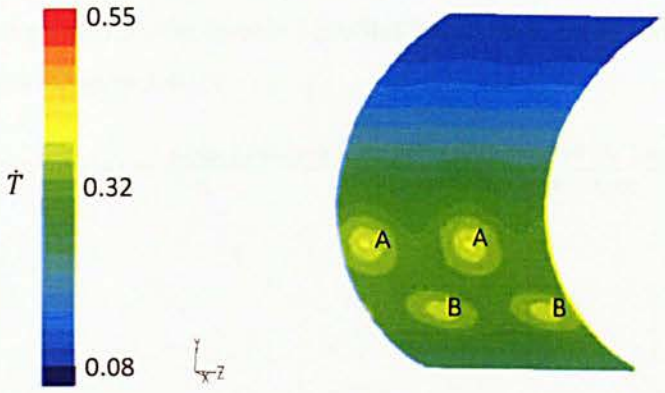

Figure 3.4.12: Dimensionless temperature contour of nacelle lip-skin at PTAI Reynolds number of 25,800

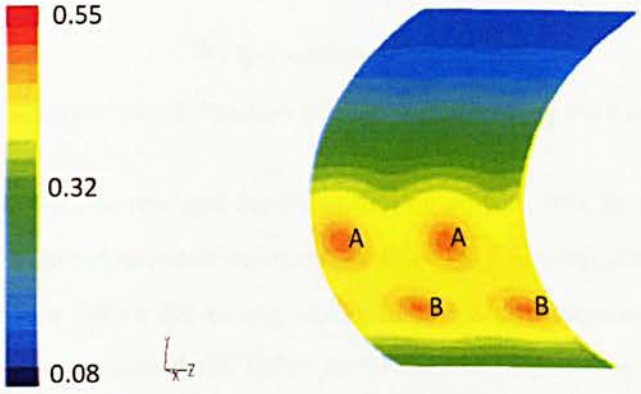

Figure 3.4.13: Dimensionless temperature contour of nacelle lip-skin at PTAI Reynolds number of 40,000

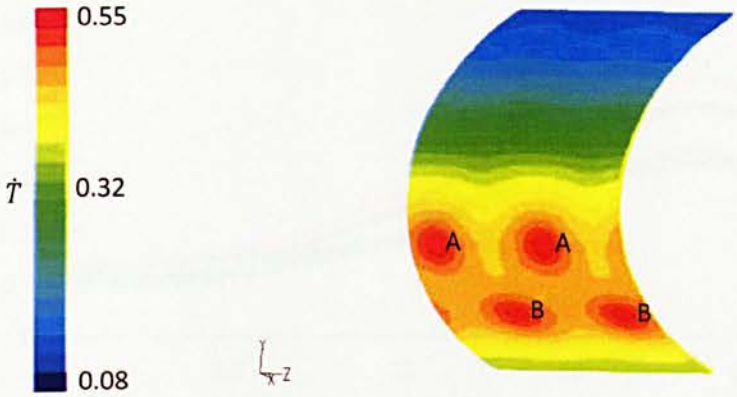

Figure 3.4.14: Dimensionless temperature contour of nacelle lip-skin at PTAI Reynolds number of 50,000

Figure 3.4.15 illustrates the position of wrap location (%) along the lip-skin; the term 'wrap location' is defined by equation 3.3. The lip-skin $\dot{T}$ profiles for climb at three different Re_{PTAI} from 25'000 to 50'000 are shown in Figure 3.4.16.

$$Wrap\ location\ (\%) = \frac{Length\ between\ local\ point\ to\ the\ end\ of\ the\ external\ lip-skin}{Total\ nacelle\ lip-skin\ length} \quad (3.3)$$

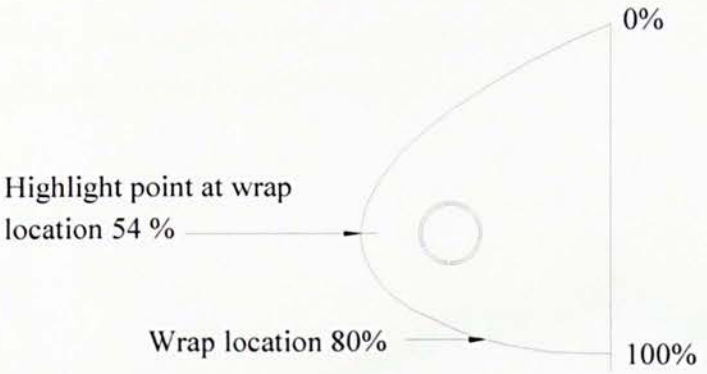

Figure 3.4.15: Position of wrap location along the nacelle lip-skin

In general, Re_{PTAI} has not changed the $\dot{T}$ distribution pattern. The lip-skin $\dot{T}$ increases tremendously from point *a* to *b*, for all Reynolds numbers. Afterwards, $\dot{T}$ reaches plateau, reduces slightly to c and increases again to d before decreasing rapidly to e. It is also observed that the lip-skin $\dot{T}$ increases with Re_{PTAI}. As Re_{PTAI} increases from 25'800 to 50'000, the magnitudes of $\dot{T}$ at points *b* and *d* increase from 0.342 to 0.480 and from 0.344 to 0.494 respectively; similarly, the cold spot $\dot{T}$ at point *a* increases to almost 0.037. The results also show that $\dot{T}$ along the wrap location increases with Re_{PTAI}.

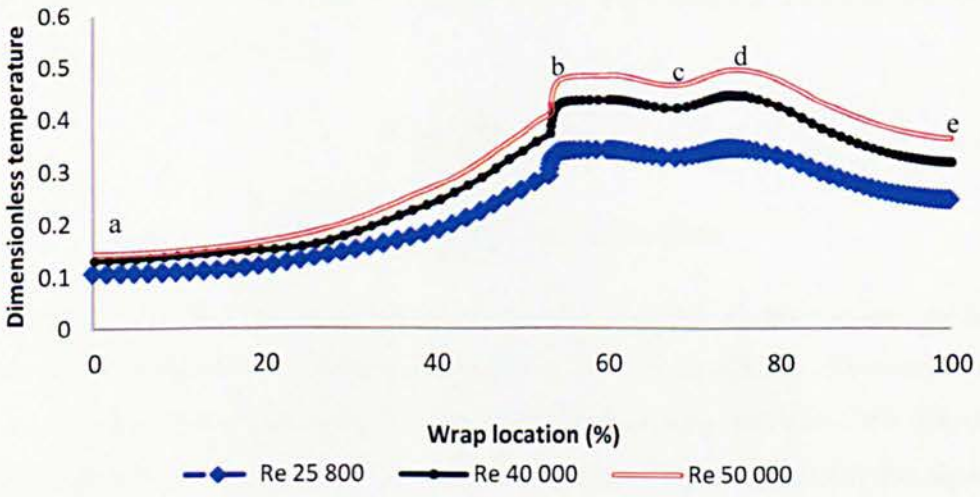

Figure 3.4.16: Nacelle lip-skin dimensionless temperature profile in climb condition for various PTAI Reynolds number

Figure 3.4.17 reveals the effect of Re_{PTAI} on lip-skin $\dot{T}$ profiles along the wrap location under descent condition. Similar to Figure 3.4.16, Figure 3.4.17 shows that the trend of $\dot{T}$ profiles against wrap location for all Re_{PTAI}, is similar. The lip-skin $\dot{T}$ increases along the wrap location from point f to g. It then flattens out from point g to h. Afterwards, $\dot{T}$ increases to peak at point i before it falls down to point j. As expected, $\dot{T}$ along wrap location increases with Re_{PTAI}. The results show that $\dot{T}$ is highest at point i with the increase of 0.088 as the Re_{PTAI} is increased from 32'300 to 50'000. Meanwhile, $\dot{T}$ is lowest at point f with 0.017 increments as Re_{PTAI} is increased from 32'300 to 50'000. Similar to climb, the lip-skin $\dot{T}$ along the wrap location increases with Re_{PTAI}.

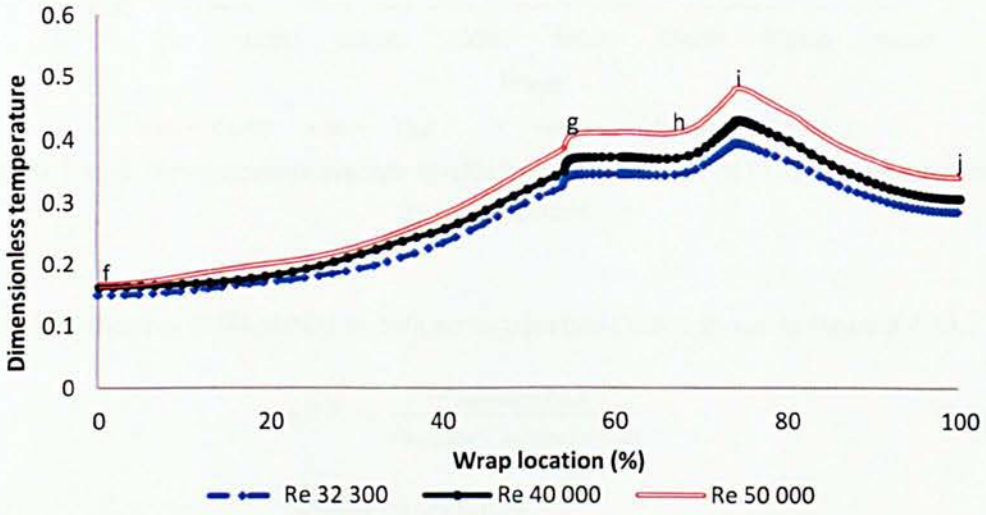

Figure 3.4.17: Nacelle lip-skin dimensionless temperature profile in Descent condition for various PTAI Reynolds numbers

The relationship between dimensionless average lip-skin temperature ($\hat{T}$) and Re_{PTAI} is illustrated in Figure 3.4.18, where $\hat{T}$ is defined as:

$$\hat{T} = \frac{T_{ave} - T_{\infty}}{T_{piccolo} - T_{\infty}} \qquad (3.4)$$

where T_{ave} = average lip-skin temperature

Figure 3.4.18 shows that, $\hat{T}$ increases with Re_{PTAI} for all conditions. As Re_{PTAI} is increased, $m_{hot\ air}$ is elevated, thus causing an increment on the amount of heat supplied to the nacelle lip-skin. In addition, the velocity of jet impinging on the inner skin increases, and hence the boundary layer thickness decreases as Re_{PTAI} increases. It is further observed that, Taxi produces the highest $\hat{T}$ and Hold shows the lowest $\hat{T}$ along Re_{PTAI}. While $\hat{T}$ is inversely related to $T_{piccolo} - T_{\infty}$, it increases with $T_{ave} - T_{\infty}$. Taxi has the lowest $T_{piccolo} - T_{\infty}$ and intermediate $T_{ave} - T_{\infty}$. As a result, Taxi produces the highest $\hat{T}$ in this study (Figure 3.4.18). Although Climb has $T_{piccolo} - T_{\infty}$ slightly higher than Hold, it

has higher $T_{ave} - T_{\infty}$ when compared to Hold. Therefore, Hold has the lowest $\hat{T}$ in the given range of Re_{PTAI}, as shown in Figure 3.4.18.

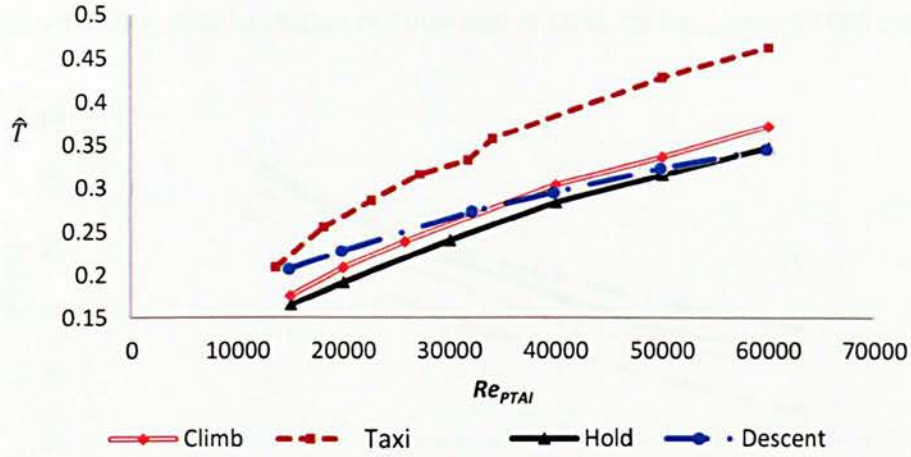

Figure 3.4.18: Dimensionless average lip-skin temperature against PTAI Reynolds number for all conditions

The anti-icing efficiency (*EFF*) of PTAI as defined by equation (3.5) is shown in Figure 3.4.19.

$$EFF = \frac{T_{piccolo} - T_{exh}}{T_{piccolo} - T_{adiabatic\,wall}} \tag{3.5}$$

where T_{exh} = Exhaust temperature

and the adiabatic temperature of lip-skin $T_{adiabatic\,wall}$ is calculated by:

$$T_{adiabatic\,wall} = T_{\infty}\,(1 + R_f(\frac{\gamma-1}{2})M_n^2) \tag{3.6}$$

where R_f is recovery factor and γ is 1.41.

EFF represents that the percentage amount of heat from hot air is absorbed by the lip-skin. According to Figure 3.4.19, the curves of *EFF* vs. Re_{PTAI} are similar in all cases. *EFF* decreases exponentially with Re_{PTAI} in the range 10'000 to 60'000. In other words, the efficiency of heat transfer from hot air to the nacelle lip-skin decreases with increase in $m_{hot\,air}$ in all conditions. The Taxi and Climb display reduction in *EFF* by almost 30.3% and 26.2% respectively for Re_{PTAI} in the range of 15'000 to 60'000. For the same range of Re_{PTAI}, Descent and Hold show EFF reduction of 27% and 24.7% respectively. Descent has the highest *EFF* for the given Re_{PTAI}, followed by Hold, Climb and Taxi. Free stream Mach number and $T_{piccolo} - T_{\infty}$ have affected EFF. The heat transfer coefficient between external surface and ambient increases with free stream Mach number, making the nacelle lip-skin absorb more heat from the hot air inside the D-chamber. However, *EFF* is

inversely related to $T_{piccolo} - T_{\infty}$. Descent and Taxi have the highest and the lowest free stream Mach number respectively. Therefore, Descent demonstrates the highest *EFF* and Taxi illustrates the lowest *EFF*. Although the free stream Mach number is higher in Climb than in Hold, Climb shows higher $T_{piccolo} - T_{\infty}$. Thus, Hold has higher *EFF* than that of Climb for Re_{PTAI} from 15'000 to 60'000.

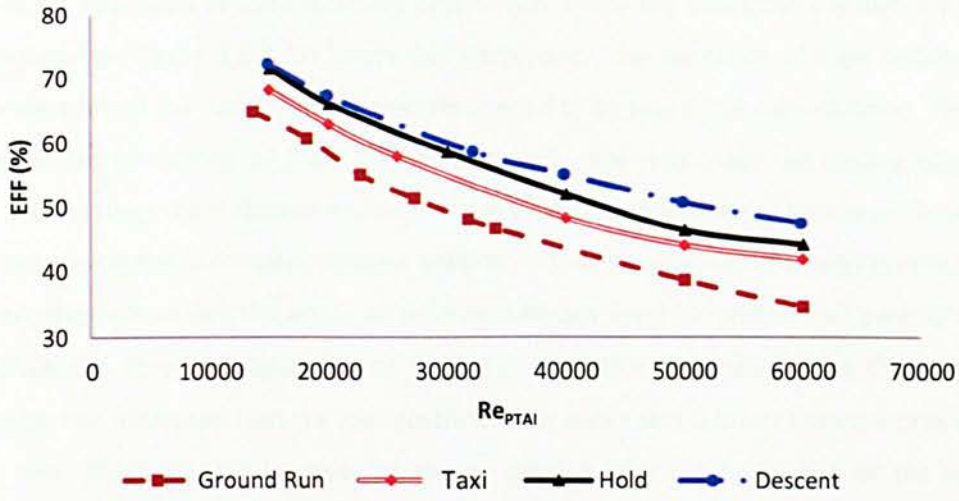

Figure 3.4.19: Effect of PTAI Reynolds number on anti-icing efficiency for all cases

3.5 Validation with Previous Results

Figure 3.5.1 shows the predicted and measured lip-skin $\dot{T}$ profiles for Taxi and Climb, while Figures 3.5.3 and 3.5.5 show those for Hold and Descent respectively, for $m_{hot\ air}$ of 0.159kg/s. In Taxi, as shown in Figure 3.5.1, $\dot{T}$ increases greatly with wrap location from point a to b. Then, the lip-skin $\dot{T}$ decreases gradually with wrap location until point c. In climb condition, $\dot{T}$ increases tremendously from point d until e, and then slightly dropped to the point f before it rises up to point g. Finally, it decreases gradually until point h.

As illustrated in Figure 3.5.1, the lip-skin $\dot{T}$ for taxi has over-predicted especially at wrap locations above 40%, while maintaining consistency with the measured values. According to Figure 3.5.2, the difference between measured and predicted temperature for taxi at wrap location of 40% and above is in the range 7.5% - 9.5%. This deviation is believed to be due to different turbulent intensities in the flight test and *CFD* simulation. The flight test is expected to experience higher turbulent intensity than that has been applied in *CFD* simulation. As the turbulence intensity increases, the heat transfer coefficient increases [117 and 118]. The flight test results imply that in reality more heat is swiped away from the nacelle lip-skin than that predicted by *CFD* simulation; consequently, the measured $\dot{T}$

profile is lower than predicted. The vibration of the wing during the Taxi phase of the flight is the main contributor to the high turbulent intensity level and thus is the cause of the difference in $\dot{T}$ between predicted and test data.

For the climb, the predicted results are shown to be in excellent agreement with the measured results with the exception of wrap locations before 47% where the discrepancy is higher than 10%, as demonstrated by Figure 3.5.2. To justify this discrepancy, the operation of a gas turbine engine and the orientation of the nacelle during the climb, need to be taken into consideration. The engine which is operated by sucking air from its surroundings is mounted under the leading edge of the wing and hence causes the turbulent intensity of the intake flow to increase. However, these factors were not included in the *CFD* model; rather a uniform turbulence intensity level was assumed for the entire atmosphere. In reality the actual turbulence intensity level for ambient air passing over the upper half of the lip-skin is apparent to be lower than that assumed in the *CFD* simulation. Consequently, the measured heat transfer coefficient for outer skin is lower than the prediction. At the same time, the turbulent intensity of the air passing over the lower half of the lip-skin is approximately the same for the real flight as set during the *CFD* simulation. In addition, the angle of attack and subsequent orientation of the nacelle during climb are major contributors to higher turbulent intensity.

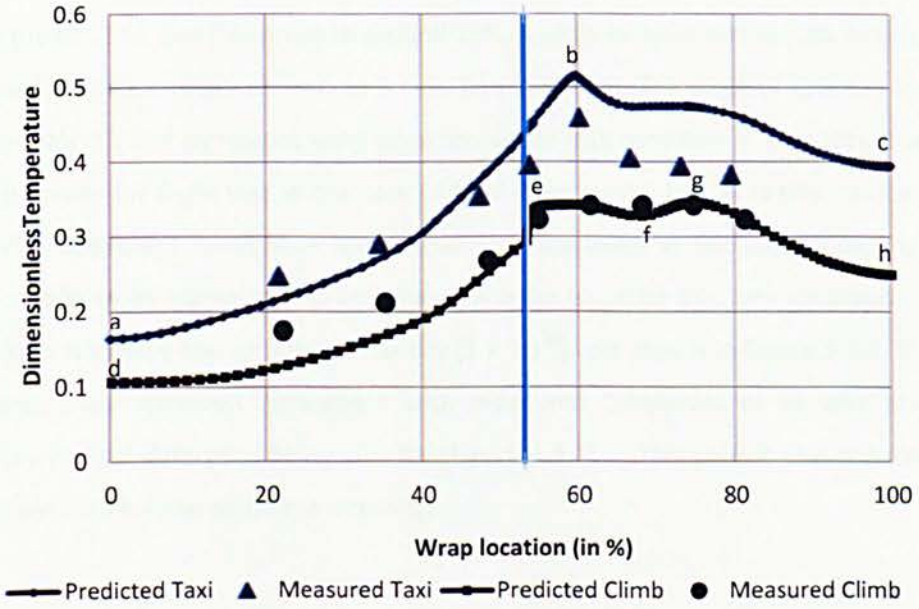

Figure 3.5.1: Predicted and Measured results for Taxi and Climb conditions

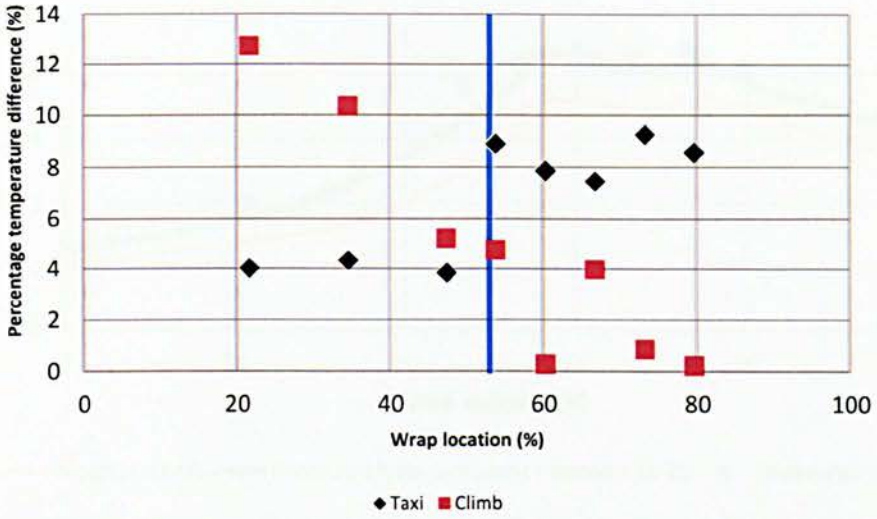

Figure 3.5.2: Percentage difference between measured and predicted results for taxi and climb conditions

In the case of Hold, Figure 3.5.3 depicts that $\dot{T}$ from point i increased tremendously with wrap location until point j. Then, it slightly decreases before increasing gradually again with the wrap location to point k. From there it decreases again to point l. Most measured $\dot{T}$ values of hold are higher than those predicted in the simulation. Figure 3.5.4 illustrates that the temperature differences between measured and predicted results for hold condition at wrap location below 50% are higher (up to 27%), and this drops to around 17% at wrap location above 50%. In this scenario, it is well known that the ambient air in hold is calm and quiescent. The angle of attack in this condition is approximately 0°, and significant wing vibration under this condition is very rare; therefore, the turbulent intensity for flight test in the case of hold is extremely low in reality. Consequently, the heat transfer coefficient in flight is lower than that assumed in the simulation, rendering the measured results to be higher than predictions. In order to prove this, one simulation was run for hold condition with very low turbulent intensity (1×10^{-20}). As shown in Figure 3.5.3, the predicted temperatures show excellent agreement with measured temperatures at very low turbulent intensity, the highest difference being only 8% (Figure 3.5.4). This reveals that the free stream of hold condition has very low turbulent intensity.

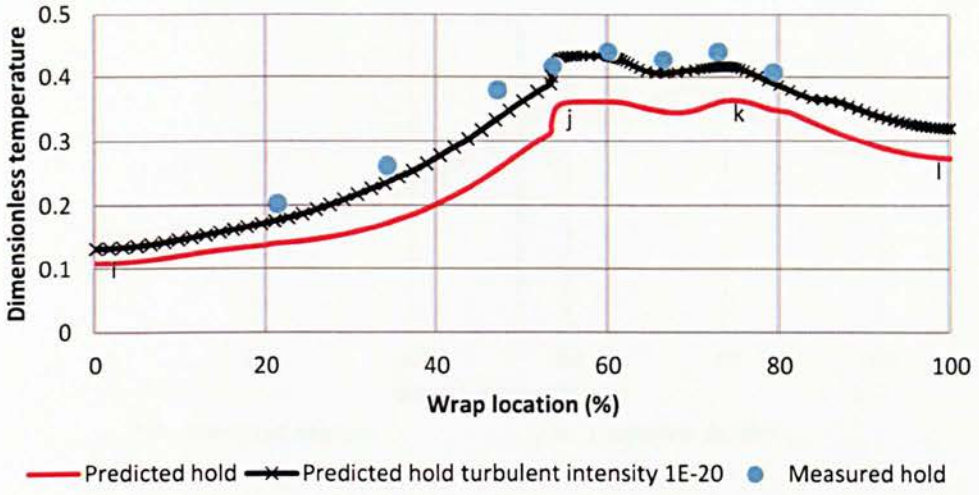

Figure 3.5.3: Predicted and Measured results for Hold condition

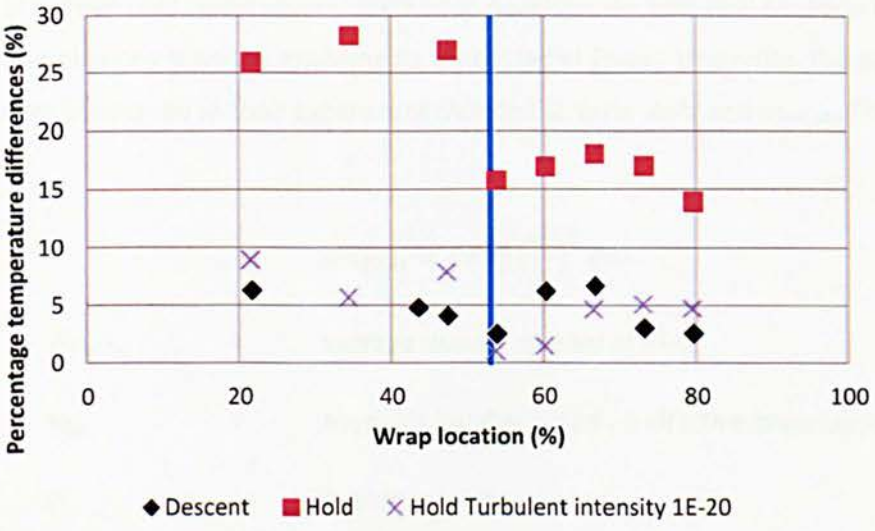

Figure 3.5.4: Percentage difference between measured and predicted results for Hold and Descent conditions

Figure 3.5.5 shows that the predicted results for descent are compared favourably with the measured data. The differences between measured and predicted results along wrap location are lower than 7% as shown in Figure 3.5.4. In this scenario, the important flow characteristics such as the effect of angle of attack, flow separation and the effect of the turbulent level, on the heat transfer coefficient in the experimental investigation are well modelled by CFD simulation. Overall, it can be deduced from Figures 3.5.1 to 3.5.5 that the predicted results are in good agreement with the measured data [100].

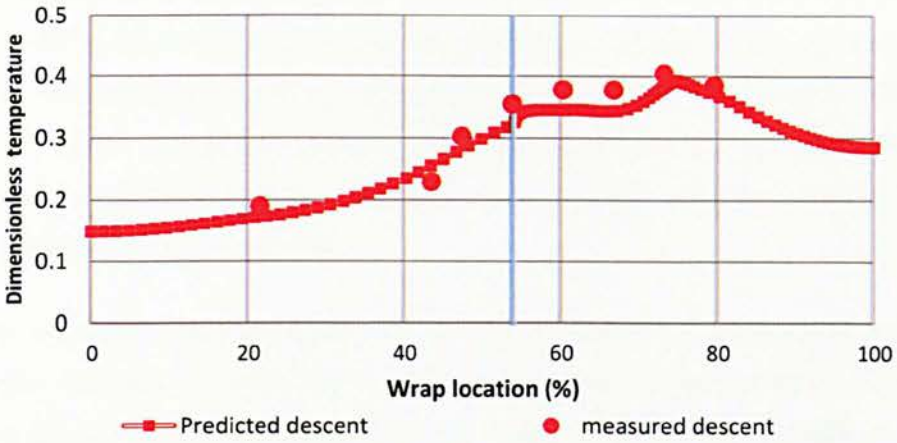

Figure 3.5.5: Predicted and Measured results for Hold condition

The following section compares CFD results of all the cases with empirical correlations proposed by Brown et al. [41]. They used "least square" method to develop their empirical equation based on the data which were obtained from the experiments conducted at Queen University. The parameters of PTAI which were considered in their experiment included *d, Cx/d, Zn/d* and $m_{hot\ air}$. They proposed the correlation:

$$Nu_{PTAI} = CRe_G^a \left(\frac{C_x}{d}\right)^b Pr^{\frac{1}{3}} \qquad (3.7)$$

where Nu_{PTAI} = average Nusselt number of PTAI

Re_G = Reynolds number based on effective-impingement-surface

Pr = Prandtl number

and Re_G can be described as

$$Re_G = \frac{4Gd}{\pi\mu} \qquad (3.8)$$

G = Hot air mass flow per unit area of effective-impingement-surface

The constants had the following values:

C = 0.577, a = 0.922 and b =0.064

Since the geometry of the nacelle lip-skin and the position of the piccolo tube in this study were similar to those used by Brown et al. [41], the effective-impingement-area was also estimated by using their method which started from highlight to 76.2d inside the highlight. The locations of hotspot 1, 2 and 3 were approximately, 12.7d, 38.1d and 63.5d from the highlight, as shown in Figure 3.5.6. The distance from the start point of the average effective impinging length to the highlight point was estimated as 12.7d.

This study adopted the method of Brown et al. to determine Nu_{PTAI}. However, in the present PTAI model, there were only 2 rows of nozzles for every *Cx* instead of 3 rows in their model. The present study also assumed the same condition that could be found for a single jet spread over approximately 12.7d in one direction from the hotspot point on the internal lip-skin surface. This means, the effective-impingement-area in this study covered the highlight point to 50.8d inside the highlight. Therefore, the heat transferred to non-effective-impingement-area was very small compared with the effective-impingement-area; therefore it was neglected in the calculation. Figure 3.5.6 shows the position of the highlight and hotspots for models from both studies.

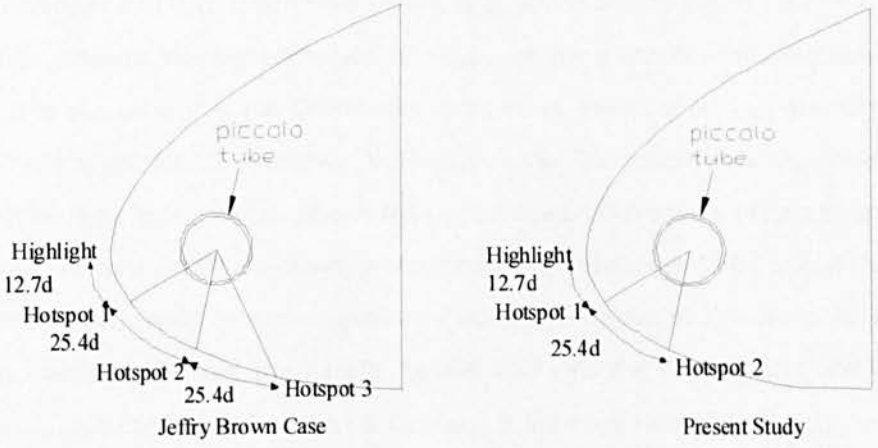

Figure 3.5.6: Position of the hotspot on the nacelle lip-skin for both studies

Figure 3.5.7 shows the plots of Nu_{PTAI} against Re_G. In this study, the following equation was used to calculate Nu_{PTAI}:

$$Nu_{PTAI} = \frac{h_{PTAI} D_h}{k_f} \tag{3.9}$$

where h_{PTAI} = average heat transfer coefficient of PTAI

k_f = fluid thermal conductivity

and h_{PPAI} could be obtained from the following equation

$$h_{PTAI} = \frac{Q}{A_{imp}(T_{piccolo} - T_{imp})} \tag{3.10}$$

Q = heat transfer from air to the lip-skin

A_{imp} = effective-impingement-surface area

T_{imp} = average temperature of effective-impingement-surface area

As Re_G increases, $m_{hot\ air}$ increases and hence the temperature of T_{imp}. All the *CFD* results under these four conditions and correlation from Brown et al. are shown in Figure 3.5.8. It is clear that the Taxi condition presents the highest values of Nu_{PPAI} at any given Re_G followed by descent, cruise and climb. It is also clear that the *CFD* results show lower values of Nu_{PPAI} compared to the Brown et al.'s empirical correlation. However, the result of the Taxi condition is the closest to Brown et al.'s prediction. The climb condition shows the largest deviation from the results of Brown et al. followed by cruise and descent. The ambient temperature (T_∞) is believed to be one of the main parameters affecting Nu_{PPAI}, which was not taken into account in Brown et al.'s study. As T_∞ decreases, more heat is swept away from the nacelle lip-skin and into the downstream ambient, which in turn reduces T_{imp}. According to Equation 3.10, h_{PPAI} is inversely related to $T_{piccolo} - T_{imp}$. Therefore, if $T_{piccolo}$ is constant, $T_{piccolo} - T_{imp}$ increases as T_{imp} decreases. Hence it could be deduced that, reduction in T_∞ decreases T_{imp}, which in turn reduces h_{PPAI} leading to the decrease of Nu_{PPAI} (according to Equation 3.9). From Table 3.3.1 it is clear that Taxi and climb conditions have the highest and lowest T_∞ respectively. Thus, they respectively produce the highest and lowest values of Nu_{PPAI}.

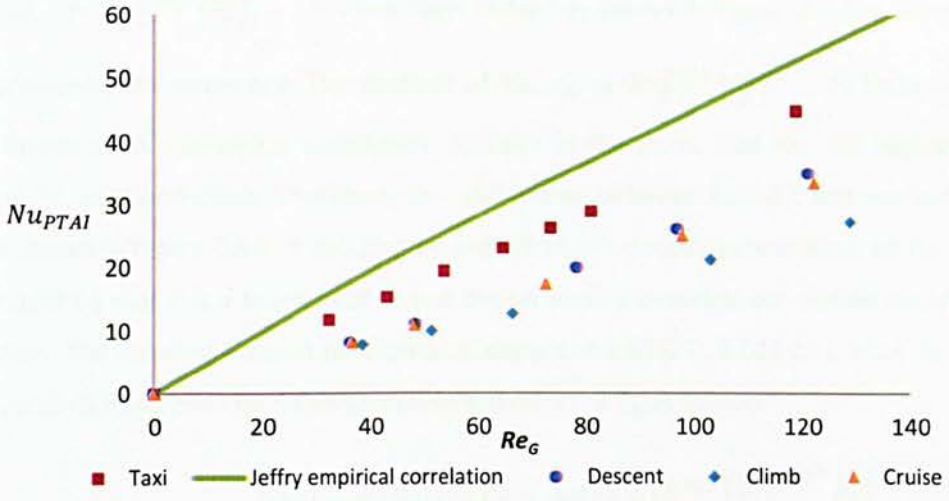

Figure 3.5.7: PTAI average Nusselt number vs. Reynolds number based on the area of impingement surface

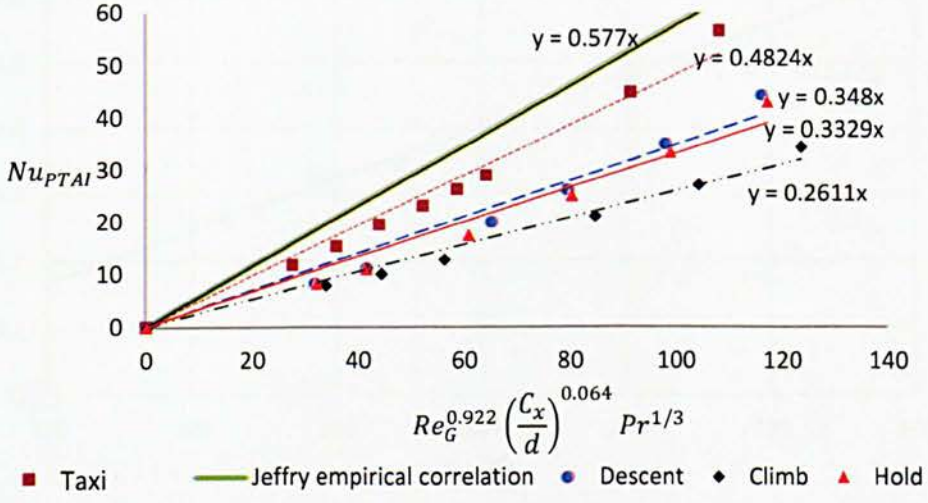

Figure 3.5.8: Nu_{PPAI} against $Re_G^{0.922}\left(\frac{C_x}{d}\right)^{0.064} Pr^{1/3}$

Nu_{PPAI} Vs. $Re_G^{0.922}\left(\frac{C_x}{d}\right)^{0.064} Pr^{\frac{1}{3}}$ has been plotted as shown in Figure 3.5.5 in order to support the aforementioned statement. The gradient of Nu_{PPAI} vs. $Re_G^{0.922}\left(\frac{C_x}{d}\right)^{0.064} Pr^{\frac{1}{3}}$ was represented by C in Brown et al.'s empirical correlation. As seen in the plots, Taxi has the highest C followed by Descent, Hold and Climb. Therefore, the relationship between T_∞ and C was studied, and the results are shown in Figure 3.5.9. It can also be seen that C is directly proportional to T_∞. Thus it could be established that C is a function of T_∞ and Brown et al.'s empirical correlation could be used if T_∞ is known. The value of C could be estimated using $C = 0.0152T_\infty 4.028$ or $C = a\times T_\infty + b$. Accordingly, Equation 3.7 has been modified to include the effect of T_∞, as follows:

$$Nu_{PPAI} = (0.0152T_\infty - 4.028)Re_G^{0.922}\left(\frac{C_x}{d}\right)^{0.064} Pr^{\frac{1}{3}} \qquad (3.11)$$

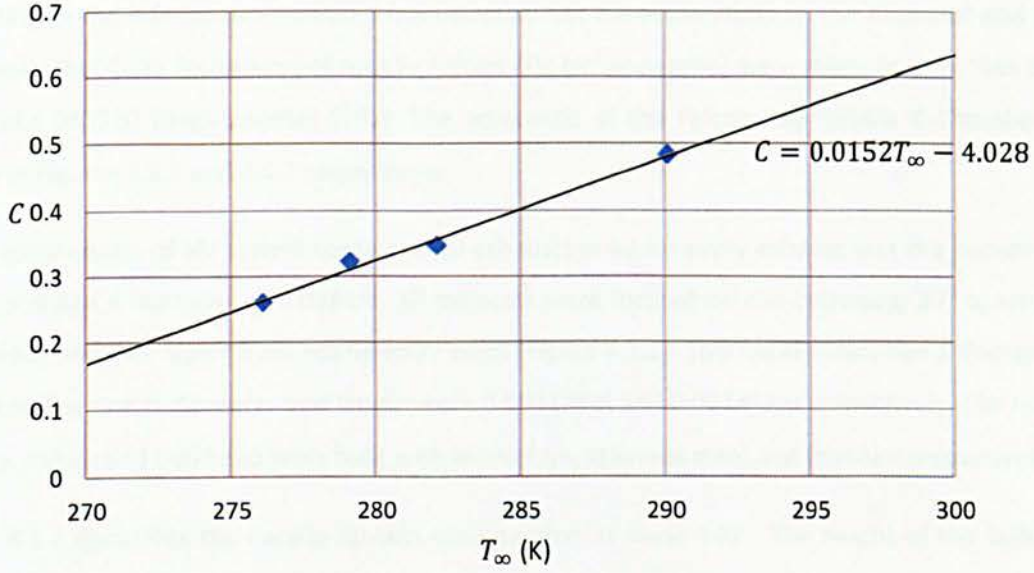

Figure 3.5.9: Relationship between C and ambient temperature

CHAPTER 4: Swirl Anti-Icing

The previous chapter demonstrated the success of CFD modelling of PTAI system by showing that the simulation results were in good agreement with the experimental data [100]. Therefore, similar modelling methodology was employed to predict the thermal performance of swirl anti-icing (SAI) system. This chapter describes the application of SAI thermal performance for Falcon 20g nacelle lip-skin. At the beginning, the thermal performance of basic or original SAI will be described. Then, some alternative designs will be studied via simulation including sloped nozzle, nozzle rotation angle (*NRA*) and length of nozzle in order to enhance SAI thermal performance. The chapter will end with discussion of the effect of nozzle shape on the thermal performance anti-icing.

4.1 SAI for Falcon 20g Nacelle Lip-skin

According to the information obtained from Bombardier Aerospace Belfast, the diameter and cross sectional area of the D-chamber of nacelle Falcon 20g (small nacelle) were much smaller than those of nacelle BR 710 (large nacelle) [100]. The schematic of the Falcon 20g nacelle D-Chamber are shown in Figures 4.1.1 and 4.1.2 respectively.

The original design of SAI system contained 10 exhausts in which every exhaust was in a semicircular shape and had a diameter of 0.0381m. 10 exhausts were located on the bulkhead, 30° apart from each other and ±45° apart from nozzle entry point (Figure 4.1.1). This nacelle inlet had a diameter of 0.6731m. The nozzle diameter and length were 0.009144m and 0.027432m respectively. The nacelle inlet lip, nozzle and bulkhead were built with aluminium, stainless steel and titanium respectively.

Figure 4.1.2 illustrates the nacelle lip-skin cross-section in plane 140°. The height of the bulkhead and the length of the D-chamber were 0.079756m and 0.09525m respectively. The nozzle was placed 0.05715m in front of the bulkhead and nacelle lip-skin thickness was of 0.0016256m. The present study was started with nozzle diameter of 0.009144m, hot air mass flow rate ($m_{hot\,air}$) of 0.0118 kg/s and total temperature of hot air inside nozzle (T_{nozzle}) of 533.15K.

The position of wrap location for small nacelle lip-skin is shown in Figure 4.1.3. At the end of the outer skin edge, wrap location was depicted as 0% and at the other end, the inner skin edge was denoted as 100%. Unlike large nacelle lip-skin, the highlight of small nacelle lip-skin was located at wrap location of 49.8%, as shown in Figure 4.1.3.

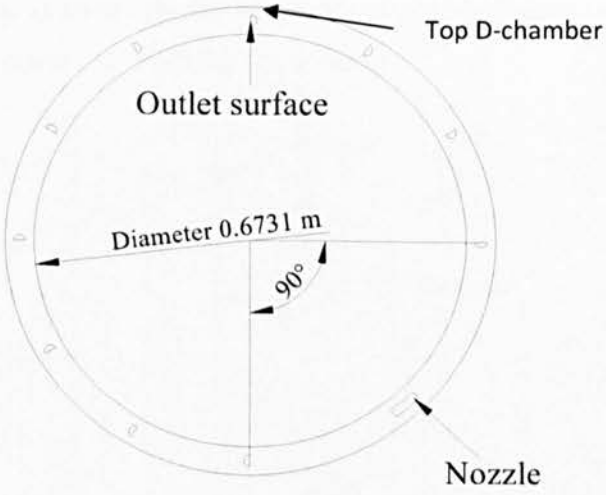

Figure 4.1.1: Schematic drawing of Falcon 20g nacelle D-Chamber

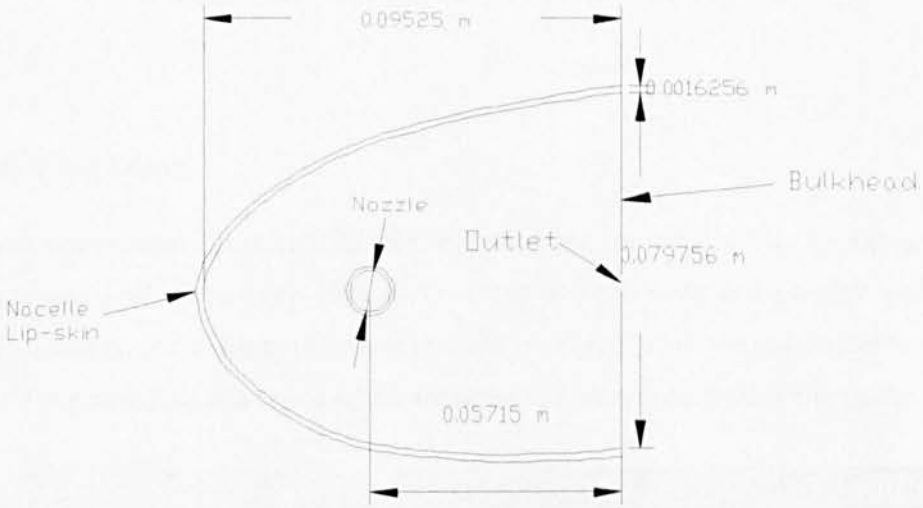

Figure 4.1.2: Schematic drawing of a cross section of nacelle lip

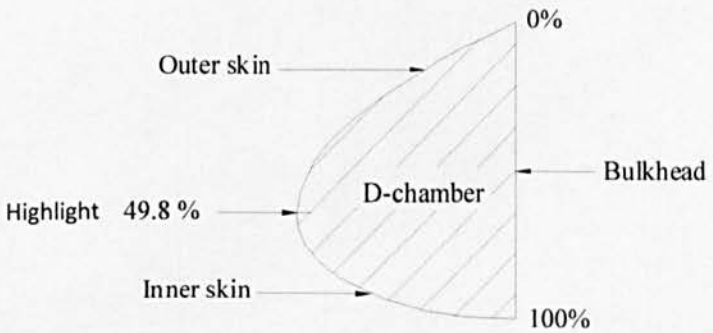

Figure 4.1.3: Position of wrap location on the nacelle D-Chamber

Figure 4.1.4 shows the positions of planes (in degrees) in the nacelle D-Chamber. As shown in the figure, the nozzle was placed in plane 135° from the top of nozzle.

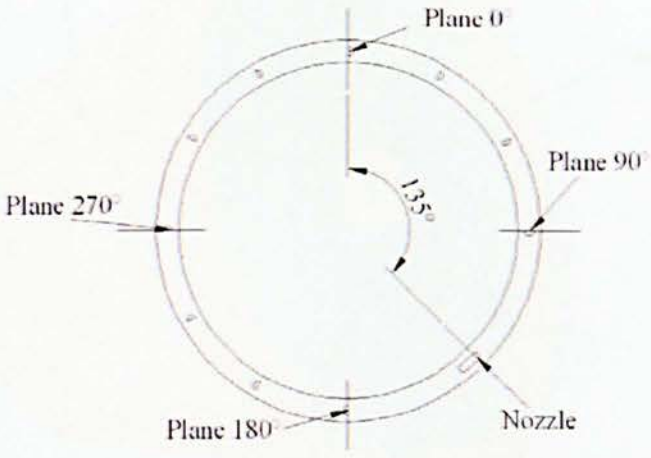

Figure 4.1.4: Plane position on the nacelle lip-skin

4.1.1 Boundary Conditions

GAMBIT [104] pre-processor was used for the modelling and meshing of SAI. The hexagonal non-uniform mesh was used in the study. High density mesh was employed at the critical areas such as impinging spot and nozzle, in order to ensure that the predicted result would be reliable, as shown in Figure 4.1.5. Figure 4.1.6a and Figure 4.1.6b show the boundary conditions in the study.

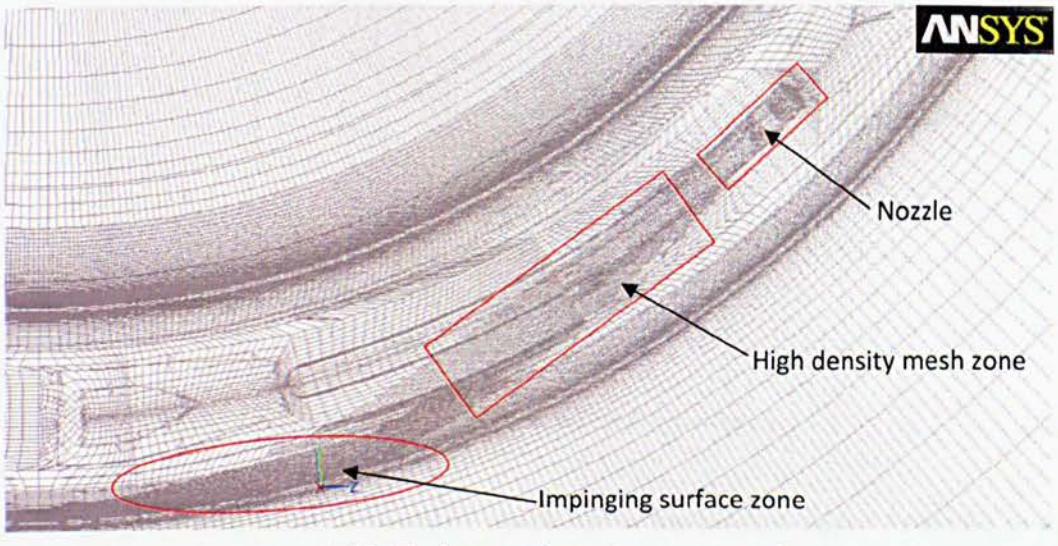

Figure 4.1.5: Mesh at nozzle and impinging surface area

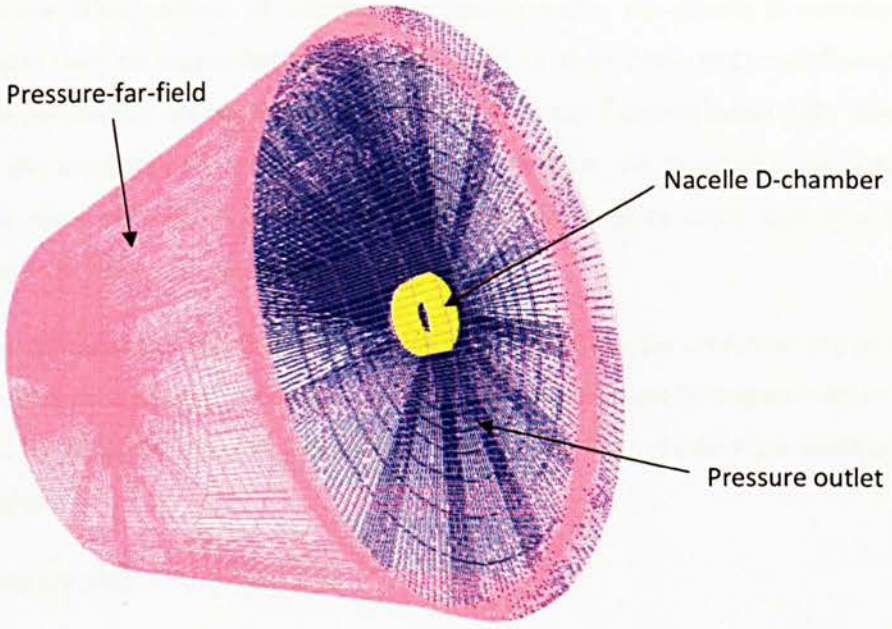

Figure 4.1.6a: Boundary condition of swirl anti-icing

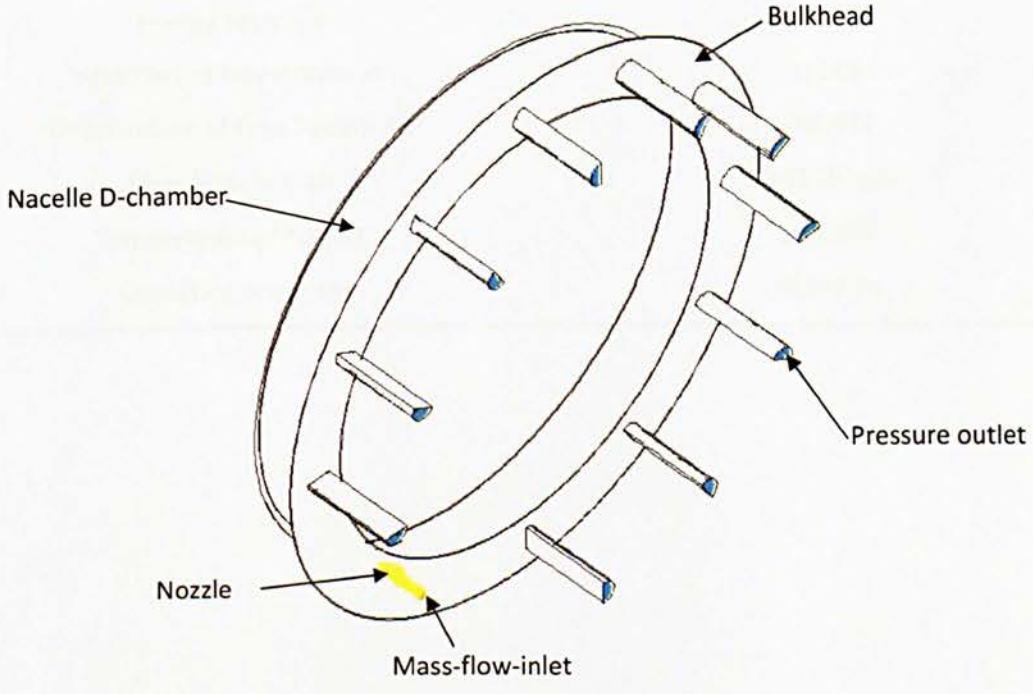

Figure 4.1.6b: Boundary condition inside D-chamber

Figures 4.1.6a and 4.1.6b illustrate boundary conditions in the present work. As shown in Figure 4.1.6a, the dimension of ambient domain was 16 times larger than typical dimension of nacelle D-chamber (yellow colour). Pressure-far-field (pink colour) and pressure outlet (blue colour) were

used to control the Mach number of ambient-free-stream. Inside the nacelle D-chamber (Figure 4.1.6b) nozzle was used to supply hot air mass flow rate to D-chamber and mass-flow-inlet was utilized at nozzle entrance to control the mass flow rate of hot air. Pressure outlet (light blue colour) was set up on the exhaust surfaces to release swirling air from the D-chamber to atmosphere. Exhaust surfaces were extended 8 times exhaust diameter in order to avoid back flow inside D-chamber. Bulkhead at the rear D-chamber was set as wall.

Unlike in chapter 3, laboratory conditions were used in the study for SAI on Falcon 20g as required by Bombardier Aerospace Belfast. The ground air pressure with ambient-free-stream Mach number of 0.149 and T_∞ of 266.483K were included as boundary conditions. Table 4.1.1 summarizes the boundary conditions.

Table 4.1.1: Summary of boundary condition

CFD Software	FLUENT 6.3.26
Turbulent flow model	*SST* k-ω
Type of flow	Ideal gas (compressible)
Energy Equation	On
Velocities of free stream air	0.149
Temperature of Free Stream Air	266.483
Mass Flow hot air	0.0118 kg/s
Temperature of hot air	533.15K
Operating pressure	96497 Pa

4.1.2 Grid Independence Test

The grid independence test was conducted before the examination of SAI performance. For the Falcon 20g nacelle D-chamber, three different mesh sizes were executed: 3,000,000 (coarse mesh), 4,750,000 (current mesh) and 7,000,000 (fine mesh).

Figure 4.1.7 shows that the lip-skin temperature contours produced by the three different meshes are very similar to each other. The cold spot and hotspot occur at points A and B in planes 170° and 245° respectively. The hotspot temperatures (T_{hi}) for coarse, current and fine meshes are 324.5K, 337.6K and 337.0K respectively, while the corresponding cold spot temperatures (T_{lo}) are 278.85K, 279.95K and 280.25K. The differences in T_{hi} and T_{lo} between coarse mesh and fine mesh are 11.6K and 1.5K respectively, and between current and fine meshes are only 0.6K for and 0.3K. In addition, current mesh needs only 14 days to converge compared to the fine mesh that takes 23 days. Therefore, current mesh is good enough to be employed in the subsequent study.

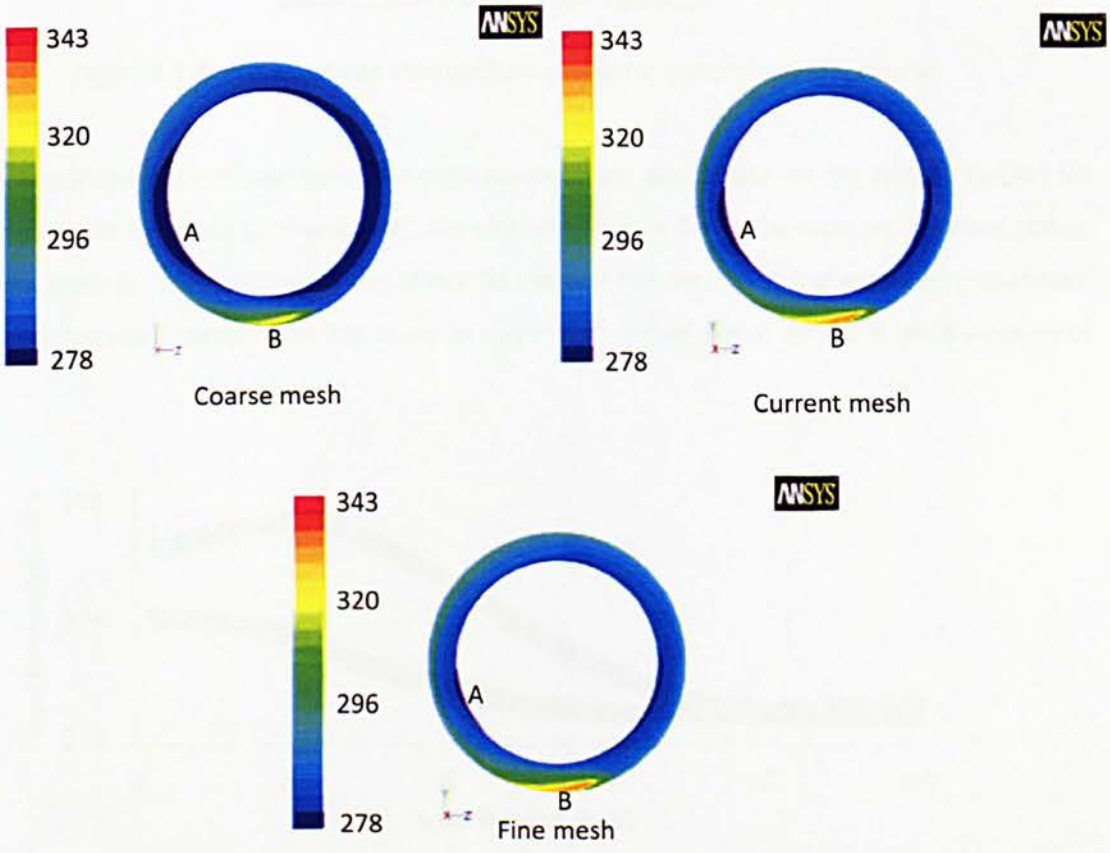

Figure 4.1.7: Contour of Lip-skin temperature (in K) for coarse, current and fine meshes

The plane average temperatures with respect to wrap location for both current and fine meshes are plotted in Figure 4.1.8. The plane average temperature for coarse mesh is not included in the figure due to the differences of T_{hi} and T_{lo} between coarse mesh and fine mesh being quite high. Both the models seem to produce similar average temperature profiles at the given plane.

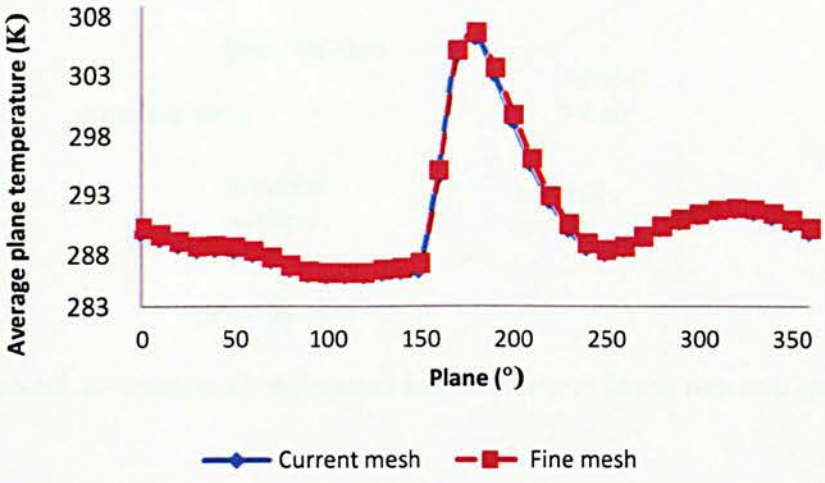

Figure 4.1.8: Plane average temperature profile for current and fine meshes

Considering individual cross-sections, the local temperature distribution on the nacelle lip-skin for both the models in planes 180° and 270°, are plotted in Figure 4.1.9. The local temperature curves of current mesh for both planes are very similar to those of fine mesh. The highest local temperature differences between current and fine mesh in plane 180° is 0.9K which occurs at wrap location of 14%.

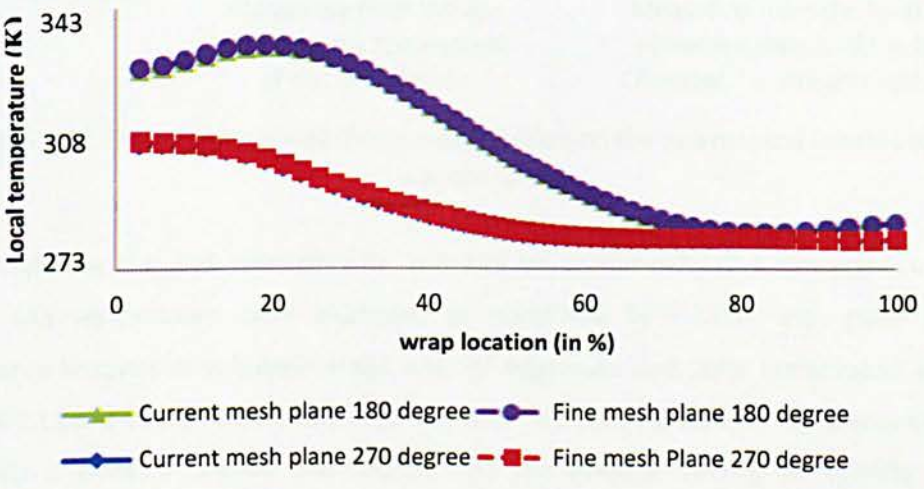

Figure 4.1.9: Local temperature profile along wrap location for both current and fine mesh

Subsequently, dimensionless wall distance (y+) distribution on the nacelle lip-skin surface was examined. The y+ distributions along the internal and external surfaces (Figure 4.1.10) are shown in Figure 4.1.11 which demonstrates that y+ for both surfaces is less than the maximum limit (30) recommended by FLUENT [103].

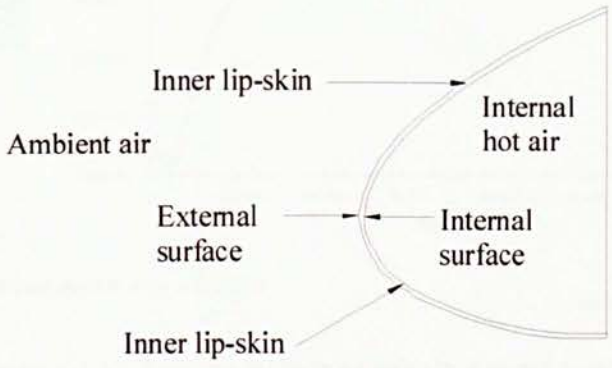

Figure 4.1.10: Location of internal and external surfaces on the nacelle D-chamber

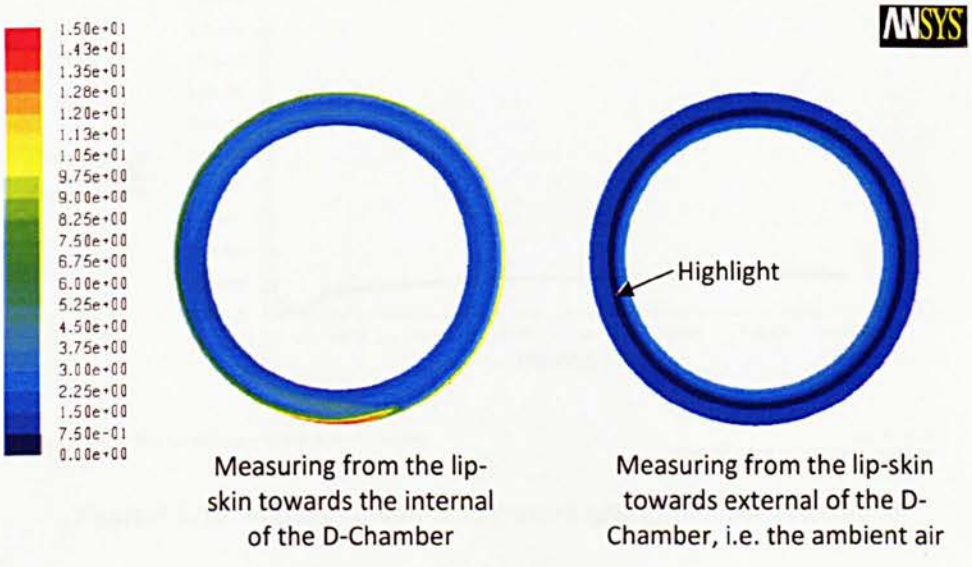

Figure 4.1.11: Dimensionless wall distance distribution on the external and internal surfaces of nacelle lip-skin

After completing the grid independence test and y+ examination, the convergence histories of velocity and temperature were examined as mandated by FLUENT user guide [103]. The convergence histories of volume-average velocity magnitude and static temperature are shown in Figures 4.1.12 and 4.1.13 respectively. It can be observed that, the number of iterations executed for all models is between 14,000 and 15,000, and the average swirling air velocity and lip-skin temperature along the lip-skin vary slightly along a platform when the number of iterations exceeds 12,000.

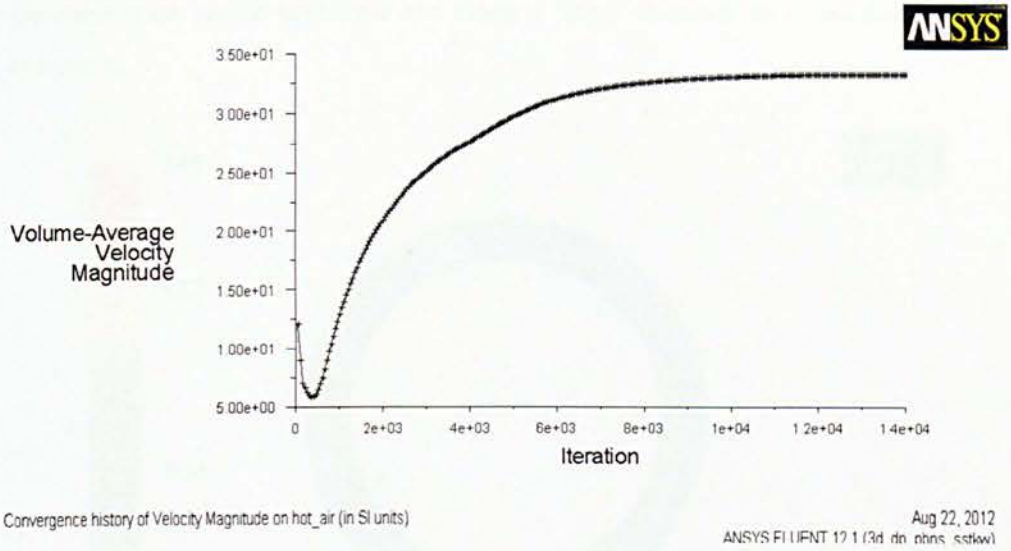

Figure 4.1.12: Average swirling air velocity against number of iteration

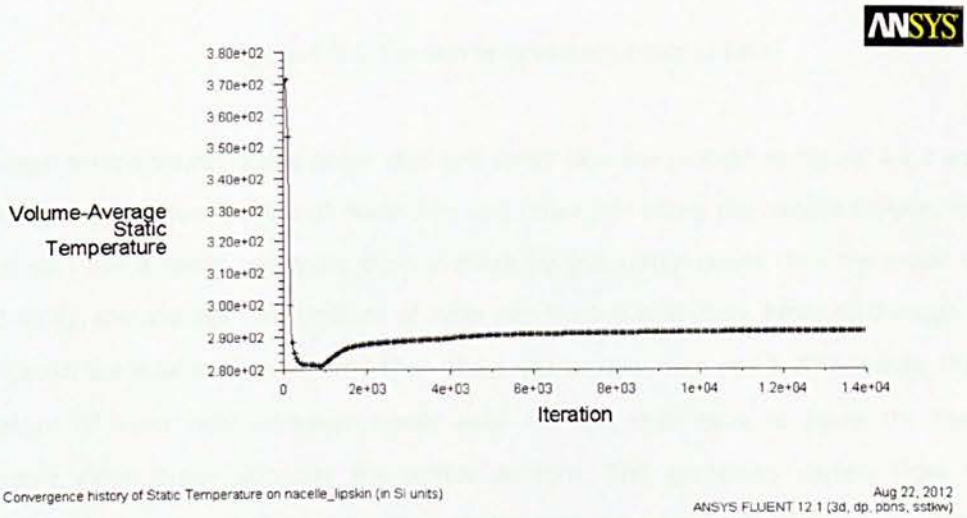

Figure 4.1.13: Average lip-skin temperature against number of iteration

4.2 Temperature Distribution on the Nacelle Lip-skin

The lip-skin temperature contour is shown in Figure 4.2.1. The cold spot occurs at point A and hotspot occurs at point B. Hotspot occurs due to the hot air exiting from the nozzle and directly impinging on point B. As a result, the thermal and hydraulic boundary layer becomes very thin causing the highest heat transfer on this spot. After hot air impinges on the outer skin, the direction of the flow is altered to along the outer skin of nacelle D-Chamber. Due to the velocity and temperature differences between the hot air from the nozzle and the cold air in the D-Chamber, the

mixing between them would take time and along a "long" distance. As a consequence, cold spot occurs at point A.

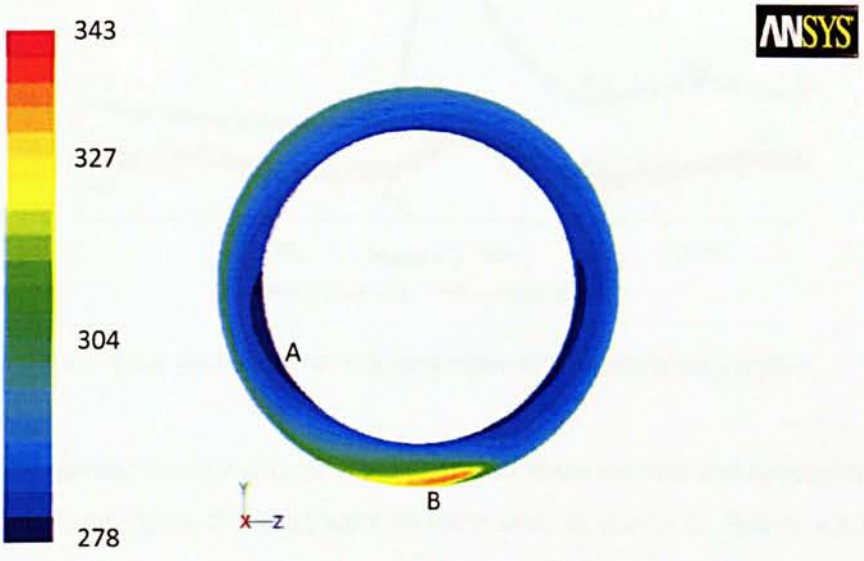

Figure 4.2.1: Lip-skin temperature contour (in K)

The average temperatures along outer skin and inner skin are plotted in Figure 4.2.2 in order to describe the temperature profile of outer skin and inner skin along the nacelle lip-skin. In general, the inner skin has a lower and more even average lip-skin temperature than the outer skin dose. From A1 to A2, the average temperature of inner skin fluctuates slightly. From A2 through A3 to A4, it increases to the maximum at A3 and then decreases to minimum at A4. Afterwards, the average temperature of inner skin increases slowly until A5, and then back to plane 0°. The average temperature along outer skin has the similar pattern; first decreases slightly from B1 to B2 whereafter increases sharply to the maximum at B3, and decreases to local minimum at B4. Finally, from B4 through B5 to B6, pattern similar to B2 to B4 is followed, but with a much smaller scale.

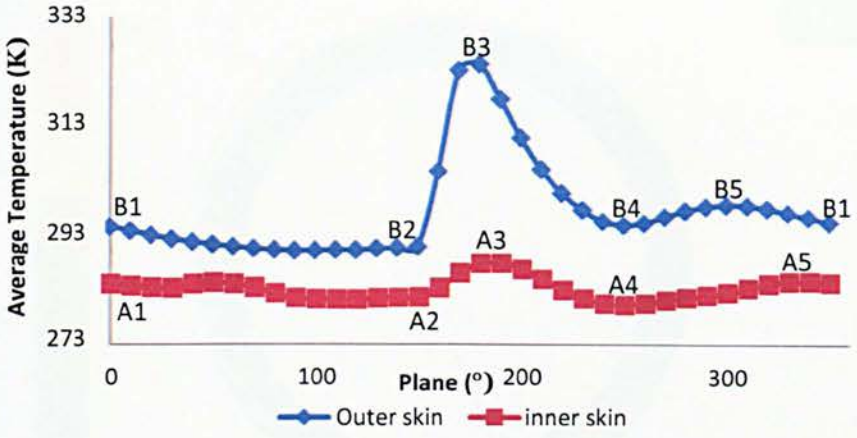

Figure 4.2.2: Average inner skin and outer skin temperatures profile

As the nacelle D-chamber forms a circular channel, the air Mach number and temperature adjacent to outer skin are higher than those adjacent to inner skin, as shown in Figures 4.2.3 and 4.2.4. Therefore, the hydraulic boundary layer adjacent to outer skin is thinner than the one adjacent to inner skin; hence, heat transfer coefficient between hot air and outer skin is higher than that between hot air and inner skin.

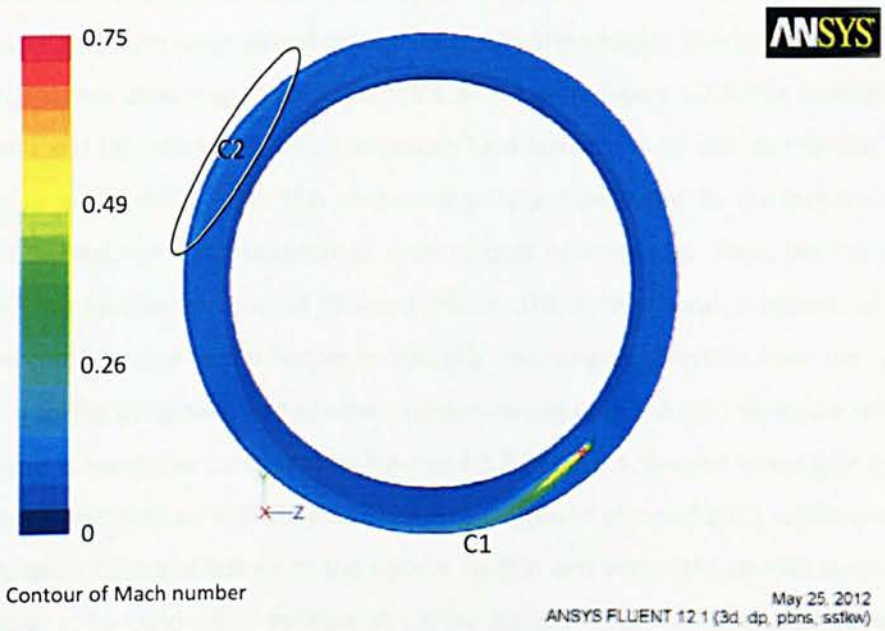

Figure 4.2.3: Air Mach number contours inside nacelle D-chamber

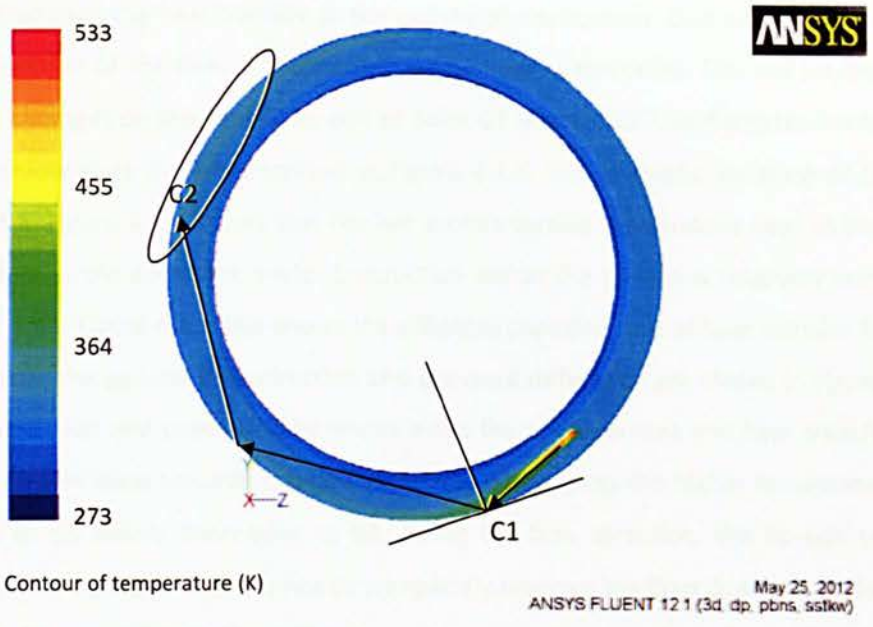

Figure 4.2.4: Air temperature inside nacelle D-chamber

According to the figures, both Mach number and temperature of hot air decrease as it flows away from the nozzle because of the mixing with cold air inside the nacelle D-Chamber. Due to the mixing, the heat and momentum pass to the cold air. Then, the hot air with high Mach number and temperature impinges on outer skin at point C1, creating the hotspot. Therefore, the average lip-skin temperature reaches peak magnitude at point B3, as shown in Figure 4.2.2. The impingement causes the jet to split and be redirected, which enhances heat transfer to lip-skin and mixing between hot air and cold air in the D-chamber. This phenomenon is demonstrated by the increase to maximum from B2 to B3 (maximum) and subsequent drop to local minimum B4. Then, the hot air "oscillates and follows" the lip-skin and moves forward-mixing. The second local maximum of the average temperature could be due to the hot air completely reversing its direction from the nozzle causing higher heat transfer to lip-skin, and another quicker mixing with the cold air inside the D-Chamber. This hypothesis is somehow confirmed by Figures 4.2.3 and 4.2.4. Second faster heat transfer to lip-skin and mixing with cold air in D-chamber happens in around plane of 280°, which is marked as C2. The heat transfers from the hot air to the nacelle lip-skin and within the lip-skin involve convection and conduction. The conduction process along the nacelle lip-skin is very small compared to the convection process [41].

Figure 4.2.5 illustrates the heat transfer at the vicinity of the hotspot. Due to the orientation of the nozzle, the direction of the flow in the nacelle D-Chamber is clockwise. The hot jet (yellow colour zone) directly impinges on the nacelle lip-skin at point B3 (plane 170°), and creates the hotspot with the highest temperature as demonstrated in Figure 4.2.5. The dramatic variation of temperature from B2 to B4 in Figure 4.2.2 shows that the hot air has carried tremendous heat to the lip-skin by convection which is the dominant mode. Conduction within the lip-skin is relatively nominal within the impinging area. Figure 4.2.2 also shows the different changing rate of heat transfer from the hot air to the lip-skin; the general flow direction and pressure difference are shown in Figure 4.2.5. The general flow direction and pressure differences make the impingement and heat transfer from hot air to nacelle lip-skin skew towards the flow direction, which gives the higher temperature increase rate from B2 to B3 before decreasing to B4. Along the flow direction, the lip-skin temperature follows the decreasing trend until the hot air completely reverses the flow direction while exiting the nozzle, which causes another local maximum.

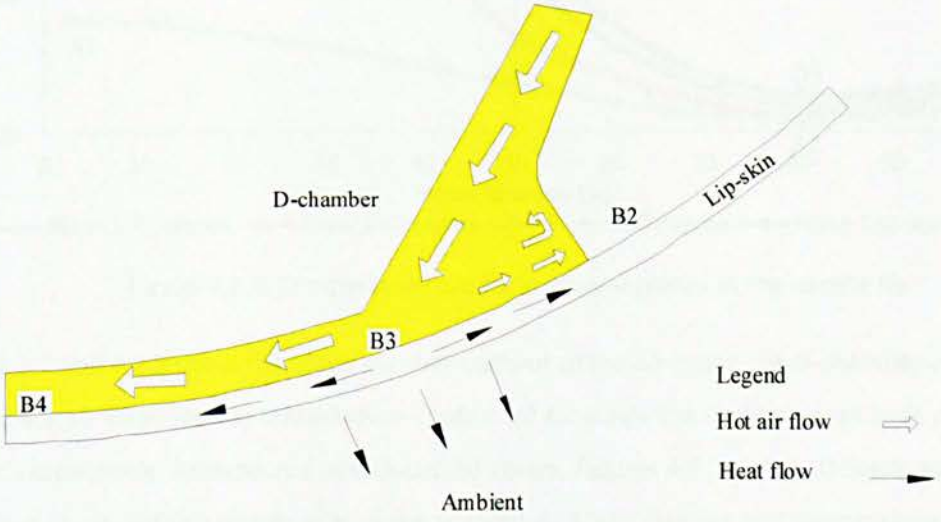

Figure 4.2.5: Conduction and convection processes in hotspot vicinity

Figure 4.2.6 shows the local temperature distribution against wrap location in four planes between 150° and 180°, because they are in the vicinity of hotspot surface/plane. The position of wrap location on the nacelle lip-skin has been shown in Figure 4.1.3. As shown in Figure 4.2.6, the plane 150° shows the beginning of the hot air impinging phenomena, and the temperature distribution is rather smooth with the temperature higher along the outer skin than that along the inner skin due to the nature of the hot air flowing close to the outer skin surface. In plane 160°, the effects of the hot air impinging becomes obvious with a maximum temperature at point B2. Plane 170° represents the plane with hotspots, which is at point C2. Then, plane 180° illustrates that the impinging effects

died away but still a local maximum temperature is observed at point D2. It is worth noting that plane 170° demonstrates lower local temperature for most of the wrap locations apart from wrap location between 20% and 45%, compared to plane 180°. This phenomenon, in fact, means that direct impinging of the hot air jet on the surface of nacelle lip-skin would create hotspot and false higher efficiency but not necessarily better performance of anti-icing, which will become clearer in the following studies. Due to the effects of hot air swirls inside the D-chamber, the location of peak temperature from plane 160° to 180° moves towards bulkhead.

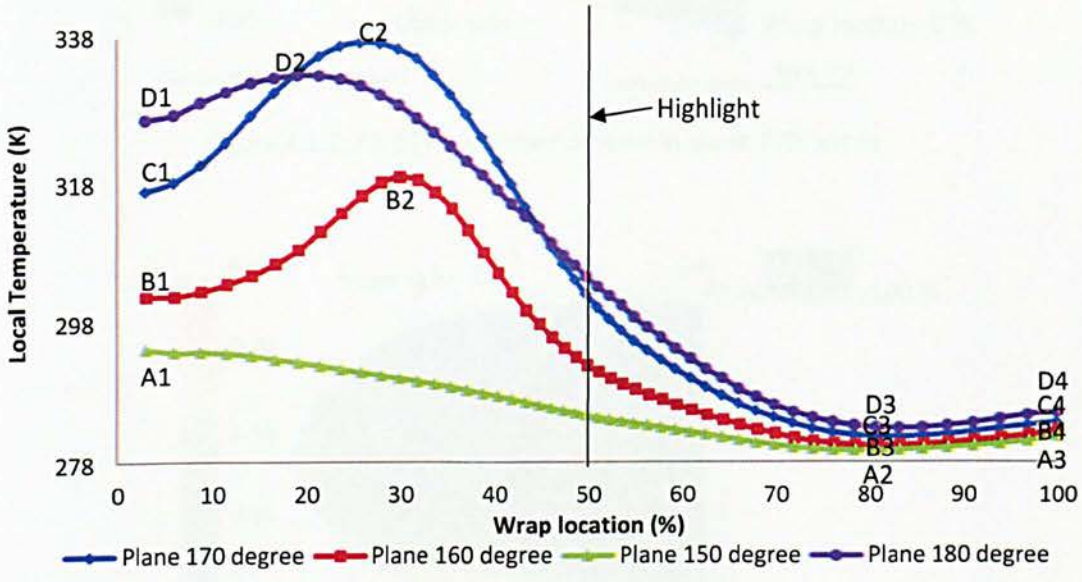

Figure 4.2.6: Temperature profile in several planes at the nacelle lip

Figures 4.2.7 and 4.2.8 show the Mach number contour of the air inside the D-chamber and, Figures 4.2.9 and 4.2.10 illustrate the temperature contour of air inside the D-chamber in both planes 170° and 180° respectively. As expected and discussed above, Figures 4.2.7 to 4.2.10 illustrate that plane 180° shows more uniform distribution of the swirling air Mach number and temperature than plane 170° does, and the direct links of peak flow Mach number and the peak temperature in the planes (point C2 and point D2). Most part of the air flow in plane 180° (except air adjacent to wrap location between 26% and 45%) has higher Mach number and temperature than plane 170°, which means that the local lip-skin temperature in plane 180° is higher than that in plane 170°, as shown in Figure 4.2.6. These figures also show the tendency of the peak air Mach number and temperature moving towards bulkhead from plane 170° to 180°. As a result, the air Mach number and temperature of hot air increases from point C3 to C4 and from point D3 to D4; then, the local lip-skin temperature increases as well for both planes, as shown in Figure 4.2.6.

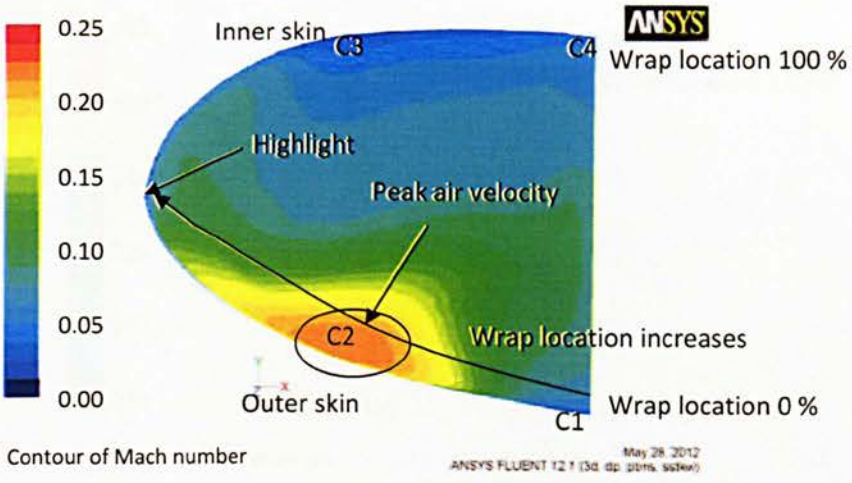

Figure 4.2.7: Air Mach number contour in plane 170° cross

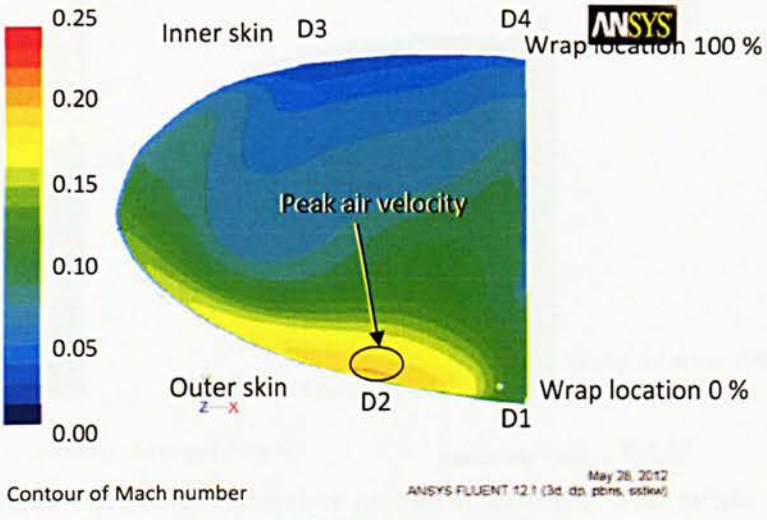

Figure 4.2.8: Contour of Mach number in plane 180°

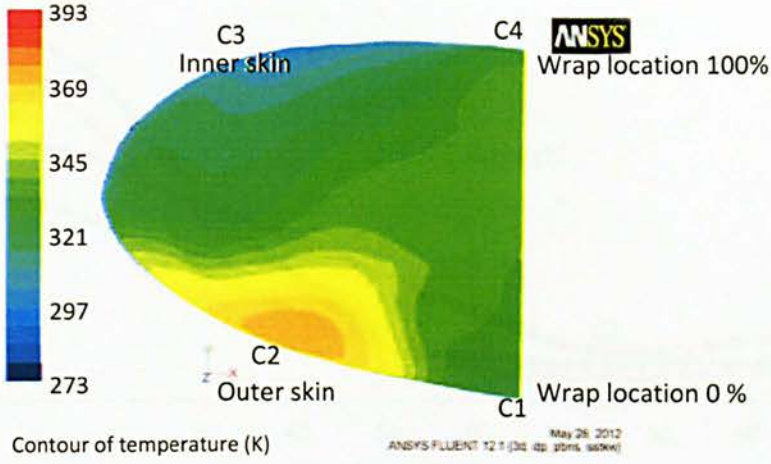

Figure 4.2.9: Air temperature contour in plane 170° cross section

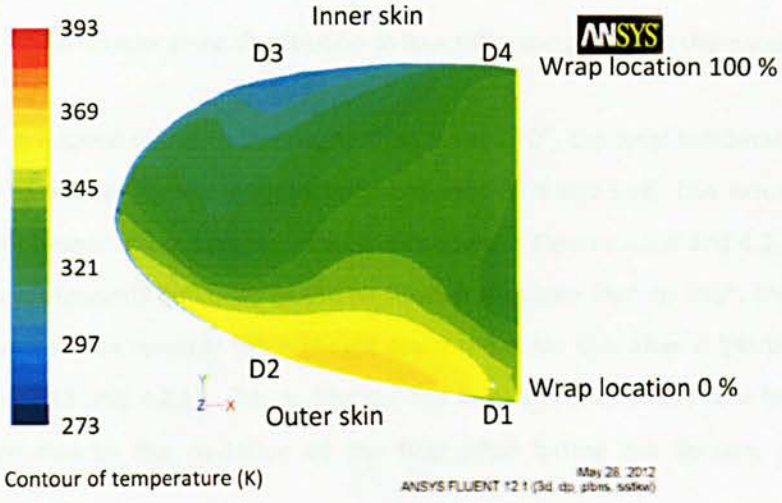

Figure 4.2.10: Air temperature contour in plane 180° cross section

Figure 4.2.11 shows the local temperature against wrap location in four different planes in the range of 0° to 270°. These planes are chosen in order to view the overall temperature distribution along the lip-skin, which cannot be described by the temperature contour. The figure shows that the local temperature of planes 240° and plane 270° are roughly inversely related to wrap location until 60% whereafter remain constant up to 100%. The impinging effects can still be seen around wrap location 0% (near the bulkhead) in both planes. Planes 0° and 90° are behind the nozzle and have more uniform distribution of the local temperature, which decreases gradually with wrap location from 0% to 74%. Then, the local temperature increases slowly against wrap location until the wrap location reaches 100%. Of course, the local temperature of plane 90° is lower than that of 0° along the entire wrap location.

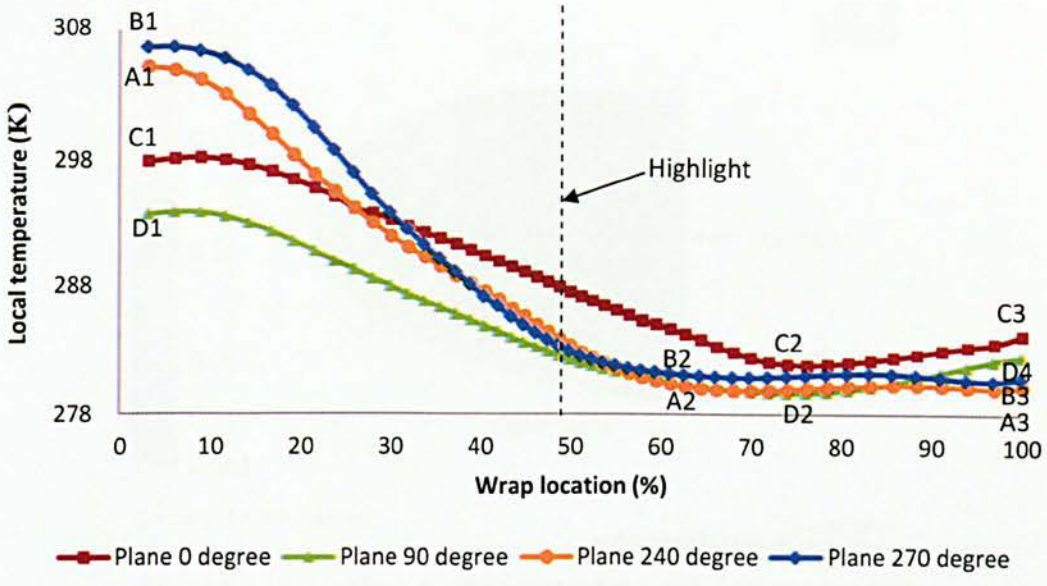

Figure 4.2.11: Local temperature distribution in four different planes on the nacelle lip

Although plane 240° is located closer to the nozzle than plane 270°, the local temperature of plane 240° is lower than 270° except for the wrap location between 37% and 54%. This would happen to the swirling air Mach number in both planes as well. As shown in Figures 4.2.8 and 4.2.12, the peak air Mach number moves towards bulkhead as the air flows from plane 180° to 240°. Thereafter, the peak air velocity bounces back towards the highlight along the outer skin after it hits the bulkhead, as shown in Figures 4.2.12 and 4.2.13. This oscillation and local increase of the flow Mach number and temperature are due to the deviation of the flow after hitting the lip-skin, as discussed previously.

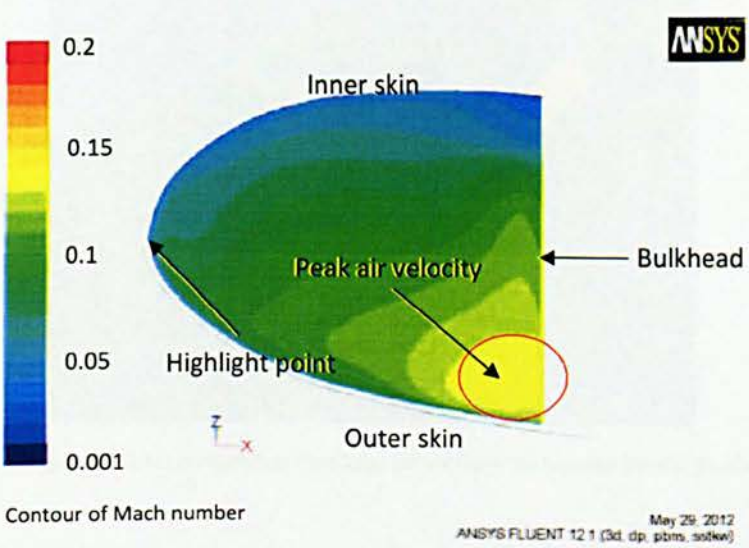

Figure 4.2.12: Air Mach number contour in plane 240° cross section

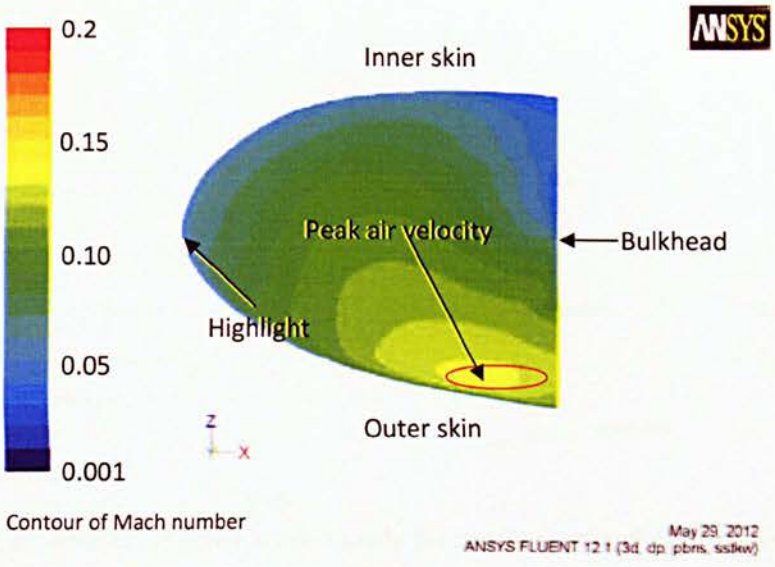

Figure 4.2.13: Air Mach number contour in plane 270° cross section

Figure 4.2.14 illustrates the air Mach number contour around the nozzle vicinity. The air flow in the D-chamber is divided into three major zones such as hot air, cold air and mixed air (intersection between hot air and cold air). The phenomenon at the nozzle vicinity is described in the following figures. The local Mach number (u_y) profiles against the length crossing D-chamber are shown in Figures 4.2.16a, b and c for planes 140°, 155° and 170° respectively. The position of the length crossing D-chamber and plane inside D-Chamber is depicted in Figure 4.2.15, which shows that the nozzle is located at the length between 45% and 55%.

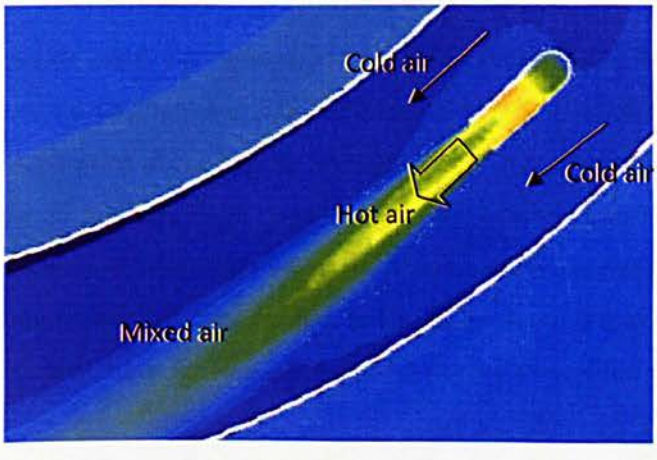

Figure 4.2.14: Air Mach number contour at vicinity of nozzle inside D-chamber

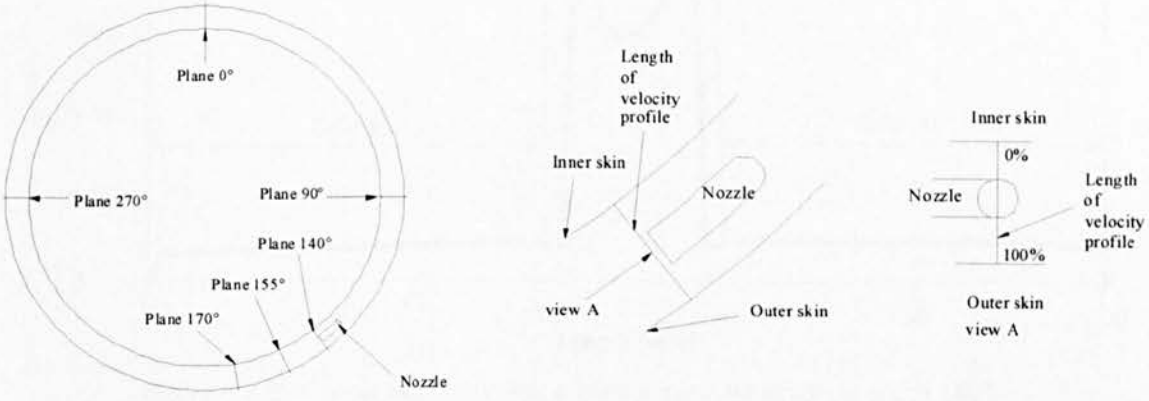

Figure 4.2.15: Position of plane inside nacelle D-Chamber and definition of length across D-Chamber

Basically, the air inside plane 140° can be categorised into three major zones: hot air, cold air and mixed air. In cold air zones, the gradient of u_y is very small and u_y is almost constant along the length as shown in Figure 4.2.16a, and then decreases a little bit to point x in the mixed flow zone before increasing tremendously to its peak. This phenomenon happens due to back flow occurring in front of the nozzle wall thickness. As plane 140° is just in front of the nozzle, the mixed air zone is still very thin with few mixing activities, and the primary flow from the nozzle still appears in this plane. u_y in the hot air zone is very high in plane 140° and is not uniform where u_y in the centre is lower than u_y close to the nozzle wall. This happens because pressure inside the nozzle is not uniform as shown in Figure 4.2.17a.

The structure of flow inside bend pipe is very complicated. According to Berger et al. [108], the severe pressure variation inside the bend pipe increases turbulent level of the flow. At the same time, it produces flow separation at the low air pressure spot. Thus, the rotating flow or secondary flow appears at the low air pressure spot. Consequently, the Mach number profiles of flow inside pipe are not uniform. As evident from Figure 4.2.17a, severe pressure variation occurs inside nozzle elbow, which leads to appearance of rotating flow at low air pressure (Figure 4.2.17b). As a result, the profile of hot air Mach number flowing out from the nozzle is not uniform as shown in Figures 4.2.16a and 4.2.17d.

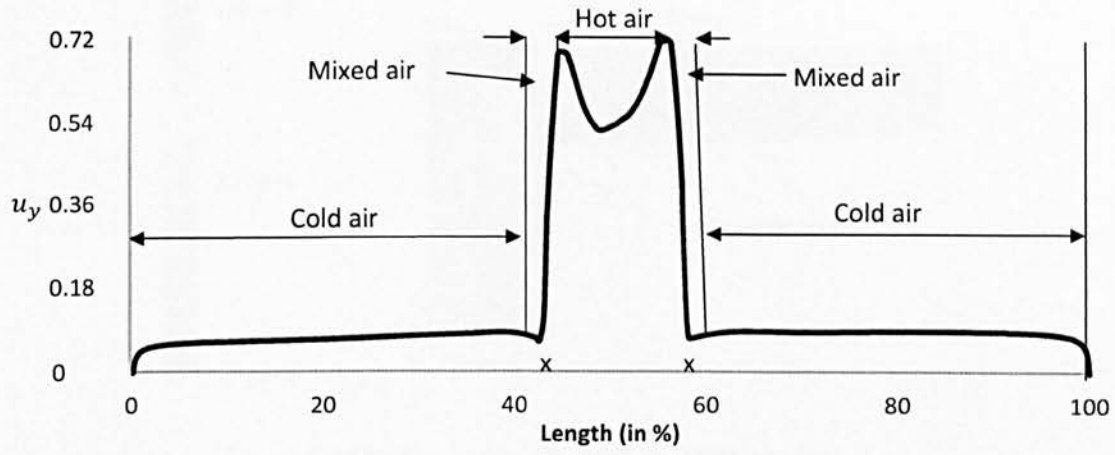

Figure 4.2.16a: Local Mach number profile across the length in plane 140°

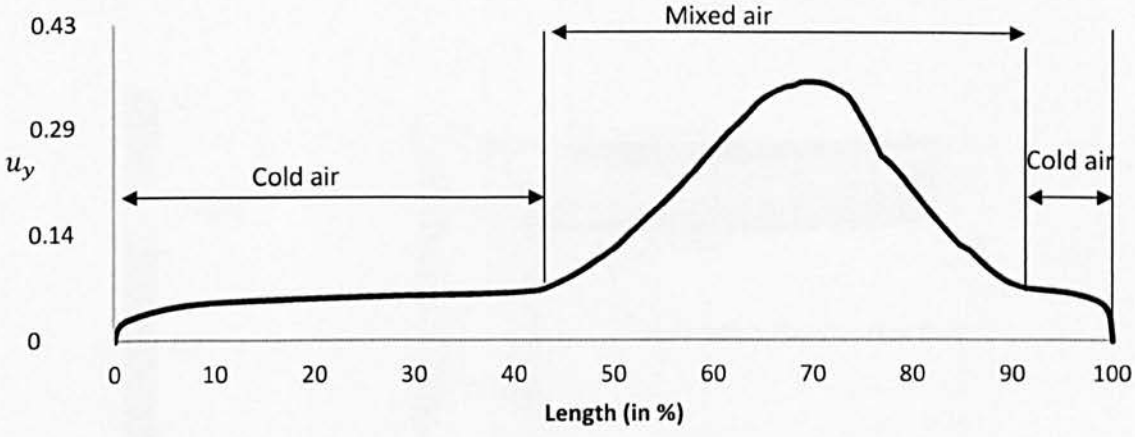

Figure 4.2.16b: Local Mach number profile across the length in plane 155°

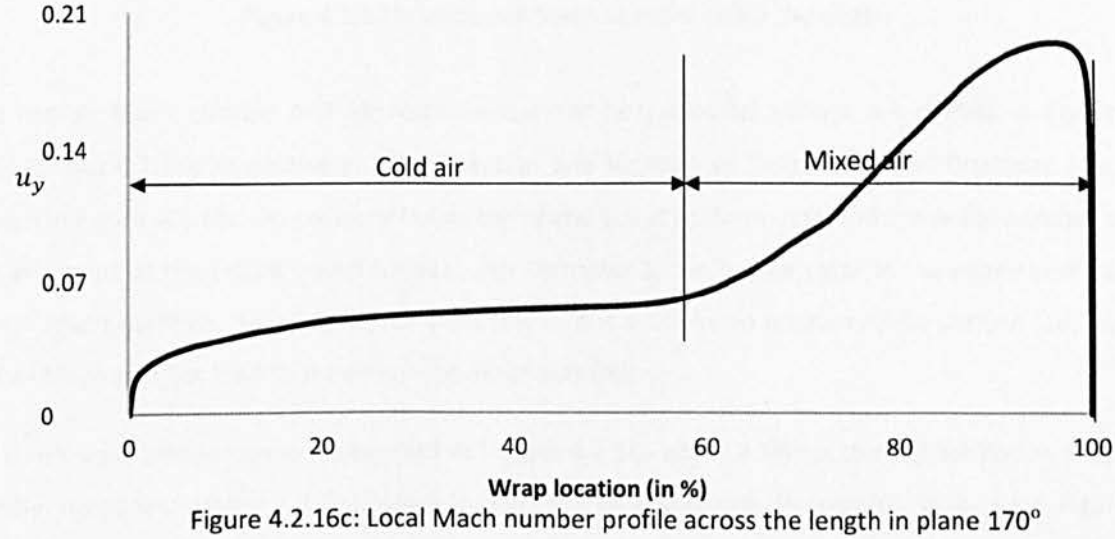

Figure 4.2.16c: Local Mach number profile across the length in plane 170°

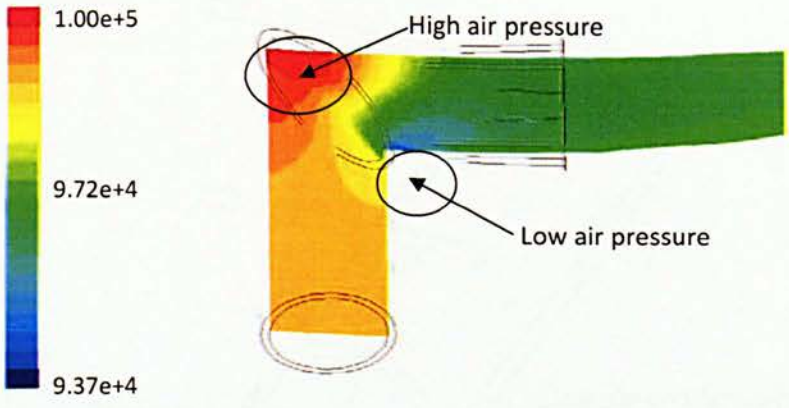

Figure 4.2.17a: Contour of air pressure inside nozzle

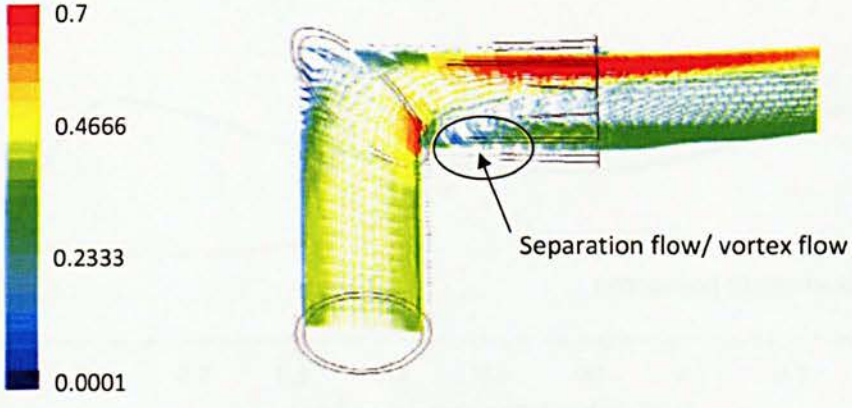

Figure 4.2.17b: Vector of Mach number inside the nozzle

The hot air Mach number and absolute pressure at nozzle outlet surface are plotted in Figures 4.2.17d and 4.2.17e respectively. The direction and location of Diameter 1 and Diameter 2 are shown in Figure 4.2.17c. As pressure inside the nozzle is not uniform, non-uniform Mach number of hot air occurs at the nozzle outlet surface. For Diameter 1, the hot air close to the nozzle wall has higher Mach number. Meanwhile, for Diameter 2, hot air close to nozzle-end-far-surface (1d) has higher Mach number than that close to the other side (0d).

No shock wave phenomenon is observed in Figures 4.2.16a and 4.2.17d as the highest hot air Mach number inside D-chamber is 0.792, which is lower than sound speed. In addition, as shown in Figure 4.2.17e, the profile of absolute pressure of hot air is almost constant, and no abrupt air pressure deviation is observed. The Mach number deficit in Figure 4.2.16a happens only because of the non-uniform air pressure inside the nozzle.

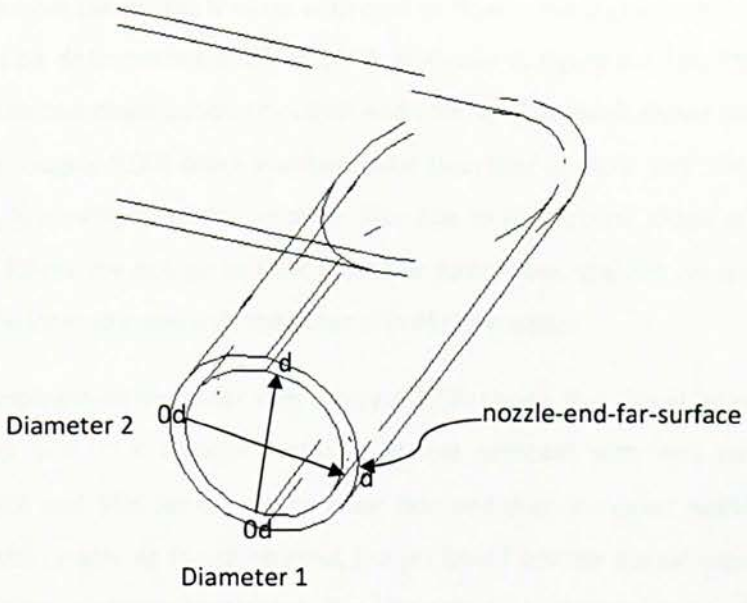

Figure 4.2.17c: Position of Diameter 1 and 2 at nozzle exit surface

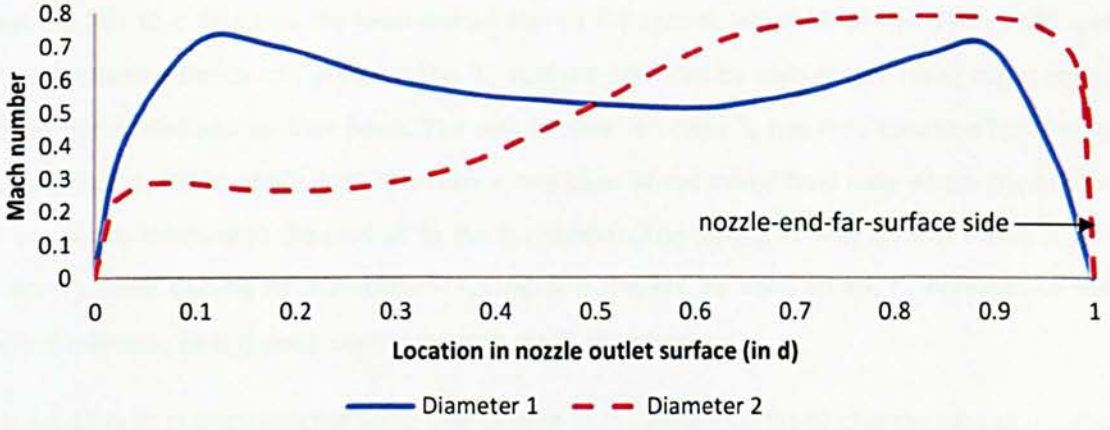

Figure 4.2.17d: Mach number of hot air at nozzle outlet surface

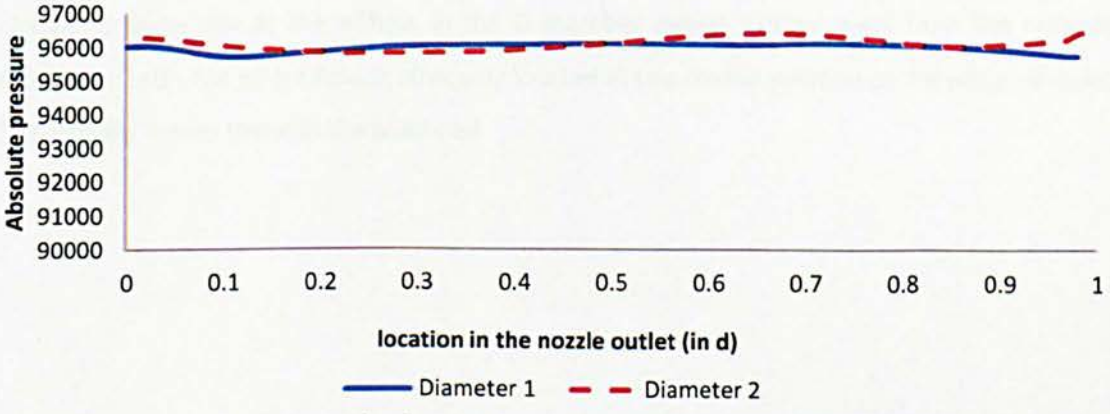

Figure 4.2.17d: Hot air absolute pressure distribution at nozzle outlet surface

As hot air jet flows away from the nozzle, it mixes with cold air flow in the D-chamber. Consequently, the hot air jet could not be distinguished in plane 155°, as shown in Figure 4.2.16b. Therefore, the air has been classified into two major zones, mixed air and cold air. The result shows that u_y of cold air flow in plane 155° is roughly 0.008 Mach number lower than that in plane 140°. The figure also shows that the peak u_y is moving towards the outer skin due to the circular shape of the nacelle circled-chamber, which forces the hot air to take a circular path. Then, the hot air and the mixed flow move away from the inner skin towards the outer skin of the nacelle.

When the hot air flow impinges on the outer skin, Figure 4.2.16c shows that mixed air region covers major part of the outer skin. It is obvious that u_y is almost constant with very small gradient between a length of 1.6% and 56% for the entire inner skin and then increases quickly along the outer skin to almost 100% length. At the same time, the jet flow from the nozzle impinges on the nacelle skin for the first time, creating the hotspot. It is also noticeable that the peak values of u_y at plane 170° are 71% lower than the highest u_y at the exit of the nozzle.

Figures 4.2.18a to c illustrate the local temperature (T_y) against length in planes 140°, 155° and 170° respectively. Similar to Figure 4.2.16a, T_y in plane 140° can be divided into three major zones — hot air jet, mixed and cold air flows. The cold air flow is where T_y has little variation from wrap location of nearly 0% to about 40%. It is then a thin layer of the mixed flow zone where the hot air from the nozzle mixes with the cold air in the D-chamber. The mixing activity is most active in this area and T_y starts gaining its momentum. Finally, it is the hot air zone where T_y increases to the peak, and intensive heat is seen moving through the D-chamber.

Figure 4.2.18 (a to c) illustrates the same phenomena as in Figure 4.2.16(a to c) in the case of u_y. The maximum T_y drops sharply from 500.5K to 413.92K when air flows from plane 140° to plane 155°, and then to 375.18K in plane 170° because of the mixing effects. However, the decreasing gradient of T_y becomes quite low as the airflow in the D-chamber moves further away from the hotspot point. In plane 140°, hot air jet flow is obviously located at the central position of the wrap location, and T_y gradually moves towards the bulkhead.

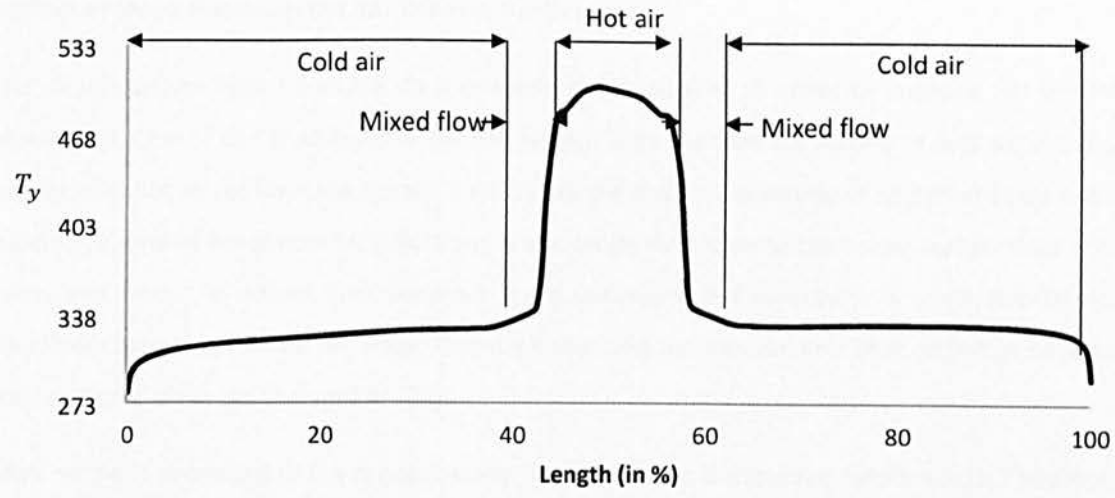

Figure 4.2.18a: Dimensionless air temperature profile across the length in plane 140° (in K)

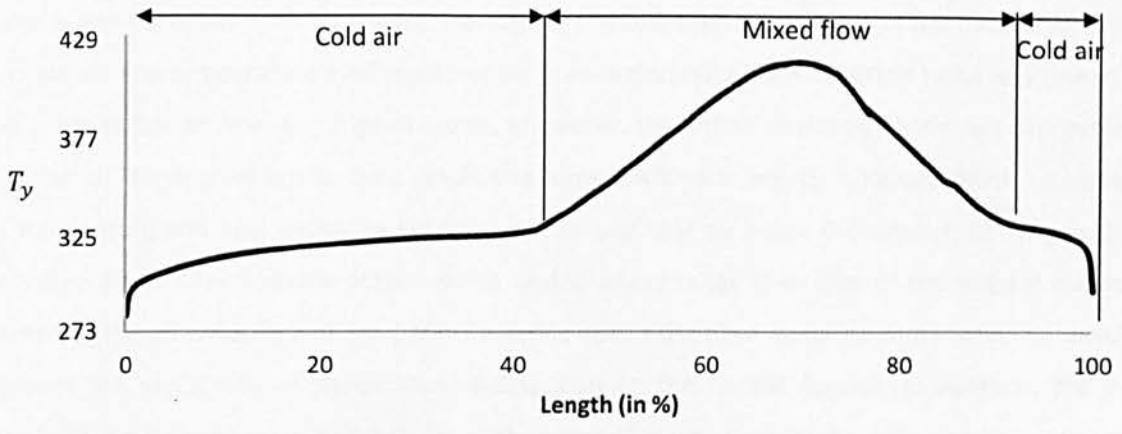

Figure 4.2.18b: Dimensionless air temperature profile across the length in plane 155° (in K)

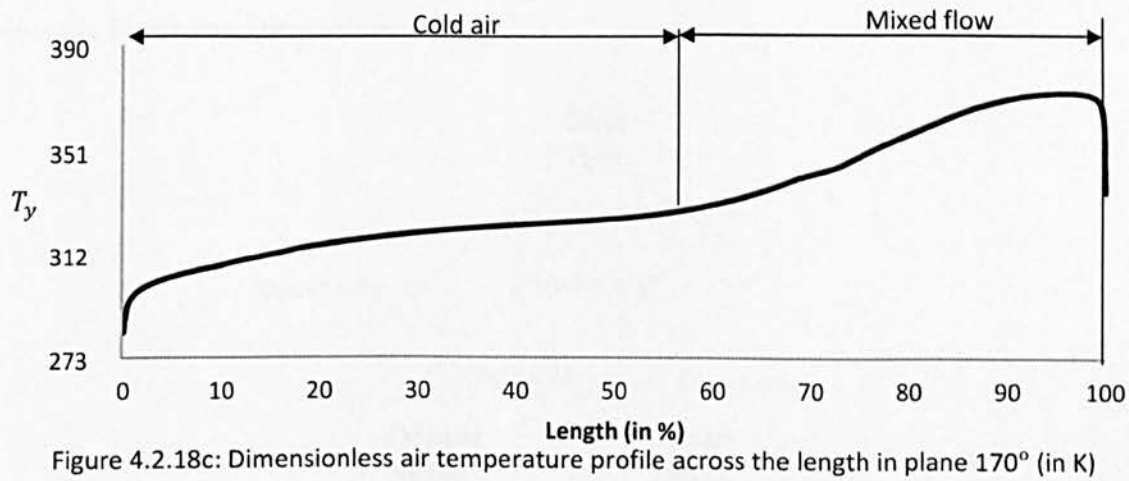

Figure 4.2.18c: Dimensionless air temperature profile across the length in plane 170° (in K)

4.3 Effect of Slope Nozzle on the SAI Thermal Performance

Some modifications must be made on the nozzle outlet surface in order to improve SAI thermal performance. One of the challenges in the SAI system is to improve the mixing of cold air in the D-chamber with hot air jet from the nozzle. To increase the chances of mixing at an earlier stage and in a wider area, one of the simple modifications is to change the shape of the nozzle outlet. The hot air velocity exit from the nozzle then becomes more turbulent and non-uniform. Consequently, the mixed flow comes in at an earlier stage, thereby enhancing momentum and heat exchange between hot air and cold air in the D-chamber [94].

Sloped nozzle is proposed in the present study (the schematic is shown in Figure 4.3.1). The sloped nozzle keeps the same nozzle length with the original nozzle at the lower side and the upper side is shortened to increase the exiting area and to bring about the mixing slightly earlier. The sloped nozzle is also expected to divert the jet flow slightly towards the inner surface of the nacelle lip-skin. The velocity and temperature profiles of hot air from sloped nozzle are expected to be less uniform than those of hot air from the original nozzle. Moreover, the hot air of sloped nozzle diverges better than that of the original nozzle. As a result, the turbulent kinetic energy increases which increases the momentum and heat exchange between hot air and cold air inside D-Chamber. Consequently, the mixed air of sloped nozzle occurs earlier and in wider range than that of the original nozzle. Therefore, the air velocity and temperature inside the D-chamber becomes more uniform, which improves the uniformity of temperature distribution on the nacelle lip-skin. In addition, the jet velocity of the sloped nozzle is slightly lower than that of the original nozzle, owing to its larger exit surface. Thus, the impinging effect of hot air from the sloped nozzle becomes less significant and it reduces T_{hi} on the impinging surface.

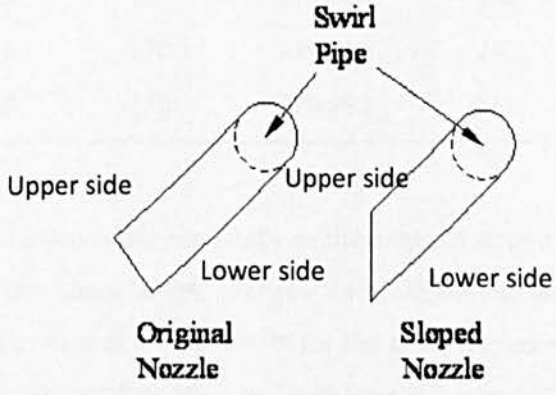

Figure 4.3.1: Schematic illustration of original and sloped nozzle

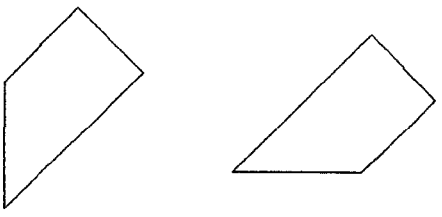

Positive sloped angle Negative sloped angle

Figure 4.3.2: Positive and negative sloped nozzle

In the present study, investigations of sloped nozzle were carried out with angles of 25°, 45°, 60° and -60°. The shape differences between the positive and negative sloped nozzle is shown in Figure 4.3.2.

Figure 4.3.3 illustrates lip-skin temperature contour for five different nozzle shapes: original nozzle, sloped nozzle 20°, 45°, 60° and -60°. There is no significant improvement by changing nozzle shape from original into sloped. Generally, all sloped nozzles produce hotspot in similar plane and almost similar T_{hi} compared to the original nozzle. The low temperature area (dark blue colour) slightly shrinks and T_{lo} rises slightly as the angle of sloped nozzle increases. The details of thermal performance of sloped nozzle are summarised in Table 4.3.1

Table 4.3.1: Summary of thermal performance of Sloped Nozzle

Nozzle shape	T_{hi} (°C)	Plane of hotspot (°)	T_{lo} (°C)	Plane of cold spot (°)	T_{ave} (°C)	*EFF (%)*
Original	337.42	170	279.646	245	291.43	81.40
Sloped 20°	337.20	170	279.888	244	291.75	81.43
Sloped 45°	337.20	170	279.023	242	291.80	81.50
Sloped 60°	335.96	170	279.238	242	291.90	81.54
Sloped -60°	334.95	170	279.352	245	291.98	81.79

According to the table, T_{hi} decreases marginally as the angle of sloped nozzle increases. The largest drop of T_{hi} is 2.47K as the nozzle shape changes from original nozzle to sloped nozzle with -60°. Moreover, the highest increase of the T_{lo} is 0.7K for the same sloped nozzle. The table also records that the average lip-skin temperature (T_{ave}) and anti-icing efficiency (*EFF*) increase up to 18.98K and 81.79% respectively for the same sloped nozzle with -60°, although all the sloped nozzles demonstrate marginal improvement.

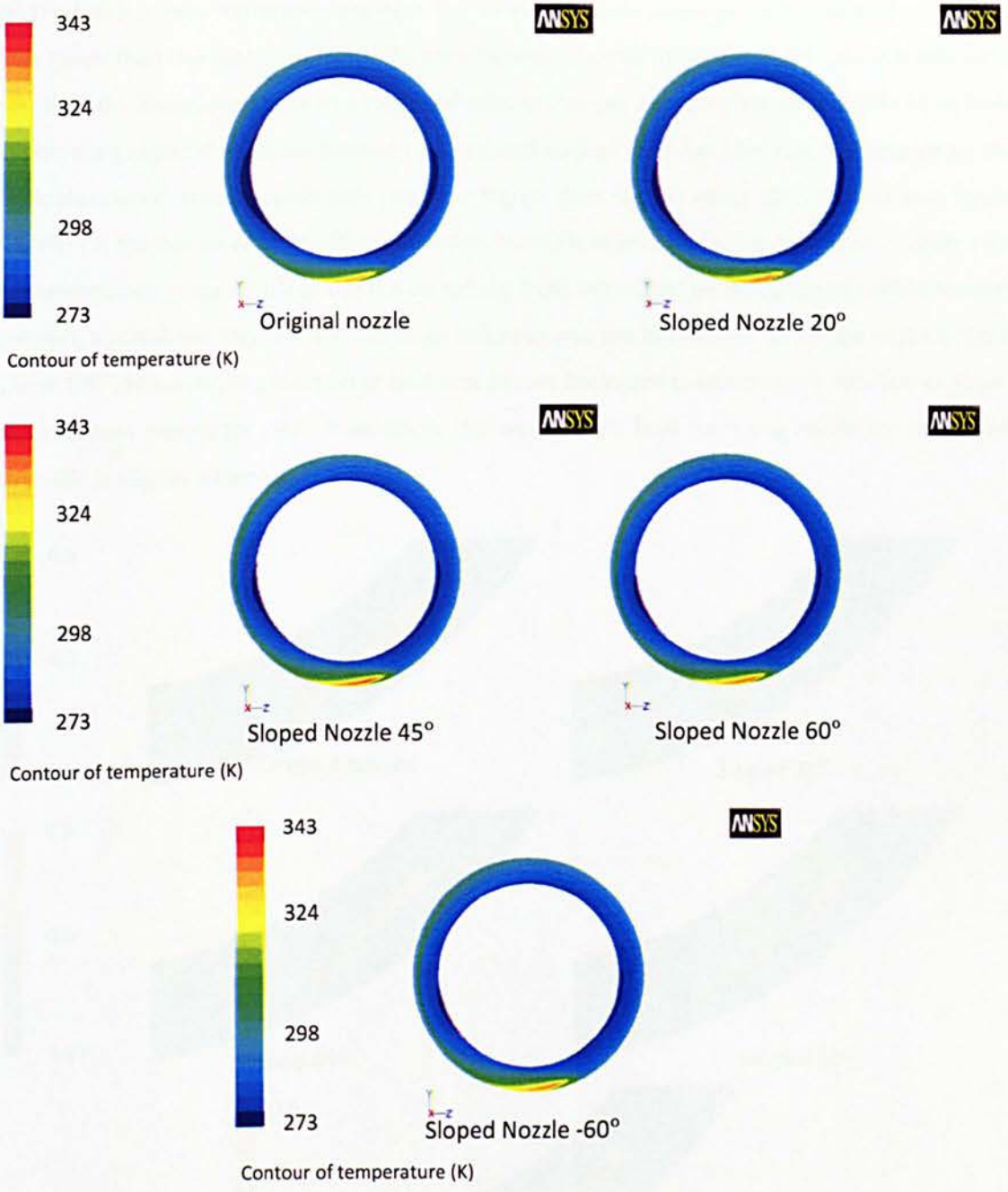

Figure 4.3.3: Temperature contour on the nacelle lip-skin for various nozzle types

According to Figure 4.3.4, sloped nozzle with -60° has the widest hot air flows exit from the nozzle. This phenomenon shows that sloped nozzle with -60° produces the highest momentum exchange between hot air and cold air [94], resulting in the highest average swirling air Mach number in D-chamber, and relatively greater T_{ave} and *EFF* as shown in Table 4.3.1.

Figure 4.3.4 also shows the air Mach number contour around the vicinity of nozzle outlet for the various nozzle designs. The hot air in lower side has higher Mach number than that in upper side. This happens due to cold air in outer skin side having higher Mach number than cold air in inner skin

side. The Mach number difference between hot air in the nozzle lower side and cold air in outer skin area is lower than the Mach number difference between hot air in nozzle upper side and cold air in inner skin side. Therefore, the momentum and heat exchanges between hot air and cold air in inner skin side are greater than those between hot air and cold air in outer skin side. Consequently, the specific dissipation rate in upper side nozzle is higher than that in lower side, as shown in Figure 4.3.5. Hence, the hot air Mach number reduction in nozzle lower side is less than that in upper side. This phenomenon is the result of the hot air exiting from sloped nozzle being slightly offset towards outer skin, as shown in Figure 4.3.4. Although this happens, the hotspot for all sloped nozzles occurs in plane 170°. However, the location of cold spot moves backward towards nozzle location as sloped angle increases except for -60°. In addition, the width of jet flow from the nozzle for the sloped nozzle -60° is slightly widened.

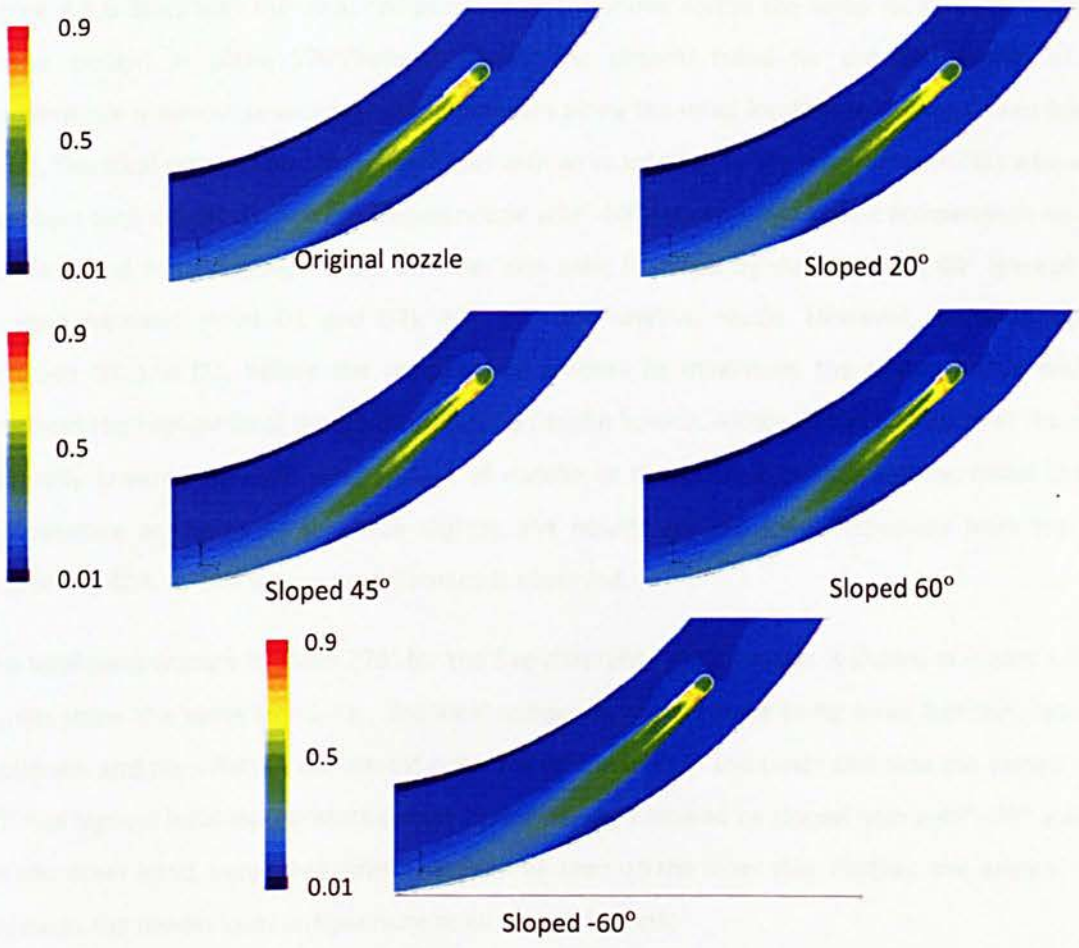

Figure 4.3.4: Air Mach number contour around the nozzle

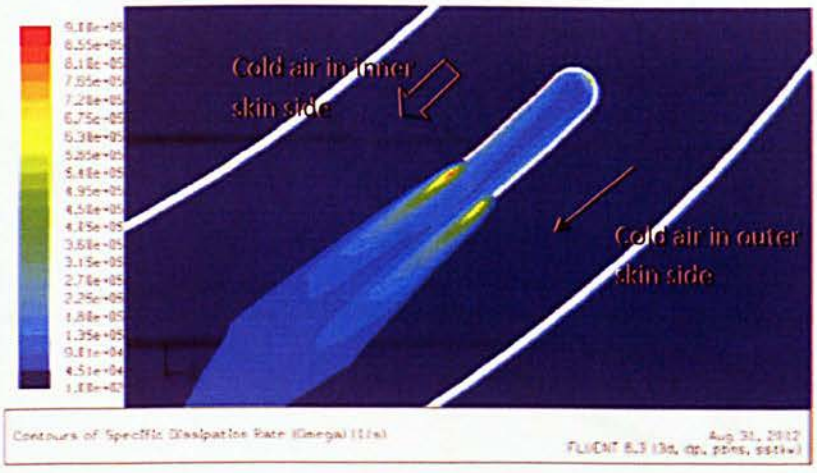

Figure 4.3.5: Contour of specific dissipation rate of hot air around vicinity of nozzle

Figure 4.3.6 illustrates the local temperature distributions across the wrap locations for different nozzle designs in plane 170°/hotspot plane. The general trend for the distribution of local temperature is almost sinusoidal, which increases along the wrap location to the maximum from D1 to D2. The local temperature then decreases with wrap location to the minimum until D3 whereafter increases with slower pace to D4. Sloped nozzle with -60° results in the lowest temperature on outer skin side and highest temperature on inner skin side, followed by sloped nozzle 60° (except wrap location between point D1 and D2), 45°, 20° and original nozzle. However, for wrap location between D1 and D2, before the temperature reaches its maximum, the sloped nozzle with 60° produces the highest local temperature on the nacelle lip-skin. Although the alteration of the nozzle generally lowered the skin temperature of nacelle at the outer skin side and increased the skin temperature at the inner skin side slightly, the results are not ideal, especially from the wrap location of 40% to 70% where no difference is observed.

The local temperature in plane 270° for the five different nozzle designs is shown in Figure 4.3.7. All curves show the same trend, i.e., the local temperatures decrease along wrap location, reach the minimum and then flatten out almost constant till the end. In the outer skin side the sloped nozzle 60° has highest local temperature (worst performance) followed by sloped nozzle 45°, 20° and -60°. On the other hand, very small differences can be seen on the inner skin. Further, the original nozzle produces the lowest local temperature at all wrap locations.

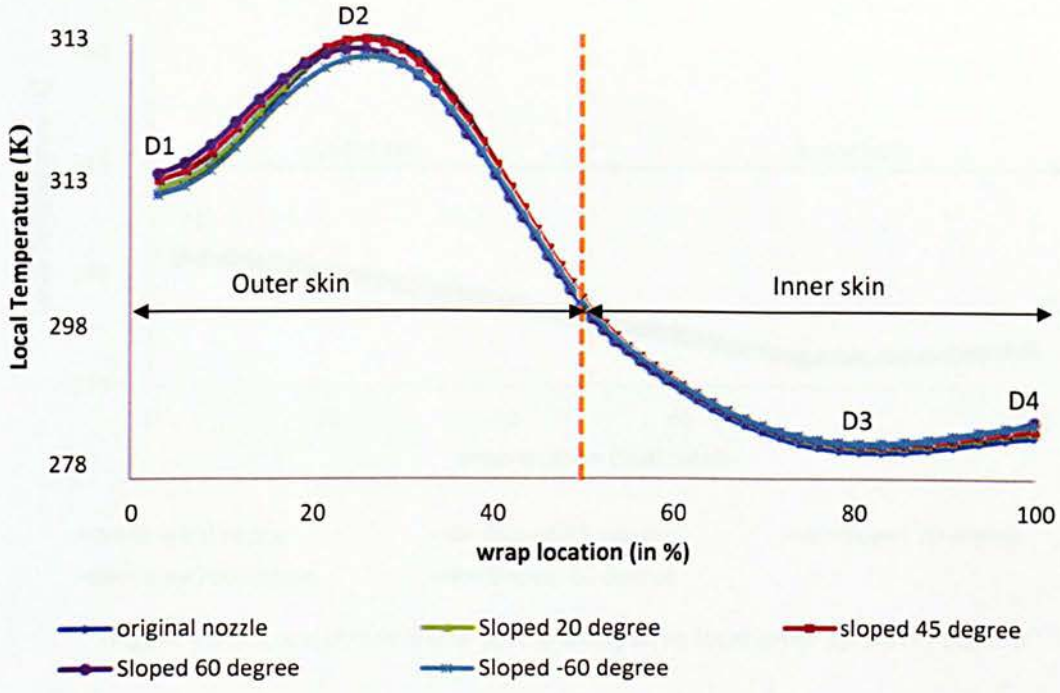

Figure 4.3.6: Local temperature profile along wrap location of lip-skin in plane 170°

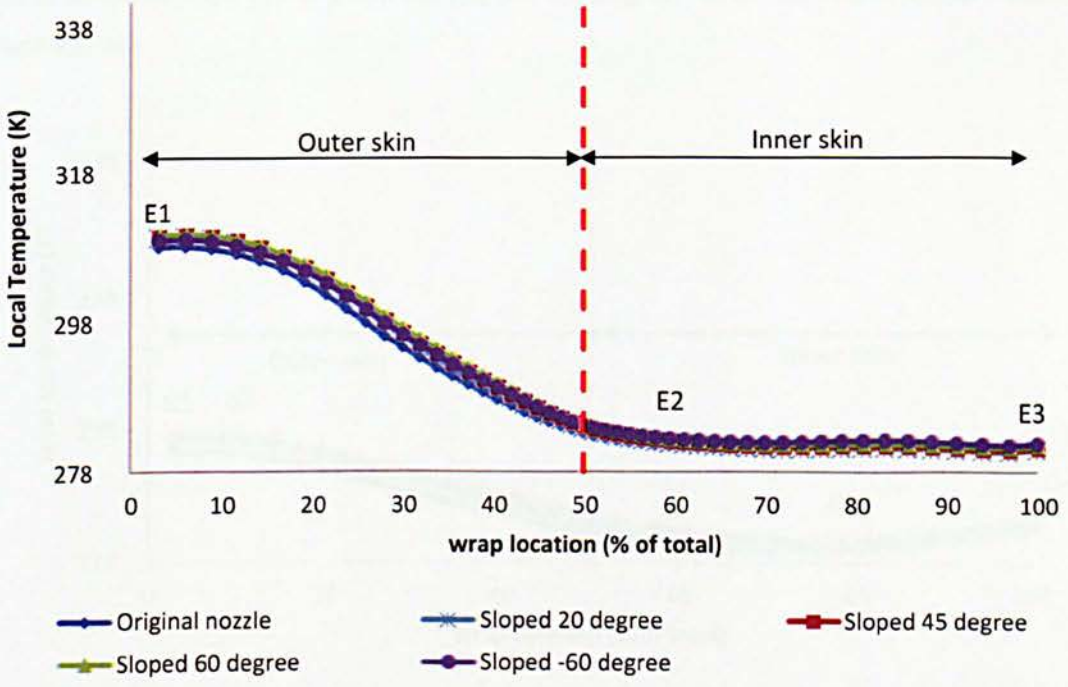

Figure 4.3.7: Local temperature profile along wrap location of lip-skin in plane 270°

The local temperature profile for the different nozzle designs in plane 0° is shown in Figure 4.3.8. In this plane, all local temperatures are very close to one another.

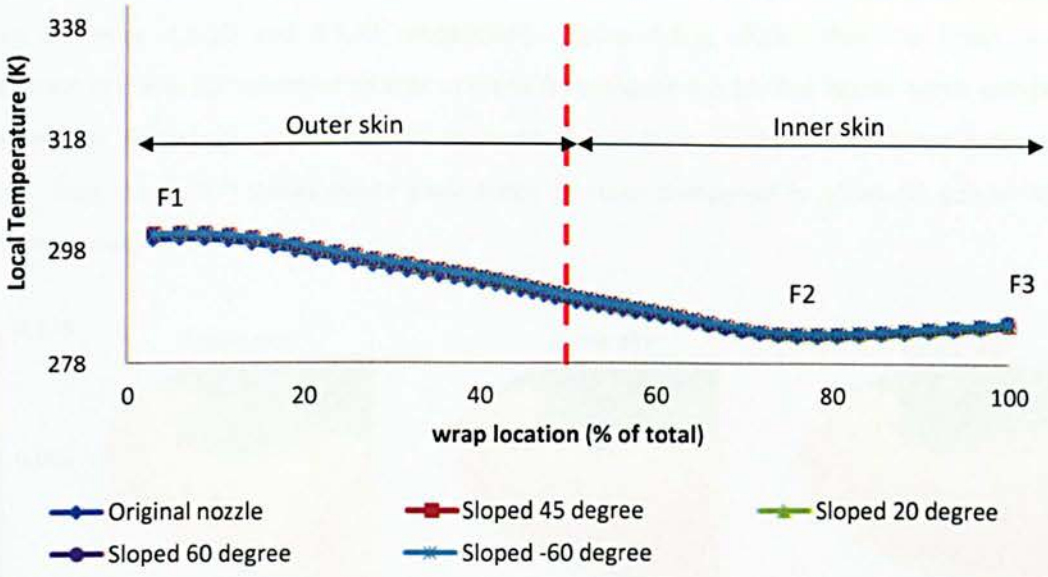

Figure 4.3.8: Local temperature profile along wrap location of lip-skin in plane 0°

The profile of local temperature for the five nozzle designs in plane 90° is shown in Figure 4.3.9 which illustrates that all the five designs follow similar trends. The figure also shows that sloped nozzles demonstrate a similar performance, but the original nozzle has inferior performance for all wrap locations.

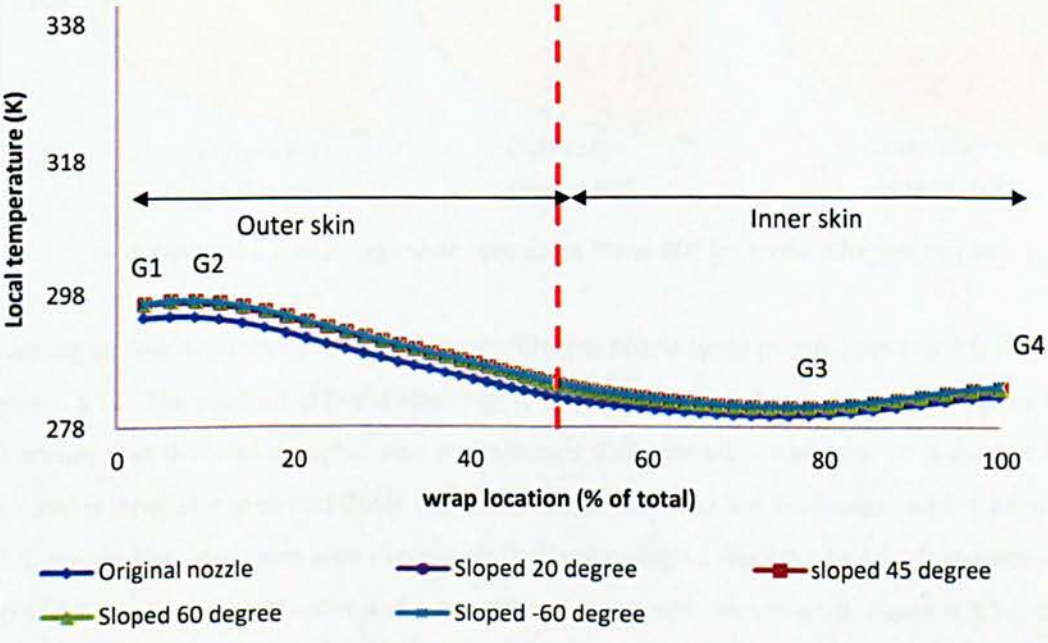

Figure 4.3.9: Local temperature profile along wrap location of lip-skin in plane 90°

The swirling air Mach number contours for three different nozzles types in planes 0° and 90° are shown in Figure 4.3.10 and 4.3.11 respectively. Figure 4.3.11 shows that the Mach number distribution in plane 90° is similar to that in plane 0° in Figure 4.3.10. The higher Mach number for sloped nozzle -60° means that it reduces momentum loss even more than the other two types of nozzles. Also, plane 90° shows lower peak Mach number compared to plane 0° due to further momentum loss.

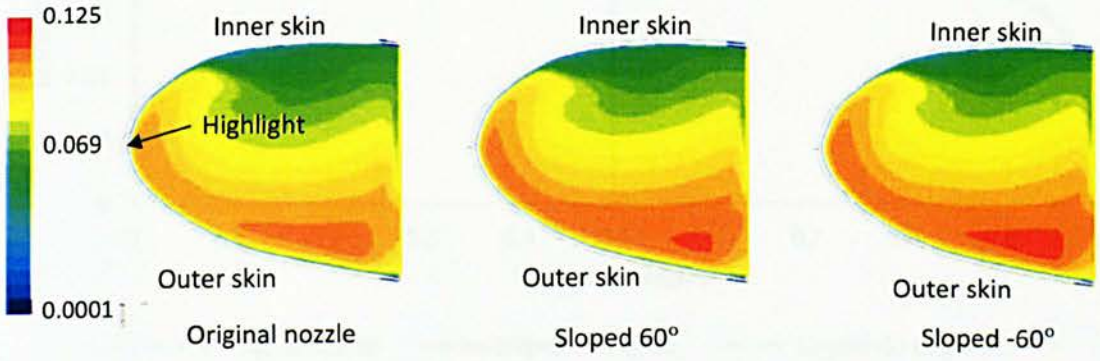

Figure 4.3.10: Mach number contour in Plane 0° for three different nozzle types

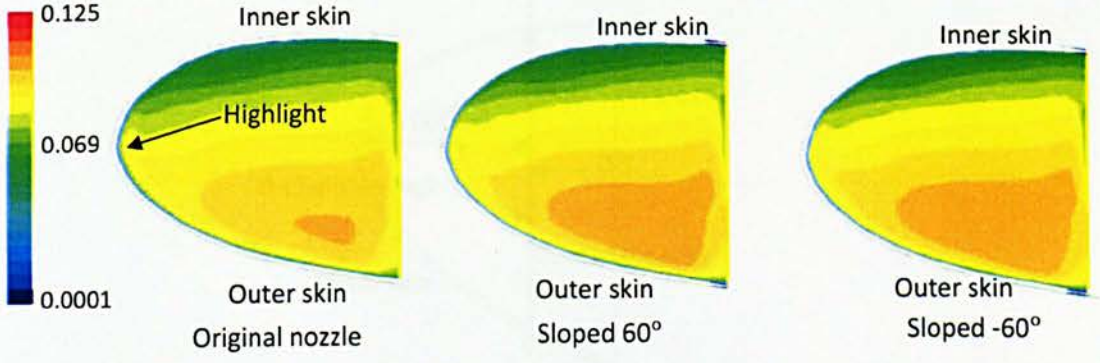

Figure 4.3.11: Mach number contour in Plane 90° for three different nozzle

The swirling air Mach number profiles for three different nozzle types in cold spot plane is illustrated in Figure 4.3.12. The position of D-chamber-high-1 line inside D-chamber is depicted in Figure 4.3.13 which shows that D-chamber-high-1 line is positioned 0.0069m after highlight. It is divided into 2 sides; namely Inner skin area and Outer skin area. Outer skin area is a D-chamber-high-1 between 0 and 0.5; meanwhile, Inner skin area represents D-chamber-high-1 from 0.5 to 1.0. D-chamber-high-1 of 0 and 1 are the walls of outer and inner skins respectively. As shown in Figure 4.3.12, the air Mach number in outer skin area is higher than that of inner skin area, meaning that outer skin area has higher heat transfer coefficient, and hence higher temperature, than inner skin area. Further,

sloped -60° nozzle produces the highest swirling air Mach number in cold spot plane, resulting in the highest cold spot temperature, followed by sloped 60° nozzle and original nozzle.

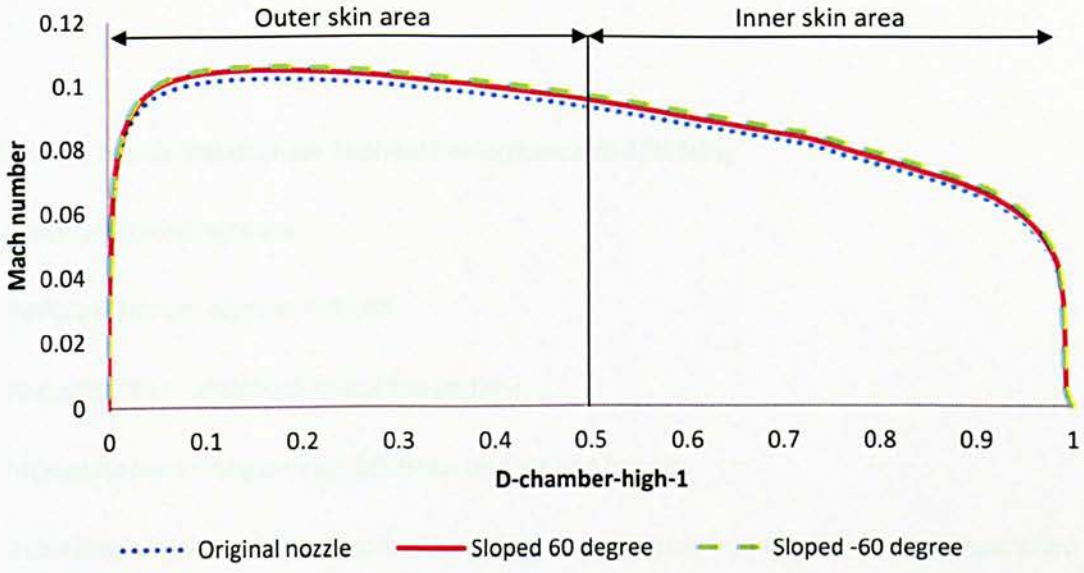

Figure 4.3.12: Mach number profile against D-chamber high 1 in Cold spot plane

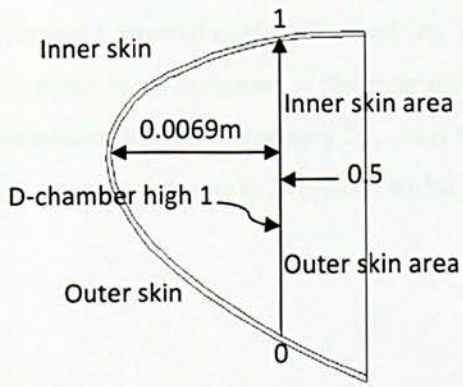

Figure 4.3.13: Location of D-chamber-high-1 line inside D-chamber

The results above show that the sloped nozzle has potential to improve thermal performance of anti-icing efficiency. As shown in Figure 4.3.3 to 4.3.11 and Table 4.3.1, sloped nozzle with -60° has the highest *EFF* and best lip-skin temperature uniformity compared to other nozzle designs. However, this improvement is not much attractive as T_{hi} is just 2.47K lower and T_{lo} is only 0.7K higher than those of original nozzle. This is attributed to the fact that sloped nozzle outlet has a normal circular nozzle shape. Similar observation was reported by Ramesh et al. [94] who identified lobed nozzle to be the best in the air mixing process and circular nozzle the worst. However, the present work did not investigate the performance of lobed nozzle, as suggested by Bombardier Aerospace

Company. The nozzle direction has then been shifted towards the inner skin in order to enhance temperature distribution on the nacelle lip-skin.

4.4 Effect of Nozzle Rotation on Thermal Performance of Anti-Icing

The challenges faced here are:

- Reducing temperature at hotspot
- Reducing the momentum loss of the jet flow
- Increasing the mixing process between cold air and hot air
- Achieving a more uniform distribution of skin temperature by increasing skin temperature on inner lip-skin with certain reduction of skin temperature at outer lip-skin

The direction of the nozzle has been recognised as one of the key factors. Therefore, its direction was altered in order to increase thermal performance of SAI. As Z increases, T_{hi} decreases and the mixing process is enhanced due to an increases in the momentum and heat exchange between hot air and cold air in the D-chamber, thereby increasing T_{ave}, heat transfer coefficient, EFF and T_{lo}. Thus, changing nozzle direction towards inner skin is proven to be a good method to improve thermal performance of SAI.

Figure 4.4.1 shows the illustration of nozzle rotation angle. The nozzle outlet was rotated towards inner skin by keeping the nozzle pipe at its original position. The study has investigated the effects of five different NRAs from 0° to 13° towards the inner lip-skin.

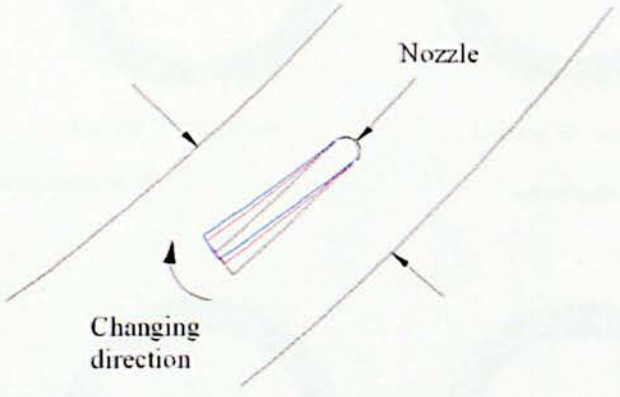

Figure 4.4.1: Illustration of nozzle rotation angle

The lip-skin temperature contours for five different NRAs, including original nozzle (0°), 5°, 7°, 9° and 13° are shown in Figure 4.4.2. As the position of T_{hi} moves further along the nacelle lip, T_{hi} in each scenario decreases as the NRA increases towards inner skin. In addition, the positions of cold spot are also transformed from point A to point B and the low temperature areas (illustrated in dark blue) diminish as the nozzle direction rotates towards inner skin.

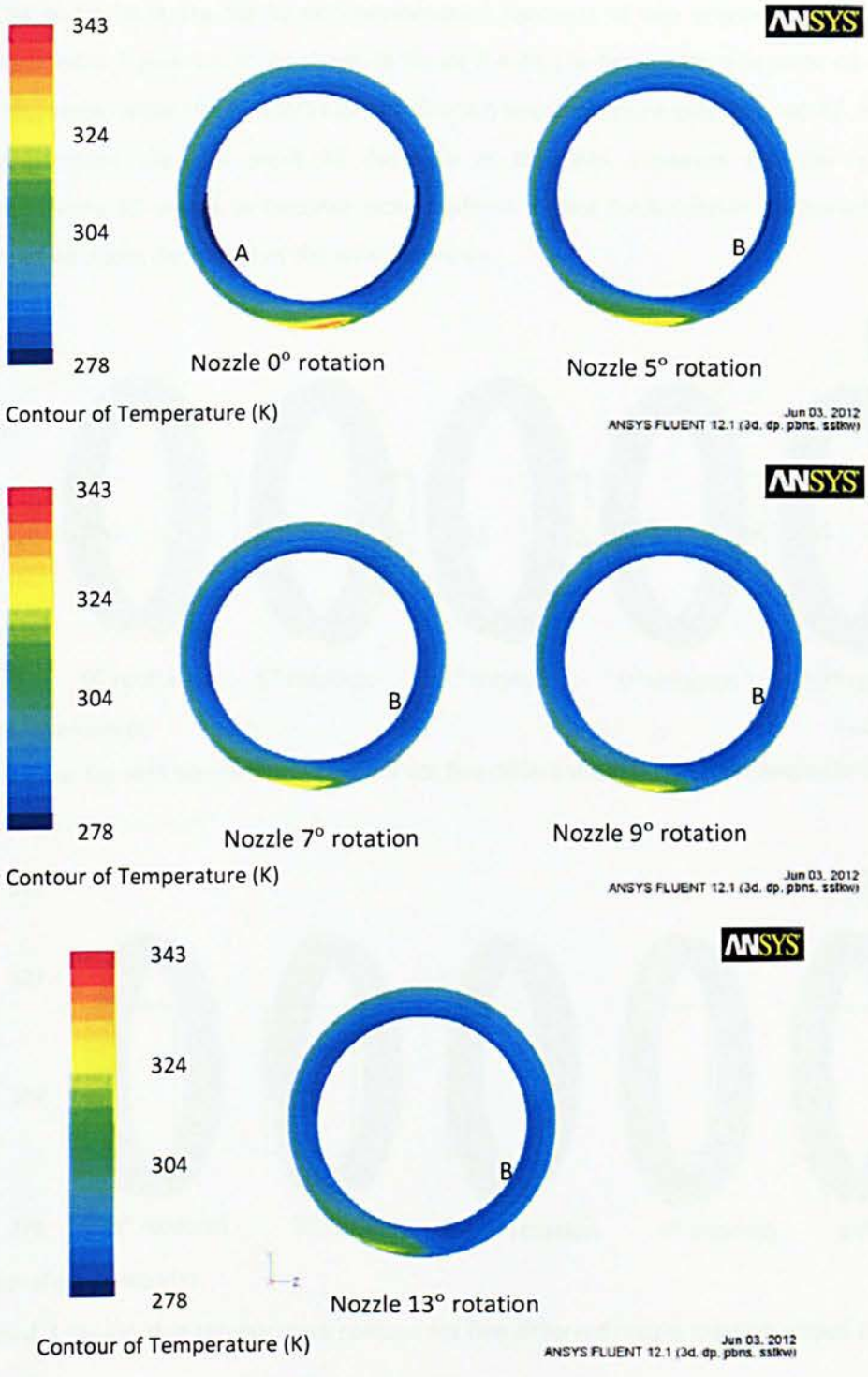

Figure 4.4.2: Lip-skin temperature contour for five different nozzle rotation angles

Figures 4.4.3a and b illustrate the lip-skin temperature contours at two different angles of views which are depicted in Figure 4.4.3c. As shown in Figure 4.4.3a, the temperature at point A1 increases as the NRA increases, while the temperature distribution becomes more even at zone A2. In View 2, the low temperature areas in point B1 decrease as the NRA increases and the outer skin temperature in zone B2 seems to become more uniform. Figure 4.4.4 further confirmed that the temperature of hotspots decreases as the NRA increases.

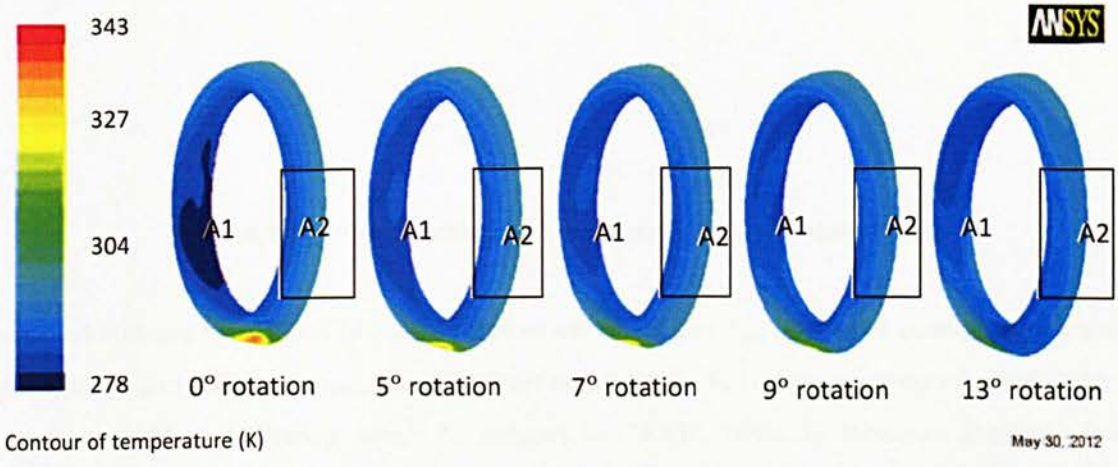

Figure 4.4.3a: Lip-skin temperature contour for five different nozzle rotation angles in View 1

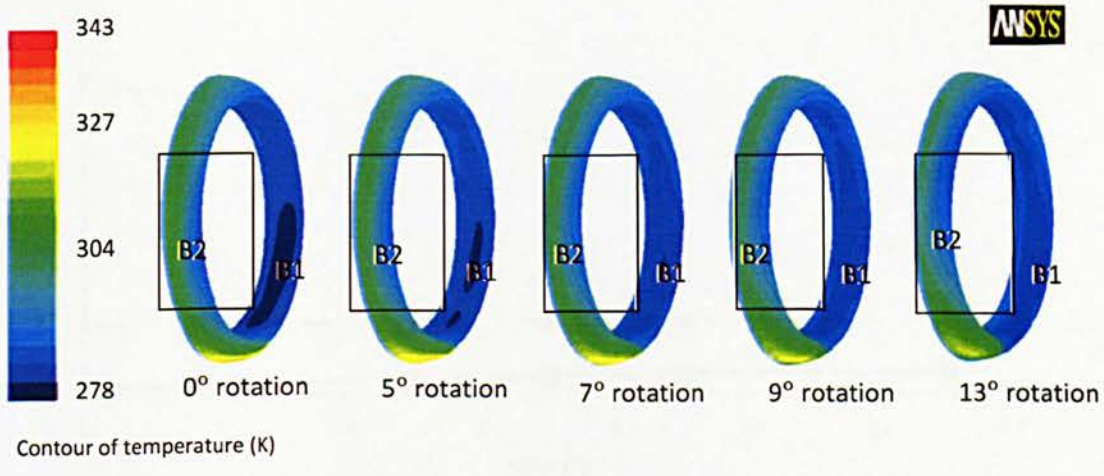

Figure 4.4.3b: Lip-skin temperature contour for five different nozzle rotation angles in View 2

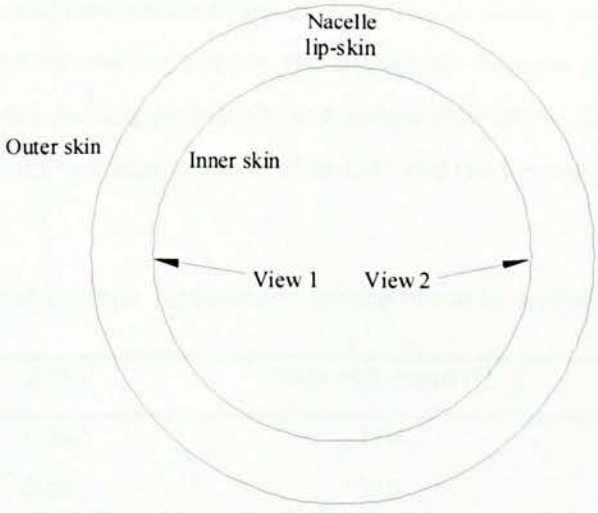

Figure 4.4.3c: View directions of View 1 and View 2 of the nacelle lip

Figure 4.4.4 shows the effects of nozzle rotation on T_{hi}, T_{lo} and T_{ave} under the conditions of the jet flow with T_{nozzle} of 533K and $m_{hot\ air}$ of 0.0178kg/s respectively. T_{hi} is inversely proportional to NRA in the range of 0° to 13°during which T_{hi} reduces by 18.53K, while T_{lo} increases gradually from 279.646K to 281.945K. However, the trend of T_{ave} is little bit different; T_{ave} increases from 18.5K to 18.87K from 0° to 9°whereafter decreases to 17.98K when NRA reaches 13°.

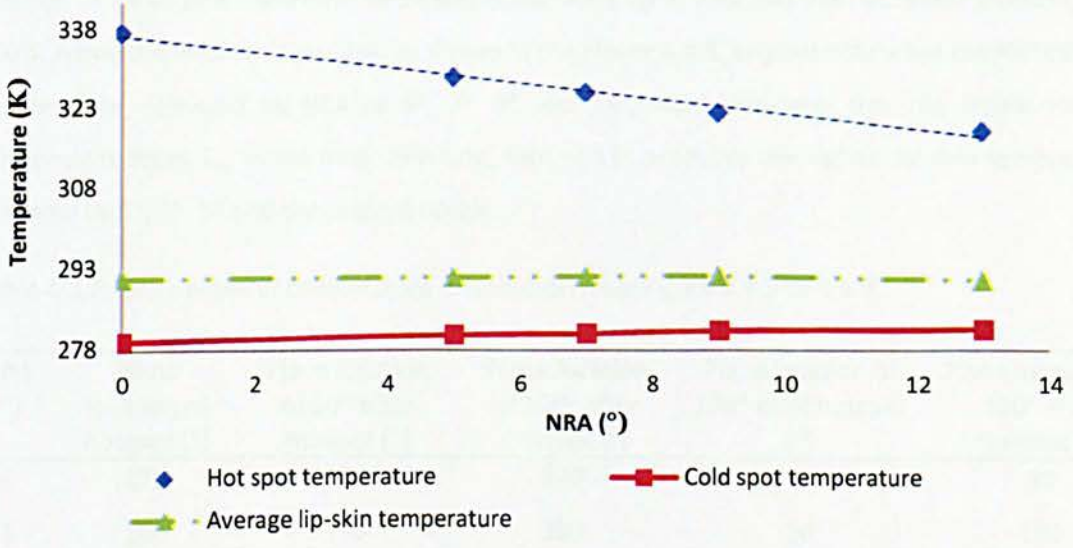

Figure 4.4.4: Effects of nozzle rotation on hotspot, cold spot and average lip-skin temperature

Table 4.4.1 summarizes the positions of the hotspot, cold spot and *Z* for the five cases. It is clear that the rotations result in the increase of *Z* by pushing hotspot location from plane 170° to 195° as NRA increases. Therefore, the jet has better opportunity to mix with cold air in the D-chamber, thereby

transferring more heat and momentum to the cold air. The air mixing process is enhanced and the swirling air velocity and temperature inside the D-chamber become more uniform as the NRA increases. As a result, the swirling air velocity and temperature along the inner skin increase. The plane of cold spot changes first from plane 245° to 114° and then moves back to 117°, as shown in Table 4.4.1.

Table 4.4.1: Summaries of T_{hi} plane, T_{lo} plane and spacing nozzle to impinging surface

NRA (°)	Z (m)	Plane of hotspot (°)	Plane of cold spot (°)
0	0.187	170	245
5	0.245	180	114
7	0.262	183	115
9	0.284	187	116
13	0.339	195	117

The temperature distributions in the hotspot planes are shown in Figure 4.4.5. Since the hotspot plane moves further from the nozzle, the lip-skin temperatures at different planes are shown. The exact planes for all the nozzle rotation angles are shown in Table 4.4.2. Generally, all nozzle rotations do not change the temperature distribution pattern, i.e. the local temperature increases from wrap location of 3% to 26% thereafter decreases moderately up to 79% and then increases gradually until 100%. Along the outer skin surface, as shown in the Figure 4.4.5, original nozzle has the highest local temperature, followed by NRA of 5°, 7°, 9° and 13°, which indicates that the nozzle rotation efficiently reduces T_{hi}. In the inner skin side, NRA of 13° produces the highest lip-skin temperature, followed by 9°, 7°, 5° and the original nozzle.

Table 4.4.2: Exact plane of temperature distribution from Figure 4.4.5 to 4.4.9

NRA (°)	Plane location of hotspot (°)	Plane location of 10° after hotspot (°)	Plane location of 100° after hotspot (°)	Plane location of 190° after hotspot (°)	Plane location of 280° after hotspot (°)
0	170	180	270	0	90
5	180	190	280	10	100
7	183	193	283	13	103
9	187	197	287	17	107
13	195	205	295	25	115

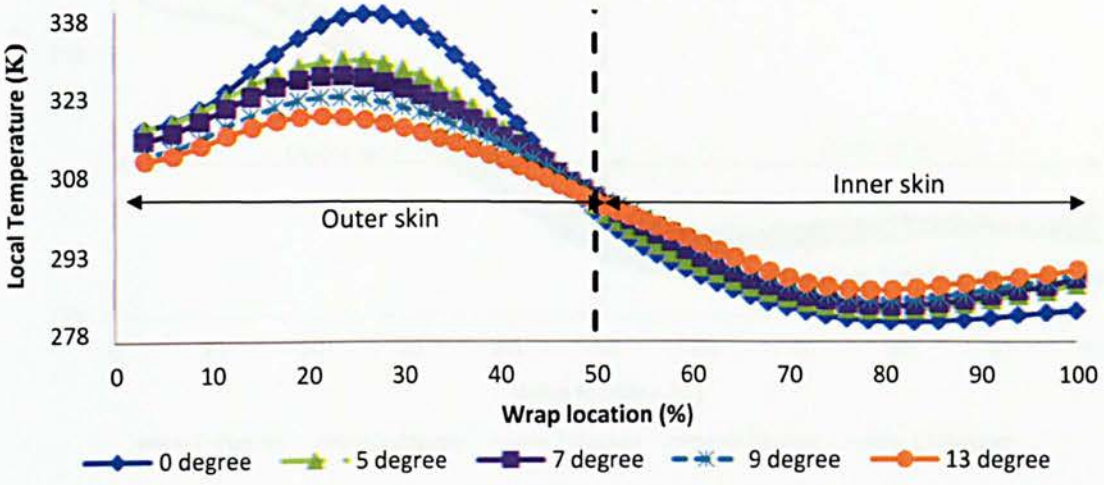

Figure 4.4.5: Local temperature distribution along wrap location in hotspot planes

For all cases, the temperature profiles in plane 100° after the hotspot plane are different from those of the hotspot plane. Figure 4.4.6 shows that all local temperatures in this plane decrease along the wrap location from 3% until 60%, with NRA of 13° having the lowest local temperature, followed by 9°, 7°, 5° and 0°. After the 60% wrap location, the local temperatures flatten out with slight changes. NRA of 0° has the lowest local temperature along wrap location between 60% and 100%.

Along the outer skin, the NRA of 13° has the lowest local temperature for the wrap location in the range of 3% to 40% thereafter overtaken by the original nozzle. The local temperature generally exhibits inverse relation with NRA with the exceptions that NRA of 5° shows the highest local temperature from wrap location of 18% to 40% and the NRA of 0° shows the lowest temperature for the wrap location between 40% and 50%. The temperature levels for all NRAs are similar and higher than that of original nozzle with NRA of 9° demonstrating a small advantage along major part of the inner skin.

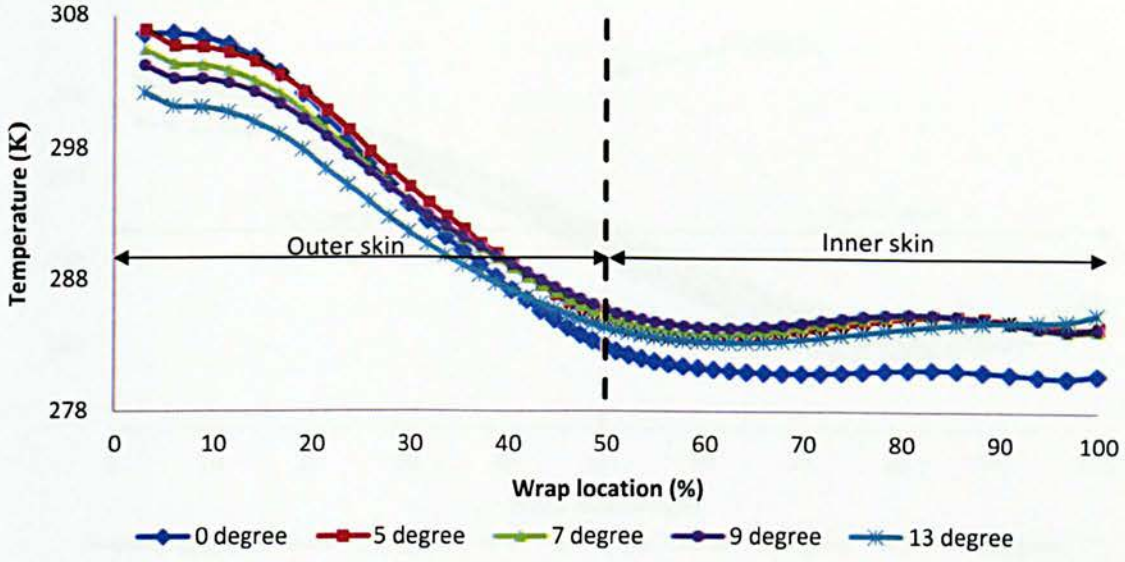

Figure 4.4.6: Local temperature distribution along wrap location in plane 100° after hot spot plane

Figure 4.4.7 illustrates the local temperature profiles for all rotated nozzles in plane 190° after the hotspot plane. The local temperature decreases gradually with wrap location and the minimum value is found at the wrap location around 78% for every nozzle. As the flow moves away from the nozzle, the difference between the highest and lowest temperature becomes smaller, and this phenomena is enhanced by nozzle rotation as well. The nozzle with 9° rotation demonstrates the highest local temperature in plane 190° after hotspot plane along most part of the skin wrap location until around 80%. The nozzle 13° rotation displays the lowest local temperature on outer skin in this plane until the highlight area, before decreasing at a lower rate compared to the other nozzles. After that, the local temperature for nozzle 13° rotation reaches the same as that for the original nozzle at the wrap location of 90% and further.

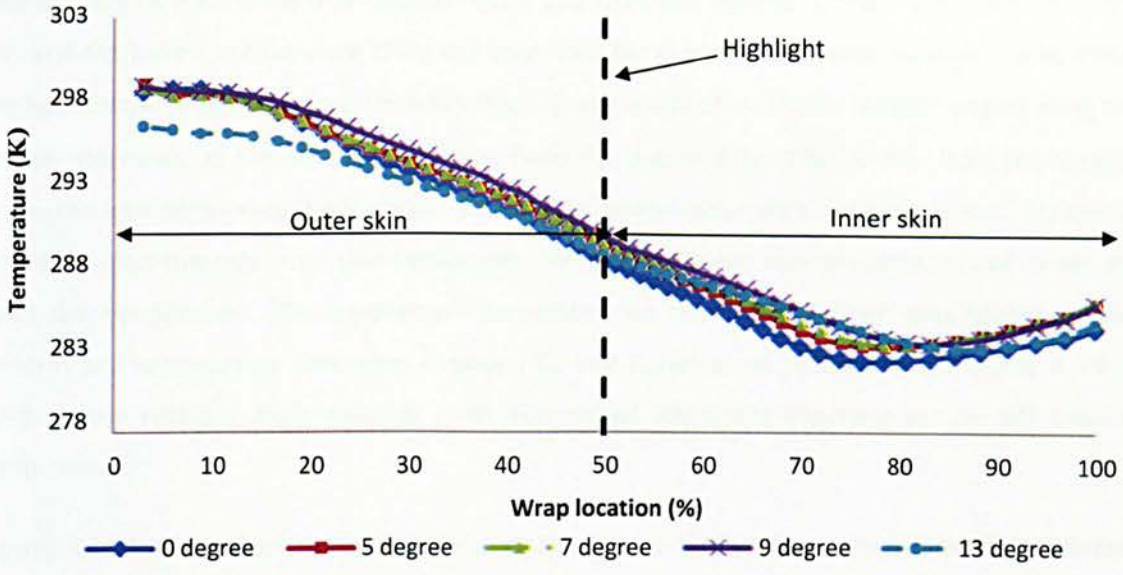

Figure 4.4.7: Local temperature distribution along wrap location in plane 190° after hot spot plane

Figure 4.4.8 illustrates the local temperature distribution against wrap location for all the five nozzles in plane 280° after hotspot plane, just behind the nozzle. Nozzle with 13° gives the best performance with lower temperature along the outer skin and higher temperature along the inner skin, followed by 9°, 7°, 5° and 0°.

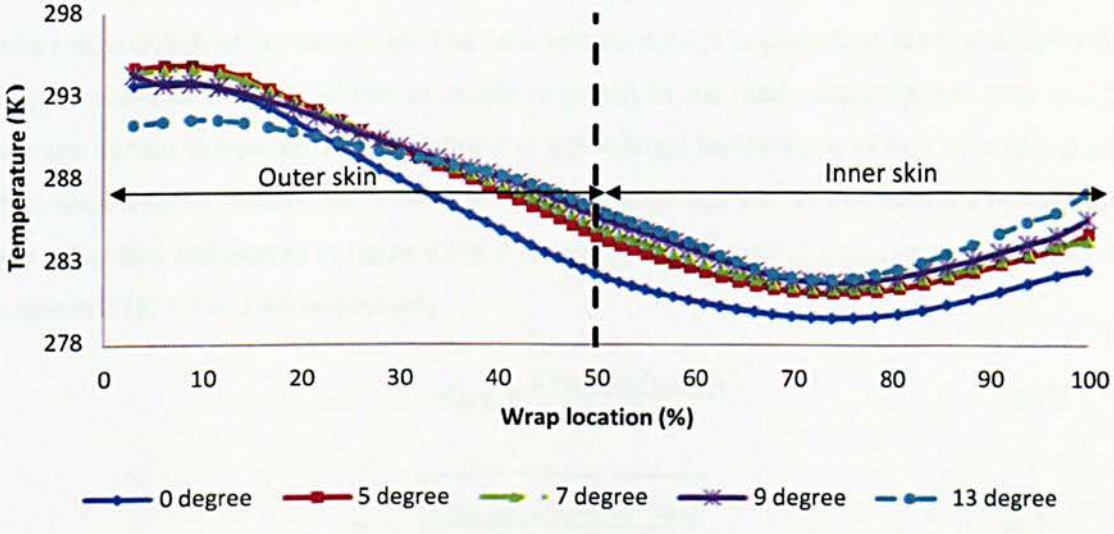

Figure 4.4.8: Local temperature distribution along wrap location in plane 280° after hotspot plane

Figures 4.4.5 to 4.4.8 show that original nozzle produces the highest temperature along the outer skin and the lowest temperature along the inner skin for almost all the wrap locations. In addition, the local temperature difference between original nozzle and other nozzle rotation angles along the lip-skin decreases, as the hot air flows away from the nozzle. After 100° further from the hotspot plane, the local temperature differences for both outer and inner skins are much closer. Therefore, nozzle rotation towards inner skin significantly reduces the outer skin temperature and raises the inner skin temperature. The temperature distribution on the nacelle lip-skin thus becomes more uniform and temperature difference between T_{hi} and T_{lo} decreases. According to Figures 4.4.5 to 4.4.8, nozzle rotation angle towards inner skin shows significant improvement on SAI thermal performance.

Figures 4.4.5 to 4.4.8 illustrate the temperature distribution profiles along the nacelle lip at different planes. However, these do not represent the temperature uniformity of the entire nacelle lip-skin since they were just extracted at certain planes along the nacelle lip. Therefore, this study has employed statistical quality control (*SQC*) and statistical methods [101, 102] to measure temperature uniformity of the nacelle lip. The parameters used to measure temperature uniformity of the nacelle lip were: T_{ave}, $T_{hi} - T_{lo}$, standard temperature deviation (σ) and coefficient of temperature deviation ($C_{tem\ deviation}$).

In order to determine σ on the nacelle lip-skin, the nacelle lip-skin was divided into several plots based on the temperature variation. In each plot, the temperature should vary as small as possible, named distinct/subset temperatures. The "percentage distinct temperature area" was defined as the percentage of the area of one or couple of plot(s) to the total nacelle lip-skin area, and the "average distinct temperature" was defined as the average temperature of one or couple plot(s). Then, the covers of "percentage distinct temperature area" vs. the "average distinct temperature" were calculated and plotted in Figure 4.4.9. Afterwards, T_{ave}, σ and $C_{tem\ deviation}$ were calculated using Equations 2.21, 4.3 and 4.5 respectively.

$$T_{ave} = \frac{\sum A_{lip-skin} T_{lip-skin}}{\sum A_{sur\ lip-skin}} \tag{2.21}$$

$$\sigma = \sqrt{\frac{\sum A_{lip-skin} (T_{lip-skin} - T_{ave})^2}{\sum A_{sur\ lip-skin}}} \tag{4.3}$$

$$C_{tem\ deviation} = \frac{\sigma}{(T_{ave} - T_{\infty})} (100) \tag{4.4}$$

Subsequently, temperature uniformity measurement was summarised as in Table 4.4.3.

Figure 4.4.9 shows the percentage of distinct area against average distinct temperature of the nacelle lip-skin for nozzle 0°, 5°, 7°, 9° and 13° rotations. The starting points of each curve on the X axis represent T_{lo}, which shows that original nozzle has the lowest T_{lo}, but the nozzle with the rotation angle of 13° displays the highest one. The peak point A is produced by the nozzle with rotation angle of 5°, with the average temperature of 10.98K and 21.41 % of the total nacelle lip-skin area. The curves end up by displaying the hotspot temperatures.

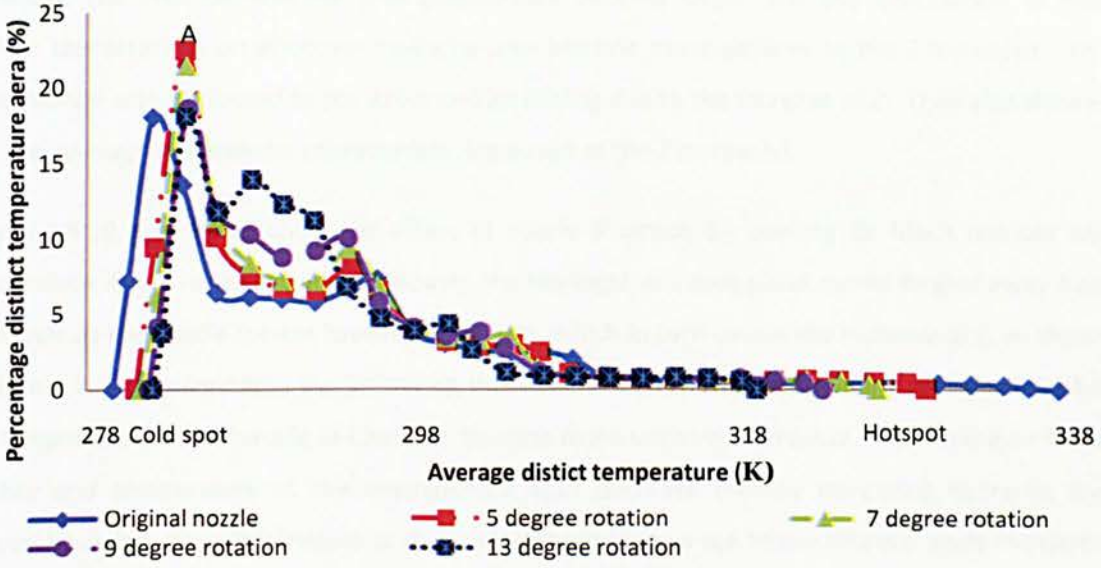

Figure 4.4.9: Percentage of distinct area along average distinct temperature of the nacelle lip-skin

Table 4.4.3: Summary of temperature uniformity for different nozzle rotation angles

NRA (°)	T_{ave}(K)	$(T_{hi} - T_{lo})$ (K)	σ (K)	$C_{tem\ deviation}$ (%)
0	291.43	57.77	10.76	42.9
5	291.71	48.27	9.48	42.5
7	291.84	45.07	8.86	34.7
9	291.87	41.18	8.12	31.8
13	290.98	36.94	7.20	29.2

The temperature uniformity in the nacelle lip-skin is inversely related to $C_{tem\ deviation}$ and σ. Lower σ and $C_{tem\ deviation}$ indicate more uniformly distributed temperature along nacelle lip-skin. In other words, the most uniform temperature distribution along lip-skin occurs when $C_{tem\ deviation}$ is 0%, in which the lip-skin local temperature is constant for the entire lip-skin surface. The table shows that $T_{hi} - T_{lo}$ decreases from 57.77K to 36.94K, and σ decreases by 3.56K, as the nozzle rotates towards inner skin from 0° to 13°. Finally, $C_{tem\ deviation}$ decreases 13.7% as the angle of nozzle increases from 0°

to 13°. Nozzle 13° has the most uniform distribution of local temperature along the nacelle lip-skin, followed by nozzle 9°, 7° and 5°, which leaves nozzle with 0° rotation as the worst design for uniform distribution of temperature. For these nozzle diameters, temperature and hot air mass flow rate, nozzle at 13° rotation contributes to the best thermal performance of the SAI system.

The above observations are consistent with those reported by San and Shiao [120] and Yang et al. [54] who demonstrated the inverse relationship of local heat transfer characteristic and *Z*. Moreover, the area of effective-impinging-surface became larger and the distribution of heat transfer characteristic on effective-impinging-area became more uniform as the *Z* increased. This phenomenon was attributed to the enhanced air mixing due to the increase of *Z*. They also showed that the average heat transfer characteristic increased as the *Z* increased.

Figures 4.4.10 and 4.4.11 show the effect of nozzle direction on swirling air Mach number and temperature at the nozzle vicinity. Obviously, the impingement spot plane moves further away from the nozzle as the nozzle rotates towards inner skin, which in turn causes the increase of *Z*, as shown in Table 4.4.1. Consequently, the air mixing process is enhanced and the swirling air Mach number and temperature inside nacelle D-Chamber become more uniform. Moreover, the swirling air Mach number and temperature at the impingement spot decrease thereby increasing hydraulic and thermal boundary layer thicknesses at the impingement spot as the nozzle rotation angle increases. As a result, heat transfer coefficient at the impinging spot decreases and so does T_{hi} on the nacelle lip-skin. In addition, the momentum and heat exchange between hot air and cold air increase as the nozzle rotation increases. It enhances the air Mach number in cold spot plane and decreases hydraulic boundary layer thickness on the cold spot. This phenomenon increases both heat transfer coefficient and T_{lo} in the cold spot plane. $C_{tem\ deviation}$ decreases just as $T_{hi} - T_{lo}$ decreases, which indicates that the uniformity of lip-skin temperature increases. This is an advantage with regard to SAI thermal performance since the study focus was to reduce T_{hi} and increase T_{lo} and T_{ave} , of the nacelle lip-skin.

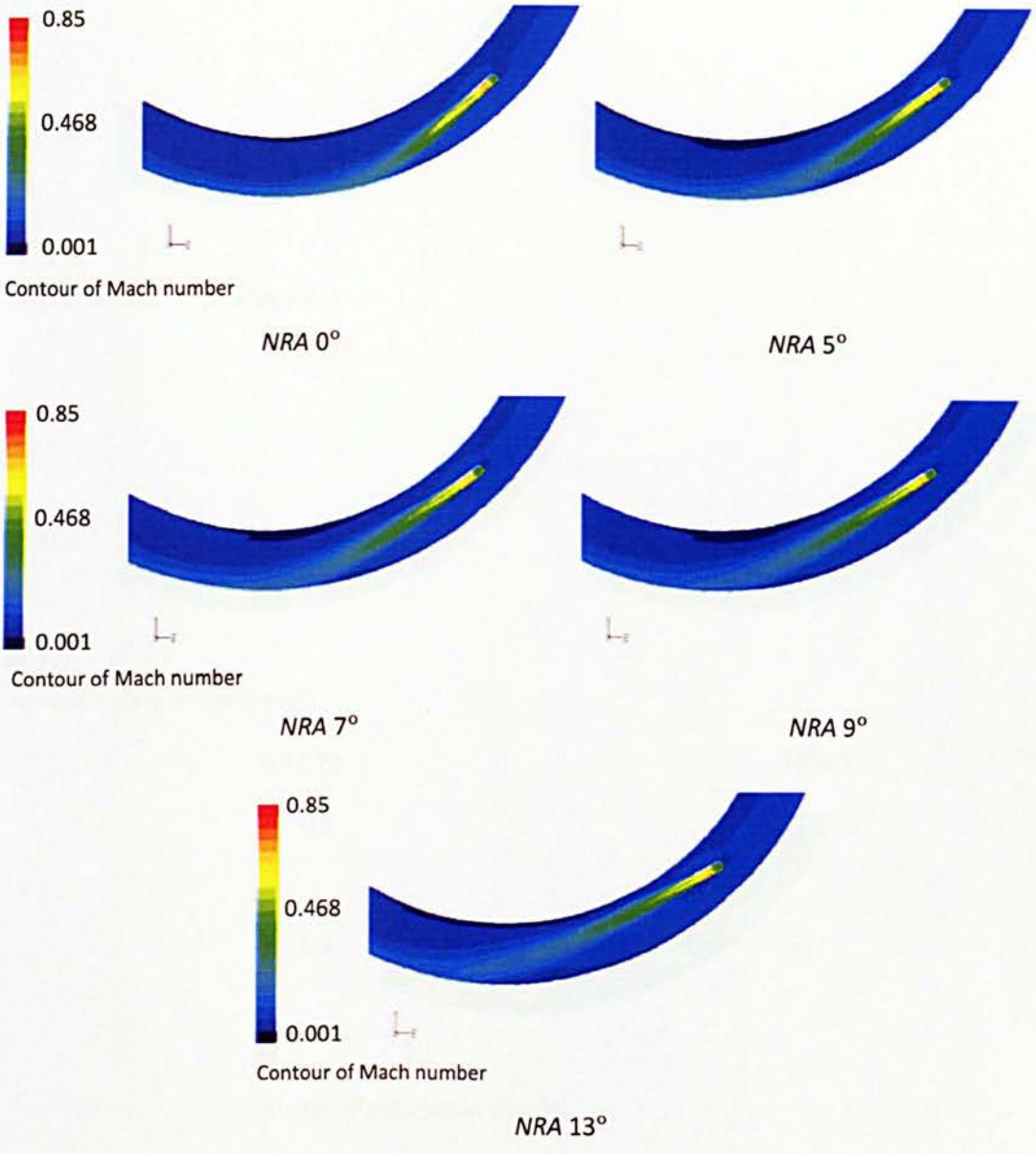

Figure 4.4.10: Contour of Mach number in vicinity of nozzle area

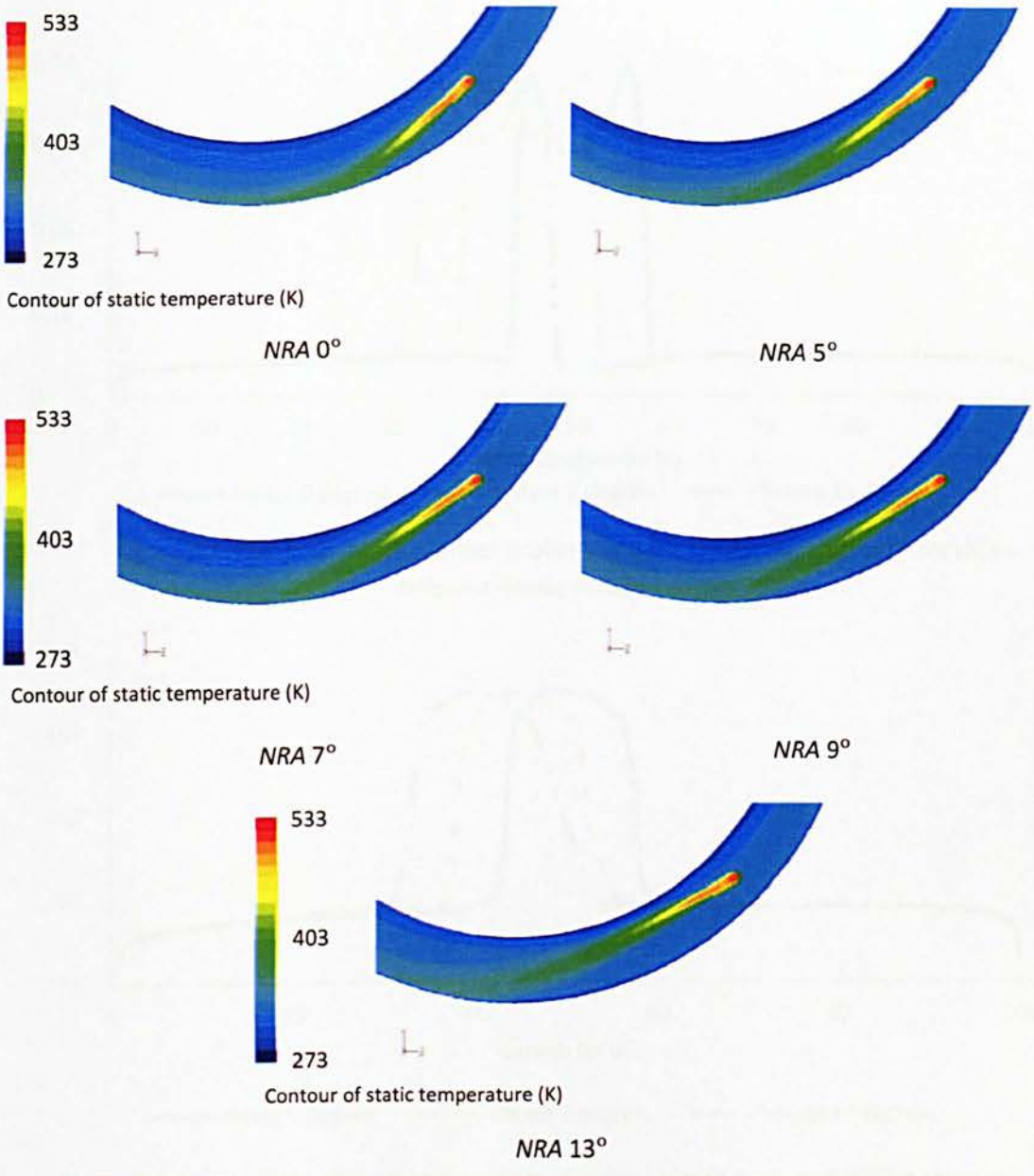

Figure 4.4.11: Air temperature contour in vicinity of nozzle area

u_j and T_j profiles in several planes plotted against length are shown in Figures 4.4.12a to 4.4.16b to elaborate the variation of air Mach number and temperature between nozzle outlets to impingement spot. The high Mach number and temperature of jet for all the three different nozzles are evident in Figures 4.4.12a and b. Although the highest value of u_j decreases slightly from 0.98 for nozzle 0°, to 0.96 for nozzle 7° and 0.90 for nozzle 13°, the rotation shifts the jet towards inner skin. However, the peak temperature T_j of hot air in plane 140° is almost the same for all nozzle rotation angles, as shown in Figure 4.4.13b.

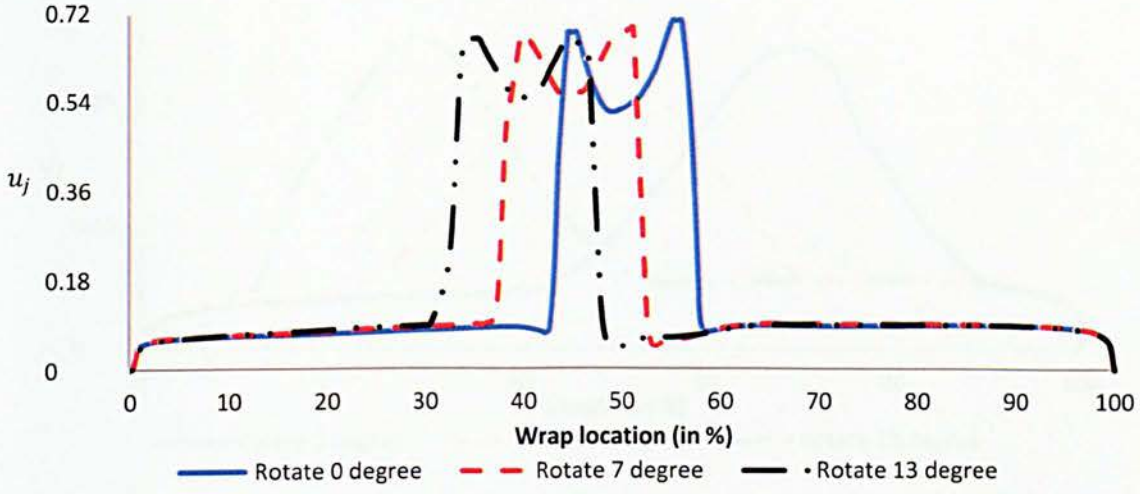

Figure 4.4.12a: Local Mach number profile along the length in plane 140° for three different nozzle rotation angles

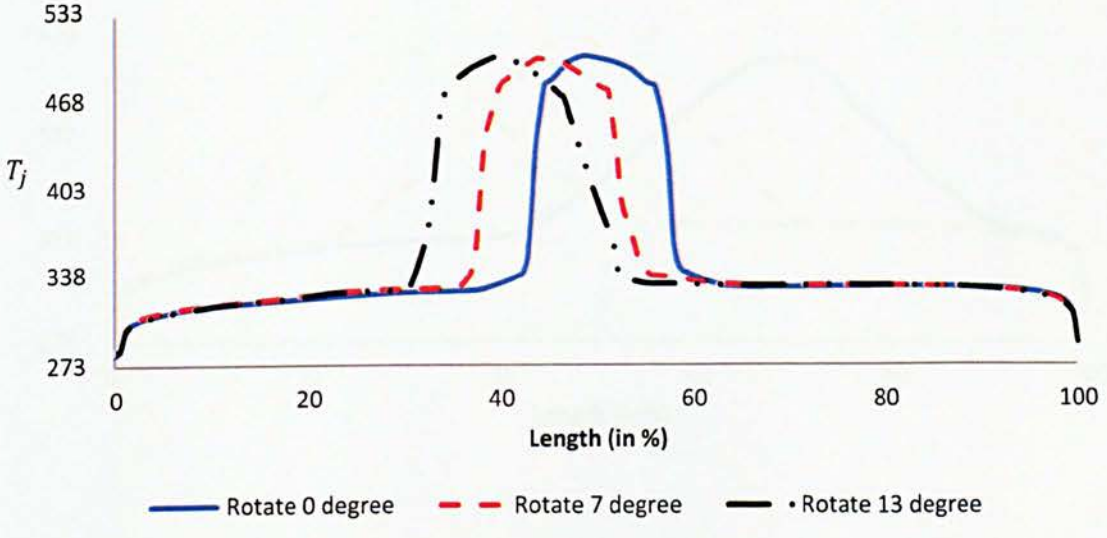

Figure 4.4.12b: Local air temperature profile along the length in plane 140° for three different nozzle rotation angles

As the swirling air in the D-chamber flows through plane 155° (Figures 4.4.13a and b), the peak values of u_j and T_j of nozzle 0° moves towards outer skin (length of 100%), while nozzle 13° shifts the peak values of u_j and T_j towards inner skin (length of 0%). However, for the nozzle 7°, the peak values of u_j and T_j are located at the centre, as shown in Figures 4.4.13a and b. The jets for all three nozzles are less obvious compared to Mach number profile in plane 140°.

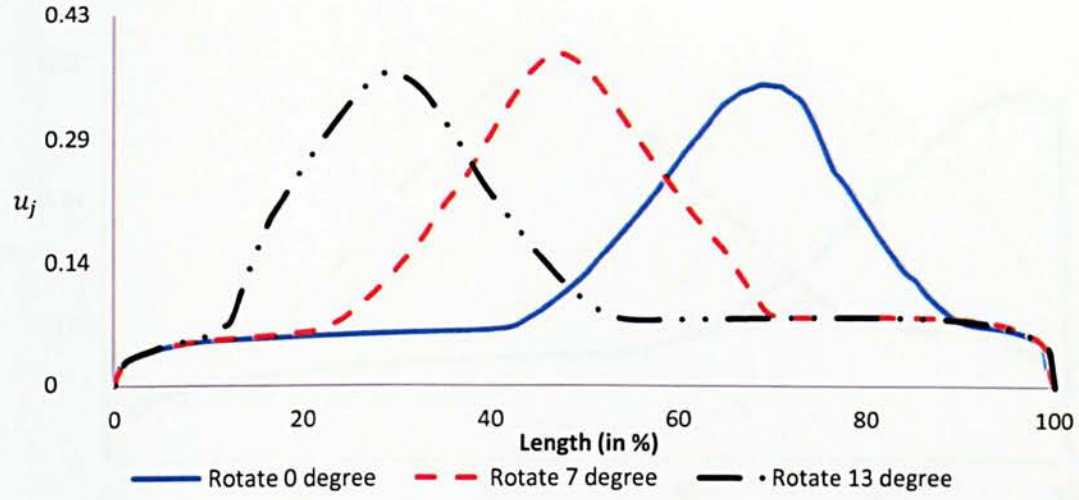

Figure 4.4.13a: Local Mach number profile along the length in plane 155° for three different nozzle rotation angles

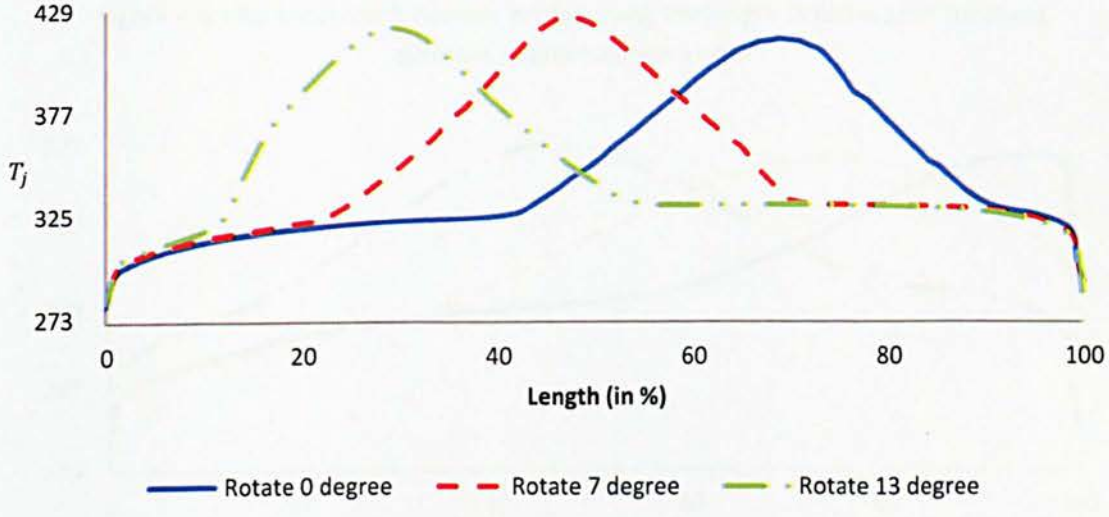

Figure 4.4.13b: Local air temperature profile along the length in plane 155° for three different nozzle rotation angles

As the hot air flows further from nozzle to plane 170°, all peak values of u_j and T_j seem to move towards outer skin for all rotated nozzles, as shown in Figures 4.4.14a and b. Besides, the distribution of the Mach number and temperature become more uniform. Figures 4.4.15 and 4.4.16 demonstrate a similar trend; the centre of jet flow moves towards the outer skin, and the distribution of the Mach number and temperature become more uniform.

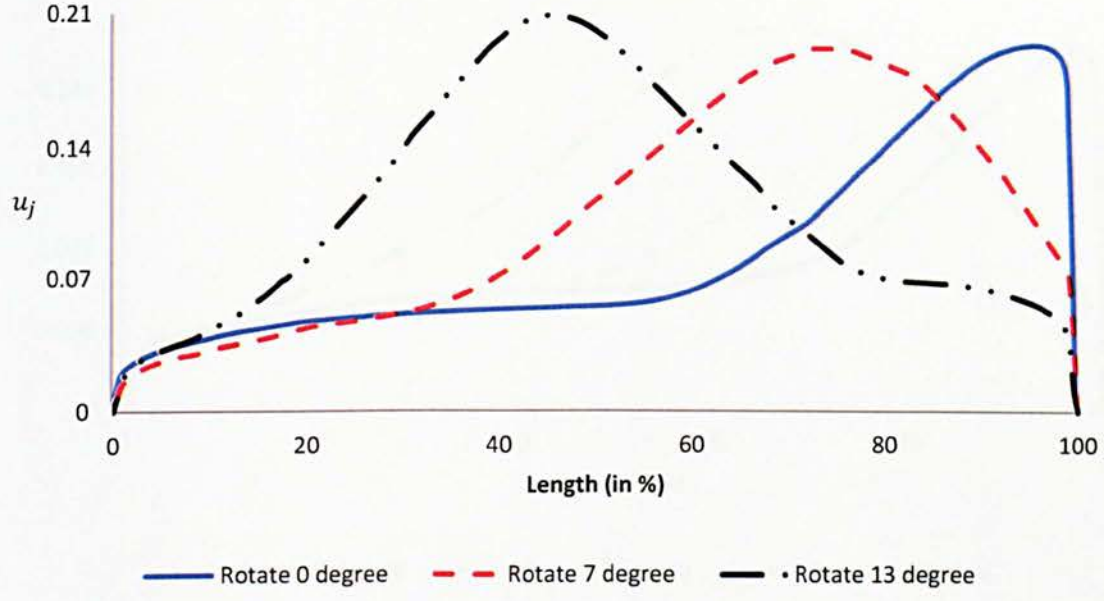

Figure 4.4.14a: Local Mach number profile along the length in plane 170° for three different nozzle rotation angles

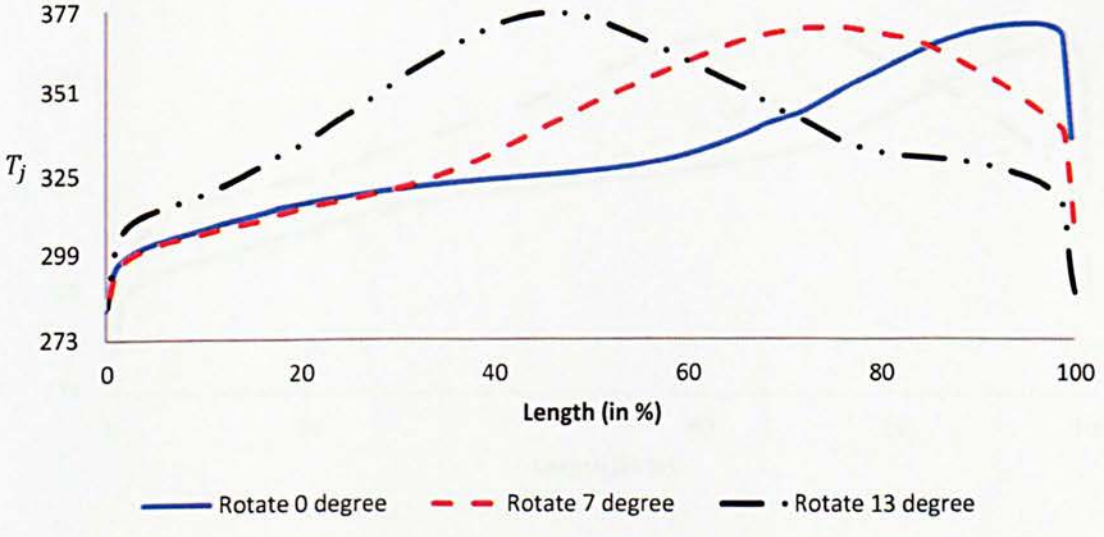

Figure 4.4.14b: Local air temperature distribution along the length for three different nozzle rotation angles in plane 170°

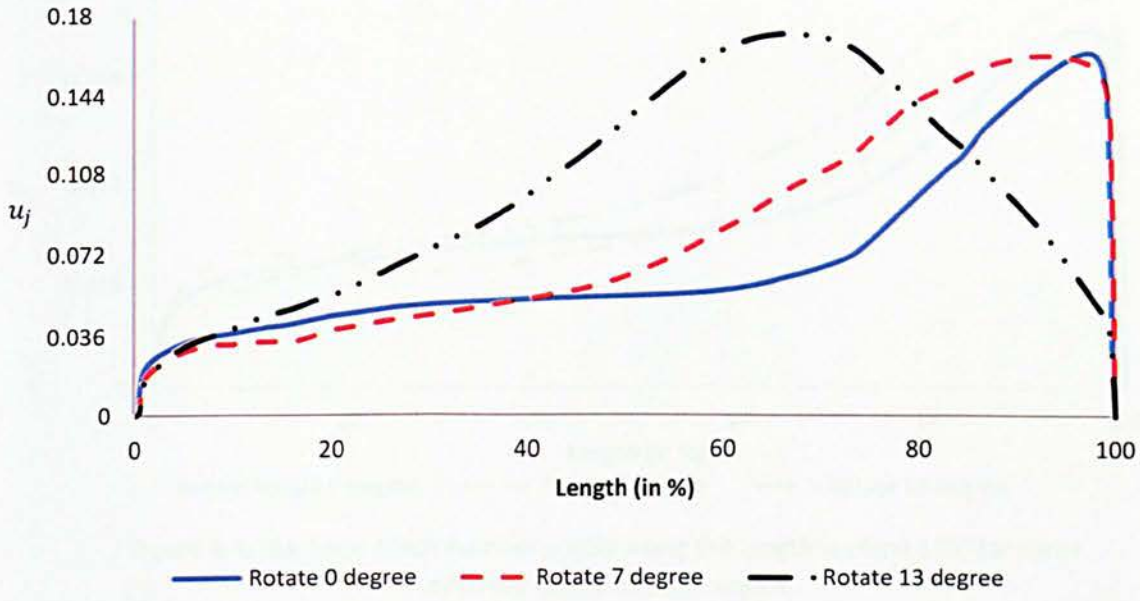

Figure 4.4.15a: Local Mach number profile along the length in plane 180° for three different nozzle rotation angles

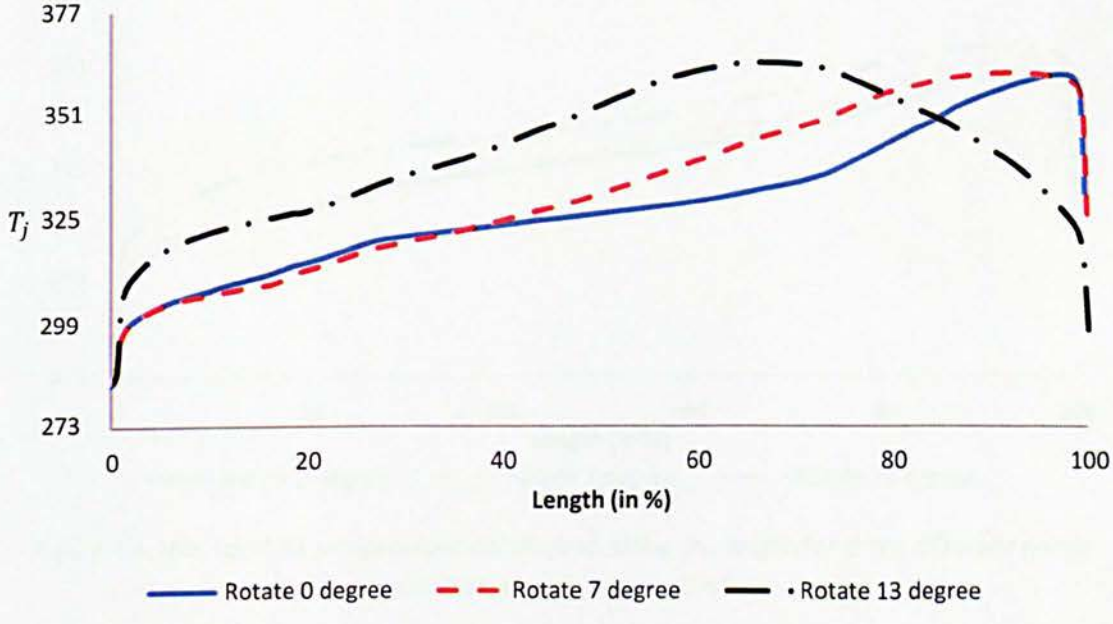

Figure 4.4.15b: Local air temperature distribution along the length for three different nozzle rotation angles in plane 180°

The results show that T_{hi} of nozzle 0° and 13° rotations occur in planes 170° and 195° respectively. The differences of peak values for Mach number and temperature for impinging planes between nozzle 0° and nozzle 13° rotation are 0.08 and 0.09 respectively. As a result, the original nozzle produces higher T_{hi} than nozzle 13° rotation.

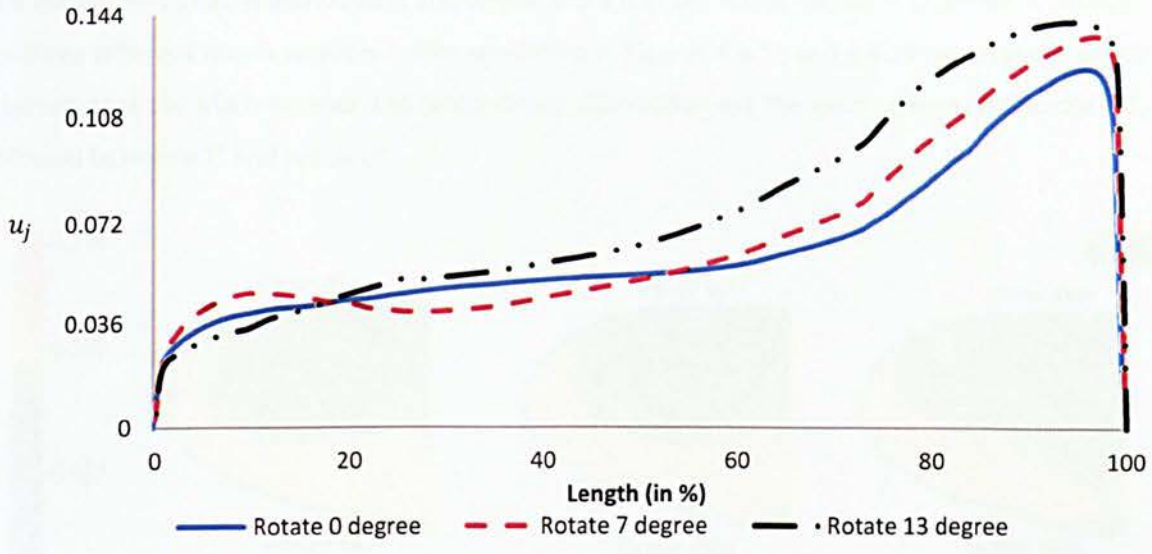

Figure 4.4.16a: Local Mach number profile along the length in plane 195° for three different nozzle rotation angles

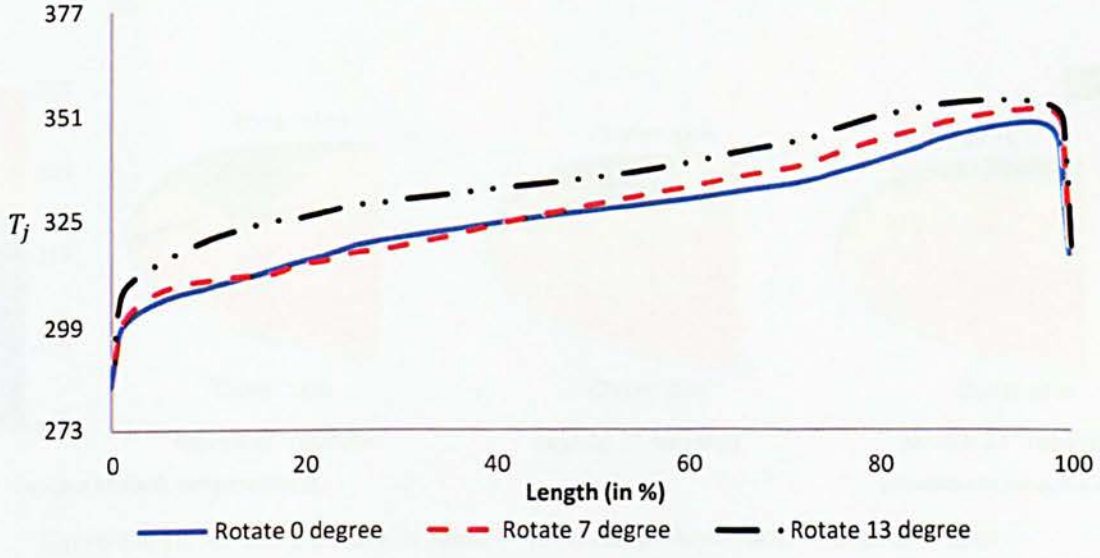

Figure 4.4.16b: Local air temperature distribution along the length for three different nozzle rotation angles in plane 195°

Since the jet of the original nozzle impinges on outer skin earlier than the jet of nozzle 13°, it has lower heat and momentum exchange with cold air. As shown in Figures 4.4.14a to 4.4.16b, the original nozzle generally has lower u_j and T_j profiles compared to nozzle 13° rotation in planes 170°, 180° and 195°. Hence it can be deduced that the original nozzle has relatively higher momentum loss and heat transfer due to impingement effect. Overall, the Mach number and the air temperature after plane 170° increase when the rotation angle.

The comparison of air Mach number and temperature contour inside nacelle D-Chamber in plane 0° for three different nozzle rotation angles are shown in Figures 4.4.17 and 4.4.18 respectively, which illustrate that the Mach number and temperature distribution are the most uniform for nozzle 13°, followed by nozzle 7° and nozzle 0°.

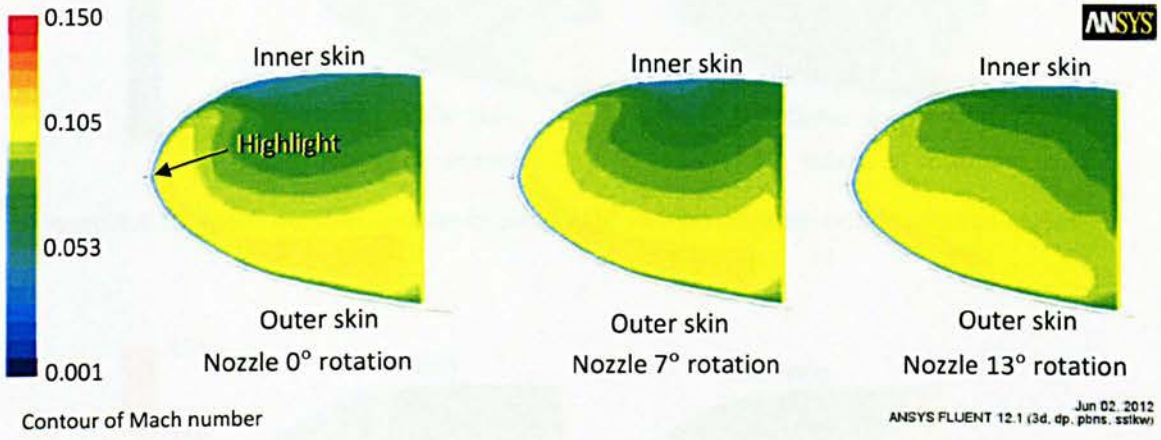

Figure 4.4.17: Air Mach number contour in plane 0° for three different nozzle rotation

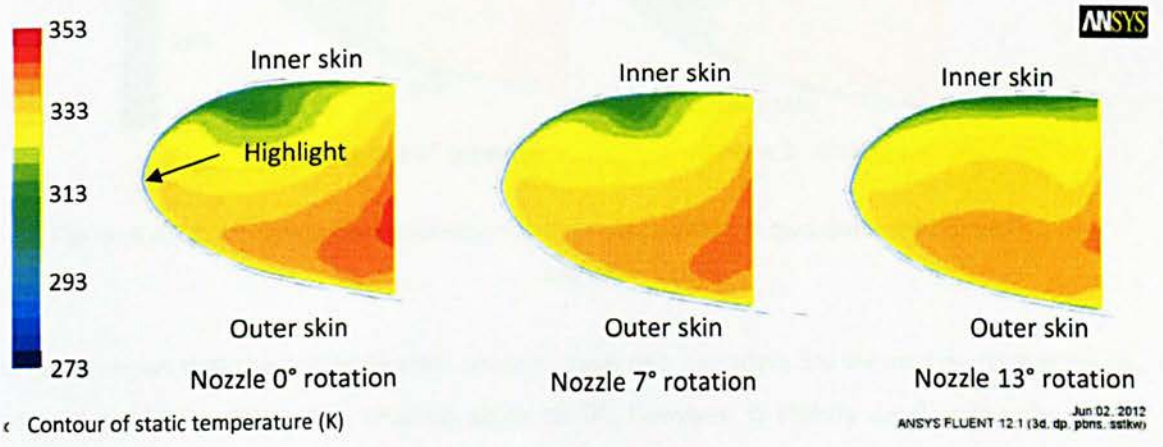

Figure 4.4.18: Air temperature in plane 0° for three different nozzle rotation angles

Previous Figure 4.4.2 shows that the cold spot moves from plane 245° to plane 116° as the nozzle rotates from 0° to 9° towards inner skin, and obtains higher value. As discussed before, the lip-skin temperature is related to the air Mach number adjacent to the wall of the nacelle D-Chamber. It means that the nozzle 9° produces better air Mach number and temperature distribution in plane 245° than nozzle 0° especially in the inner skin area, as shown in Figures 4.4.19 and 4.4.20. Thus, the temperature of inner skin in plane 245° increases as the nozzle rotation increases. As a result, cold spot is no longer in plane 245° as the nozzle is rotated towards inner skin, as shown in Figure 4.4.3a.

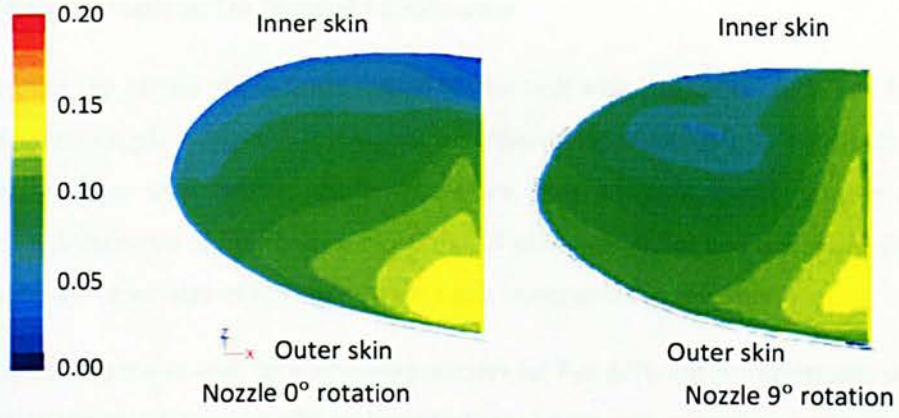

Figure 4.4.19: Mach number contour in plane 245° for two different nozzle rotation angles

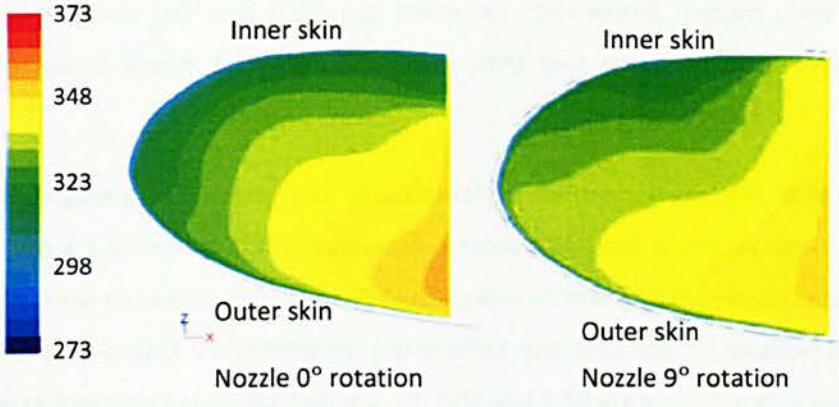

Figure 4.4.20: Air temperature contour (in K) in plane 245° for two different nozzle rotation angles

The result shows that the nozzle rotation towards inner skin enhances SAI thermal performance. T_{ave} increases gradually with nozzle rotation angle till 9°; however, it slightly drops when the nozzle further rotates to reach 13°. As shown in Table 4.4.3, $C_{tem\ deviation}$ and $T_{hi} - T_{lo}$ decrease as *NRA* increases from 0° to 13°. In conclusion, nozzle rotation angle towards inner skin offers good temperature uniformity on the nacelle lip-skin.

4.5 Effect of Nozzle Length on SAI Thermal Performance

Since the jet from the nozzle needs some spaces to mix well with stagnation air in the D-Chamber, alteration of nozzle length changes *Z*. It is logical that shorter nozzle length, as expected, has better anti-icing performance than longer nozzle. Therefore, five different nozzle lengths namely 1-diameter (1d), 1.5-diameter (1.5d), 2-diameter (2d), 2.5-diameter (2.5d) and the original length (3d) for single nozzle with diameter of 9.144mm, have been investigated in this study.

Figure 4.5.1 illustrates the lip-skin temperature contours for five different nozzle lengths in the range of 3×d to 1×d. In Figure 4.5.1, no significant temperature change occurs on the nacelle lip-skin as the nozzle length changes. However, nozzle length has changed the location of hotspot. For nozzle length of 3d to 2d, the hotspot occurs in plane 170° while for nozzle length of 1.5d and 1d, the hotspots occur in plane 169° and 167° respectively. In other words, hotspot plane moves towards nozzle as the nozzle length decreases. Moreover, cold spot occurs in plane 245° for all nozzle lengths.

To further investigate the characteristics of temperature contours, two views have been created as shown in Figure 4.5.3. The lip-skin temperature contours in View 1 are shown in Figure 4.5.2. In Figure 4.5.2, the low temperature area (dark blue area) is shrinking as the nozzle length is shortened; nozzle 3d shows the largest low temperature area while nozzle 1d has the smallest low temperature area. The low temperature areas for nozzle 2.5d, 2.0d and 1.5d are similar to one another. There are no significant effects on hotspots temperature by reducing the nozzle length. Figure 4.5.4 shows that the temperature contours in View 2 for various nozzle lengths are in the range of 3d to 1d. Nozzle 3d produces the largest low temperature area and the nozzle 1.5d produces the smallest low temperature area. Meanwhile for nozzle 1d, the low temperature area diminishes.

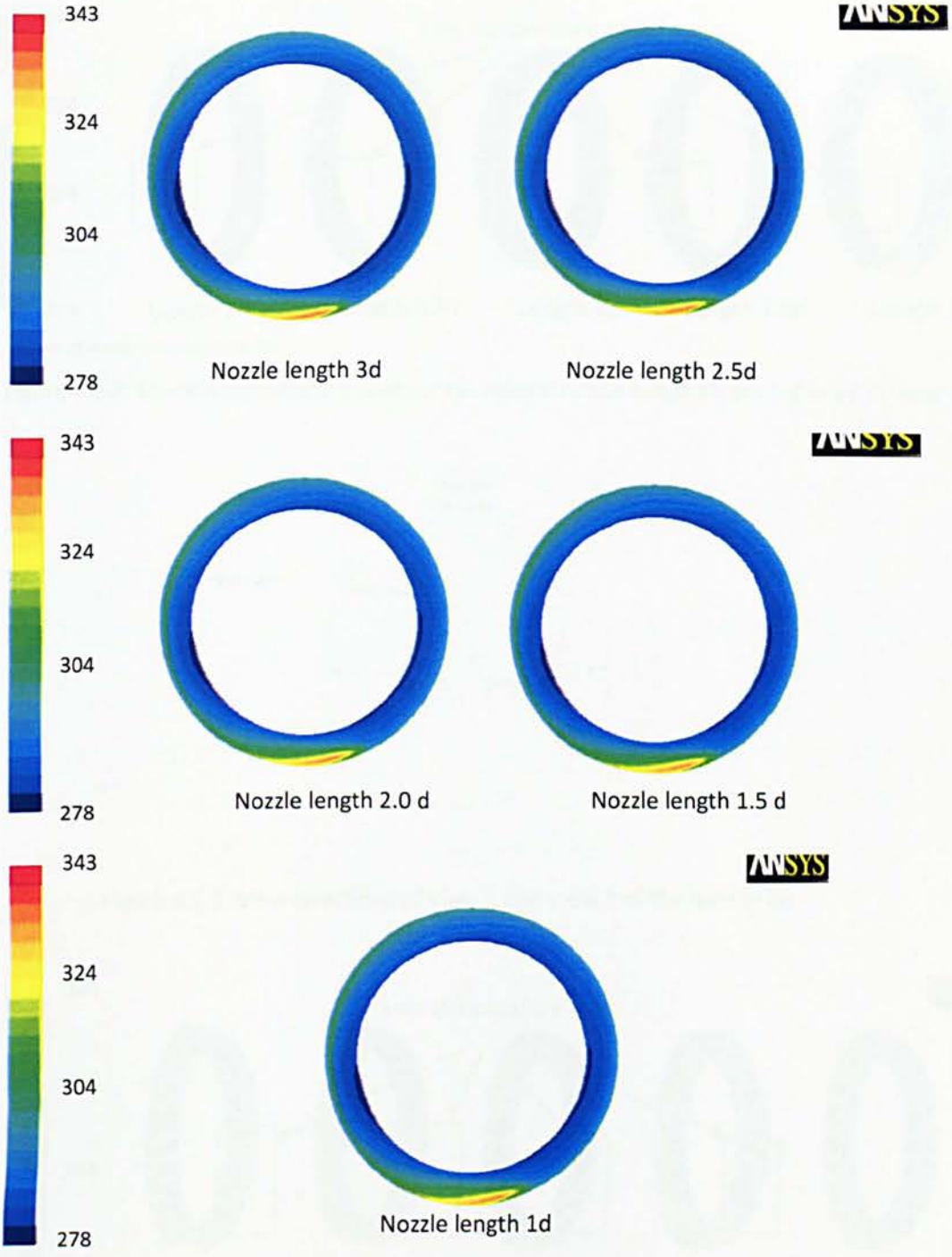

Figure 4.5.1: Lip-skin temperature contour (in K) for several nozzle lengths in the range of d to 3d

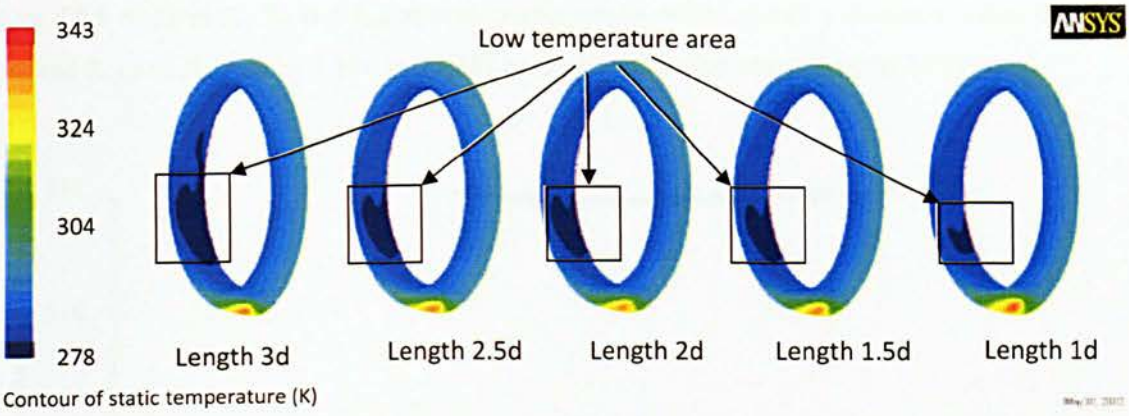

Figure 4.5.2: Lip-skin temperature contour for several nozzle lengths from 1 d to 3d in View 1

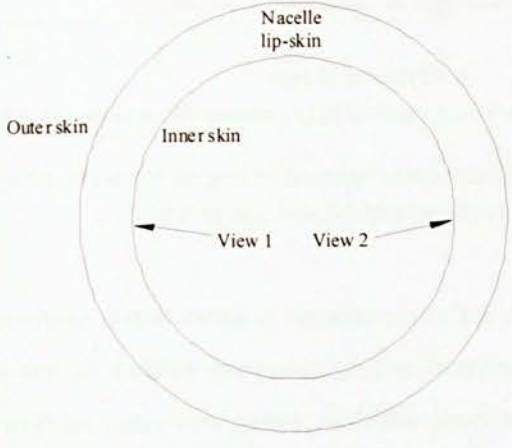

Figure 4.5.3: View directions of View 1 and View 2 of the nacelle lip

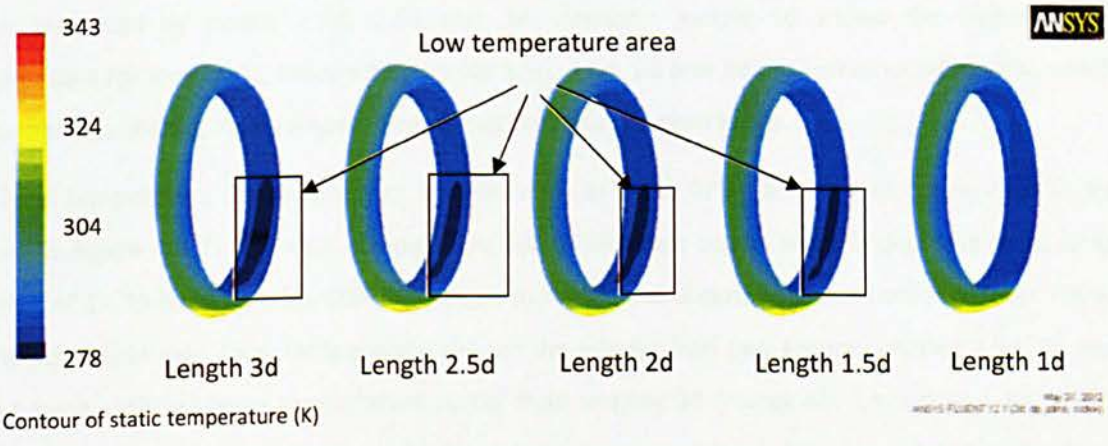

Figure 4.5.4: Lip-skin temperature contour for different nozzle lengths from 1 d to 3d in View 2

Figure 4.5.5 displays T_{hi}, T_{lo} and T_{ave} against nozzle length, which shows a minimum value for T_{hi} at 1.5d, and T_{ave} and T_{lo} drop by 1.15K and 1.38K respectively for the nozzle lengths 1d to 3d.

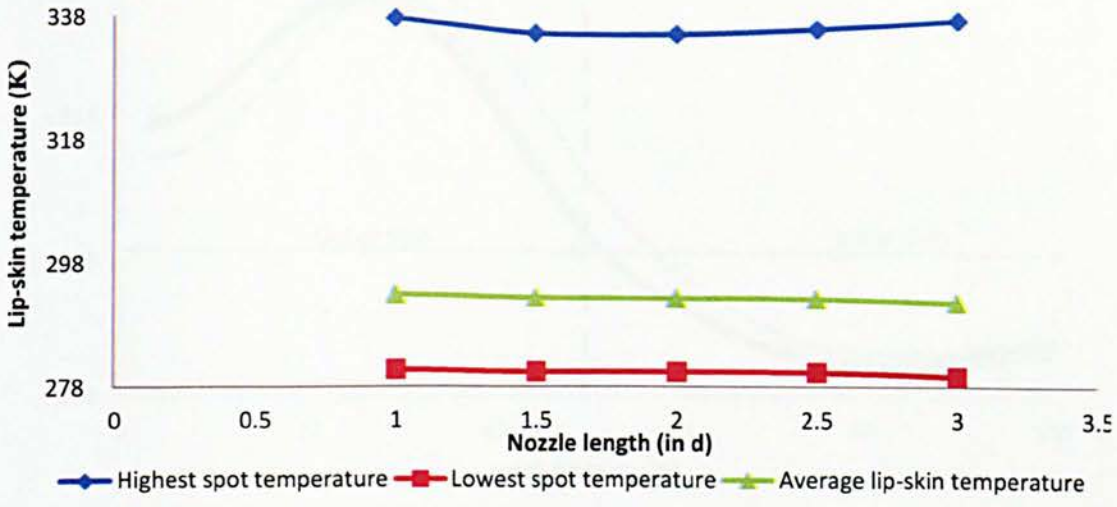

Figure 4.5.5: Effect of nozzle length to hotspot temperature, cold spot temperature and average lip-skin temperature

The lip-skin local temperature distributions in hotspot plane are shown in Figure 4.5.6. In general, the local temperature for all nozzles increases to the maximum thereafter decreases to the minimum and finally increases again very gently, with the wrap location. Along the outer skin, the hotspot happens at wrap location of 30% for nozzle 1d, and at wrap location of 26% for nozzle 3d, 2.5d, 1.5d and 2d. The highest values of T_{hi} are similar for nozzle 1d and 3d which are higher than those produced by nozzle 2.5d, 1.5d and 2d. However, nozzle 1d shows the highest local temperature for inner skin, followed by nozzle 1.5d, 2.5d, 2d and 3d until wrap location 70%, which are undistinguishable; local temperature for nozzle 3d drops even lower.

The local temperature distributions vs. wrap location in plane 270° for different nozzle lengths are shown in Figure 4.5.7. The local temperature for all different nozzle lengths decrease from wrap location of 3% to wrap location 60%, and begin to flatten out almost constant until it reaches 100%. In the outer skin side, local temperature divides the nozzles into two groups; nozzles 2.5d, 2d and 1.5d having slightly higher temperature (1.1K) than nozzles 3d (marginally better) and 1d. In the inner skin side, nozzle 1d has the highest local temperature. Meanwhile, the other nozzles have similar local temperature which is 1K lower than that of nozzle 1d. Besides, nozzle 3d gives the lowest temperatures along the inner skin.

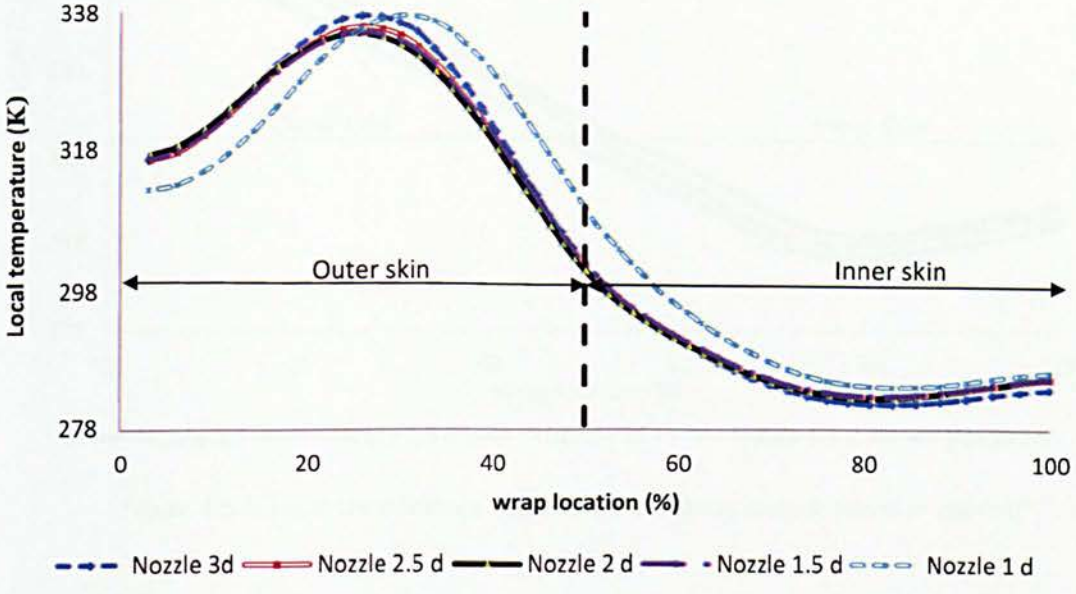

Figure 4.5.6: Local temperature distribution along the wrap location in hotspot plane

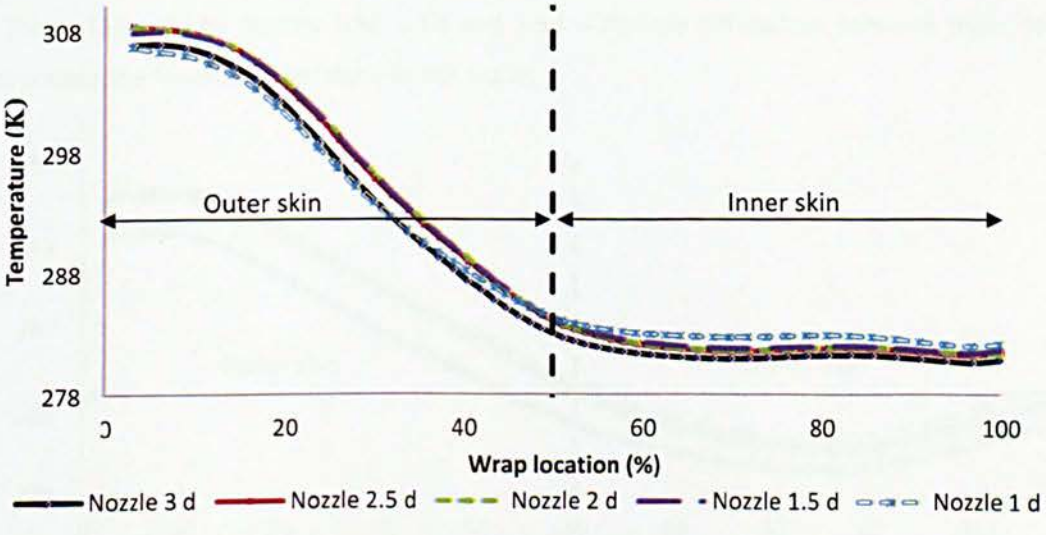

Figure 4.5.7: Local temperature distribution along the wrap location in plane 270°

The lip-skin temperature distributions for different nozzle lengths along nacelle lip-skin in plane 0° are shown in Figure 4.5.8. The lip-skin temperature from wrap location of 3% slightly increases up to the peak at 8.8% whereafter decreases gradually until 76% and finally increases again until 100%. Nozzle 1d shows the highest local temperature and nozzle 3d produces the lowest local temperature, along wrap location. Nozzles 2.5d, 2d and 1.5d show quite similar trends for all wrap locations.

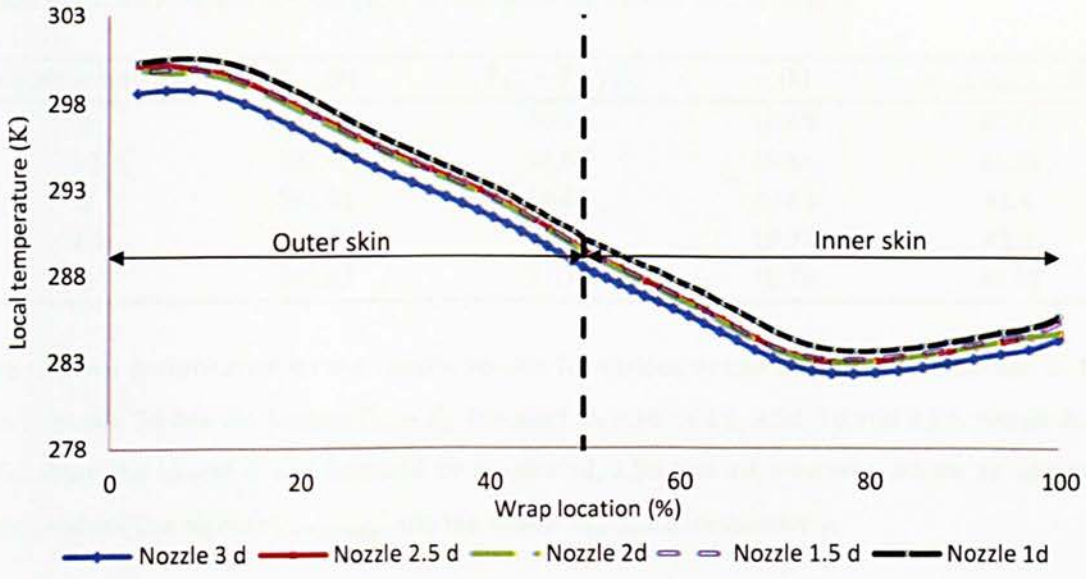

Figure 4.5.8: Local temperature distribution along the wrap location in plane 0°

Figure 4.5.9 illustrates the local temperature distributions in plane 90° for five different nozzle lengths from 1d to 3d. The temperature profiles in Plane 90° are similar to those in plane 0°. Similar to Figure 4.5.8, nozzle 1d shows the highest local temperature for all wrap locations, especially after 72%. This is followed by nozzles 1.5d, 2.0d and 2.5d with little differences between them. Nozzle 3.0d produces the lowest temperature in this plane.

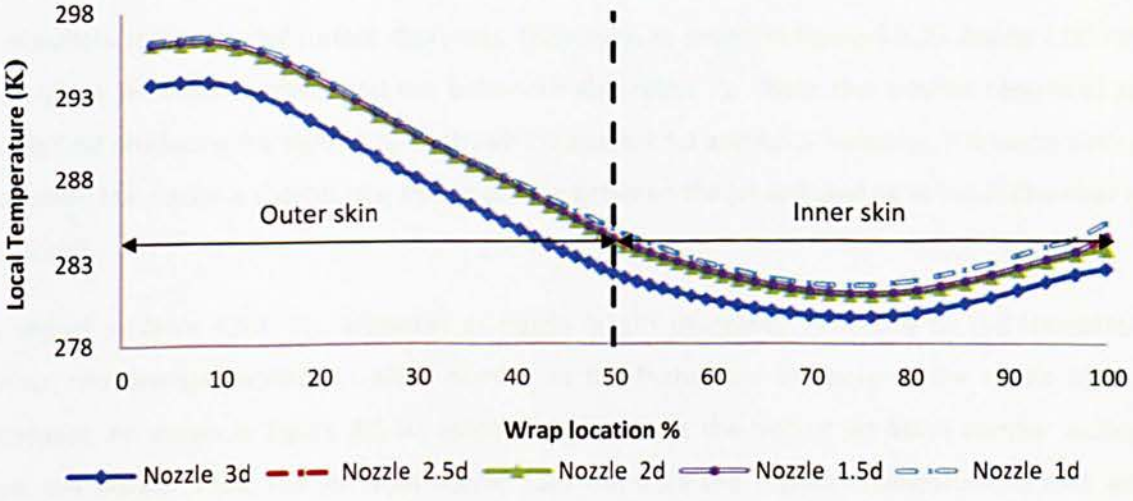

Figure 4.5.9: Local temperature distribution along the wrap location in plane 90°

Table 4.5.1: Summary of temperature uniformities for various nozzle lengths

Nozzle length (d)	T_{ave}(K)	$(T_{hi} - T_{lo})$ (K)	σ (K)	$C_{tem\ deviation}$ (%)
1	292.58	56.75	10.69	40.73
1.5	292.07	54.60	10.63	41.30
2	292.01	54.63	10.63	41.4
2.5	292.01	55.66	10.77	41.9
3	281.43	57.77	10.78	42.91

The thermal performance on the nacelle lip-skin for various nozzle lengths is summarised in Table 4.5.1. Nozzle 3d has the biggest $T_{hi} - T_{lo}$ followed by nozzles 1d, 2.5d, 2d and 1.5d. Nozzle 2d and 1.5d share the lowest σ and followed by nozzles 1d, 2.5d and 3d. However, nozzle 3d and nozzle 1.5d produce the highest $C_{tem\ deviation}$ and the lowest $C_{tem\ deviation}$ respectively.

The results show that the jet of nozzle 1d impinges the outer skin earlier compared to jets from the other nozzles. In fact, the jet from the nozzle outlet seems to be moving towards highlight as nozzle length decreases. As shown in Figure 4.5.10, nozzle 1.0d shows an obvious change of jet direction towards "highlight", followed by nozzle 1.5d. However, the jet from nozzle 2.0d and 2.5d are moving in the same direction with the jet from the nozzle 3.0d. Therefore, hotspots for nozzles 1.0d and 1.5d are located in plane 167° and 169° respectively, while those for the other nozzles are in plane 170°. The jets for nozzle 1.0d and 1.5d change their directions towards "highlight".

As the direction of the jet from nozzle 1.0d deviates towards "highlight", the spacing between nozzle 1.0d outlets and impinging surface decreases. Moreover, as shown in Figure 4.5.10, nozzle 1.0d has the highest jet Mach number, and this behaviour also raises T_{hi}. These two reasons contribute to nozzle 1.0d producing the highest T_{hi}, as shown in Figures 4.5.1 and 4.5.5. However, it is worth noting that when the nozzle is shorter, the mixing activity between the jet and cold air in the D-Chamber is enhanced.

As shown in Table 4.5.1, T_{ave} increases as nozzle length decreases. According to the simulation results, the average swirling air Mach number in the D-chamber increases as the nozzle length decreases. As shown in Figure 4.5.10, nozzle 1.0d produces the highest jet Mach number exiting from the nozzle. Thus, the jet from nozzle 1.0d transfers the highest momentum to cold air. Consequently, nozzle 1.0d produces the highest average swirling air Mach number inside the D-chamber along nacelle lip-skin and 90°, as shown in Figure 4.5.11. This is characterized by the highest lip-skin temperature profile of nozzle 1.0d in 90°, as shown in Figure 4.5.9.

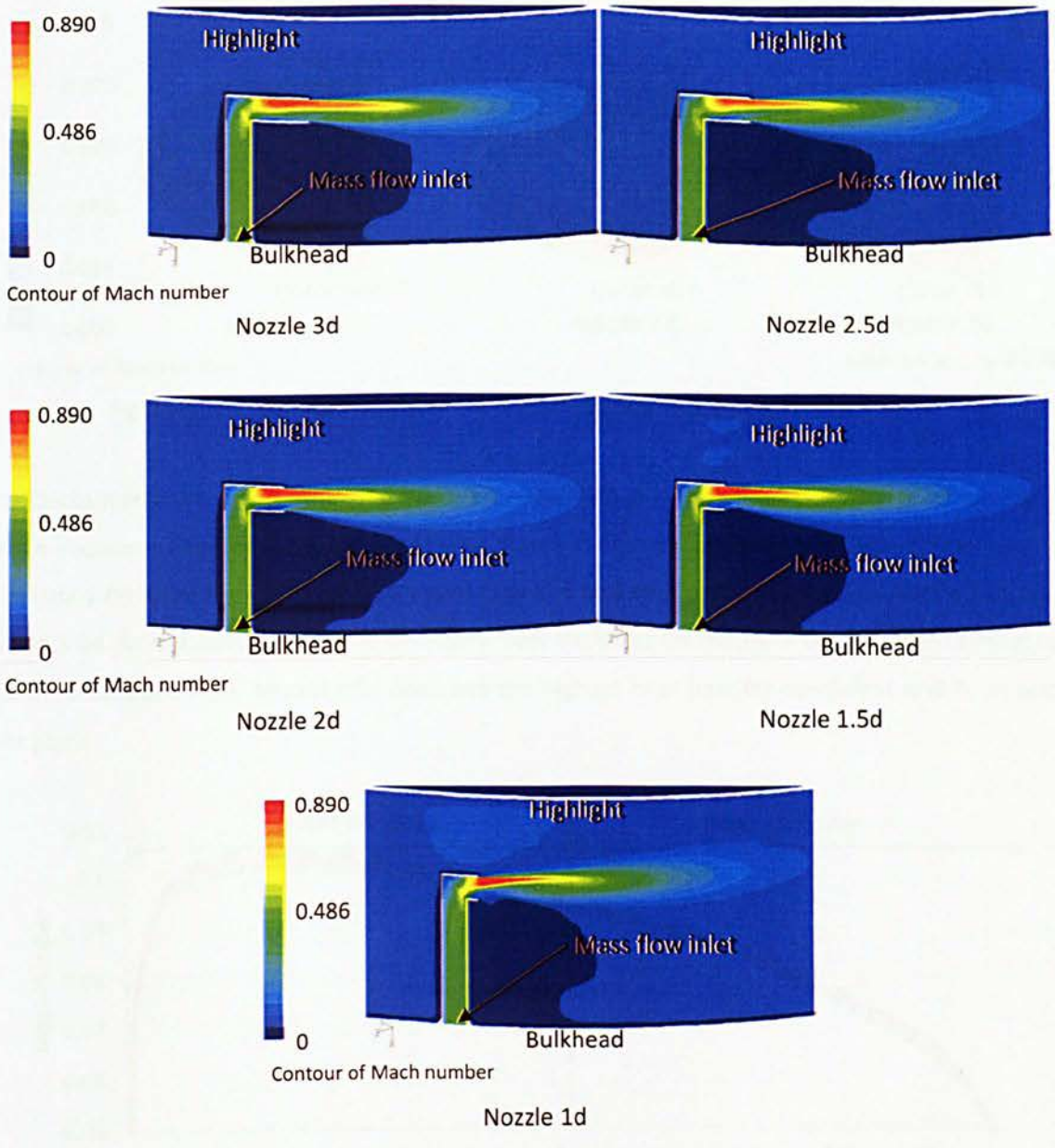

Figure 4.5.10: Mach number contour around nozzle area for various nozzle lengths

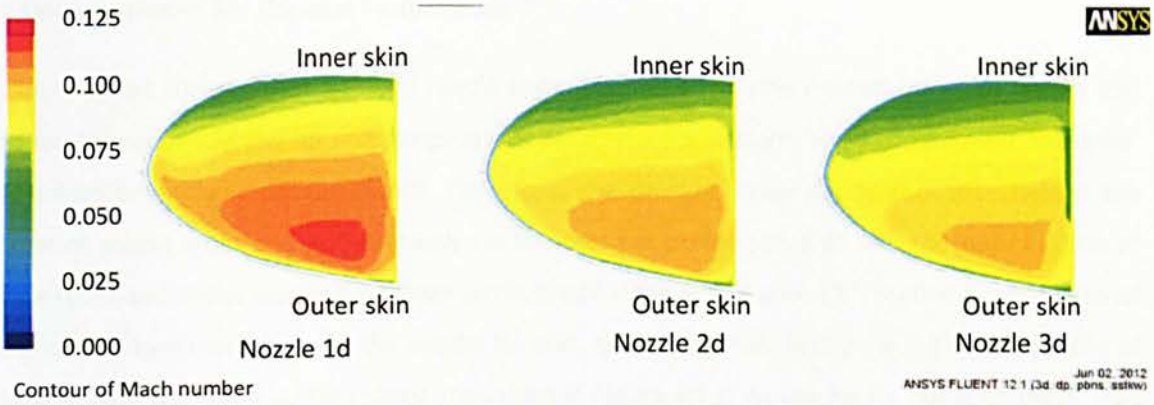

Figure 4.5.11: Air Mach number contour of various nozzle lengths in plane 90°

The low temperature area shrinks and the average swirling air Mach number increases when nozzle length decreases (Figures 4.5.2 and 4.5.4). As shown in Figure 4.5.12, the air Mach number profile of Nozzle 1.0d is the highest along D-chamber-high-1 in cold spot plane, followed by Nozzle 2.0d and Nozzle 3.0d. As discussed before, the boundary layer thickness decreases as the air Mach number or velocity increases. Thus, Nozzle 1.0d produces the highest heat transfer coefficient and T_{lo} in cold spot plane.

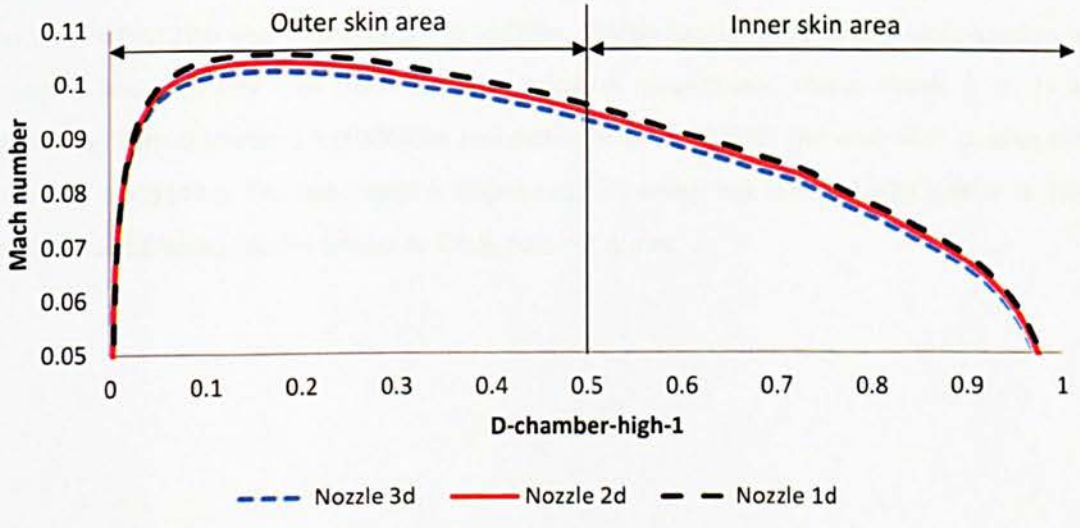

Figure 4.5.12: Air Mach number profile in cold spot plane

The results show that T_{ave}, T_{lo} and T_{hi} increase as nozzle length decreases, as shown in Figure 4.5.5. However, T_{hi} starts to increase when nozzle length is shorter than 1.5d. According to Table 4.5.1, the $C_{tem\ deviation}$ increases as the nozzle length increases. In conclusion, the overall temperature distribution on the nacelle lip-skin becomes less uniform as the nozzle length increases.

4.6 Optimization of SAI Thermal Performance

Section 4.3 has showed that a sloped nozzle enhanced the air mixing process between hot air and cold air. Subsequently, the lip-skin temperature became more uniform and T_{ave} increased. However, this enhancement was not significant. Therefore, the present study has further investigated the effects of nozzle types and outlet shapes on the thermal performance of SAI. The optimization of nozzle types and outlet shapes have been performed for the nozzle with 13° rotation angle due to its best temperature uniformity on the nacelle lip-skin, as evident from Section 4.4. The schematics of various nozzle types and outlet shapes are shown in Figure 4.6.1. As the nozzle outlet changes, that the jet velocity and temperature profile exiting from the nozzle are expected to change. Consequently, the air mixing process between hot air and cold air inside the D-chamber enhances, thereby improving the temperature distribution on the nacelle lip-skin.

Figure 4.6.1 illustrates the nozzle types and outlet shapes under investigation; five different models have been created, namely Circle nozzle, Ellipse nozzle, Ellipse nozzle 1, Ellipse nozzle 2 and Circle nozzle 1. The length for all nozzle types is 0.02667m and the distance from cross-section centre of the nozzle to bulkhead is fixed at 0.05715m. Circle nozzle has circular inlet and outlet, of diameter of 0.009144m. Circle nozzle 1 has circular inlet of diameter 0.009144m and elliptical outlet of diameter 1 = 0.0127m and diameter 2 = 0.00635m. Ellipse nozzle has elliptical cross-section with diameter 1 and diameter 2 of 0.00635m and 0.0127m respectively. Ellipse nozzle 1 starts with elliptical inlet with diameter 1 = 0.00635m and diameter 2 = 0.0127m, and ends with circular outlet of diameter 0.009144m. The last model is Ellipse nozzle 2 which has elliptical inlet similar to Ellipse nozzle inlet and Elliptical outlet similar to Circle nozzle 1 outlet.

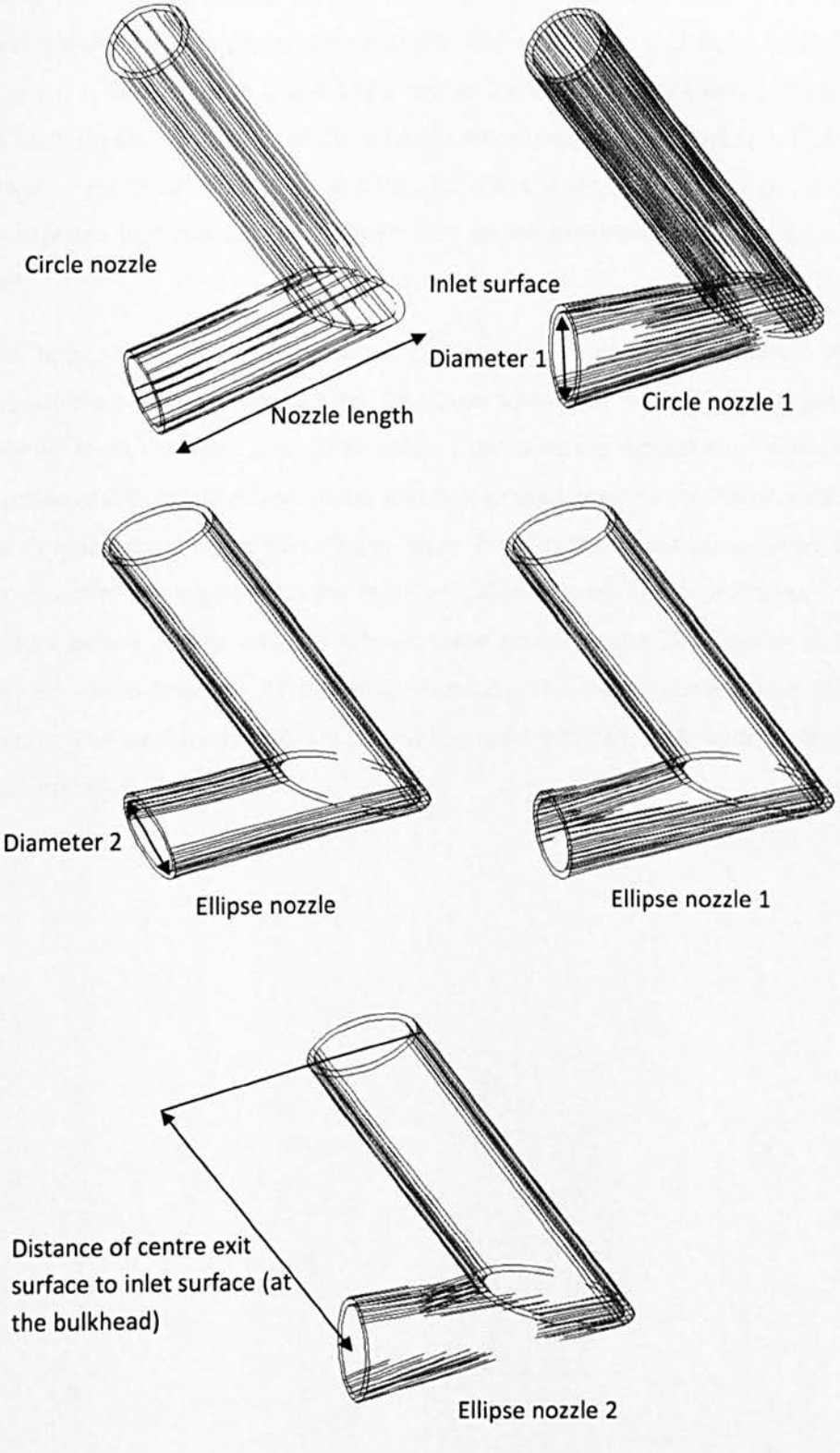

Figure 4.6.1: Schematic illustration of nozzle types and outlets

Figure 4.6.2 shows the lip-skin temperature contour for the five different nozzle types. The hotspots of all nozzle types occur in planes between 193° and 197°. The T_{hi} of Circle nozzle, Ellipse nozzle, Ellipse nozzle 1, Ellipse nozzle 2 and Circle nozzle 1 are 318.89K, 321.04K, 317.43K, 317.03K and 321.02K respectively, while the T_{lo} of Circle nozzle, Ellipse nozzle, Ellipse nozzle 1, Ellipse nozzle 2 and Circle nozzle 1 are 281.95K, 281.85K, 282.51K, 281.69K and 281.75K respectively occurring in planes (area B) between 117° and 122° in the inner skin, except for Ellipse nozzle which has a cold spot in plane 165°.

The local temperature distributions across the wrap location for five different nozzle types in hotspot planes are shown in Figure 4.6.3. All nozzle types have similar local temperature profile in these planes. Along the outer skin, Circle nozzle 1 produces the highest local temperature until the wrap location of 22% where Ellipse nozzle start to produce higher values than the other types at the selected wrap locations. In addition, Ellipse nozzle 2 shows the lowest temperature along the most part of outer skin. While getting to the inner skin, Ellipse nozzle keeps producing the highest local temperature before getting values which are quite similar to the Circle nozzle in the process of reaching 75% wrap location. At the wrap location 75%, every nozzle shows the lowest local temperature. The local temperature is almost the same and hard to be distinguished further from the wrap location of 75%.

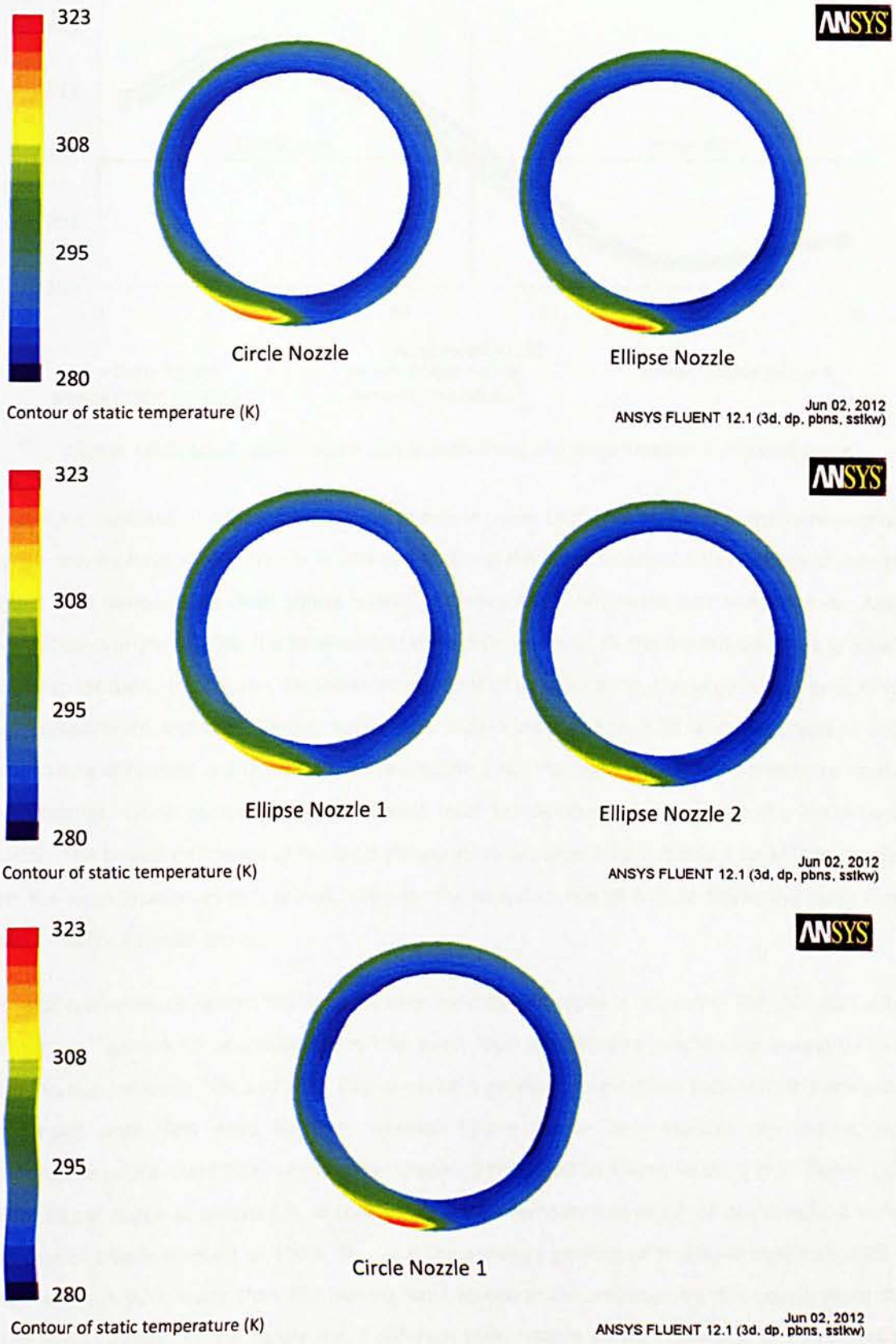

Figure 4.6.2: Temperature contour on the nacelle lip-skin for various nozzle types

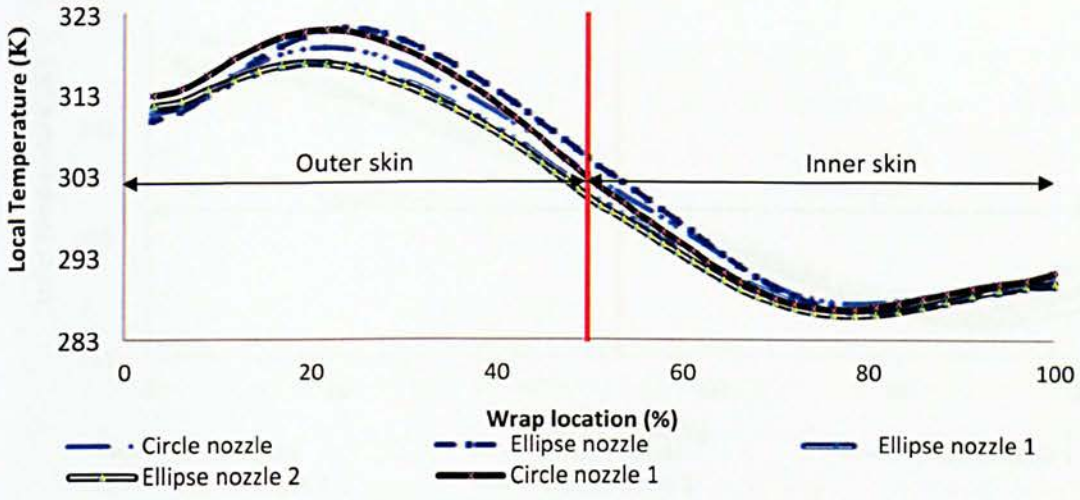

Figure 4.6.3: Local temperature distribution along the wrap location in hotspot plane

Figure 4.6.4 illustrates the local temperature profile in plane 190° after hotspot, which demonstrates that all nozzles have similar trends in this plane. Along the wrap location, Ellipse nozzle shows the highest local temperature while Ellipse nozzle 2 demonstrates the lowest local temperature. Along wrap location of 3% to 80%, the local temperature differences of all the nozzles decrease gradually with wrap location. In addition, for the same segment of wrap location, the largest difference of the local temperature between Ellipse nozzle and Ellipse nozzle 2 is 1.7K and the average local temperature difference is around 0.9K. Ellipse nozzle 1 has the highest local temperature compared other nozzles. Circle nozzle 1 has the lowest local temperature along almost the entire wrap location. The largest difference of the local temperature between Ellipse nozzle 1 and Circle nozzle 1 after the wrap location of 80% is 2.3K. Even for the wrap location of 80% to 100%, the other three nozzles display a similar trend.

The local temperature against the wrap location for different types of nozzles in the cold spot plane is shown in Figure 4.6.5 which illustrates that every local temperature reaches the lowest value at wrap location between 70% and 80%. Ellipse nozzle 1 produces the highest local temperature along the lip-skin until 78% wrap location, whereas Ellipse nozzle demonstrates the lowest local temperature until around 74%. The local temperature produced by Ellipse nozzle 1 is 3K higher than that of Ellipse nozzle at around 6%. In contrast, the local temperature of Ellipse nozzle is 3.6K higher than that of Ellipse nozzle 1 at 100%. The local temperature generated by Ellipse nozzle at 100% is 16.5K which is 0.3K lower than the highest local temperature produced by this nozzle along the entire wrap location. Ellipse nozzle has a different temperature profile compared to the others as the cold spot of this nozzle is located in plane 165°. However, the cold spot of the other nozzles are located in planes between 117° and 122°.

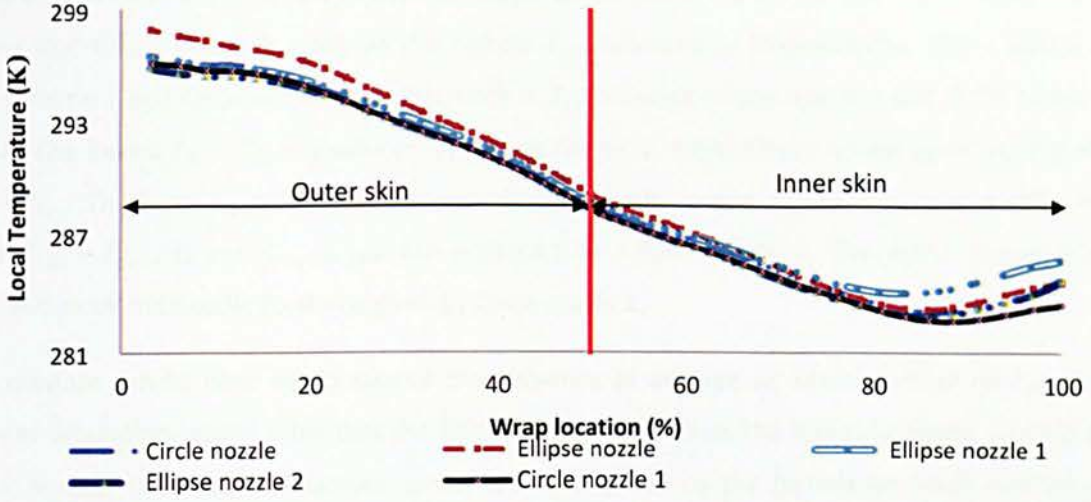

Figure 4.6.4: Local temperature distribution along the wrap location in plane 190° after hotspot

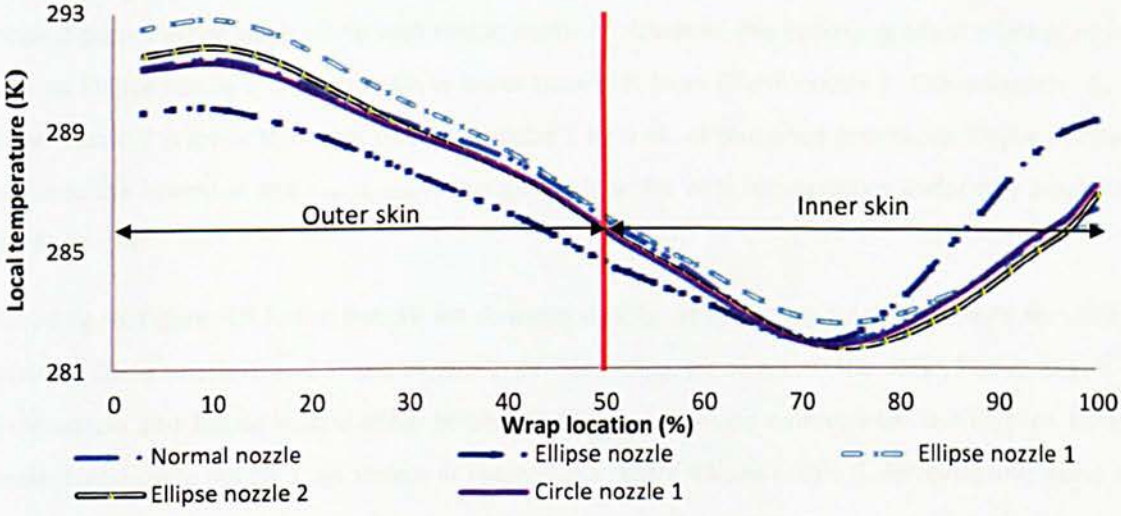

Figure 4.6.5: Local temperature profile along the wrap location in cold spot plane

Table 4.6.1: Summary of temperature uniformity for various nozzle types

Nozzle type	T_{ave} (K)	$(T_{hi} - T_{lo})$ (K)	σ (K)	$C_{tem\ deviation}$ (%)
Circle nozzle	290.98	36.94	7.20	29.21
Circle nozzle 1	291.01	39.31	7.56	30.64
Ellipse nozzle	291.42	39.36	7.60	30.29
Ellipse nozzle 1	291.66	34.54	6.81	26.89
Ellipse nozzle 2	291.03	35.34	6.95	28.14

Table 4.6.1 records the summary of the thermal performances of SAI for the five nozzle types, which shows that Ellipse nozzle 1 produces the highest T_{ave}, followed by Ellipse nozzle, Ellipse nozzle 2, Circle nozzle 1 and Circle nozzle. The difference in T_{ave} between Ellipse nozzle 1 and Circle nozzle is 0.68K. The lowest $T_{hi} - T_{lo}$ is produced by Ellipse nozzle 1, while Ellipse nozzle gives the highest $T_{hi} - T_{lo}$. The $T_{hi} - T_{lo}$ difference between Ellipse nozzle 1 and Ellipse nozzle is 4.82K. The lowest $T_{hi} - T_{ave}$, σ and $C_{tem\ deviation}$ are produced by Ellipse nozzle 1. The worst temperature distribution on the nacelle lip-skin is given by Circle nozzle 1.

The previous results have demonstrated the influence of average air Mach number on T_{ave}. The present simulation results show that the Ellipse nozzle 1 produces the highest average swirling air Mach number inside the D-chamber, which is characterized by the highest jet Mach number as shown in Figures 4.6.6 and 4.6.7. Therefore, Ellipse nozzle 1 produces the highest T_{ave}.

Ellipse nozzle 2 provides the lowest T_{hi} among all of the nozzles. According to the results, T_{hi} of Ellipse nozzle 2 occurs in the same plane with Ellipse nozzle 1. However, the impinging Mach number of hot air from Ellipse nozzle 2 on outer skin is lower than that from Ellipse nozzle 1. Consequently, T_{hi} of Ellipse nozzle 2 is lower than that of Ellipse nozzle 1 by 0.4k, as discussed previously. Ellipse nozzle 1 produces the lowest σ and $C_{tem\ deviation}$, thus generating the best temperature uniformity along the nacelle lip-skin.

According to Figure 4.6.6, the hot air jet diverges widely while exiting from the nozzle for Ellipse nozzle 2, Circle nozzle 1 and Ellipse nozzle 1, in front view. However, in top view, Ellipse nozzle 1, Circle nozzle and Ellipse nozzle show better air divergence while exiting from outlet than Ellipse nozzle 2 and circle nozzle 1, as shown in Figure 4.6.7. Since Ellipse nozzle 1 demonstrates good air divergence in both views, it transfers the highest amount of momentum and heat to the cold air in the D-Chamber. As a result, the lip-skin temperature generated by Ellipse nozzle 1 is the most uniformly distributed over the nacelle lip-skin, for these five designs.

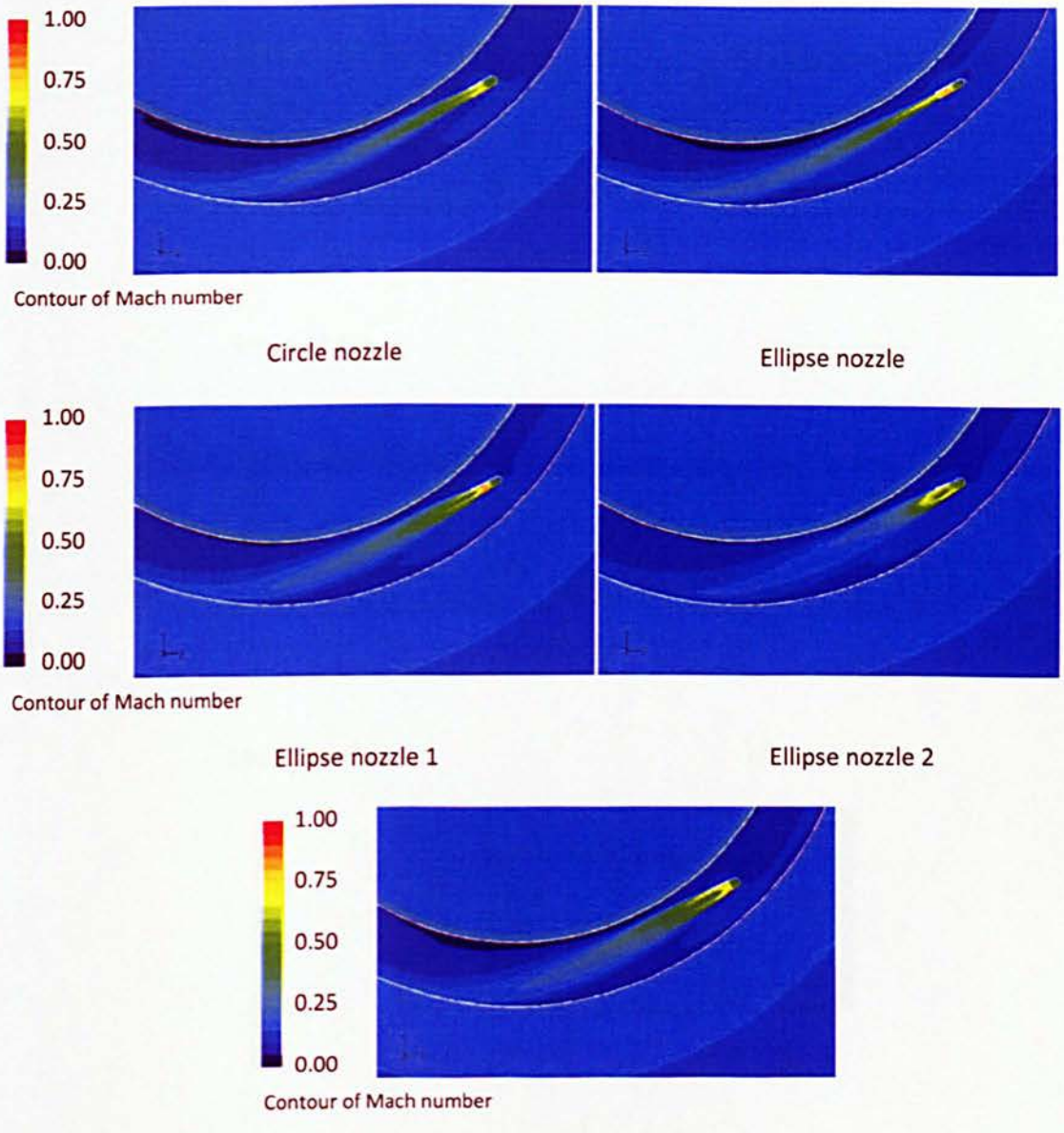

Figure 4.6.6: Air Mach number contour at nozzle vicinity in front view

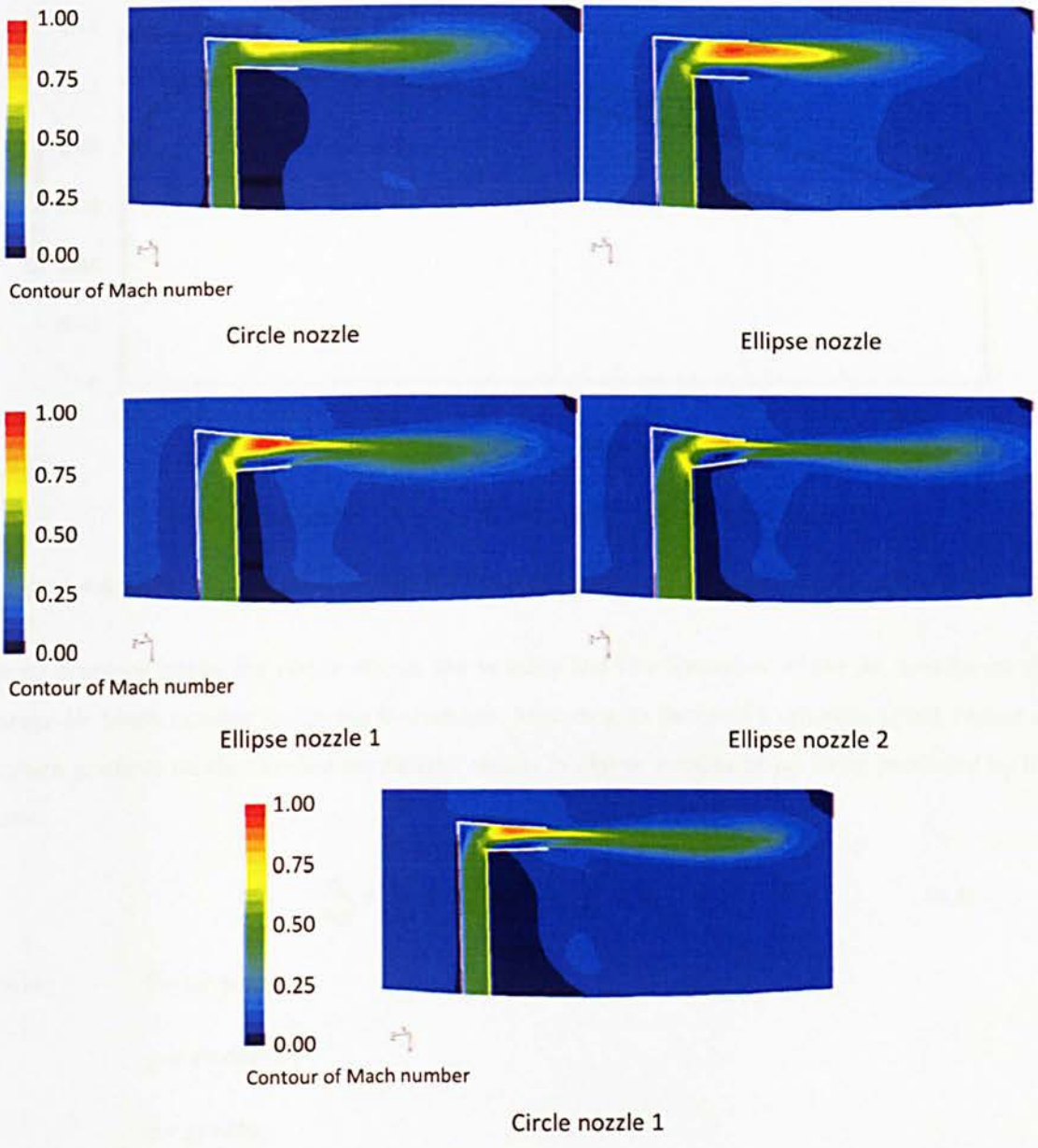

Figure 4.6.7: Air Mach number contour inside nozzle for various nozzle types in top view

Figure 4.6.8 illustrates the air Mach number profile for three different nozzle designs in cold spot plane. The position of line D-chamber-high-1 is shown in Figure 4.3.13. As Ellipse nozzle 1 provides the highest Mach number along D-chamber-high-1, it produces the highest average swirling air Mach number inside D-chamber, followed by Circle nozzle 1 and Circle nozzle. Therefore, Ellipse nozzle 1 produces the thinnest boundary layer thickness in cold spot plane. Consequently, the cold spot plane of Ellipse nozzle receives the highest heat from the nozzle, thereby providing the highest T_{lo} in the present SAI system for all nozzles.

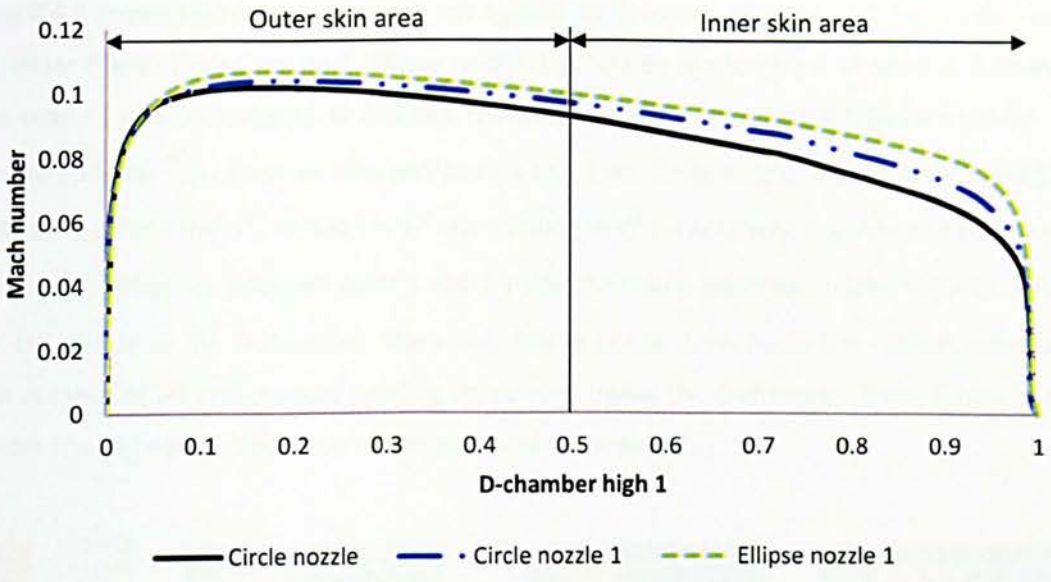

Figure 4.6.8: Air Mach number profile for three different nozzle designs in cold spot plane

The air pressure inside the nozzle affects the velocity and Mach number of the jet, and hence the average air Mach number inside the D-chamber. According to Bernoulli's equation [106], higher air pressure gradient on the far side nozzle wall results in higher velocity of jet being produced by the nozzle.

$$\frac{P_1}{\rho_1 g} + \frac{u_1^2}{2g} + \dot{z}_1 = \frac{P_2}{\rho_2 g} + \frac{u_2^2}{2g} + \dot{z}_2 \qquad (4.4)$$

where P = air pressure

ρ = air density

g = gravity

$\dot{z}$= elevation head

In this study, points 1 and 2 in Figure 4.6.9 have almost the same elevation head and gravity since the altitude of points 1 and 2 are the same (ground condition). Therefore, $\dot{z}$ and g are cancelled. Meanwhile, the velocity at point 1 is almost 0 due to the turning corner of the nozzles. Thus, Bernoulli's equation becomes:

$$\frac{P_1}{\rho_1} - \frac{P_2}{\rho_2} = \frac{u_2^2}{2} \qquad (4.5)$$

Figure 4.6.9 shows that Circle nozzle has the highest air pressure (P) at point 1 and Circle nozzle 1 has similar P with Ellipse nozzle 1. Ellipse nozzle 1 produces the lowest P at point 2, followed by Circle nozzle 1 and Circle nozzle. In addition, the air densities for all of nozzle types are similar. Thus, the differences in $^{P}/_{\rho}$ of hot air between point 1 and 2 for Circle nozzle, Circle nozzle 1 and Ellipse nozzle 1 are 58'800 $(m/s)^2$, 61'532 $(m/s)^2$ and 66'500 $(m/s)^2$ respectively. According to Equation 4.5, a higher $^{P}/_{\rho}$ difference between point 1 and 2 inside the nozzle generates higher velocity of jet out from the nozzle to the D-chamber. Therefore, Ellipse nozzle 1 produces the highest velocity and Mach number of jet and average swirling air velocity inside the D-chamber. Thus, Ellipse nozzle 1 provides the highest T_{ave} and Circle nozzle produces the lowest T_{ave}.

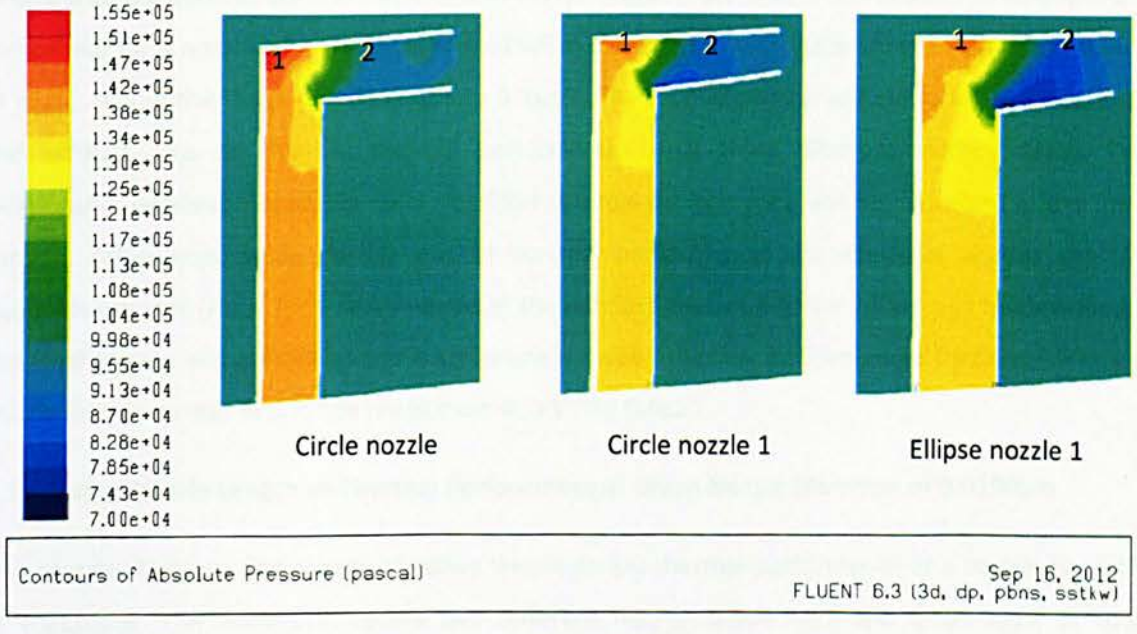

Figure 4.6.9: Air pressure contour inside nozzles

The results in this study demonstrate that the nozzle type affects the thermal performance of SAI. The nozzle type influences hot air pressure inside the nozzle, thus affecting the average air velocity, Mach number inside the D-chamber and eventually, T_{ave} of the nacelle lip-skin. In addition, the shape of nozzle outlet alters the air mixing process between hot air and cold air, as shown in Figures 4.6.6 and 4.6.7. In fact, Ellipse nozzle 1 has the most uniform temperature distribution along the nacelle lip-skin due to the better divergence of exit jet compared to other nozzles. However, the manufacturing and geometric complexities of Ellipse nozzle make it unfeasible for the SAI system. Therefore Circle nozzle has been chosen for the remaining part of this research, as will be elaborated in the next chapter as requested by Bombardier Aerospace.

CHAPTER 5: Larger Nozzle of SAI Thermal Performance

Chapter 5 examined the thermal performances of SAI, including hotspot temperature (T_{hi}), cold spot temperature (T_{lo}), average lip-skin temperature (T_{ave}) and temperature uniformity, for three different nozzle diameters, 0.0127m, 0.01905m and 0.0254m. The first section of this chapter discusses the effects of nozzle length on the thermal performance of swirl anti-icing at given nozzle diameter of 0.01905m. This is because the simulation on small nozzles crashed when $m_{hot\ air}$ increased beyond 0.04536kg/s with a nozzle diameter of 0.01905m utilized, instead of small nozzle with diameter of 0.009144m. The reason for the crash is that the hot air pressure gradient at the impinging surface could reach extremely high value in simulations at $m_{hot\ air}$ of 0.04536kg/s, which happened to the nozzle with diameter of 0.0127m at $m_{hot\ air}$ of 0.07257kg/s. Therefore, in this chapter simulations are performed for a nozzle with diameter of 0.01905m in order to investigate SAI thermal performance at $m_{hot\ air}$ within the range of 0.0118kg/s to 0.2kg/s. The second section will elaborate the effects of the exhaust area on the SAI thermal performance using three different exhaust areas. The relationship between nozzle diameters and SAI thermal performance will be described in the third section. Afterwards, some correlations of thermal performance characteristics against the SAI Reynolds number (Re_{sw}) for a small nozzle at the exhaust area of $4.210 \times 10^{-3} m^2$ will be developed. The final section will elaborates the correlations between thermal performances for three different nozzle diameters and Re_{sw} in the range from 4.1×10^4 to 5.4×10^5.

5.1 Effect of Nozzle Length on Thermal Performance at Given Nozzle Diameter of 0.01905m

This section discusses the effects of nozzle length on SAI thermal performance at a nozzle diameter of 0.01905m. The discussion covers two different $m_{hot\ air}$; 0.059 kg/s and 0.109 kg/s, at total temperature of hot air within nozzle (T_{nozzle}) of 533K. In studying a small nozzle, a shorter nozzle enhances the thermal performance of SAI. However, in the case of a nozzle diameter of 0.01905m, the position of hotspot plane on the nacelle lip-skin surface is changed. This phenomenon occurs because that the distance between nozzle and impinging spot (Z) increases from 0.187m to 0.2m as the nozzle diameter changes from 0.009144m to 0.01905m. This may affect the pattern of thermal performance, leading to the alteration of the anti-icing efficiency. Moreover, in order to avoid the clashing of the nozzle to the outer skin of the nacelle, the distance from cross section centre of the nozzle to bulkhead was fixed at 0.04763m, as shown in Figure 5.1.1. Under these conditions, the study investigates the effect of nozzle length on the thermal performance of nacelle lip-skin at the given nozzle diameter of 0.01905m.

Similar issues were discussed in Chapter 4. Nozzle 2d, which represents the nozzle length, is equal to two times nozzle diameter, and shows the best thermal performance without changing hotspot and cold spot locations. For this reason, two different nozzle lengths; 0.05715m (nozzle 3d, represent nozzle length=3×diameter) and 0.0381m (nozzle 2d), will be examined in this section. The heat transfer characteristics studied in this section included $T_{hi.}$, $T_{lo.}$, temperature contour, temperature profiles on the nacelle lip-skin at given planes, T_{ave}, σ and $C_{tem\ deviation}$. The dimensions of nozzle 3d and nozzle 2d are shown in Figure 5.1.1:

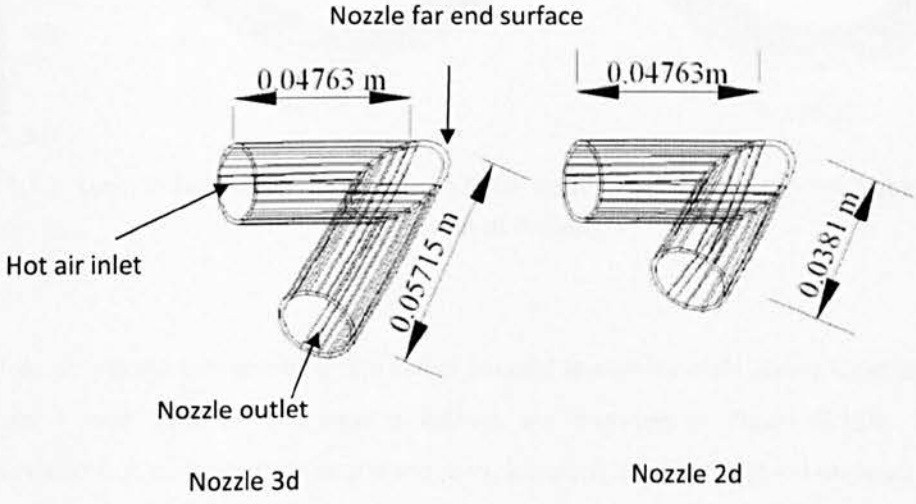

Figure 5.1.1: Dimension of nozzle 3d and nozzle 2d

Figure 5.1.2 illustrates that the lip-skin temperature contour for two different nozzle lengths, 2d and 3d, at $m_{hot\ air}$ of 0.059 kg/s. As per the figure, there are no significant differences on the nacelle lip-skin as the nozzle length changes. Hotspots of both nozzles occur in plane 178° as shown in the figure. As expected, T_{hi} of nozzle 2d is 411.7K and 0.9K lower than T_{hi} of nozzle 3d because that Z of nozzle 3d is shorter than Z of nozzle 2d. Because of the longer distance, nozzle 2d produces more heat and momentum exchanges between hot air and cold air inside the D-chamber. Then, when the hot air from nozzle 2d impinges on outer skin surface, the temperature and momentum are lower than those of the hot air from nozzle 3d.

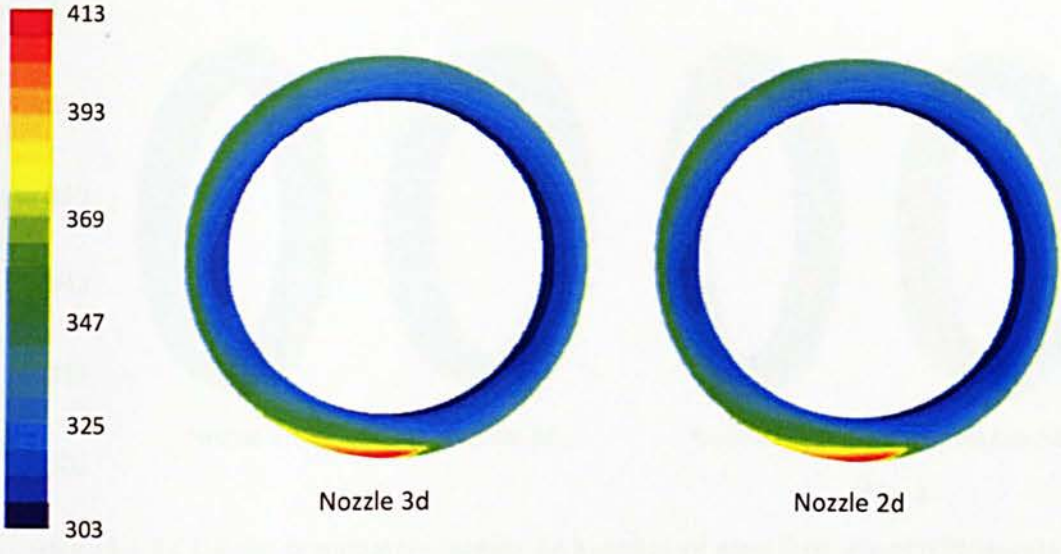

Figure 5.1.2: Lip-skin Temperature contour (in K) for both nozzle lengths (2d and 3d) at hot air mass flow rate of 0.059kg/s

Figure 5.1.3a shows the temperature contour of nacelle lip-skin for both nozzle lengths at different views, View 1 and View 2. The view directions are depicted in Figure 5.1.3b. Overall, the temperature contour of nozzle 3d is nearly the same as nozzle 2d. As shown in the figure, T_{lo} for both nozzles occur in plane 122°; which marked by L at View 2. According to the result, nozzle 2d has T_{lo} of 304K; which is 0.2K higher than that of nozzle 3d. That is because the distance Z of nozzle 2d is longer than that of nozzle 3d, mixing hot air from the jet with the cold air in the D-chamber is better in the sense of heat and momentum transfer for nozzle 2d than nozzle 3d. As a result, when swirling air reaches the cold spot, it has a higher temperature and Mach number for nozzle 2d than for nozzle 3d.

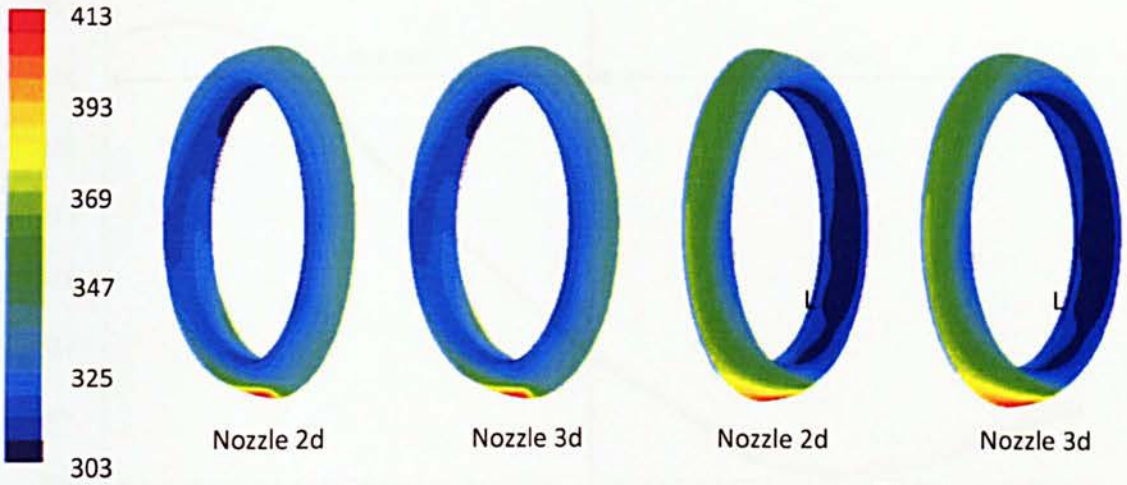

Figure 5.1.3a: Lip-skin temperature contour (in K) at hot air mass flow rate of 0.059kg/s in View 1 and View 2

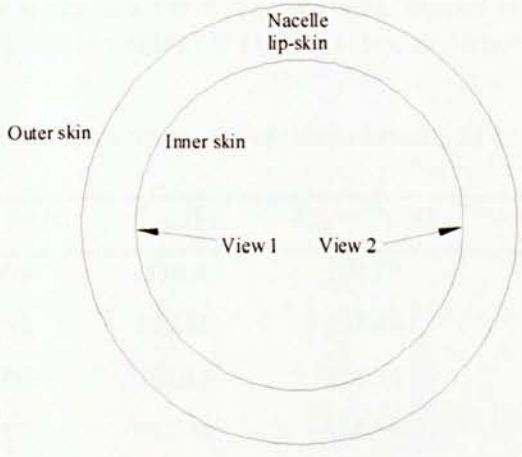

Figure 5.1.3b: View directions of View 1 and View 2 in the nacelle lip-skin

Figure 5.1.4 shows the local temperature profile across wrap location in both nozzle lengths; 2d and 3d, in planes 90°. The figure shows that the nozzle 3d and nozzle 2d have similar temperature trend. As shown in the figure, the local temperature in plane 90° decreases gradually with wrap location from 0% to 74%. Then, the local temperature increases slowly against wrap location until the wrap location reaches 100%. The figure also shows that nozzle 3d has a lower local temperature than nozzle 2d in the inner skin, especially after the wrap location of 75%. That occurs because of nozzle 2d has higher swirling air Mach number adjacent to inner skin than nozzle 3d. The phenomenon implies that the hot jet of nozzle 2d transfers more momentum to cold air than the hot jet of nozzle 3d.

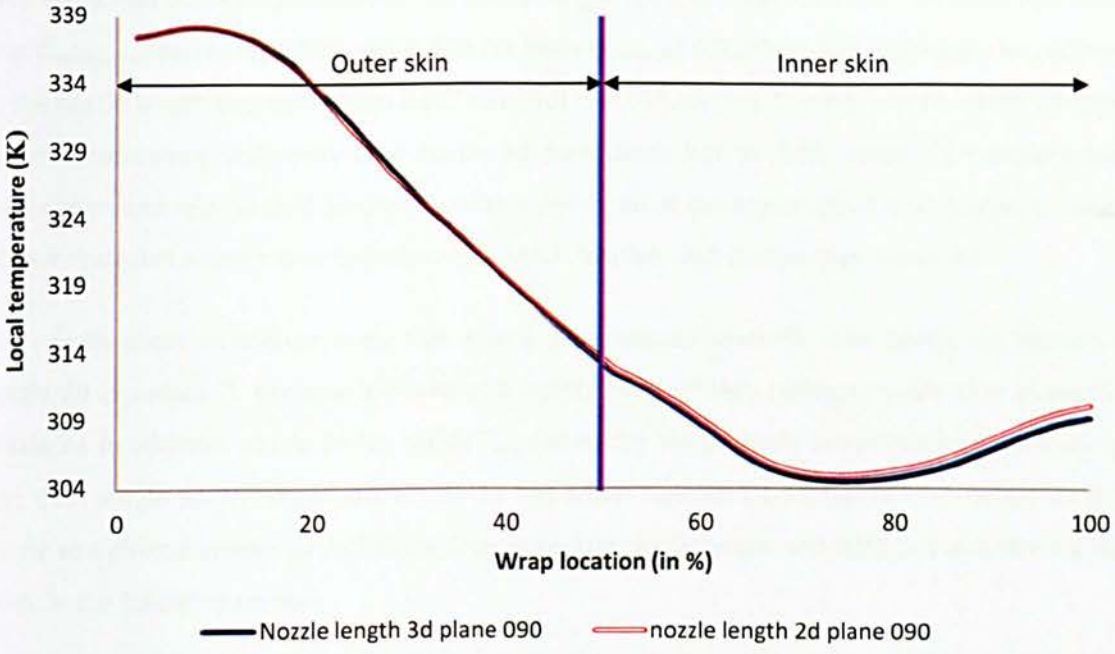

Figure 5.1.4: Local temperature profile across wrap location in the nacelle lip-skin in plane 90° for both nozzle lengths (2d and 3d) at hot air mass flow rate of 0.059kg/s

Table 5.1.1: Summary of thermal performance of Nozzle lengths 3d and 2d

Nozzle Length	$m_{hot\ air}$ (kg/s)	T_{ave}(K)	$T_{hi} - T_{lo}$(K)	σ (K)	$C_{tem\ deviation}$ (%)
3d	0.059	330.3	108.63	21.03	32.95
2d	0.059	330.55	107.48	20.76	32.40
3d	0.109	361.19	114.74	22.82	24.10
2d	0.109	361.44	114.66	22.59	23.79

Table 5.1.1 records a summary of the thermal performance for nozzle 3d and nozzle 2d. According to the table, T_{ave} for both $m_{hot\ air}$; 0.059 kg/s and 0.109 kg/s, increase slightly by 0.35K and 0.25K respectively, as the nozzle length reduces from 3d and 2d. This is due to nozzle 2d having higher average Mach number of swirling air and a higher heat transfer coefficient inside D-chamber than nozzle 3d. The table also shows that T_{ave} increases with $m_{hot\ air}$ for both nozzle lengths. As $m_{hot\ air}$ increases, the heat and momentum supplied to the cold air inside D-chamber increases. Subsequently, the heat transfer from swirling air in D-chamber to nacelle lip-skin increases with $m_{hot\ air}$. As a result, T_{ave} increases with $m_{hot\ air}$ as shown in the table. The table also shows that the nozzle length 2d has lower $T_{hi} - T_{lo}$ than nozzle length 3d for both $m_{hot\ air}$ of 0.059 kg/s and 0.109 kg/s by 1.15K and 0.08K respectively. As a result, both σ and $C_{tem\ deviation}$ also decrease as the nozzle length decreases, as shown in the table. According to the table, σ for $m_{hot\ air}$ of 0.059kg/s and 0.109kg/s

drop 0.27K and 0.23K respectively as the nozzle length reduces from 3d to 2d. The table also shows that $C_{tem\ deviation}$ decreases 0.59% and 0.32% for both $m_{hot\ air}$ of 0.059 kg/s and 0.109 kg/s, respectively, as the nozzle length decreases from 0.05715m (3d) to 0.0381m (2d). In other words, nozzle 2d shows better temperature uniformity than nozzle 3d does. Since hot air from nozzle 2d transfers more momentum and heat to cold air than that from nozzle 3d at the beginning of mixing process, nozzle 2d demonstrates a uniform temperature and Mach number distribution than nozzle 3d.

The results abovementioned show that nozzle 2d produces lower T_{hi} than nozzle 3d. Moreover, nozzle 2d increases T_{lo} because it produces a higher hot air Mach number in cold spot plane than nozzle 3d. In addition, nozzle 2d has higher T_{ave} and better temperature uniformity on the nacelle lip-skin than nozzle 3d. In conclusion, nozzle 2d has better thermal performance than nozzle 3d for a nozzle at a given diameter of 0.01905m. Therefore, the nozzle length of 0.0381m is used for the next study in the following section.

5.2 Effect of Exhaust Area to Thermal Performance Anti-Icing System

It is believed that the exhaust area has influences over SAI thermal performance. As the exhaust area decreases, the air pressure increases. Then the density and temperature of air change, affecting the swirling air velocity/Mach number and flow resistance. These explained that the air pressure in D-chamber and exhaust area affect the thermal performance of SAI. Moreover, the pressure difference between hot air in nozzle and swirling air in D-chamber decrease with air pressure increases in D-chamber. Thus, the jet Mach number exiting from nozzle decreases which affects the thermal performance characteristics. Therefore, the effects of three different exhaust areas; $1.263 \times 10^{-3}m^2$, $2.105 \times 10^{-3}m^2$ and $4.210 \times 10^{-3}m^2$, on the SAI thermal performance at given nozzle diameter of 0.01905m will be described in this section. To simplify discussion, the exhaust area of $4.210 \times 10^{-3}m^2$ is denoted as Model A, while, Model B and Model C represent an exhaust area of $2.105 \times 10^{-3}m^2$ and $1.263 \times 10^{-3}m^2$, respectively. Similar to section 5.1, $m_{hot\ air}$, 0.059 kg/s and 0.109 kg/s, are used in this section. These parameters are used to describe SAI thermal performances including T_{hi}, T_{lo}, temperature contour, T_{ave}, σ and $C_{tem\ deviation}$.

Figure 5.2.1 displays the lip-skin temperature contour for three different exhaust areas at the nozzle diameter of 0.01905m. $m_{hot\ air}$ and T_{nozzle} in Figure 5.2.1 are 0.109 kg/s and 533K respectively. According to the figure, no significant differences in lip-skin temperature contour are shown in the figure by decreasing the exhaust area from $4.210 \times 10^{-3}m^2$ to $1.263 \times 10^{-3}m^2$. The figure shows that

all Models, A, B and C, have T_{hi} at plane 178°. The T_{hi} for models A, B and C are 443.7K, 440.7K and 440.5K, respectively.

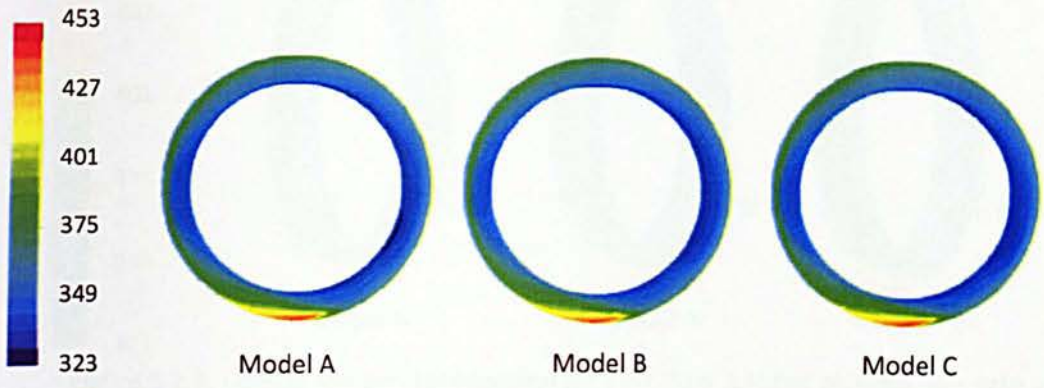

Figure 5.2.1: Lip-skin temperature contour (in K) for three different exhaust areas

Figure 5.2.2 shows the lip-skin temperature contours in View 1. As shown in Figure 5.2.2, temperature at the low temperature area circled as A increases as the exhaust area decreases. Figure 5.2.3 illustrates that the lip-skin temperature contours in View 2, especially T_{lo} of all Models A, B and C, occur in Plane 122° or in Circle B. In this view, the temperature of cold spot vicinity indicated by Circle B increases as the exhaust area decreases from $4.210 \times 10^{-3} m^2$ to $2.105 \times 10^{-3} m^2$. Then, the temperature in Circle B seems to experience a slight temperature drop as the exhaust area decreases further to $1.263 \times 10^{-3} m^2$. According to these results, Model B produces the highest T_{lo}, which are 3.1K and 1.0K higher than T_{lo} of Model A and Model C, respectively.

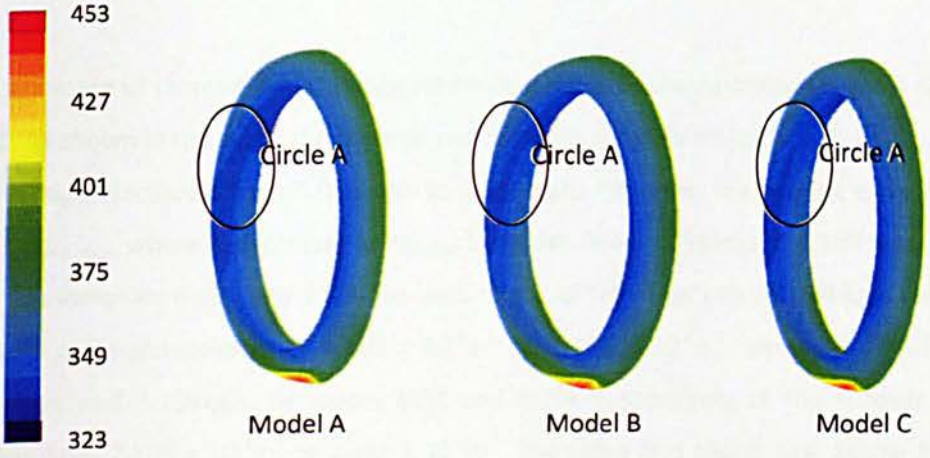

Figure 5.2.2: Lip-skin temperature contour (in K) in View 1 at hot air mass flow rate of 0.109kg/s

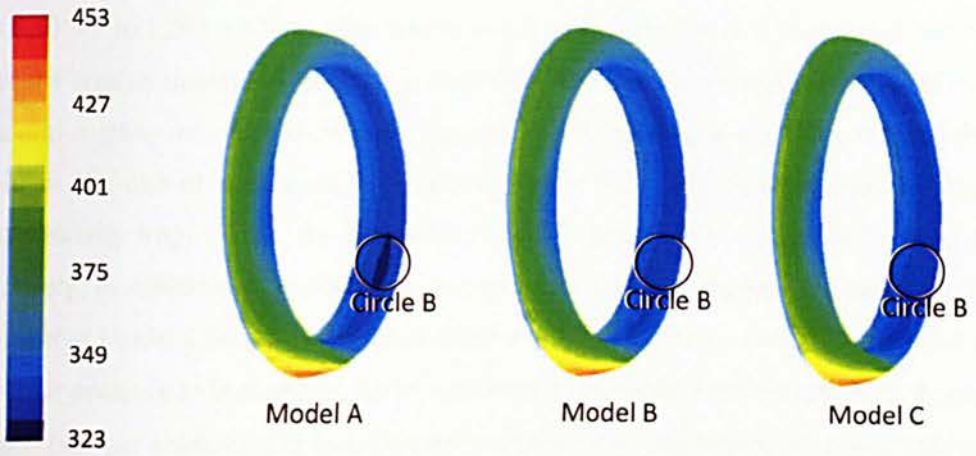

Figure 5.2.3: Lip-skin temperature contour (in K) in View 2 at hot air mass flow rate of 0.109kg/s

Table 5.2.1: Summary of thermal performance of Nozzle length 3d and Nozzle length 2d

Model of Exhausts area	$m_{hot\ air}$ (kg/s)	T_{ave} (K)	(T_{hi}-T_{lo}) (K)	σ (K)	$C_{tem\ deviation}$ (%)
Model A	0.059	330.55	107.48	20.76	32.40
Model B	0.059	331.48	105.05	20.42	31.42
Model C	0.059	330.98	107.09	20.70	32.09
Model A	0.109	361.44	114.66	22.59	23.79
Model B	0.109	363.02	111.05	22.03	22.82
Model C	0.109	362.79	113.23	22.23	23.08

The summary of thermal performance for three different exhaust areas has been recorded in Table 5.2.1. As shown in the table, the thermal performance characteristics, T_{ave}, $T_{hi} - T_{lo}$, and σ, increase as the $m_{hot\ air}$ increases from 0.059 kg/s to 0.109 kg/s. However, the reverse effect has been shown for $C_{tem\ deviation}$, where it decreases as $m_{hot\ air}$ increases from 0.059kg/s to 0.109 kg/s. The table shows that T_{ave} increases 0.93K and 1.58K for both $m_{hot\ air}$ of 0.059 kg/s and 0.109 kg/s respectively as the exhaust area decreases from 4.210 x 10^{-3}m^2 to 2.105 x 10^{-3}m^2. However, T_{ave} for both $m_{hot\ air}$, 0.059kg/s and 0.109kg/s, decreases 0.5K and 0.23K respectively as the exhaust area decreases further from 2.105 x 10^{-3}m^2 to 1.263 x 10^{-3}m^2. The table also shows that Model B has the lowest $T_{hi} - T_{lo}$ for both $m_{hot\ air}$, which followed by Model C and Model A. Model B has the lowest σ and $C_{tem\ deviation}$ and Model A produces the highest σ and $C_{tem\ deviation}$ as shown in Table 5.2.1. For both $m_{hot\ air}$, Model A demonstrates the worst thermal performance while Model B demonstrates the best thermal performance.

According to these results, T_{hi} decreases from 443.7K to 440.5K as the exhaust area decreases from $4.210 \times 10^{-3}m^2$ to $1.263 \times 10^{-3}m^2$. That happens due to air pressure in D-chamber is inversely related to exhaust area as shown in Figure 5.2.4. Therefore, the pressure difference between hot air inside nozzle and swirling air inside D-chamber decreased with exhaust area, which reduces the jet Mach number at the exit of the nozzle as shown in Figure 5.2.5. The result shows that the jet Mach number exiting from nozzle for Model A = 1.340, Model B = 1.338, and Model C = 1.319, respectively. In addition, flow resistance increases as the air pressure increases. Therefore, it is believed that Model C has the highest jet Mach number reduction along Z, since it has the highest swirling air pressure in D-chamber, which is followed by Model B and Model A. As a result, the hot air Mach number gradient and heat transfer coefficient on the impinging surface decrease as the exhaust area decreases. Consequently, T_{hi} decreases as the exhaust area decreases from $4.210 \times 10^{-3}m^2$ to $1.263 \times 10^{-3}m^2$.

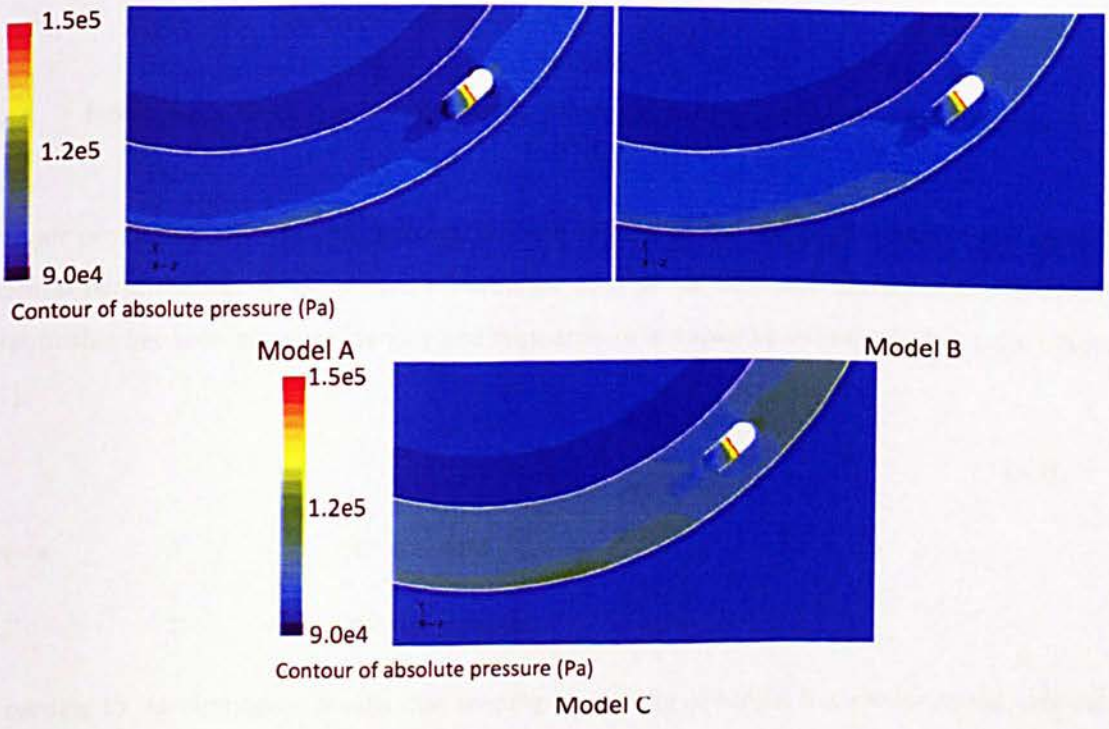

Figure 5.2.4: Air pressure contour for Models A, B, and C at hot air mass flow rate of 0.109kg/s

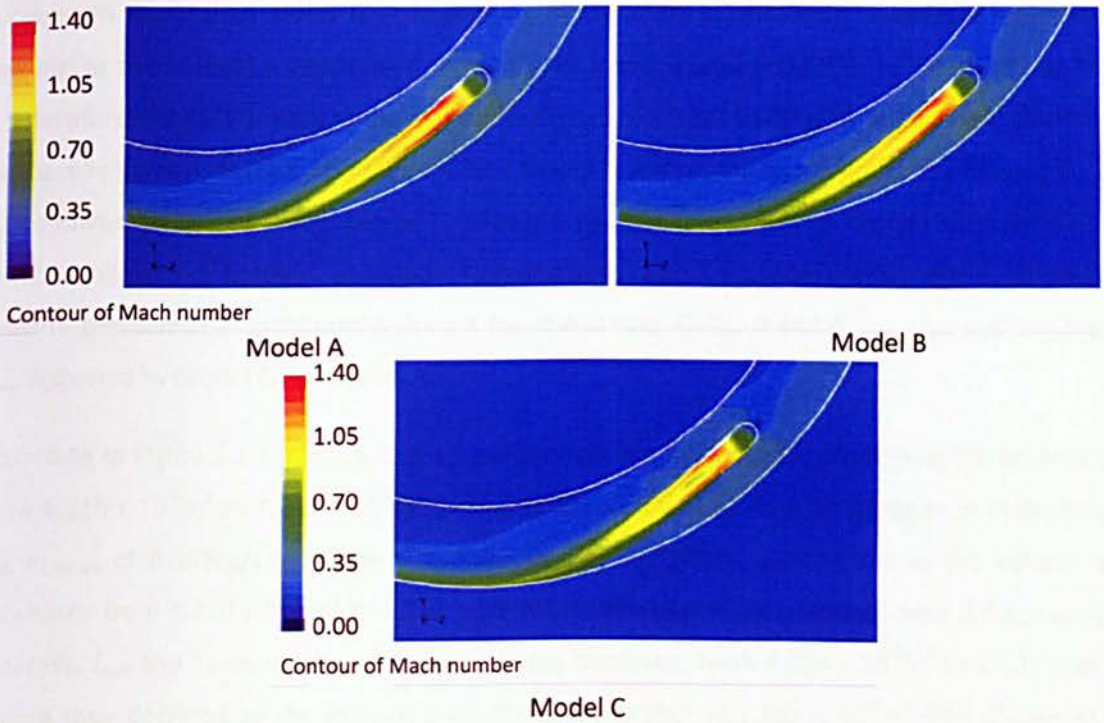

Figure 5.2.5: Mach number contour for Models A, B, and C at hot air mass flow rate of 0.109kg/s

Two air properties, density and temperature, are related to the effect of exhaust area on the SAI thermal performance. As air pressure increases, both air density and temperature increase. The relationship between pressure, density and temperature is shown by the equation of state (Equation 5.1):

$$P = \rho RT \tag{5.1}$$

where R = air constant

T = air temperature

According to the simulation results, the swirling air density of Model B is similar to the swirling air density of Model A. Then, the alteration of pressure drop from Model A to Model B is not very small and not significant. Therefore, Model B has average swirling air Mach number similar to that of Model A due to $m_{hot\ air}$ of both models are same. Instead of that, Model B has a higher average temperature of swirling air in the D-chamber than Model A. As the exhaust area decreases further, the average density of swirling air increases from 0.869kg/m^3 to 0.889kg/m^3. According to Darcy-Weisbach equation, fluid density, hydraulic diameter of tube, fluid flow rate and tube length are the parameters affect on head loss and pressure drop inside tube [116]. Thus, the swirling air pressure drop increases from Model B to Model C. As a result, Model C produces average swirling air Mach

number 8% lower than Model B. Furthermore, Model C has slightly lower average temperature of swirling air than Model B which even shows higher average temperature of swirling air than Model A. Therefore, Model B produces the highest heat transfers from swirling air inside the D-chamber to the nacelle lip-skin; followed by Model C and Model A, which demonstrated by the highest T_{ave} and T_{lo}, followed by Model C and Model A. Model B has the most uniform temperature distribution, which is followed by Model C and Model A. In addition, Table 5.2.1 shows that Model B has the most uniform temperature distributions since it has the lowest T_{hi}-T_{lo}, σ and $C_{tem\ deviation}$, and the highest T_{ave}, followed by Model C and Model A.

According to Figure 5.2.1 to 5.2.5, there is no dramatic improvement by decreasing the exhaust area from 4.210 x $10^{-3}m^2$ to 1.263 x $10^{-3}m^2$. However, the absolute swirling air pressure in D-chamber at the $m_{hot\ air}$ of 0.059kg/s increases tremendously from 97'200Pa to 99'900Pa as the exhaust area decreases from 4.210 x $10^{-3}m^2$ to 1.263 x $10^{-3}m^2$. T_{hi} decreases when exhaust area is decreasing, in contrast, T_{ave} and T_{lo} increase as the exhaust area decreases from 4.210 x $10^{-3}m^2$ to 2.105 x $10^{-3}m^2$ before they decrease as the exhaust area decreases further to 1.263 x $10^{-3}m^2$. The change of the heat transfer performance with number of exhausts is from low to high then lower down, means there may be a maximum there. In conclusion, Model B produces the best thermal performance as per Figure 5.2.1 to 5.2.5, followed by Model C and Model A, so Model B is used in following study.

5.3: Effect of Nozzle Diameter on the Thermal Performance of SAI

The effect of nozzle diameters on SAI thermal performance will be analysed in this section. At any given $m_{hot\ air}$, T_{hi} is expected to decrease with nozzle diameter because that the hot air Mach number gradient on the impinging surface is inversely related to nozzle diameter. Moreover, T_{lo} and T_{ave} are expected to decrease with nozzle diameter since the hot air of smaller nozzle transfers higher momentum to cold air in D-chamber. For these reasons, the nozzle diameter seems to have tremendous effect on the thermal performance of SAI. Therefore, the study investigates the effect of 3 different nozzle diameters; 0.0127m, 0.01905m and 0.0254m on the thermal performance of SAI. Two different $m_{hot\ air}$, 0.04536kg/s and 0.059kg/s at T_{nozzle} of 533K are employed in this investigation. Since exhaust area of 2.105 x $10^{-3}m^2$ shows the best thermal performance, therefore, this exhaust area has been used in this section. T_{hi}, T_{lo}, T_{ave}, lip-skin temperature contour, σ and $C_{tem\ deviation}$ are used to represent the thermal performance characteristics and are studied in this section.

Figure 5.3.1 shows the lip-skin temperature contours for three different diameters at the $m_{hot\ air}$ and T_{nozzle} of 0.04536 kg/s and 533K respectively. The hotspot occurs in plane 178° for nozzles with

diameter 0.0127m and 0.01905m, and in plane 175° for nozzle 0.0254m. The figure shows that there is significant deterioration of thermal performance occurring on the nacelle lip-skin as nozzle diameter increases. The result shows that T_{hi} are 393.33K, 398.73K and 402.4K for nozzle with diameter 0.0127m, 0.01905m, and 0.0254m, respectively.

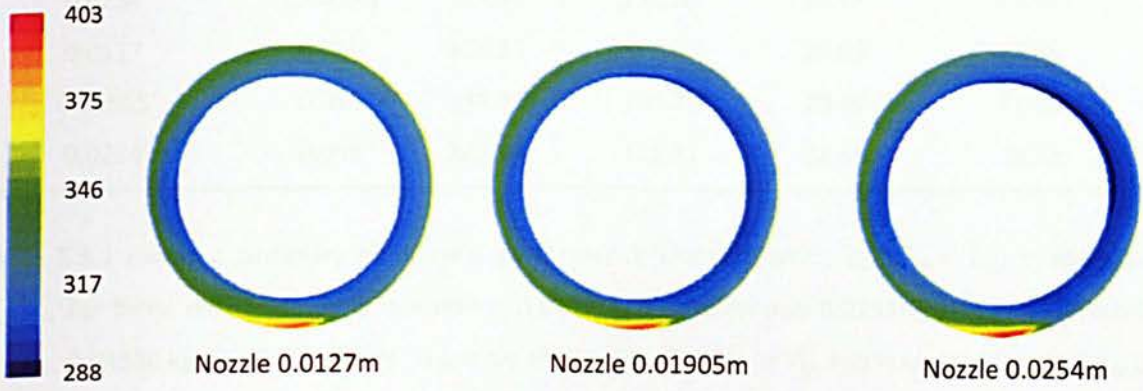

Figure 5.3.1: Lip-skin Temperature contour (in K) for various nozzle diameters at hot air mass flow rate of 0.04536kg/s

Figure 5.3.2 shows lip-skin temperature contours for different nozzle diameters at two different views, View 1 and View 2. In View 1, the figure shows that the inner skin temperature inside rectangle A increases with nozzle diameter. However, the temperature in rectangle B decreases with nozzle diameter. Thereafter, nozzle 0.0127m has the highest temperature on outer skin in rectangle C, which is followed by Nozzles 0.01905m and 0.0254m. The figure also shows that nozzle 0.0127m has the highest lip-skin temperature in View 2 on both inner and outer skins, which is followed by Nozzle 0.01905m and Nozzle 0.0254m. T_{lo} for these three Nozzles with diameter 0.0127m, 0.01905m, and 0.0254m are 301.78K, 290.75K, and 279.37K respectively.

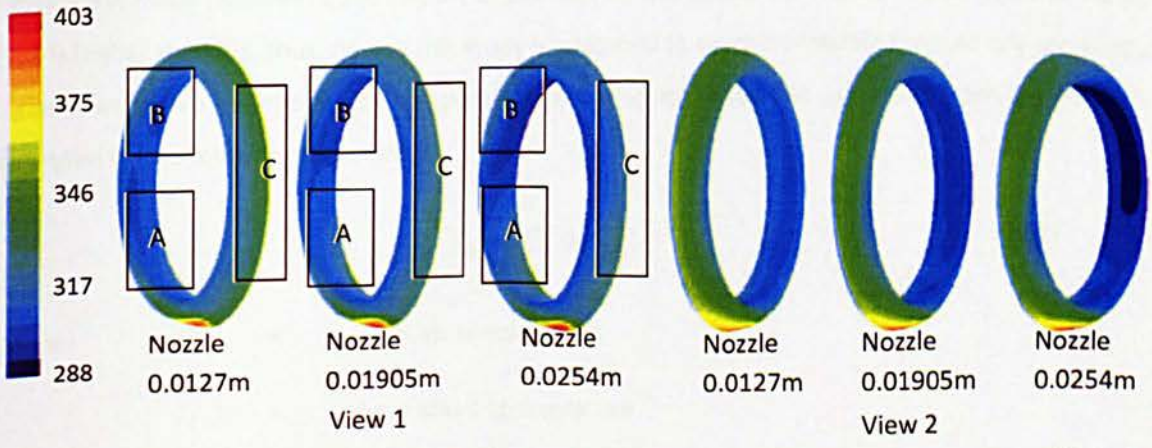

Figure 5.3.2: Lip-skin temperature contour (in K) for various nozzle diameters in View 1 and View 2 at hot air mass flow rate of 0.04536kg/s

Table 5.3.1: Summary of temperature uniformity on the nacelle lip-skin

Nozzle diameter (m)	$m_{hot\ air}$ (kg/s)	T_{ave}(K)	$T_{hi} - T_{lo}$(K)	σ (K)	$C_{tem\ deviation}$ (%)
0.0127	0.04536	324.04	91.55	18.24	31.61
0.01905	0.04536	320.01	100.89	19.03	35.45
0.0254	0.04536	317.37	111.65	20.17	39.52
0.0127	0.059	335.13	97.8	19.85	28.85
0.01905	0.059	331.33	104.72	20.42	31.42
0.0254	0.059	322.98	116.31	22.60	39.92

Table 5.3.1 shows a summary of thermal performance characteristics, T_{ave}, $T_{hi} - T_{lo}$, σ and $C_{tem\ deviation}$, for three different nozzle diameters; 0.0127m, 0.01905m and 0.0254m, and two different $m_{hot\ air}$; 0.04536 kg/s and 0.059 kg/s. The table shows that T_{ave}, $T_{hi} - T_{lo}$ and σ increase as the $m_{hot\ air}$ increases for any nozzle diameter. However, $C_{tem\ deviation}$ shows an opposite trend, inversely related to $m_{hot\ air}$. At the given $m_{hot\ air}$, nozzle 0.0127m has the highest T_{ave}, which is followed by nozzle 0.01905m and 0.0254m. The highest $T_{hi} - T_{lo}$ is produced by nozzle 0.0254m and followed by nozzle 0.01905m and then 0.0127m. The lowest σ and $C_{tem\ deviation}$ are shown by nozzle 0.0127m, followed by nozzle 0.01905m and finally nozzle 0.0254 for both $m_{hot\ air}$ of 0.04536kg/s and 0.059kg/s.

In contrast to the behaviour of hot air Mach number, the results show that the smaller nozzle has a lower T_{hi} at hotspot than the larger nozzle. The heat supplied to SAI system is defined as:

$$Q_{inlet} = m_{hot\ air} c_p T_{nozzle} \tag{5.2}$$

Where Q_{inlet} = heat supplied to SAI

The highest Mach number of the hot air at the exit of the nozzle for different diameters in Figure 5.3.3 is higher than 0.3, thus, flow in this study is assumed to be compressible flow. At any given $m_{hot\ air}$, the relationship between static temperature and velocity of the hot air exiting from the nozzle is expressed by the following equation:

$$T_0 = T_s + \frac{u_y^2}{2C_p} \tag{5.3}$$

Where T_0 = total air temperature

T_s = local static temperature

Since the heat and total temperature at the nozzle inlet surface for all nozzle diameters at the given mass flow rate are the same, nozzle 0.0127m produces the lowest static temperature exit from nozzle in Figure 5.3.4, followed by nozzles 0.01905m and 0.0254m. It has long been known that the boundary layer thickness and temperature gradient within laminar sub-layer influences the heat transfer coefficient on the surface [115]. Although nozzle 0.0127m has thinner boundary layer thickness due to higher air Mach number gradient on the impinging surface, the static temperature of air in the vicinity of impinging surface is lower than the static temperatures for nozzles 0.01905m and 0.0254m. Thus, the temperature gradient within laminar sub-layer underneath turbulent flow for nozzle 0.0127m is lower than the temperature gradients within laminar sub-layer underneath turbulent flow for nozzles 0.01905m and 0.0254m. This is a reason for nozzle 0.0127m to be producing lower T_{hi} than nozzle 0.01905m and 0.0254m. The relationship between heat flux and swirling air temperature gradient within laminar sub-layer underneath turbulent flow is expressed by Equation 2.2:

$$q = -k_f \frac{dT}{dy} \tag{2.2}$$

Another reason is that the ratio of distance between the nozzle and impinging spot to nozzle diameter (Z/d) of nozzle 0.0127m is much larger than Z/d of nozzle 0.01905m and 0.0254m. In fact, the Z values of all nozzles in Figure 5.3.4 is approximately 0.22m. Therefore, Z/d of nozzle 0.0127m is 17.3, which is followed by nozzle 0.01905m (11.5) and nozzle 0.0254m (8.7). Raghunathan et al. [39] mentioned that the optimum heat transfer rate on the impingement surface occurs when Z/d in the range of 5 to 7. Then, the heat transfer rate decreases when the Z/d larger than 7. In addition, at any given air velocity and temperature, Chan et al. [56] revealed that the local heat transfer characteristic decreases as Z/d beyond 8. Nozzle 0.0254 m has Z/d of 8.7; which is the nearest to the optimum value of Z/d. The nozzle 0.0127m should have the lowest T_{hi} in this study due to its highest Z/d; this is coincident with results being published by other researchers on PTAI system, which should be justified for explaining the phenomena around SAI hotspots.

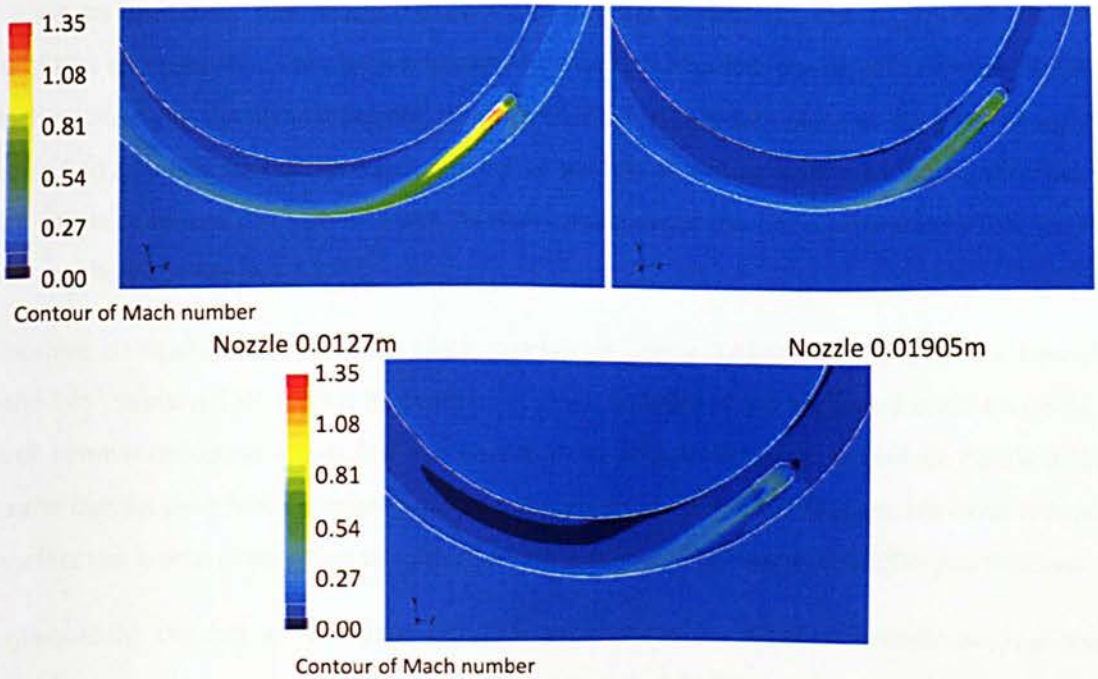

Figure 5.3.3: Air Mach number contour inside D-chamber at hot air mass flow rate of 0.04536kg/s

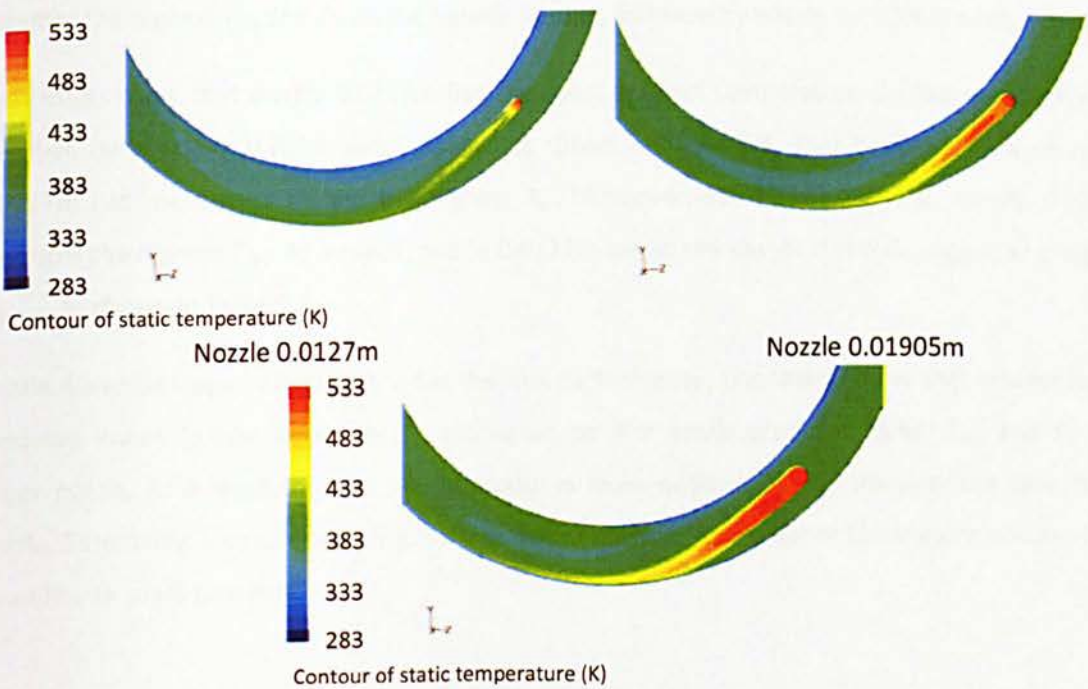

Figure 5.3.4: Air temperature contour inside D-chamber at hot air mass flow rate of 0.04536kg/s

The results also show that nozzle 0.0127m provides the highest T_{ave} and T_{lo}, followed by nozzles 0.01905m and 0.0254m. That occurs because nozzle 0.0127m has the highest average swirling air Mach number and the highest swirling air Mach number in cold spot plane at any given $m_{hot\ air}$. Since nozzle 0.0127m has the highest Mach number of the hot air exiting from the nozzle and largest Z/d, that nozzle produces the highest Mach number reduction of the hot air from plane 145° to plane 175°, as shown in Figure 5.3.5.

According to Figure 5.3.5, the peak Mach number of nozzle 0.0127m drops 58% as it flows from plane 145° to plane 175°. This is followed by nozzle 0.01905m (47%) and nozzle 0.0254m (39%). The Mach number reduction occurs due to momentum transfer from hot air to cold air. Nozzle 0.0127m has the highest peak Mach number reduction shown in Figure 5.3.5, therefore, hot air of that nozzle transfers the largest momentum to cold air, which is followed by nozzle 0.01905m and 0.0254m.

Consequently, the hot air of nozzle 0.0127m experiences the smallest momentum loss due to impinging effect between hot air and outer skin. As nozzle 0.0127m transfers the largest momentum from hot air into cold air inside D-chamber, it produces the highest average swirling air Mach number in D-chamber and swirling air Mach number in cold spot plane. Therefore, nozzle 0.0127m provides the highest T_{ave} and T_{lo} on the nacelle lip-skin, followed by nozzle 0.01905m and 0.0254m.

The results show that nozzle 0.0127m has the most uniform temperature on the nacelle lip-skin, followed by nozzle 0.01905m and 0.0254m as shown in Table 5.3. That happens because nozzle 0.0127m has the lowest T_{hi} and the highest T_{lo}. Moreover, at the given $m_{hot\ air}$, nozzle 0.0127m produces the highest T_{ave}. As a result, nozzle 0.0127m shows the lowest σ and $C_{tem\ deviation}$ at the given $m_{hot\ air}$, as shown in Table 5.3.

Nozzle diameter has an effect on the SAI thermal performance. The result shows that smaller nozzle produces lower T_{hi} than larger nozzle. Moreover, smaller nozzle produces higher T_{ave} and T_{lo} than larger nozzle. As a result, smaller nozzle produces more uniform lip-skin temperature than larger nozzle. Essentially, a smaller nozzle produces better thermal performance than larger nozzle at any given hot air mass flow rate.

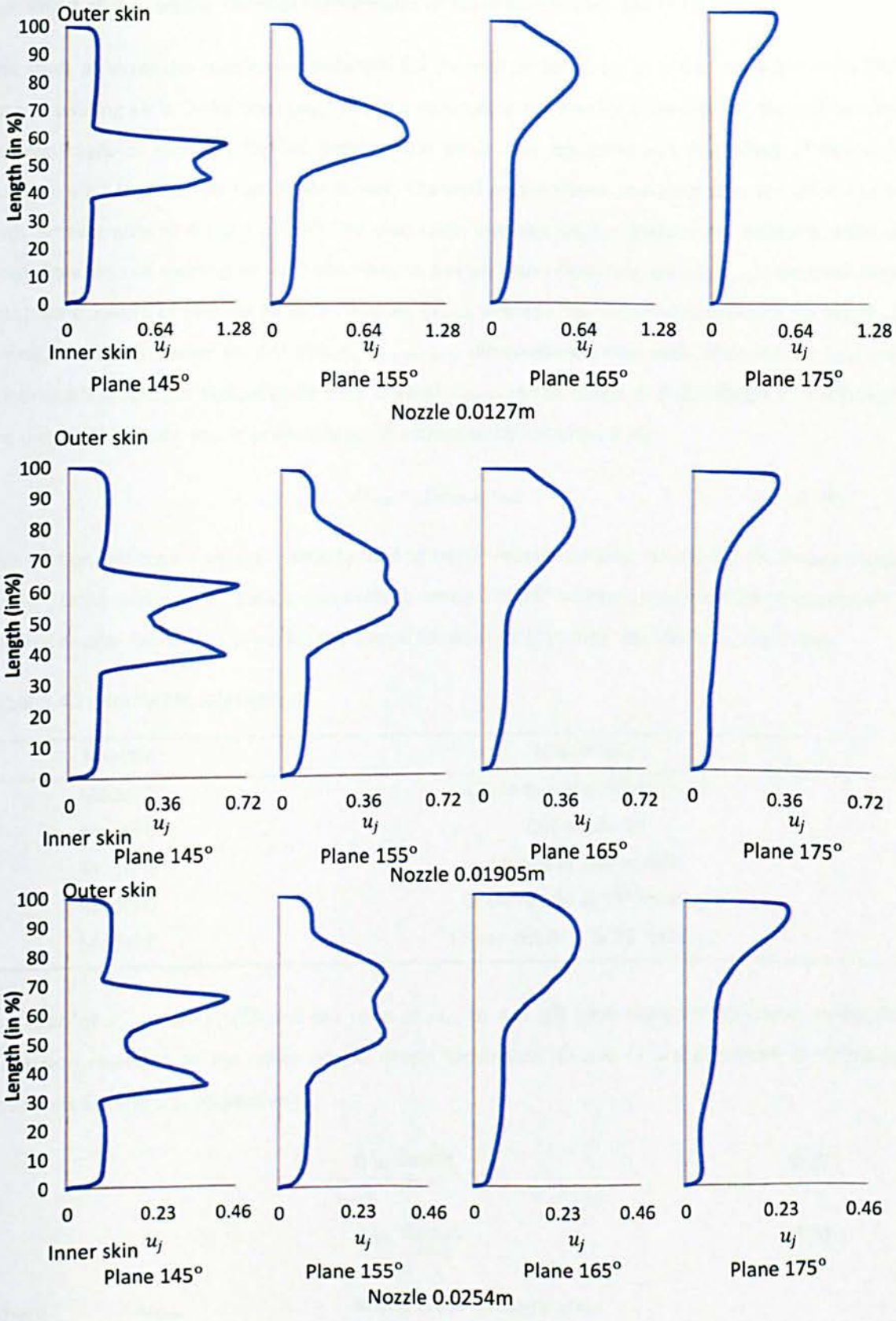

Figure 5.3.5: Local Mach number profile before it impinge on outer skin at hot air mass flow rate of 0.04536kg/s

5.4: Effect of Re_{sw} on the Thermal Performance of Small Nozzle (d=9.144 mm)

The study analyzes the relationship between SAI thermal performance of small nozzle and mass flow rate of swirling air in D-chamber (m_{sw}) in order to develop the empirical correlation, Nusselt number against Reynolds number, for SAI system. The study also demonstrates the effect of Reynolds number for SAI (Re_{sw}) on the dimensionless thermal performance characteristics for small nozzle with exhaust area of 4.210 x $10^{-3}m^2$. The discussion involves various parameters including, ratio of mass flow rate of swirling air in D-chamber to hot air mass flow rate ($m_{sw}/m_{hot\ air}$), dimensionless total temperature of swirling air in D-chamber ($\check{T}_{tsw}$), average heat transfer coefficient for SAI (h_{sw}), average Nusselt number for SAI (Nu_{sw}), $C_{tem\ deviation}$, dimensionless cold spot temperature (σ_{lo}) and dimensionless hotspot temperature (σ_{hi}). Several $m_{hot\ air}$ in the range of 0.00588kg/s to 0.0454kg/s are used in this study. m_{sw} in present study is estimated by Equation 2.24:

$$m_{sw} = \rho A_{D-C} u_{ave} \tag{2.24}$$

This section will covers several nozzle types and nozzle rotation angles; cut nozzle 2D, sloped nozzle at -60°, circle nozzle at 13° rotation and ellipse nozzle 1 at 13° rotation, which will be compared with original nozzle. Table 5.4.1 provides the legend for all models to ease the following discussion:

Table 5.4.1: Nozzle Models Legend

Models	Nozzle type
Model A	Circle nozzle at 0° rotation
Model B	Cut nozzle 2d
Model C	Sloped nozzle at -60°
Model D	Circle nozzle at 13° rotation
Model E	Ellipse nozzle 1 at 13° rotation

The ratio of A_{nozzle} to $A_{D\text{-}C}$ ($\check{D}$) and the ratio of m_{sw} to $A_{D\text{-}C}$ ($\hat{G}$) have been introduced to make the discussion relatable to the other nozzle design/dimension. $\check{D}$ and $\hat{G}$ are described in following Equations 5.4 and 5.5, respectively:

$$\check{D} = \frac{A_{nozzle}}{A_{D-C}} \tag{5.4}$$

$$\hat{G} = \frac{m_{hot\ air}}{A_{D-C}} \tag{5.5}$$

Where A_{nozzle} = Nozzle cross-sectional area

According to Equation 5.4, $\check{D}$ of small nozzle is 0.0108.

The effects of $\hat{G}$ on $m_{sw}/m_{hot\ air}$ for five different nozzle types, A to E, are shown in Figure 5.4.1. This graph has been developed in order to estimate m_{sw}, then average swirling air Mach number, at any given $m_{hot\ air}$ for nozzle $\check{D}$ of 0.0108. The figure shows that $m_{sw}/m_{hot\ air}$ for all types of nozzles varies with $\hat{G}$ follow a similar trend, which inversely related to $\hat{G}$. As shown in the figure, Nozzle E displays the highest $m_{sw}/m_{hot\ air}$ ratio along $\hat{G}$ due to Nozzle E produces the highest average Mach number of the swirling air and m_{sw} at any given $\hat{G}$. The figure also reveals that there is no significant alteration of $m_{sw}/m_{hot\ air}$ by rotating nozzle direction towards inner skin.

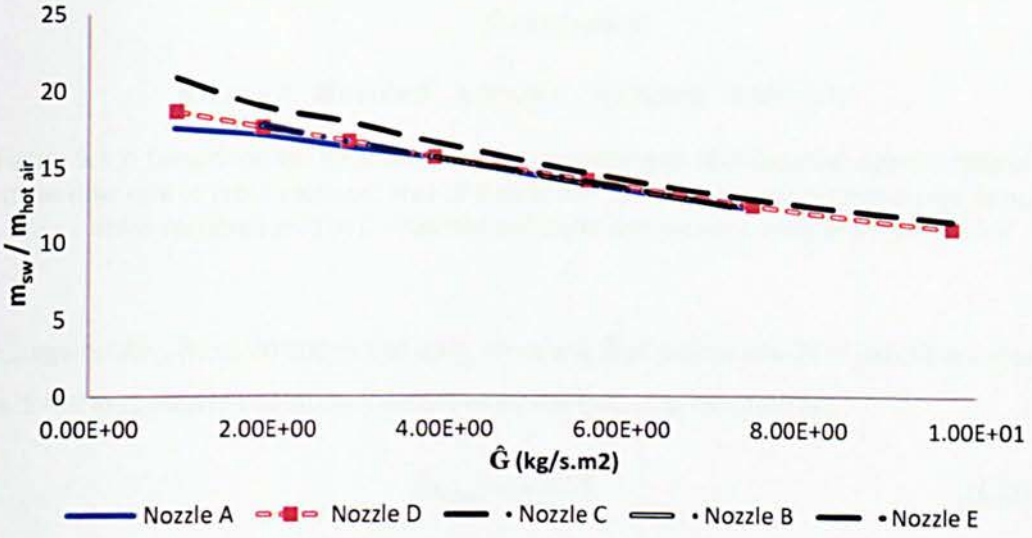

Figure 5.4.1: Ratio mass flow rate of swirling air velocity to hot air mass flow rate against ratio of hot air mass flow rate to cross sectional area of D-chamber for various Nozzle

Figure 5.4.2 illustrates the dimensionless total temperature of swirling air in D-chamber ($\check{T}_{tsw}$) along with $\hat{G}$ for five different nozzles types. This figure is drawn in order to estimate the mean total temperature of swirling air inside D-chamber (T_{tsw}) at a given $m_{hot\ air}$ for nozzle $\check{D}$ of 0.0108 and T_{nozzle} of 533K. $\check{T}_{tsw}$ in Figure 5.4.2 is defined in Equation 5.6 below:

$$\check{T}_{tsw} = \frac{T_{tsw} - T_{\infty}}{T_{nozzle} - T_{\infty}} \qquad (5.6)$$

Figure 5.4.2 shows that $\check{T}_{tsw}$ is proportional to $\hat{G}$ for all nozzles. As $m_{hot\ air}$ increases, the heat supplied to nacelle lip-skin increases as well. Therefore, $\check{T}_{tsw}$ increases since the heat from nozzle to hot air inside D-chamber increases with $\hat{G}$. The figure also shows that all nozzle types share similar magnitude of $\check{T}_{tsw}$ for the same values of $\hat{G}$.

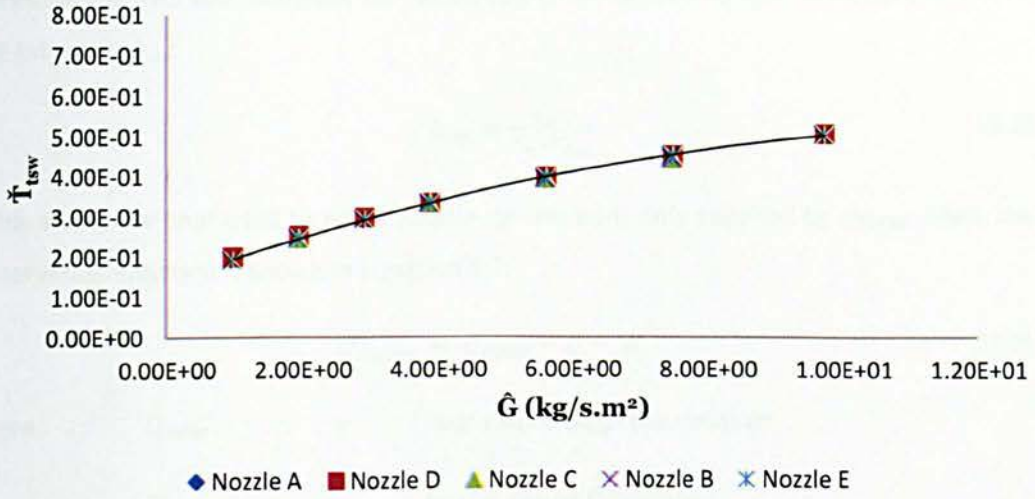

Figure 5.4.2: Dimensionless total temperature of swirling air in D-chamber against ratio of hot air mass flow rate to cross sectional area of D-chamber for ratio of cross sectional area of nozzle to cross sectional area of D-chamber of 0.0108 with exhaust area of 4.210 x $10^{-3}m^2$

The h_{sw} against Re_{sw} (from 80 000 to 430 000), for nozzle $\check{D}$ of 0.0108 and T_∞ of 266.5K are shown in Figure 5.4.3. Re_{sw} used in this study is described by the following formula [44]:

$$Re_{sw} = \frac{m_{sw} D_h}{A_{D-C}\mu} \tag{2.25}$$

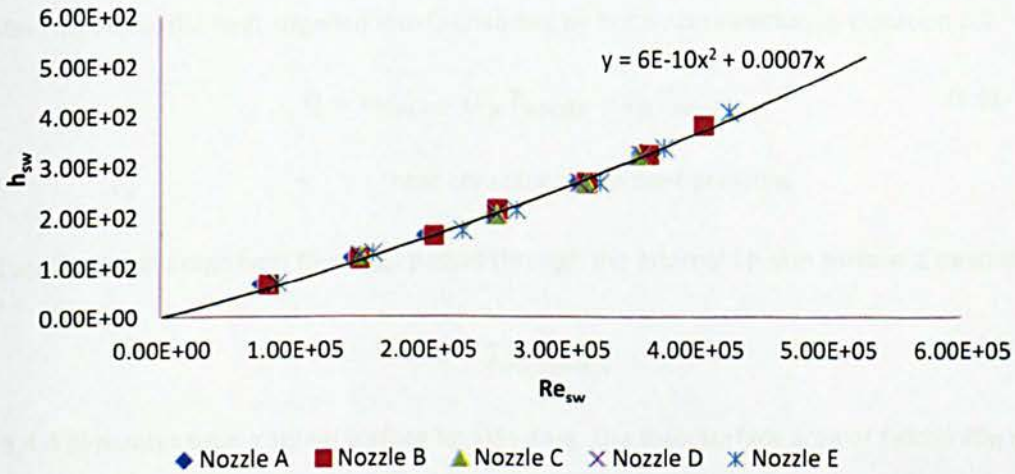

Figure 5.4.3: Effect of SAI Reynolds number on SAI average heat transfer coefficient

Since the D-chamber is a non-circular duct, the hydraulic diameter of D-chamber has been estimated by Equation 2.16:

$$D_h \equiv \frac{4A_{D-C}}{P_w} \tag{2.16}$$

Therefore, the hydraulic diameter for Falcon 20g (small nacelle lip-skin) is 0.085782421m. Equation 2.18 estimates h_{sw}:

$$h_{sw} = \frac{q_{ave}}{T_m - T_{ave}} \tag{2.18}$$

In this study, the heat used to warm nacelle lip-skin up is only supplied by $m_{hot\ air}$. Then, the energy conservation equation is shown in Equation 5.7:

$$Q_{outlet} = Q_{inlet} - Q - W \tag{5.7}$$

Where Q_{outlet} = heat exit through the exhausts

Q_{inlet} = heat entering D-chamber

Q = heat transfer through lip-skin

W = work done

Since there is no work done inside nacelle lip, the item of work done in equation 5.7 becomes zero. Then, Q is rearranged again to become Equation 5.8.

$$Q = Q_{inlet} - Q_{outlet} \tag{5.8}$$

According to continuity equation, $m_{hot\ air}$ entering D-chamber is same with $m_{hot\ air}$ leaving through the exhausts. Therefore, the heat supplied into D-chamber by hot air is rewritten as Equation 5.9.

$$Q = m_{hot\ air}\,(C_p\,T_{nozzle} - C_p\,T_{exh}) \tag{5.9}$$

Where C_p = heat constant at constant pressure

Subsequently, the average heat flux (q_{ave}) passes through the internal lip-skin surface is described as:

$$q_{ave} = \frac{Q}{A_{sur\ lip-skin}} \tag{2.19}$$

Figure 5.4.4 illustrates total internal surface lip-skin area. The total surface area of Falcon 20g nacelle lip-skin is 0.47166032 m^2 (obtained from FLUENT CFD).

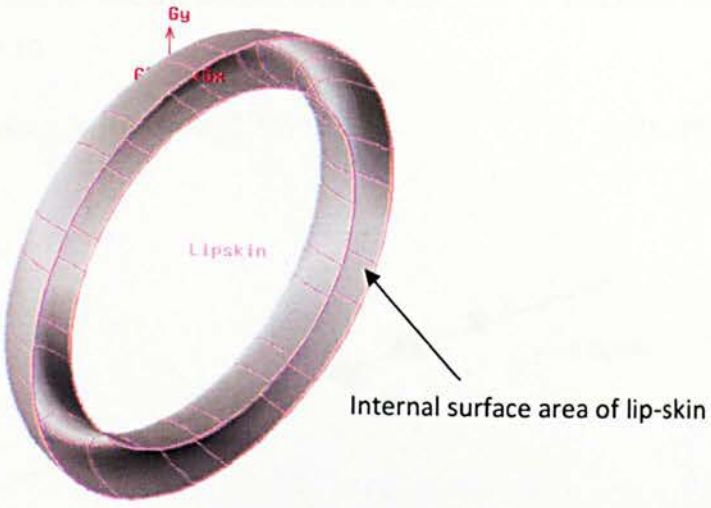

Figure 5.4.4: Surface area of lip-skin

According to Figure 5.4.3, h_{sw} is increases exponentially with Re_{sw} for all nozzle cases. The result shows that all small nozzle types have similar Re_{sw} at all given $m_{hot\ air}$. Thus, the average boundary layer thickness for all nozzle types is similar at all given Re_{sw}. Therefore, the nozzle type does not have significant effects on the h_{sw} as the function of Re_{sw}. However, the boundary layer thickness decreases as Re_{sw} increases. Subsequently, the temperature gradient within laminar sub-layer increases, which leads to increase of h_{sw} with Re_{sw} as shown in Figure 5.4.3.

The relationship between Nu_{sw} and Re_{sw} for nozzle $\check{D}$ of 0.0108 is shown in Figure 5.4.5, which was used to develop correlation between Nu_{sw} and Re_{sw}. Therefore, h_{sw} then T_{ave} can be estimated from this correlation. Nu_{sw} in Figure 5.4.5 is determined by Equation 2.22:

$$Nu_{sw} = \frac{h_{sw}D_h}{k_f} \tag{2.22}$$

The figure shows that Nu_{sw} is proportional to ${Re_{sw}}^{0.975}Pr^{0.3}$. In fact, Nu_{sw} is related to h_{sw} (see Equation 2.22). Since nozzle types do not have big effect on h_{sw}, nozzle types also do not affect Nu_{sw}. Thus, Nozzles A to E follow the similar Nu_{sw} vs. Re_{sw} profile as shown in the figure. The relationship between Nu and Re for smooth, long tube and fully develop flow, is expressed as follows:

$$Nu = ARe_d^B Pr^C \tag{2.12}$$

According to Dittus and Boelter [48, 115], the coefficient of C in Equation 2.13 is 0.3 because the heat is transferred from the hot air in D-chamber to nacelle lip-skin. By using least square methods, the most appropriate value of B in Equation 2.13 for Falcon 20g is 0.975. Finally, A has been determined by taking the gradient Nu_{sw} vs. ${Re_{sw}}^{0.975}Pr^{0.3}$ as shown in Figure 5.4.5. Therefore, the

empirical correlation of Nu_{sw} vs. Re_{sw} for SAI, the exhaust area of 4.210 x 10^{-3} m^2 and given ambient condition is defined in Equation 5.10.

$$Nu_{sw} = 0.0036 Re_{sw}^{0.975} Pr^{0.3} \quad (5.10)$$

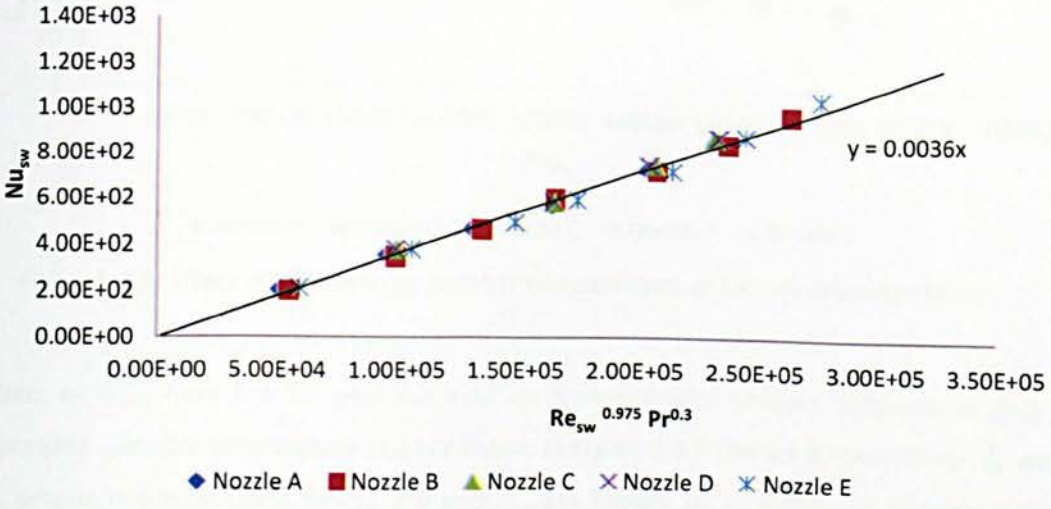

Figure 5.4.5: Nu_{sw} against $Re_{sw}^{0.975} Pr^{0.3}$ for nozzle ratio of cross sectional area of nozzle to cross sectional area of D-chamber of 0.0108 with exhaust area of 4.210 x $10^{-3}m^2$

Figure 5.4.6 illustrates $C_{tem\ deviation}$ vs. Re_{sw} for different nozzle types with exhaust area and T_∞ of 4.210 x $10^{-3}m^2$ and 266.5K respectively. Thus, σ can be determined from this relationship. The nozzle rotation angles for Nozzles A, B and C are 0° and Nozzle D and E are rotated 13° towards inner skin. The figure shows that $C_{tem\ deviation}$ decreases while Re_{sw} increases for all nozzle types. That means the uniformity of temperature distribution enhances with hot air mass flow rate for all nozzle types. The result also shows that the correlations between $C_{tem\ deviation}$ and Re_{sw} for Nozzles A, B and C are almost the same as illustrated in the figure. However, nozzles with 13° rotation towards inner skin show a significant $C_{tem\ deviation}$ reduction. As shown in the figure, Nozzles D and E show much lower $C_{tem\ deviation}$ than Nozzles A, B and C. Therefore, nozzle rotation towards inner skin improves temperature distribution on the nacelle lip-skin towards uniform. In general, $C_{tem\ deviation}$ decreases with increases of nozzle rotation angle, which indicates that, the uniformity of temperature distribution on the nacelle lip-skin increases with nozzle rotation angle.

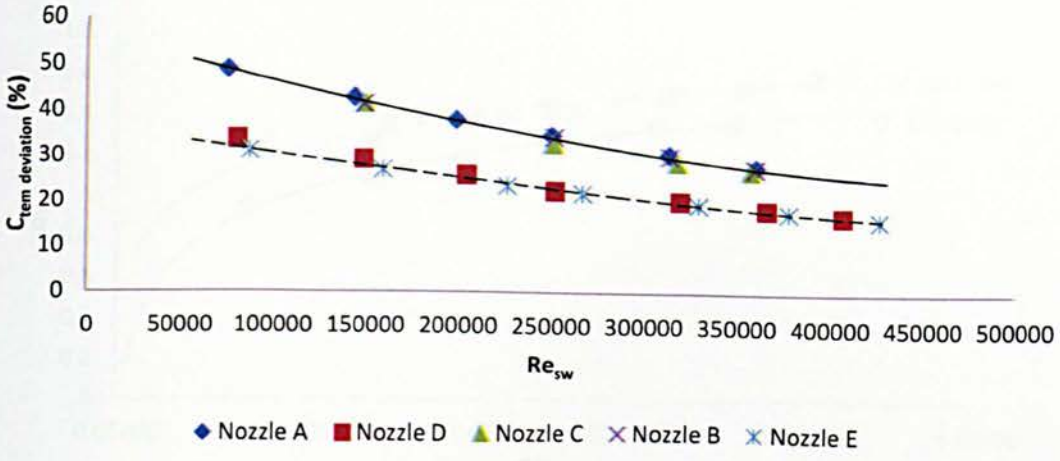

Figure 5.4.6: Effect of SAI Reynolds number on coefficient of temperature deviation

The effect of Re_{sw}, from 8 x 10^4 until 4.2 x 10^5 on dimensionless hotspot temperature (σ_{hi}) and dimensionless cold spot temperature (σ_{lo}) are shown in Figure 5.4.7 and 5.4.8 respectively. T_{hi} and T_{lo} can be determined from these figures if σ and T_{ave} are known. σ_{lo} in Figure 5.4.7 is calculated by Equation 5.11, and (σ_{hi}) is defined by Equation 5.12.

$$\sigma_{lo} = \frac{T_{ave} - T_{lo}}{\sigma} \tag{5.11}$$

$$\sigma_{hi} = \frac{T_{hi} - T_{ave}}{\sigma} \tag{5.12}$$

Similar to Figure 5.4.6, Figure 5.4.7 shows that the nozzle types; A to C, demonstrate insignificant effects on the curves of σ_{lo} vs. Re_{sw}. Figure 5.4.7 also show that σ_{lo} increases with Re_{sw} for all nozzles. However, σ_{lo} increases as the nozzle rotation angle increases from 0° to 13° towards inner skin. Considering σ_{hi}, Figure 5.4.8 shows that the nozzle rotation angle only affects σ_{hi} at low values of Re_{sw} (2 x 10^5 and below). Nozzle A has the highest σ_{hi} at Re_{sw} of 1.5 x 10^5 and below, which followed by Nozzles B, C, D and E. Afterwards, all nozzles produce similar σ_{hi} after Re_{sw} beyond 2.0 x 10^5 as shown in Figure 5.4.8. As shown in the figure, σ_{hi} decreasing as Re_{sw} increases for all nozzle types. Therefore, the uniformity of temperature distribution along the nacelle lip-skin improves as Re_{sw} increases for all small nozzles shown by this study.

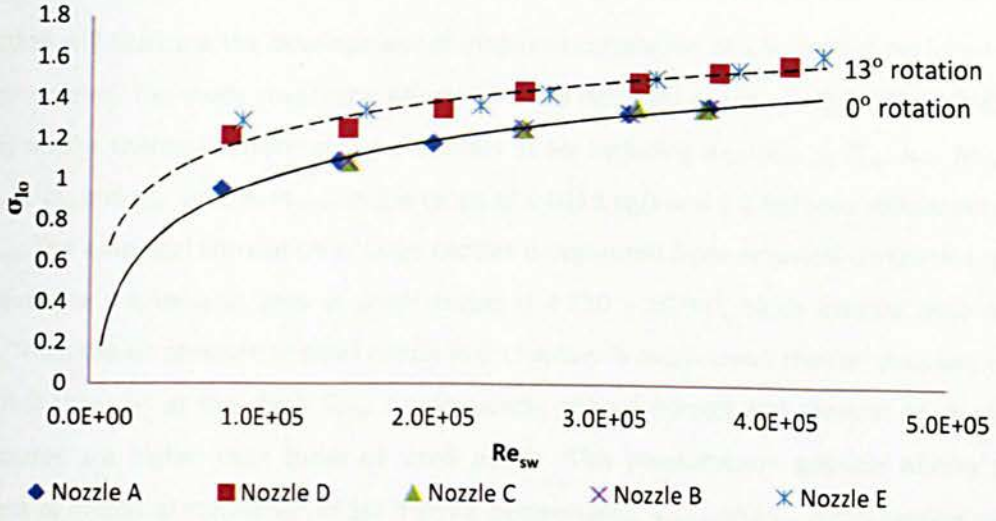

Figure 5.4.7: Dimensionless cold spot temperature against SAI Reynolds number for nozzle ratio of cross sectional area of nozzle to cross sectional area of D-chamber of 0.0108 at exhaust area of 4.210×10^{-3} m^2

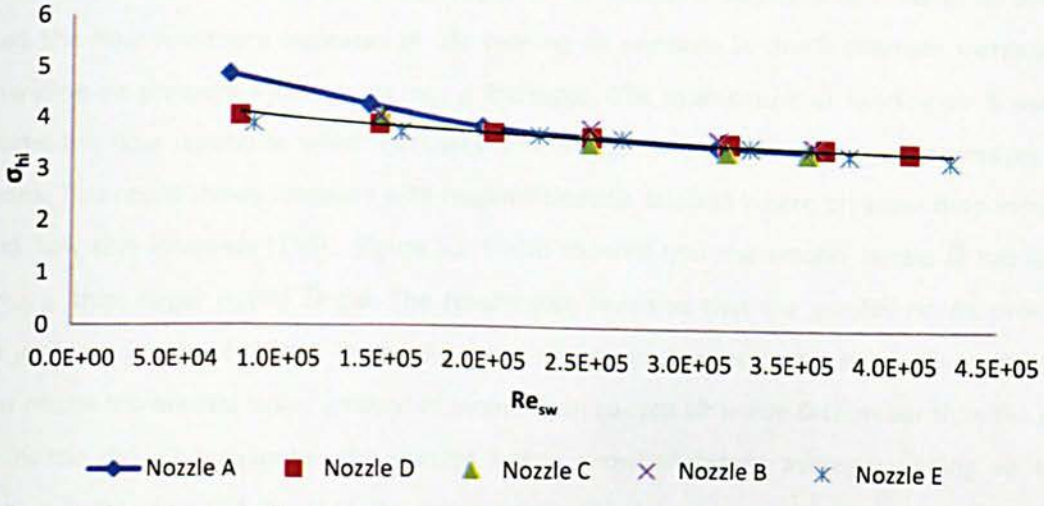

Figure 5.4.8: Dimensionless hotspot temperature against SAI Reynolds number for nozzle ratio of cross sectional area of nozzle to cross sectional area of D-chamber of 0.0108 with exhaust area of 4.210×10^{-3} m^2

The results demonstrate that nozzle type has no effect on the thermal performance of SAI. However, nozzle rotation angle towards inner skin enhances the uniformity of temperature distribution on the nacelle lip-skin. The result also shows that all thermal performance characteristics are related to $\hat{G}$ and Re_{sw} except $m_{sw}/m_{hot\ air}$ which is inversely related to $m_{hot\ air}$. The performance of SAI seems to increase with $m_{hot\ air}$ and Re_{sw}.

5.5: Thermal Performance of Different Nozzle Diameters with an Exhaust Area of $2.105 \times 10^{-3} m^2$

This section will illustrate the development of empirical correlation of SAI thermal performance for the large nozzles. The study covers the effects of three different nozzles $\check{D}$ (0.02089, 0.04699 and 0.08355) on the thermal performance parameters of SAI including $m_{sw}/m_{hot\ air}$, $\check{T}_{tsw}$, h_{sw}, Nu_{sw}, Re_{sw}, $C_{tem\ deviation}$, σ_{lo} and σ_{hi}. Several $m_{hot\ air}$ in the range of 0.0118 kg/s and 0.2 kg/s are applied in order to vary Re_{sw}. The empirical correlation of large nozzles is separated from empirical correlation of small nozzle because the exhaust area of small nozzle is $4.210 \times 10^{-3} m^2$; twice exhaust area of large nozzles. Thus, the air pressure of small nozzle in D-chamber is much lower than air pressure of large nozzle in D-chamber at the given Re_{sw}. Consequently, the air density and thermal conductivity of large nozzles are higher than those of small nozzle. This phenomenon possibly affects on the coefficient of empirical correlation of SAI thermal performance. T_{nozzle} and T_{∞} in this section are 533K and 266.5K respectively.

Figure 5.5.1 illustrates the effects of $\hat{G}$ on $m_{sw}/m_{hot\ air}$ for three different nozzles $\check{D}$ (0.02089, 0.04699 and 0.08355). As shown in the figure, $m_{sw}/m_{hot\ air}$ for all nozzles $\check{D}$ decrease as $\hat{G}$ increases which is because the flow resistance increases as the swirling air pressure in the D–chamber increases. In fact, swirling air pressure increases as $m_{hot\ air}$ increases. The momentum of swirling air is used to overcome the flow resistance which increases with $m_{hot\ air}$. As a result, $m_{sw}/m_{hot\ air}$ decreases as $\hat{G}$ increases. This result shows similarity with Hagen-Poiseuille relation where pressure drop increases as fluid flow rate increases [116]. Figure 5.5.1 also showed that the smaller nozzle $\check{D}$ had higher $m_{sw}/m_{hot\ air}$ than larger nozzle $\check{D}$ did. The results also revealed that the smaller nozzle produced higher jet Mach number (u_j) from the nozzle and u_j reduction than the larger nozzle. Thus, the jet of smaller nozzle transferred larger amount of momentum to cold air inside D-chamber than the jet of larger nozzle did. Consequently, the smaller nozzle provided higher average swirling air Mach number in D-chamber and m_{sw} than the larger nozzle did at a given $m_{hot\ air}$. Therefore, the smaller nozzle has higher $m_{sw}/m_{hot\ air}$ than the larger nozzle.

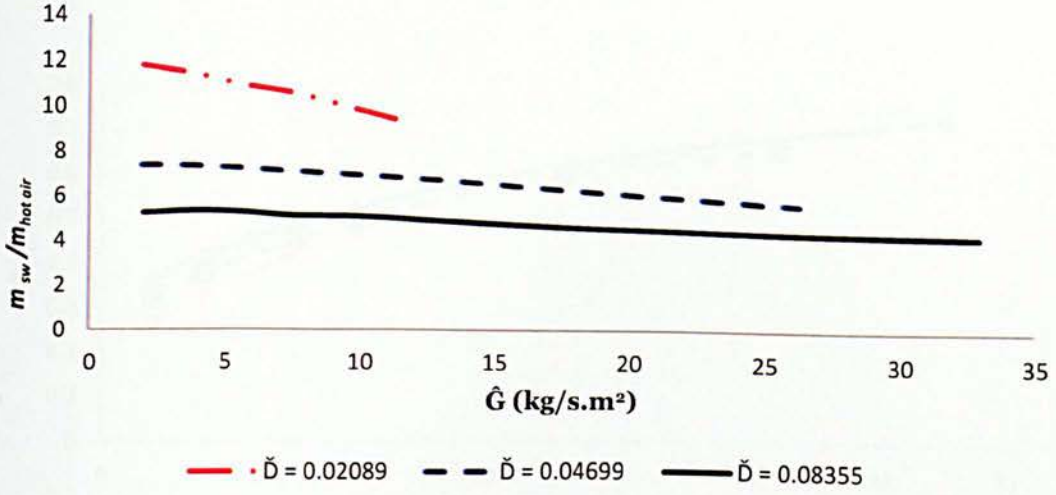

Figure 5.5.1: Ratio mass flow rate of swirling air velocity to hot air mass flow rate against ratio of hot air mass flow rate to cross sectional area of D-chamber for various nozzles diameters at exhausts area of 2.105 x 10^{-3}m^2

The relationship between $\check{T}_{tsw}$ and $\hat{G}$ at three different nozzles $\check{D}$ are shown in Figure 5.5.2. Overall, the results show that the local temperature is proportional to $\hat{G}$. The heat which is supplied to D-chamber increases with $m_{hot\ air}$. Consequently, $\check{T}_{tsw}$ for all nozzles increased as $\hat{G}$ does as shown in the figure. The figure also shows that the smaller nozzle has a lower $\check{T}_{tsw}$ than larger nozzle does. At any given $\hat{G}$, the heat supplied to all nozzles are the same. Therefore, the swirling air in D-chamber received the same quantity of heat from all sizes of nozzles. Since the smaller nozzle has higher average Mach number of swirling air in D-chamber and produces thinner boundary layer than larger nozzle does, at any given hot air mass flow rate, smaller nozzle has higher h_{sw} than larger nozzle. Thus, the swirling air in D-chamber of smaller nozzle transfers more heat to nacelle lip-skin than swirling air of larger nozzle does. As a result, $\check{T}_{tsw}$ of smaller nozzle is lower than $\check{T}_{tsw}$ of larger nozzle along $\hat{G}$ as shown in Figure 5.5.2. For instance, at $\hat{G}$ of 9.4 kg/s.m^2, Q_{inlet} for all nozzles $\check{D}$ are 14102W. In the meantime, Q_{outlet} for nozzles $\check{D}$ of 0.02089, 0.04699 and 0.08355 are 6156W, 6591W and 7025W respectively. Thus, Q for nozzles $\check{D}$ of 0.02089, 0.04699 and 0.08355 are 7946W, 7511W and 7079W respectively. In other words, nozzle $\check{D}$ of 0.02089 has the lowest remaining heat in swirling air inside D-chamber since it transfers the highest heat to the lip-skin despite this nozzle received similar heat from it's inlet compared to the other two nozzles with different diameters. Therefore, nozzle $\check{D}$ of 0.02089 produces the lowest T_{tsw} of swirling air inside D-chamber, which is followed by nozzles $\check{D}$ of 0.04699 and nozzles $\check{D}$ of 0.08355. As a result, Nozzle $\check{D}$ of 0.02089 shows the lowest $\check{T}_{tsw}$ along $\hat{G}$; then followed by nozzle $\check{D}$ of 0.04699 and $\check{D}$ of 0.08355.

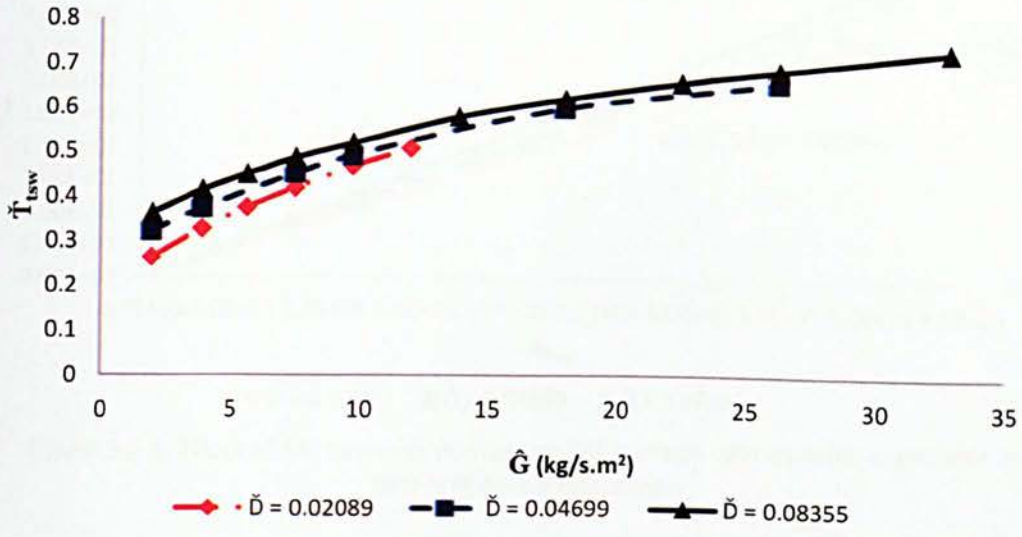

Figure 5.5.2: Relationship between dimensionless total temperature of swirling air in D-chamber against ratio of hot air mass flow rate to cross sectional area of D-chamber at three different nozzles diameters

Figure 5.5.3 illustrates h_{sw} vs. Re_{sw} from 0 to 4.3 x 10^5, for three different nozzles $\check{D}$. The general trend of h_{sw} for all nozzles is similar; which is directly proportional to Re_{sw}. It is well believed that the boundary layer thickness decreases with the increases of average swirling air Mach number inside D-chamber. Therefore, h_{sw} increases as the average swirling air Mach number inside D-chamber and Re_{sw} increase for all nozzles $\check{D}$.

Figure 5.5.3 also shows that h_{sw} is inversely related to nozzle $\check{D}$. In fact, at the given Re_{sw}, the average swirling air Mach number inside D-chamber for all nozzle diameters are similar since Re_{sw} is related to m_{sw}, not $m_{hot\ air}$ as shown in Equations 2.24 and 2.25. Consequently, the average boundary layer thicknesses, which have been produced by all nozzles, are similar as well. Figure 5.5.1 shows that the smaller nozzle has a higher m_{sw} and average swirling air Mach number inside D-chamber than the larger nozzle does at any given $\hat{G}$. Therefore, the larger nozzle requires higher $\hat{G}$ or $m_{hot\ air}$ than the smaller nozzle in order to produce similar u_{ave} and Re_{sw}. Consequently, larger nozzle supplies higher heat to the swirling air in the D-chamber than smaller nozzle does at the similar Re_{sw}. Thus, the swirling air of larger nozzle transfers more heat to the nacelle lip-skin than the swirling air of smaller nozzle does. As a result, larger nozzle produces higher h_{sw} than smaller nozzle does at any given Re_{sw} as shown in Figure 5.5.3.

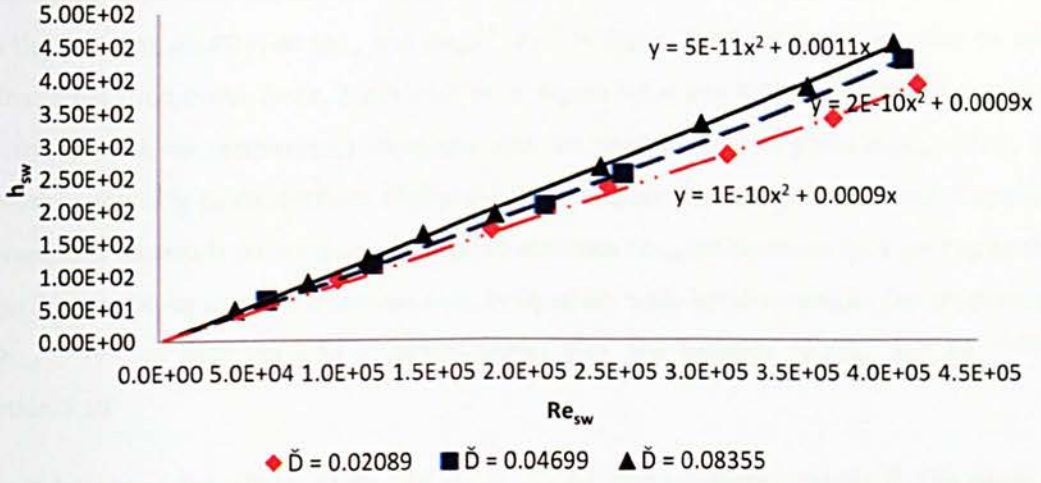

Figure 5.5.3: Effect of SAI Reynolds number on SAI average heat transfer coefficient at different nozzle diameters

The relationship between Nu_{sw} and $Re_{sw}^{0.975}Pr^{0.3}$ for three different nozzles $\check{D}$ is displayed in Figure 5.5.4 in order to develop empirical correlation of heat transfer for SAI system with exhaust area of 2.105 x $10^{-3}m^2$. As shown in the figure, the Nu_{sw} is proportional to $Re_{sw}^{0.975}Pr^{0.3}$ for all nozzles $\check{D}$ and the empirical correlation between Nu_{sw} and $Re_{sw}^{0.975}Pr^{0.3}$ at the given conditions is expressed in Equation 5.13.

$$Nu_{sw} = 0.0041Re_{sw}^{0.975}Pr^{0.3} \quad (5.13)$$

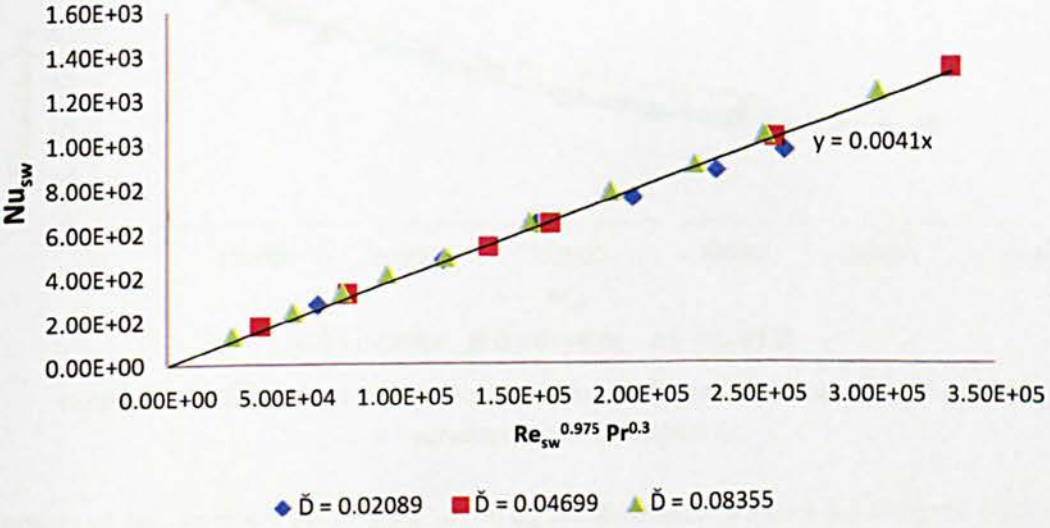

Figure 5.5.4: Nu_{sw} against $Re_{sw}^{0.975}Pr^{0.3}$ for several nozzles diameters at exhaust area of 2.105 x $10^{-3}m^2$

According to Equation 5.13, the gradient of Nu_{sw} vs. $Re_{sw}^{0.975}Pr^{0.3}$ in Figure 5.5.4 is higher (0.0041) than the gradient (0.0036) of Nu_{sw} and $Re_{sw}^{0.975}Pr^{0.3}$ in Figure 5.4.5. This happens due to different exhaust areas used in the cases, 2.105 x $10^{-3}m^2$ in Figure 5.5.4 and 4.210 x $10^{-3}m^2$ in Figure 5.4.5. In fact, the swirling air temperature increases with air pressure at the given $m_{hot\ air}$. Thus, the air properties especially air conductivity changes with swirling air pressure in D-chamber. Therefore, the air properties especially air conductivity used to estimate Nu_{sw} for Equation 5.13 are higher than air properties, are being used to determine Nu_{sw} in Equation 5.10. For that reason, the gradient of Nu_{sw} vs. $Re_{sw}^{0.975}Pr^{0.3}$ in Equation 5.13 is slightly higher than the gradient of Nu_{sw} and $Re_{sw}^{0.975}Pr^{0.3}$ in Equation 5.10.

Figure 5.5.5 shows the effects of Re_{sw} on $C_{tem\ deviation}$ for three different nozzles $\check{D}$. The figure shows that $C_{tem\ deviation}$ decreases as Re_{sw} increases for all nozzles $\check{D}$, which indicates the uniformity of temperature distribution enhances as Re_{sw} increases and the smallest nozzle $\check{D}$ of 0.02809 has the highest $C_{tem\ deviation}$, followed by nozzle $\check{D}$ of 0.04699 and 0.08355. $C_{tem\ deviation}$ decreases faster for larger nozzles. At a given Re_{sw}, larger nozzle produces higher T_{ave} and T_{lo} than smaller nozzle because larger nozzle has higher h_{sw} than smaller nozzle at a given Re_{sw}. Therefore, the larger nozzle has better temperature distribution on the nacelle lip-skin than the smaller nozzle as shown in the figure.

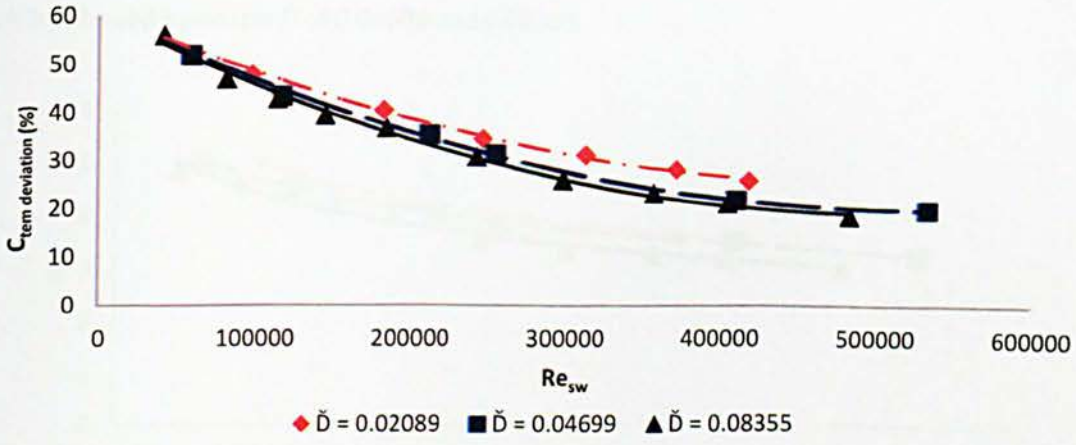

Figure 5.5.5: Effect of SAI Reynolds number on coefficient of temperature deviation for various nozzles diameters

The effects of Re_{sw} from 4 x 10^4 to 4.3 x 10^5 on σ_{lo} are illustrated in Figure 5.5.6. Figure 5.5.6 shows σ_{lo} increases along with Re_{sw} for all nozzles, and Nozzle $\check{D}$ of 0.02089 produces the lowest σ_{lo} along with Re_{sw}, which is followed by nozzle $\check{D}$ of 0.04699 and 0.08355. As a given Re_{sw}, smaller nozzle has lower T_{ave} and higher σ than larger nozzle does. Therefore, the temperature difference between T_{ave} and T_{lo} for smaller nozzle is lower than for larger nozzle. Therefore, nozzle $\check{D}$ of 0.02089 has the

lowest σ_{lo}, which is followed by nozzle $\check{D}$ of 0.04699 and 0.08355.

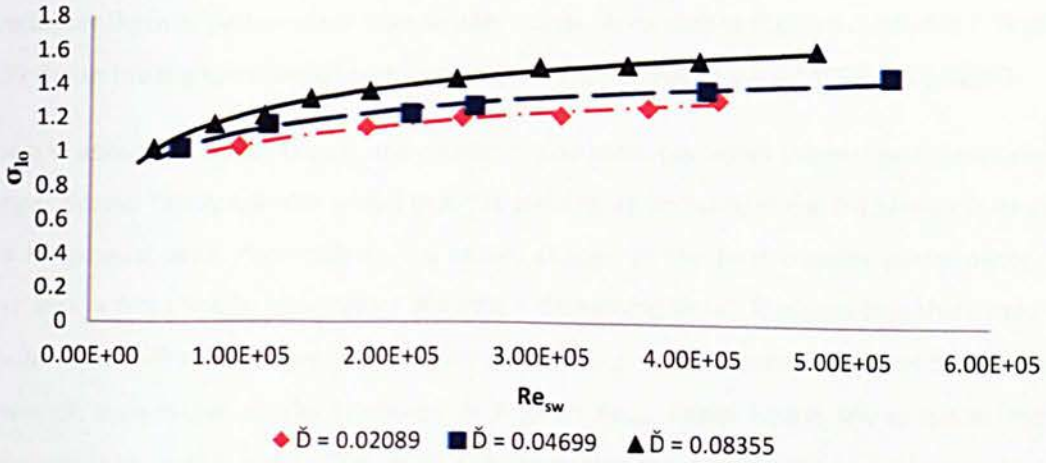

Figure 5.5.6: Dimensional cold spot temperature along SAI Reynolds number for different nozzle diameters at exhausts area of 2.105 x $10^{-3}m^2$

Figure 5.5.7 shows σ_{hi} against Re_{sw} for different nozzle $\check{D}$ in the range of 0.02089 to 0.08355. The figure shows that σ_{hi} is inversely related to Re_{sw} for all nozzles $\check{D}$ and Nozzle $\check{D}$ of 0.02089 gives the highest σ_{hi} along with Re_{sw} which is followed by Nozzle $\check{D}$ of 0.04699 and 0.08355. Since smaller nozzle has lower h_{sw} at a given Re_{sw}, the temperature difference between T_{hi} and T_{ave} increases along with Re_{sw}. Therefore, nozzle $\check{D}$ of 0.02089 shows the highest σ_{hi} at the given Re_{sw} in Figure 5.5.7, which is followed by nozzle $\check{D}$ of 0.04699 and 0.08355.

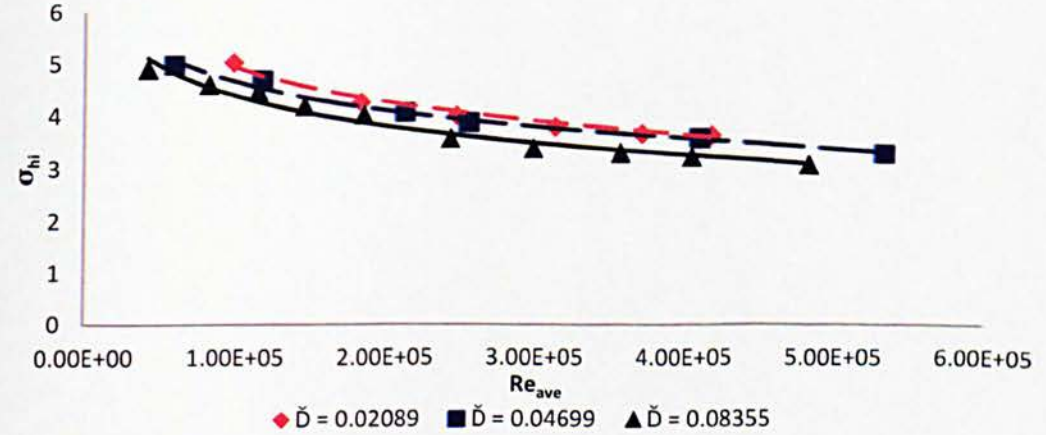

Figure 5.5.7: Dimensionless hotspot temperature against SAI Reynolds number for several nozzle diameters at exhausts area of 2.105 x $10^{-3}m^2$

The result shows that $m_{sw}/m_{hot\ air}$, $C_{tem\ deviation}$ and σ decrease with the increase of nozzle $\check{D}$. At the same time, h_{sw} and σ_{lo} increases as the nozzle $\check{D}$ increases. At any given Re_{sw}, the larger nozzle seems to have better thermal performance than smaller nozzle. According to Figure 5.5.3 to 5.5.7, Nozzle $\check{D}$ 0.08355 shows the highest thermal performance, which is followed by $\check{D}$ 0.04699 and 0.02089.

As shown in abovementioned results, the shorter nozzle produces better thermal performances than the longer nozzle. The result also shows that the swirling air pressure in the D-chamber is inversely related to exhaust area. According to the result, change of the heat transfer performance with exhaust area is from low to high before showing a decreasing trend. It means that there may be a maximum value within the whole trend. At any given $m_{hot\ air}$, smaller nozzle produces better thermal performance than larger nozzle. However, at a given Re_{ave}, larger nozzle shows better thermal performance than smaller nozzle. The result also shows that the nozzle rotation angle towards inner skin enhances uniformity of temperature distribution on the nacelle lip-skin.

Chapter Six: Effect of Augmentor on Thermal Performance of the SAI System

This chapter demonstrates the application of the augmentor or ejector in the SAI system. It is well believed that the augmentor enhances the thermal performance of SAI. Besides, the augmentor system has several advantages including no moving part and no direct energy input [121]. Therefore, this application is widely used in many industries, for instance, aerospace [88] and refrigeration [83]. Since the augmentor is placed after the nozzle outlet, the hot air with high velocity and Mach number (*Mn*) generates low air pressure inside the augmentor throat, as shown in Figure 6.0.1a. Thus, the cold air with higher pressure is entrained to flow through the augmentor throat and mixes together with the hot air, as shown in Figure 6.0.1b. Subsequently, the momentum and heat exchange between hot air and cold air inside the augmentor is enhanced. Then the Mach number of the mixed air decreases when it approaches augmentor's outlet owing to the gradual increase of cross sectional area from throat to outlet, in the diffuser section. The mixed air exits from the augmentor with lower Mach number, which reduces hotspot temperature on the nacelle lip-skin. Moreover, the mixing facilitated better uniform distribution of Mach number and temperature with augmentor than the case without mixing, as shown in Figures 6.0.1c and 6.0.1d. This study therefore has analysed the effects of the augmentor on the thermal performance of SAI system.

The augmentor consisted of two major sections: intake section and diffuser section. The intake section is a finite volume from the inlet to throat, and the diffuser section is a finite volume between the throat and outlet. The augmentor inlet has a large area in order to facilitate "sucking" of cold air from the D-chamber, as adopted by Chou et al. [83] and Rusly et al. [85]. Then, the cross-sectional area decreases towards the throat (increases the velocity of cold air), and diverges thereafter towards the exit (reduces the velocity of mixed air exiting from the augmentor) as illustrated in Figure 6.0.2.

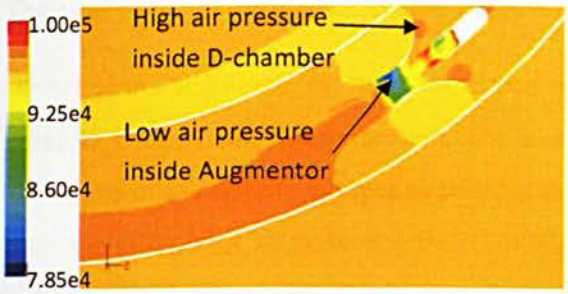

Contour of absolute pressure (Pa)

(a) Absolute Air pressure contour

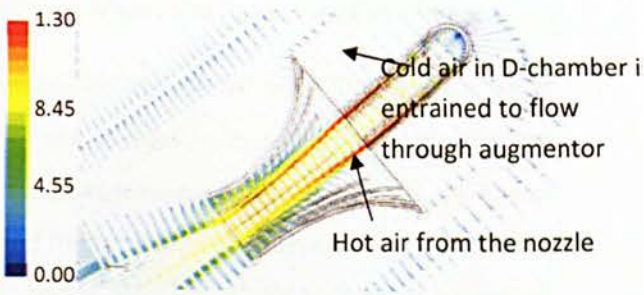

Vector of Mach number

(b) Mach number vector

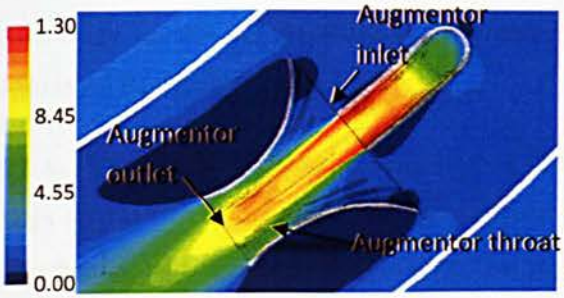

Contour of Mach number

(c) Mach number contour SAI with

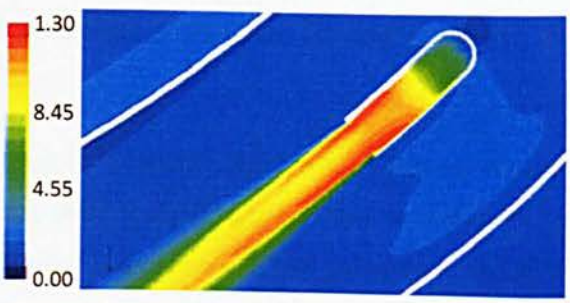

Contour of Mach number

(d) Mach number contour SAI with no

Figure 6.0.1: Air Mach number/pressure contour and Mach number vector at nozzle vicinity with and without augmentor

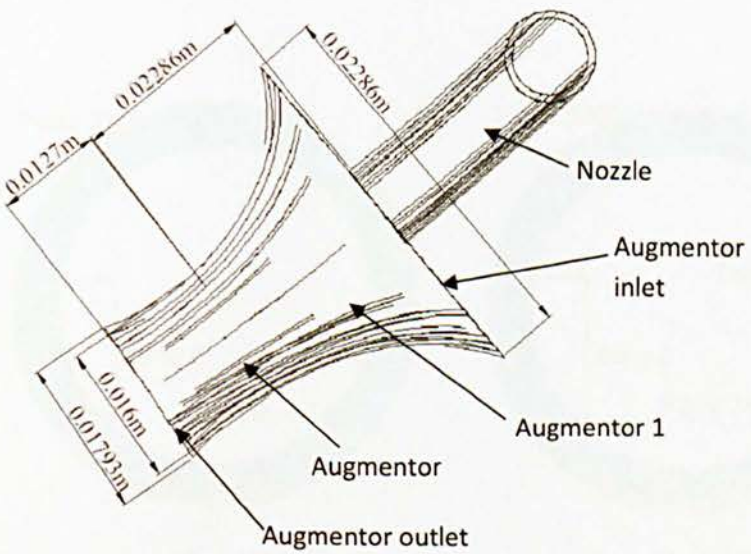

Figure 6.0.2: Schematic illustration of Augmentor

6.1 The application of Augmentor in SAI System for Hot Air Mass Flow Rate of 0.0118 kg/s

The effect of the augmentor on the thermal performance for low hot air mass flow rate ($m_{hot\ air}$ of 0.0118kg/s) is described in this section. The aim of the discussion is to compare the thermal performances of SAI systems without augmentor and with Augmentor 1. The nozzle and augmentor rotation angles for both SAI systems were set as 0°, and the total exhaust area and T_{nozzle} were 4.210 x $10^{-3}m^2$ and 533K respectively. In addition, the small nozzle diameter (0.009144m) was employed. The thermal performance characteristics studied included lip-skin temperature contour, local temperature distribution on four different planes, hotspot temperature (T_{hi}), cold spot temperature (T_{lo}), average lip-skin temperature (T_{ave}), standard temperature deviation (σ) and coefficient of temperature deviation ($C_{tem\ deviation}$).

Figure 6.1.1 illustrates the lip-skin temperature contours for SAIs with Augmentor 1 (Model W) and without augmentor (Model X). It can be observed that there is significant variation in temperature distribution along the nacelle lip-skin after the augmentor is employed in the SAI system. Model X produces T_{hi} in plane 170°; however, T_{hi} of Model W occurs in plane 165°. Moreover, when the augmentor is used, the cold spot occurring in Zone B for Model X is transferred to Zone C; also, the temperature of Zone B increases, but the temperature in Zone C decreases. The results reveal that, T_{hi} and T_{lo} of Model W are 337.2K and 279.52K respectively which are lower than those of Model X by 0.2K and 0.13K respectively.

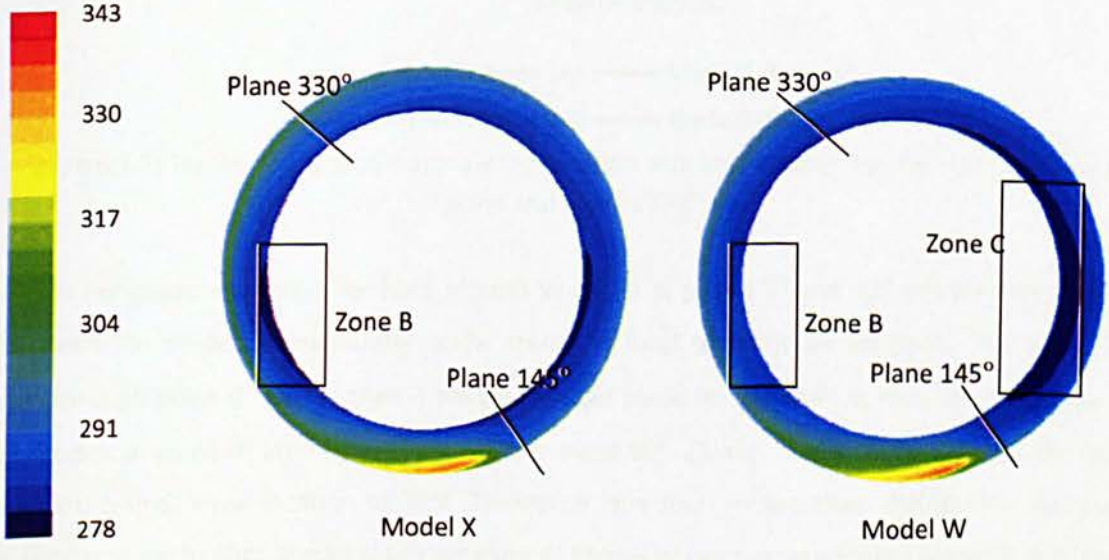

Figure 6.1.1: Lip-skin temperature contours (in K) of SAI with and without Augmentor 1

Figure 6.1.2 illustrates the local temperature distribution along wrap location for Models W and X in the hotspot planes and plane 270°. It is obvious that the local temperature distribution changes dramatically in the hotspot plane, and is rather uniformly distributed in plane 270°. Along the outer skin, Model X shows higher local temperature than Model W does until wrap location 26%, and then displays lower local temperature than Model W. Model W demonstrates higher local temperature than Model X does for the entire inner skin. In plane 270°, the local temperature distributions for both models are much uniformly distributed along the nacelle lip-skin than those for hotspot planes. Before wrap location 38%, Model X shows higher local temperature; however, the situation is reversed after wrap location 38%, and Model W demonstrates higher local temperature until wrap location 100%.

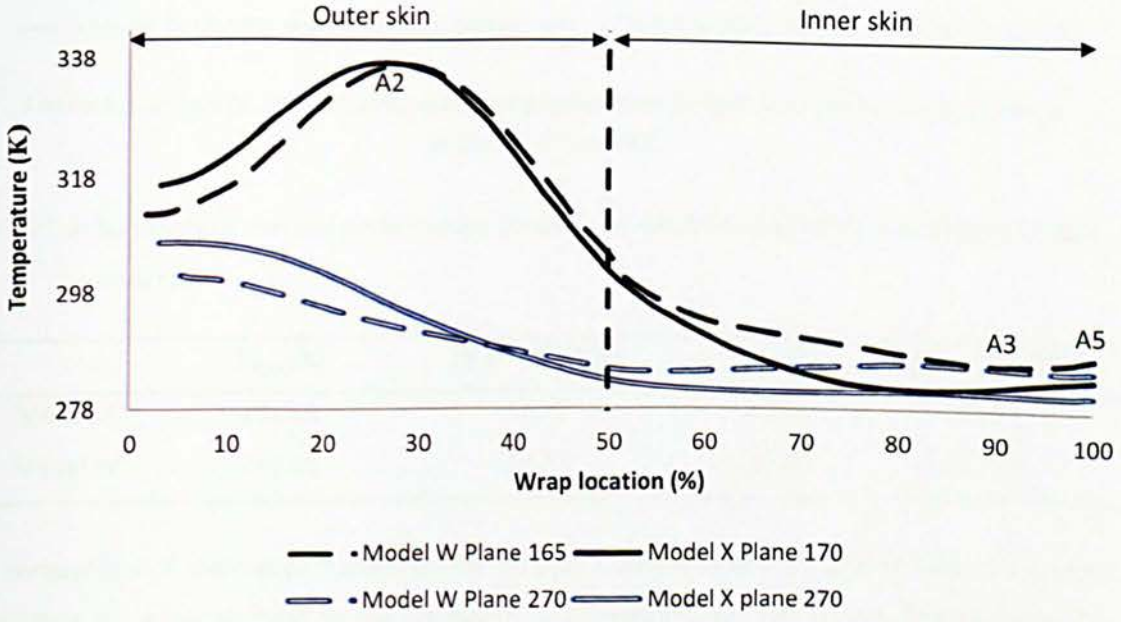

Figure 6.1.2: Temperature profile along wrap location with and without Augmentor 1 in hotspot plane and plane v270°

The local temperature profiles for both Models W and X in planes 0° and 90° are shown in Figure 6.1.3. Both the models demonstrate similar trends in local temperature variation. The mixed air passes through plane 0° earlier than it passes through plane 90°. Therefore, local temperatures of both models in plane 0° are higher than those in plane 90°. Finally, Model X produces higher local temperature until wrap location of 70%. Thereafter, the local temperature distribution becomes very similar to each other; the local temperature of Model W catches up with the Model X, and then keeps roughly constant.

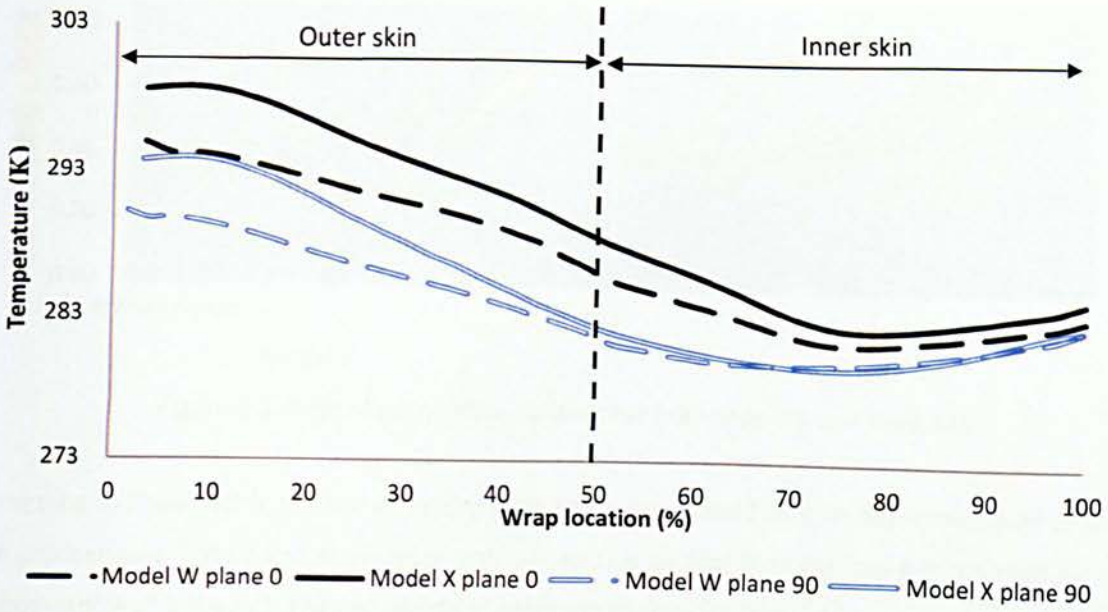

Figure 6.1.3: Temperature distribution along wrap location with and without Augmentor 1 in planes 0° and 90°

Table 6.1.1: Summary of thermal performance between Model X and Model W at low hot air mass flow rate

	T_{ave} (K)	$(T_{hi} - T_{lo})$ (K)	σ (K)	$C_{tem\ deviation}$ (%)
Model X	291.43	57.77	10.76	42.87
Model W	290.01	57.73	10.06	42.49

The comparison of thermal performances for Models X and W is summarised in Table 6.1.1 which shows that T_{ave} drops by 1.42K as the augmentor is employed in the SAI system. Furthermore, $T_{hi} - T_{lo}$, σ and $C_{tem\ deviation}$ of SAI with augmentor are slightly lower than those without augmentor.

Model W was expected to produce lower T_{hi} than Model X. However, the result shows that T_{hi} of Model W is almost the same with that of Model X. According to Figure 6.1.4, although SAI with augmentor produces lower hot air Mach number from augmentor outlet to impinged surface, the hot air from the augmentor deviates towards the outer skin. Thus, in Model W, the hot air from the nozzle reaches the nacelle lip-skin earlier than in Model X. As a result, Model W produces T_{hi} almost similar to Model X, even though Model W shows slightly lower air Mach number, as highlighted by rectangle A in Figure 6.1.4.

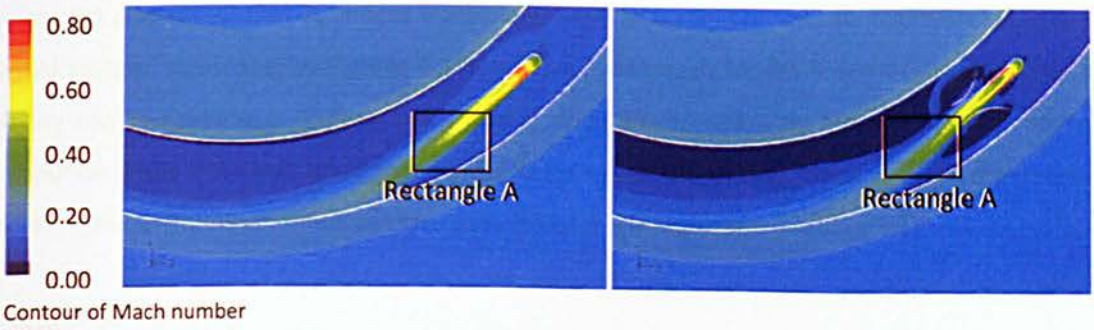

Figure 6.1.4: Air Mach number contour for both Model X and Model W

According to Figure 6.1.5, the hot air exiting from the nozzle flows closer to Augmentor wall 1. Thus, the gap between hot air and Augmentor wall 1 (Gap 1) is smaller than the gap between hot air and Augmentor wall 2 (Gap 2). The magnitude of momentum transfer from hot air to cold air in Gap 2 is higher than that of the total momentum transfer from hot air to cold air in Gap 1. Consequently, Gap 2 has a higher Mach number drop of the hot air compared to Gap 1. As a result, the hot air exiting from the augmentor experiences a small flow diversion towards the outer skin, as shown in Figure 6.1.5.

Figure 6.1.5: Contour of Mach number in augmentor vicinity

The result reveals that the average swirling air velocity from Model X is much higher than that of Model W along the nacelle D-Chamber. Model W produces an average velocity of swirling air of 25.636 m/s, which is 7.211 m/s lower than that of Model X. Thus, the average heat transfer coefficient (h_{ave}) of Model X is higher than that of Model W. Therefore, Model W generates lower T_{ave} compared to Model X.

The results also reveal that T_{lo} moves from plane 245° to plane 120° as the augmentor is utilised in the SAI system. According to Figures 6.1.6 and 6.1.7, although Model X demonstrates higher peak velocity and temperature in plane 245°, Model W produces relatively more uniform temperature distribution. Thus it is established that Model W enhances the mixing of hot air from the nozzle and cold air in the D-Chamber, and therefore the cold spot is postponed.

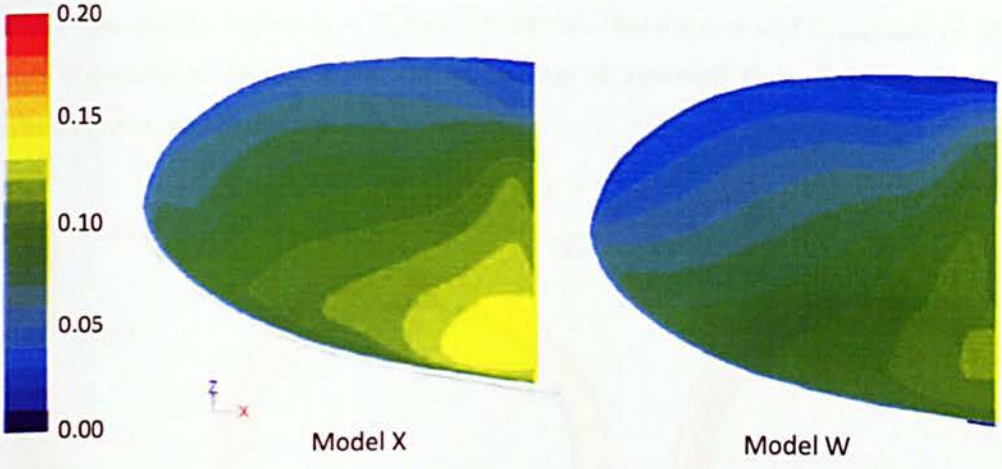

Figure 6.1.6: Air Mach number contour inside D-Chamber in plane 240°

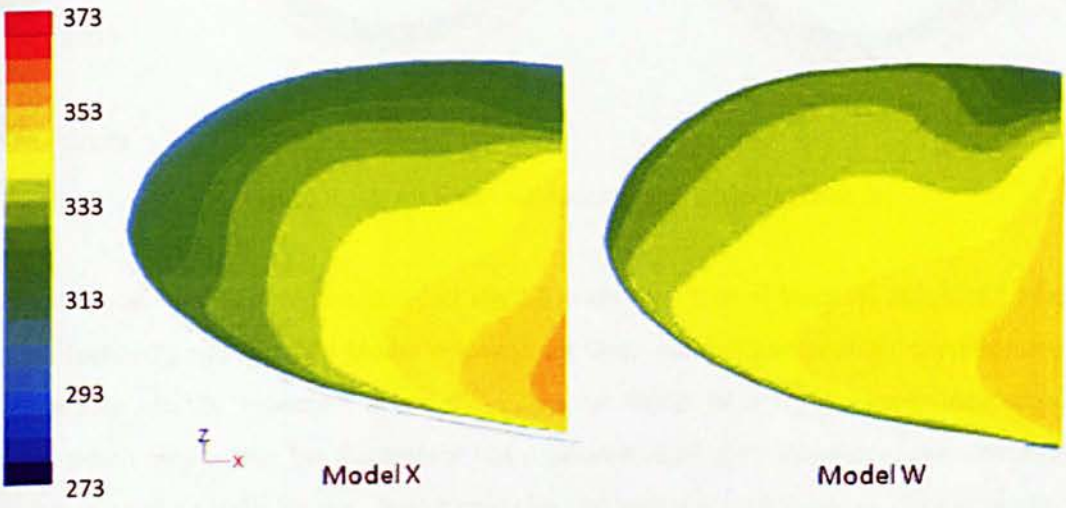

Figure 6.1.7: Air temperature contour (in K) inside D-Chamber in plane 240°

The results also show that Model W has better uniform distribution of temperature on the nacelle lip-skin than Model X in planes between 145° and 330°; this is attributed to the relatively better uniform velocity of swirling air in the D-chamber for Model W. This is consistent with the previous studies [86-88] which demonstrated that air velocity exit from augmentor was more uniform than air velocity exit from nozzle alone. Thereafter, Model W has a lower temperature on both inner and

outer skins along the nacelle lip-skin in planes from 330° to 145°. This phenomenon occurs due to the swirling air Mach number of Model X being much higher than the swirling air Mach number of Model W, as shown in Figure 6.1.8. The augmentor produces higher air pressure and momentum drop, especially at its vicinity. This reduces swirling air Mach number along the D–chamber, particularly in planes between 330° and 145°. As a result, the inner skin temperature of Model W in planes between 330° and 145° is lower than that of Model X, as shown in Figure 6.1.1. In addition, Model X has slightly higher $T_{hi} - T_{lo}$ than Model W. Therefore, σ and $C_{tem\ deviation}$ of Model W are almost the same as Model X and the augmentor is apparent to have produced no significant improvement in the temperature uniformity.

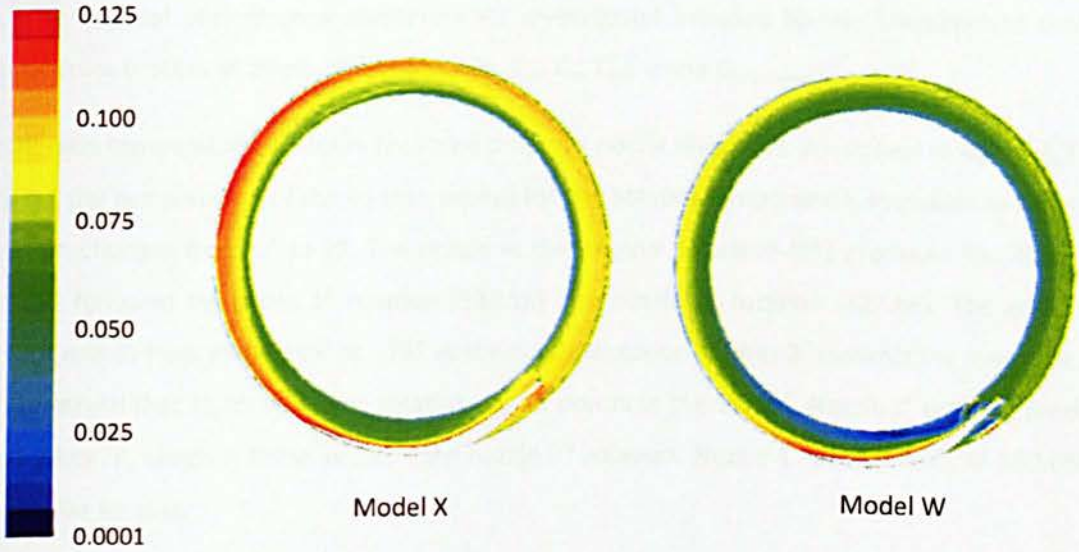

Figure 6.1.8: Air Mach number contour inside nacelle lip

The results show that T_{hi} of Model W is just slightly lower than that of Model X. Moreover, Model X produces higher T_{lo} and T_{ave} than Model W due to air Mach number and pressure drop occurring at the augmentor vicinity. However, σ and $C_{tem\ deviation}$ for Model W is slightly lower than those for Model X, which means that the augmentor has produced slight enhancement in the uniformity of temperature on the nacelle lip-skin. Thus it could be deduced that, at low hot air mass flow rate, the augmentor contributes for slight enhancement in the thermal performance of SAI despite decrease of T_{ave}. For the next analysis, nozzle outlet direction is rotated towards the inner skin in order to reduce T_{hi} and increase T_{lo} on the nacelle lip-skin.

6.2 Effect of Nozzle Rotation on SAI Thermal Performance

This section describes the effect of nozzle rotation angle in the range of 0° to 2° on the thermal performance of anti-icing. The abovementioned results have shown that the hot air from the augmentor has slightly deviated towards the outer skin. As T_{hi} of SAI with augmentor is similar to that without augmentor, the study seeks the appropriate nozzle angle for enhancing the thermal performance of anti-icing.

The study investigated the effect of three different nozzle rotation angles (0°, 1° and 2°) towards the inner skin on the thermal performance of anti-icing. Augmentor 1 was used in this investigation. The exhaust area, nozzle diameter, $m_{hot\ air}$ and T_{nozzle} are the same to those investigated in section 6.1. The thermal performance characteristics investigated included lip-skin temperature contour, temperature profiles at three different planes, T_{hi}, T_{lo}, T_{ave}, σ and $C_{tem\ deviation}$.

The lip-skin temperature contours for three different nozzle directions are shown in Figure 6.2.1. In general, the temperature of the lip-skin, except for the hotspot temperature, increases as the nozzle direction changes from 0° to 2°. The nozzle in the original direction (0°) produces the highest T_{hi} (337.2K) followed by nozzle 1° rotation (332.1K) and nozzle 2° rotation (327.8K). The position of hotspot moves from plane 165° to 173° as the nozzle direction rotates 2° towards the inner skin. It is also observed that T_{lo} for all nozzle rotation angles occurs at plane 120°. Nozzle 2° rotation produces T_{lo} of 280.47K, which is 0.95K higher than nozzle 0° rotation. Nozzle 1° produces T_{lo} of 280.05K on the nacelle lip-skin.

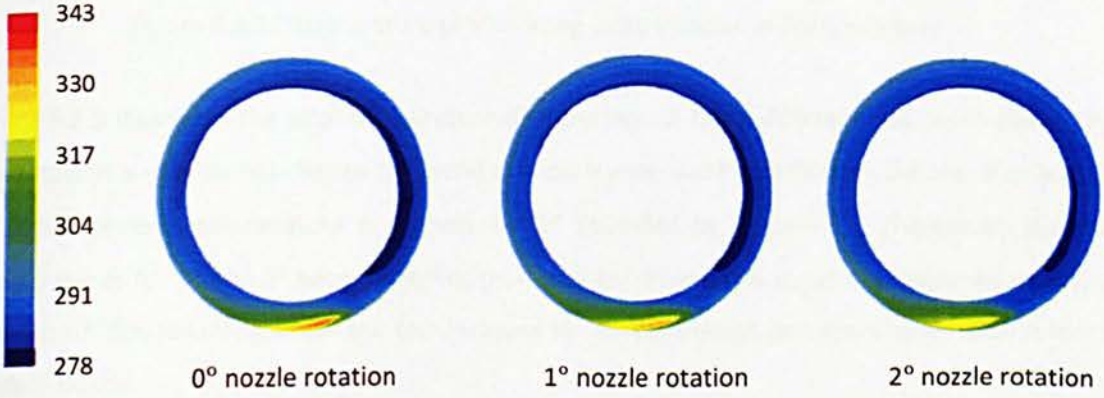

Figure 6.2.1: Comparison of lip-skin temperature contour (in K) at three different nozzle rotation angles

The local temperature distributions in the hotspot planes for three different nozzles with respect to wrap location are shown in Figure 6.2.2. In general, all nozzle directions demonstrate similar trends of temperature changes. Along the outer skin, before wrap location 38%, original nozzle generates the highest local temperature, followed by nozzle 1° and 2°. After wrap location of 38%, local temperatures produced by nozzle 1° and 2° overtake the local temperature produced by original nozzle, and the local temperature generated by nozzle 2 becomes slightly higher than that produced by nozzle 1 after wrap location of 43%. Along the entire inner skin, nozzle 2° demonstrates the highest local temperature. The nozzle 1° produces second highest local temperature, which gradually approaches to the same temperature by nozzle 0° rotation.

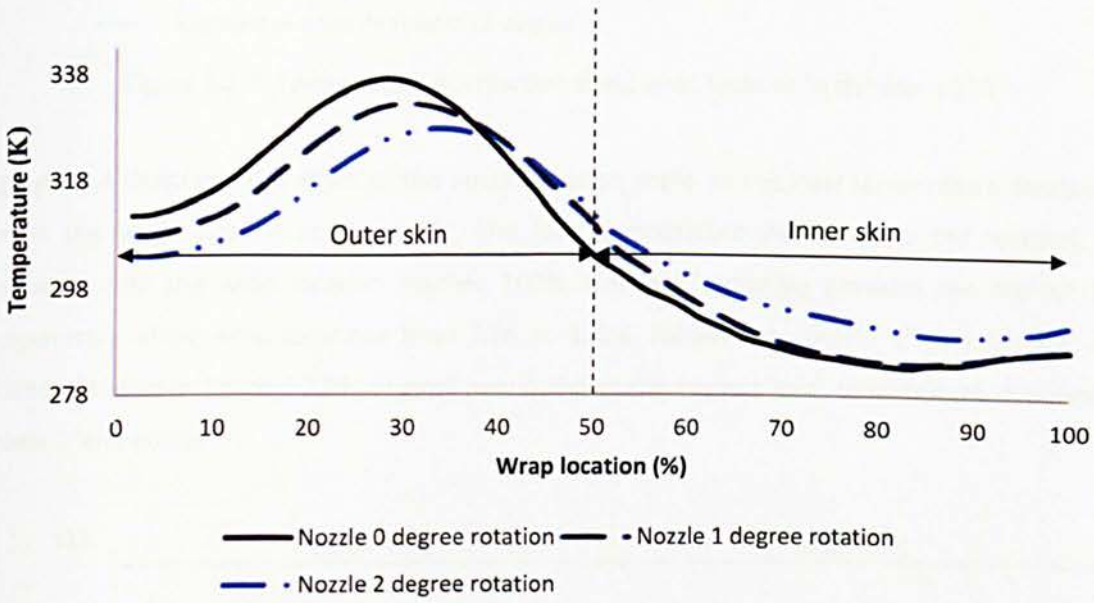

Figure 6.2.2: Temperature profile along wrap location in hotspot plane

Figure 6.2.3 illustrates the local temperature distributions of three different nozzles in plane 270°. The rotation angles do not change the trend of local temperature distribution. Before wrap location of 35%, the local temperature is highest for 0° followed by 1° and 2°. Thereafter, the local temperatures for 1° and 2° become higher than that for 0° and this trend is maintained until wrap location of 88% following which the temperature for nozzle 1 drops and approaches to that for the original nozzle.

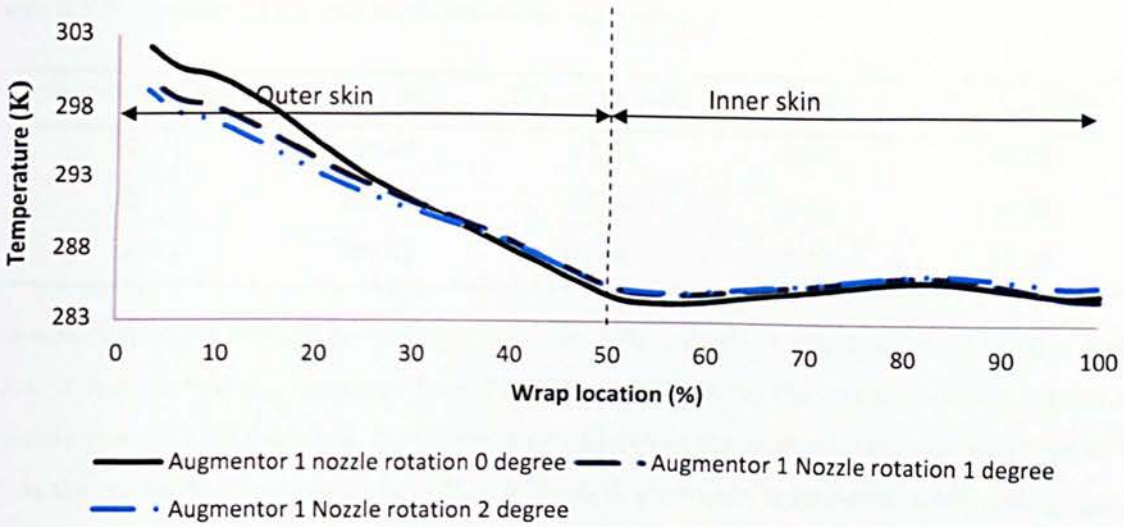

Figure 6.2.3: Temperature distribution along wrap location in the plane 270°

Figure 6.2.4 illustrates the effect of the nozzle rotation angle on the local temperature distribution across the wrap location in plane 90°. The local temperature decreases to the minimal, and increases until the wrap location reaches 100%. Nozzle 2° rotation provides the highest local temperature along wrap locations from 22% to 100%, followed by nozzle 1° and 0°. For wrap locations between 3% and 22%, original nozzle shows the highest local temperature, followed by nozzle 1°and nozzle 2°.

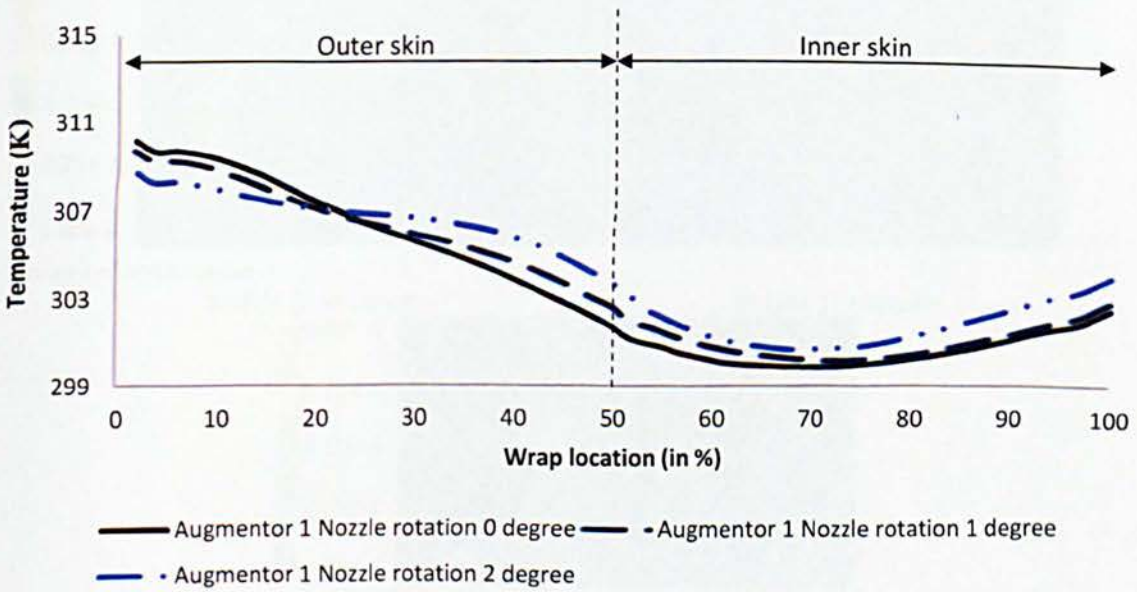

Figure 6.2.4: Local temperature profile along wrap location in plane 90° for Augmentor 1

Table 6.2.1: Summary of thermal performance for Augmentor 1

Nozzle rotation angle (°)	T_{ave} (K)	$(T_{hi} - T_{lo})$ (K)	σ (K)	$C_{tem\ deviation}$ (%)
0	290.01	57.73	10.06	42.49
1	290.29	52.44	9.56	39.90
2	290.51	47.44	8.82	35.48

The summary of the thermal performance for three different nozzle directions is recorded in Table 6.2.1. It is clear that T_{ave} increases from 290.01K to 290.51K as the nozzle direction rotates 2° towards inner skin. Furthermore, $T_{hi} - T_{lo}$ decreases 10.29K as the rotation angle increases from 0° to 2°. As the nozzle direction rotates from 0° to 2° towards inner skin, σ decreases 1.24K and $C_{tem\ deviation}$ drops 7.01%, which means that the nozzle rotation towards the inner skin enhances the uniformity of temperature distribution along the nacelle lip-skin.

The results show that the nozzle rotation angle moves T_{hi} from plane 165° to 173°. As shown in Figure 6.2.5, the jet of original nozzle seems to deviate towards the outer skin, which results in T_{hi} occurring in plane 165°. However, the jet of nozzle 2° is directed towards the inner skin, and T_{hi} of nozzle 2° occurs in plane 173°. As a result, the nozzle 2° shows the lowest T_{hi} because the hot air from it reaches the skin late compared to the other cases.

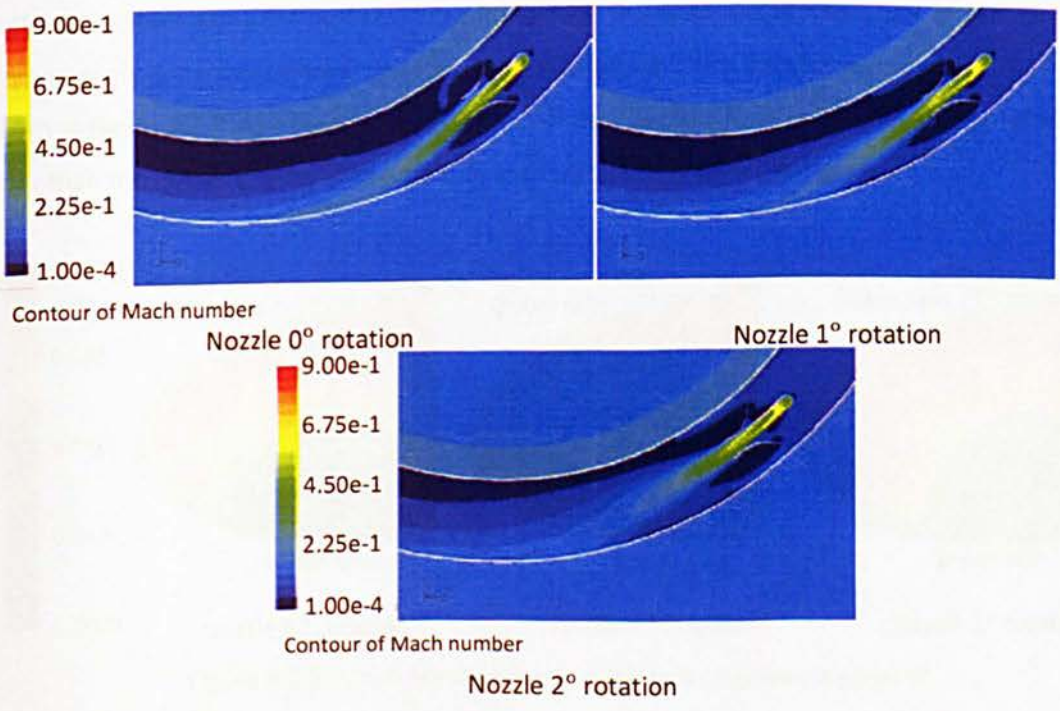

Figure 6.2.5: Air Mach number contour in augmentor vicinity

As the jet from nozzle 2° flows close to the augmentor wall 2, Gap 1 becomes larger than Gap 2. The heat and momentum exchanges in Gap 1 are therefore higher than those in Gap 2, resulting in higher Mach number drop in Gap 1. Therefore, the jet exiting from the augmentor seems to deviate towards the inner skin, as shown in Figure 6.2.6. The Z for nozzle 2° is longer than that for nozzle 0°. As a result, nozzle 2° produces the highest T_{ave} (Table 6.2.1) followed by nozzles 1° and 0°.

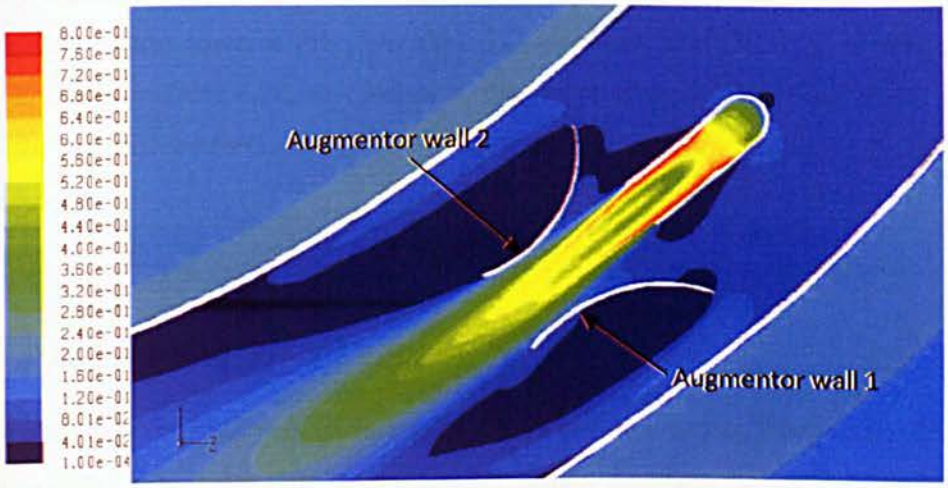

Figure 6.2.6: Air Mach number contour in Augmentor 1 vicinity

It can also be inferred from the results that increase of the nozzle rotation angle causes decrease in local temperature along the outer skin and increase in the inner skin temperature. In fact, the nozzle rotation angle enhances uniform distribution of swirling air Mach number inside the D–chamber, as shown in Figure 6.2.7. As a result, the hot air of nozzle 2° exiting from the augmentor outlet expands wider than the hot air exiting from nozzle 1° and nozzle 0°, as shown in Figure 6.2.5.

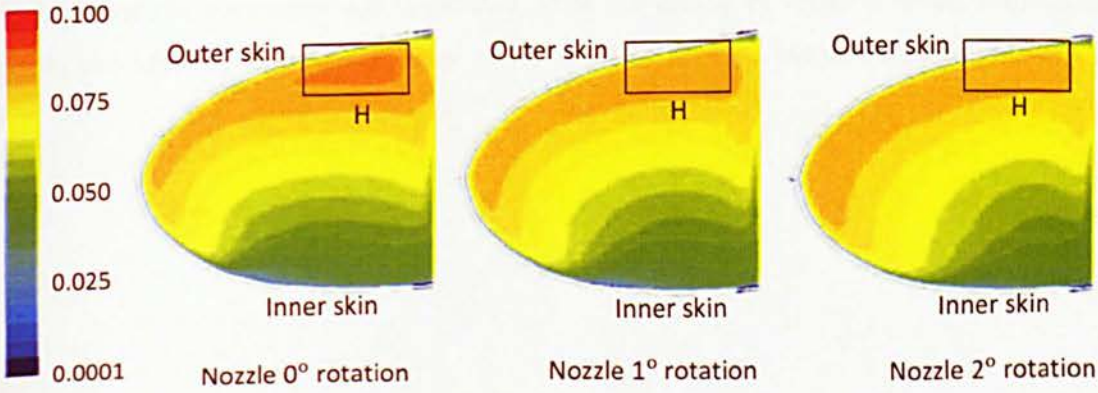

Figure 6.2.7: Mach number contour inside D-chamber in plane 0°

Figure 6.2.7 illustrates that nozzle 2° generates the most uniform distribution of air velocity inside the D-chamber. Therefore, nozzle 2° produces the lowest peak local temperature on the outer skin, followed by nozzles 1° and 0° rotation, as confirmed by Figure 6.2.4. Since nozzle 2° demonstrates the most uniform Mach number distribution of swirling air in the D-chamber, it produces the most uniform Mach number distribution of swirling air in the cold spot plane. As a result, nozzle 2° provides the highest T_{lo} in this section, followed by nozzles 1° and 0° rotation. Furthermore, as the nozzle direction rotates towards the inner skin, T_{ave} increases, and $(T_{hi} - T_{lo})$, σ and $C_{tem\ deviation}$ decrease, as shown in Table 6.2.1. In conclusion, the nozzle rotation of 2° towards the inner skin increases the thermal performance of anti-icing; thus, the nozzle 2° is used in the following augmentor study.

6.3 Effects of Augmentor Features on SAI System

The study discusses the thermal performance of several augmentor designs on the thermal performance of SAI system. Although Augmentor 1 improves the Mach number profile uniformity of swirling air inside the nacelle D-Chamber, it retards the momentum and Mach number of swirling air inside the D-chamber. This happens due to the pressure drop in the augmentor vicinity (Figure 6.3.1), which develops the air vortex behind the augmentor wall, as shown in Figure 6.3.2. This vortex seems to slow down the swirling air crossing the nozzle and the augmentor, though it enhances mixing of hot air and cold air.

In fact, the pressure drop is unavoidable since the augmentor is employed in the SAI system. However, it is known that the thermal performance of SAI normally increases as the volume of vortex behind the augmentor wall is reduced. Since the volume of vortex is reduced, the average velocity and Mach number of swirling air increase, which prevents momentum loss of the swirling air.

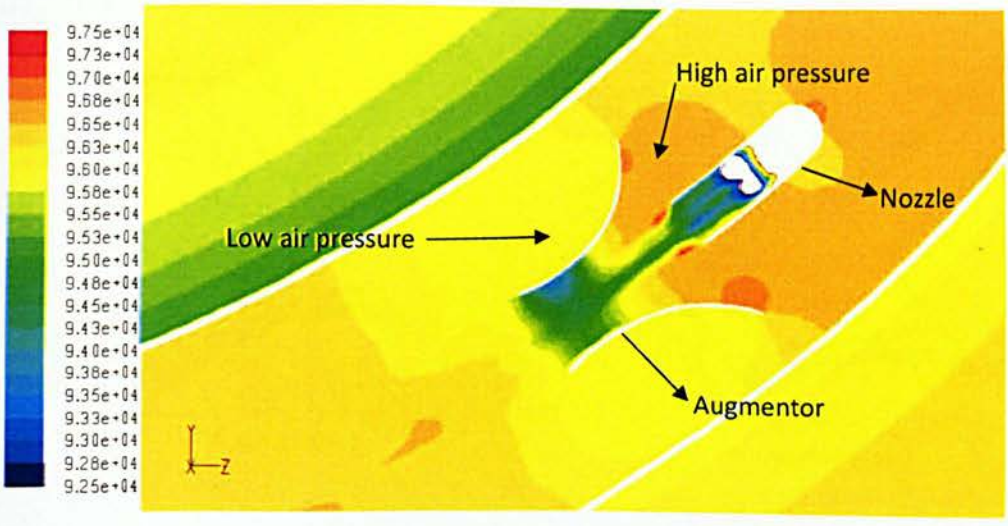

Figure 6.3.1: Air pressure contour in augmentor vicinity

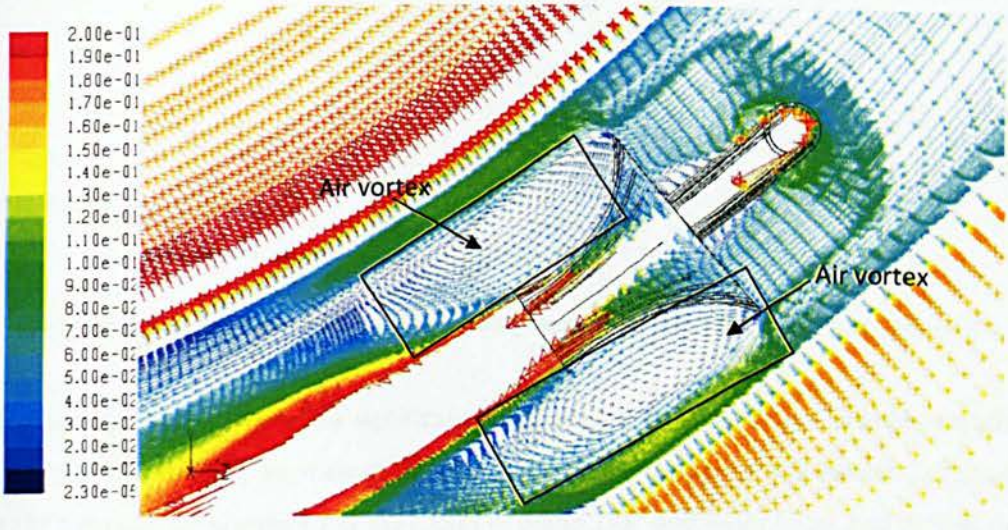

Figure 6.3.2: Mach number vector in augmentor vicinity

The thermal performances of three different augmentor designs are presented in this section. The augmentor dimensions are depicted in Figure 6.3.3. The small nozzle (nozzle diameter of 0.009144m) at 2° rotation towards the inner skin is used to supply the hot air to the D-chamber. The operating parameters such as $m_{hot\ air}$, T_{nozzle}, T_{∞} etc. used in this section are the same as those in section 6.2. The temperature contour, lip-skin temperature profile in three different planes such as T_{hi}, T_{lo} and T_{ave}, and σ and $C_{tem\ deviation}$ are used as thermal performance characteristics in this part.

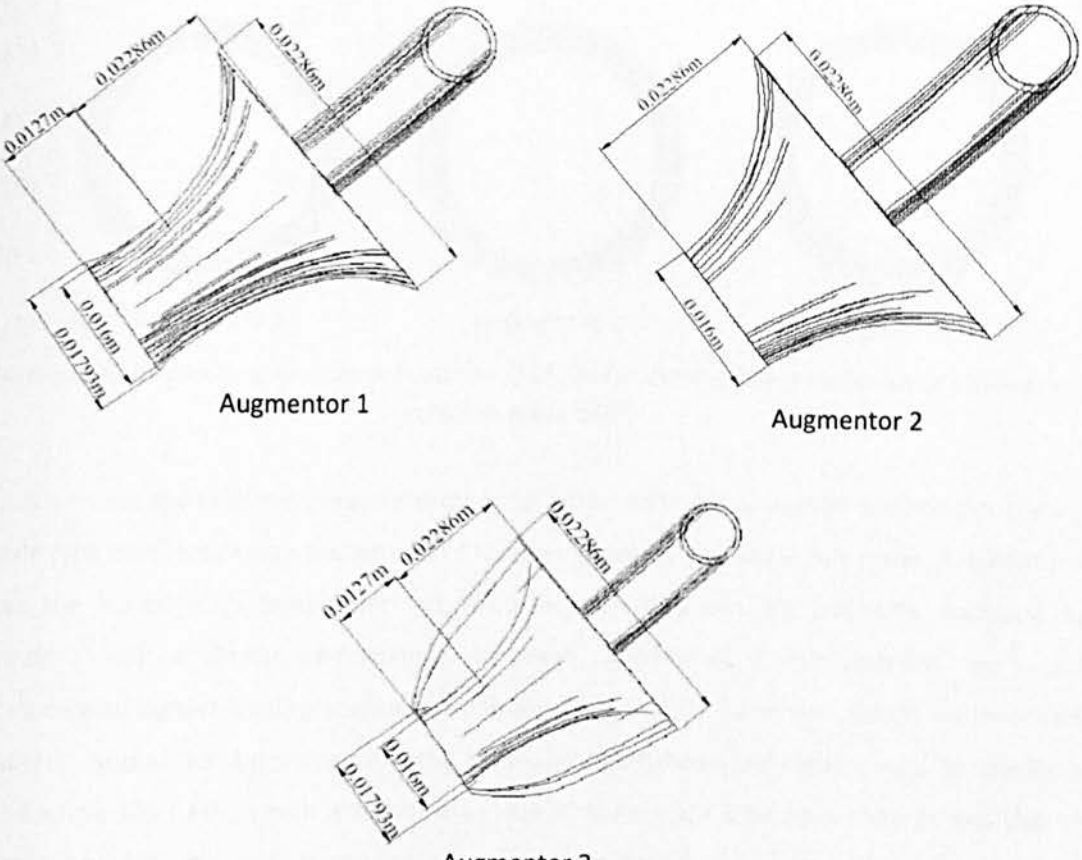

Figure 6.3.3: Schematic illustration of Augment 1, Augmentor 2 and Augmentor 3

According to Figure 6.3.4, there is a significant improvement of temperature distribution along the nacelle lip-skin by changing augmentor design. Augmentor 3 produces the lowest T_{hi} (326.01K) in plane 173° followed by Augmentor 1 (327.83K) in plane 173° and Augmentor 2 (336.33K) in plane 165°. Also, Augmentor 3 shows the highest T_{lo} (281.26K) followed by Augmentor 1 (280.47K) and Augmentor 2 (279.36K), all of which occur on a plane between 120° and 130°.

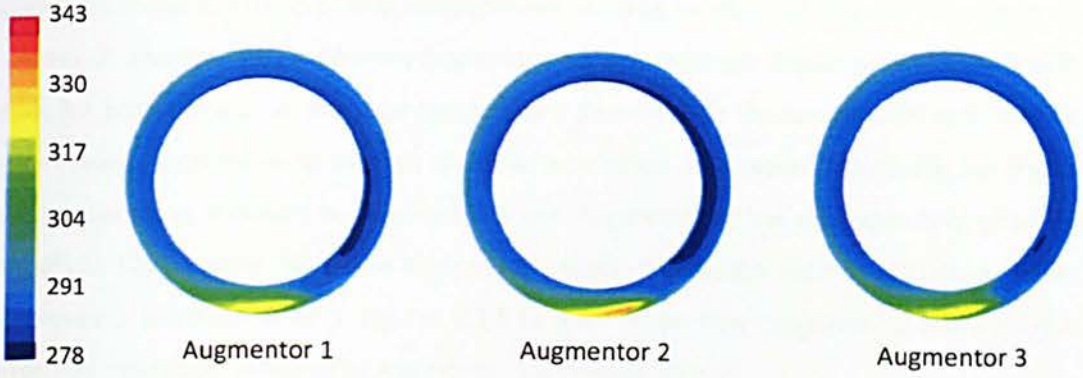

Figure 6.3.4: Lip-skin temperature contour (in K) of SAI for three different augmentors at nozzle rotation angle of 2°

Figure 6.3.5 shows the local temperature profiles for three different designs in the hotspot planes. The nozzle type does not change the pattern of local temperature profiles in this plane. Augmentor 3 produces the lowest local temperature at wrap location between 3% and 42%, followed by Augmentor 1 with a similar performance. However, Augmentor 2 demonstrates the worst performance with highest local temperature along almost the entire outer skin. When the inner skin is considered, Augmentor 3 demonstrates the advantages and shows the highest local temperature along the whole inner skin, which is higher than that of Augmentor 1 by more than 9K and that of Augmentor 2 by 18K. However Augmentor 3 produces the lowest local temperature on the outer skin.

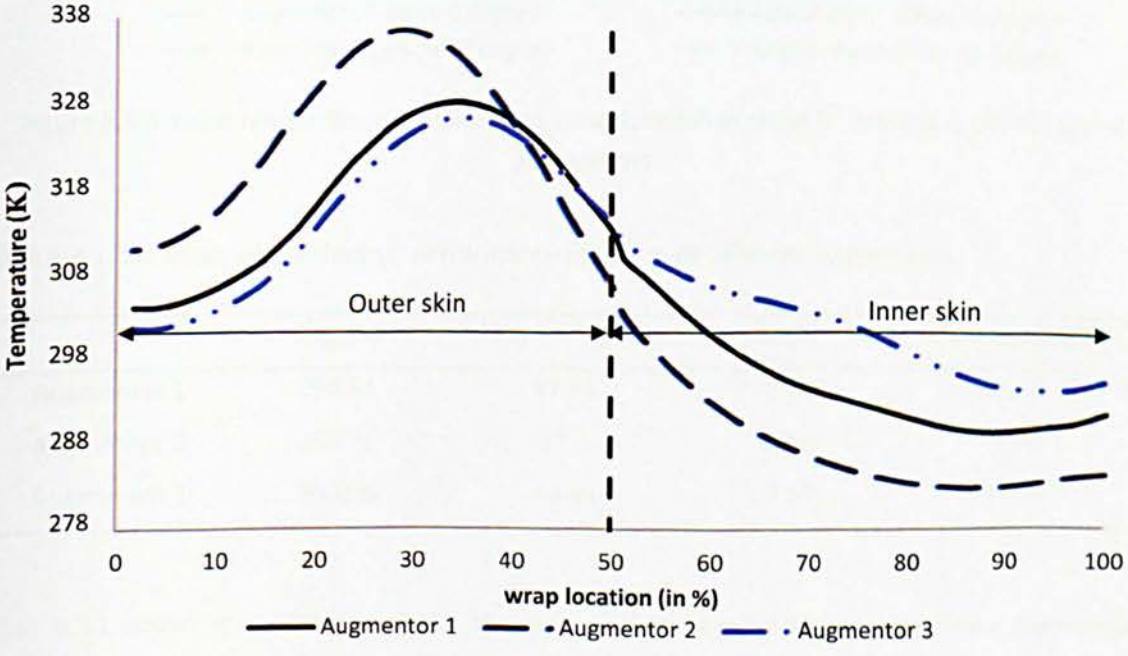

Figure 6.3.5: Local temperature distribution along wrap location in the hotspot plane for various augmentors

Figure 6.3.6 shows the trend of local temperatures vs. wrap location for different augmentor designs in planes 0° and 90°. Three different Augmentor designs illustrate similar temperature distribution trends for both planes; i.e. the local temperature decreases to the lowest local temperature, and then increases until the wrap location of 100%. In addition, Augmentor 3 generally has the highest local temperatures followed by Augmentor 1 and Augmentor 2; the exception is at wrap location from 0% to 12% in plane 90° where Augmentor 2 shows the highest local temperature, followed by Augmentor 3 and Augmentor 1. Figures 6.3.5 to 6.3.7 reveal that Augmentor 3 produces the most uniform temperature, followed by Augmentor 1 and Augmentor 2.

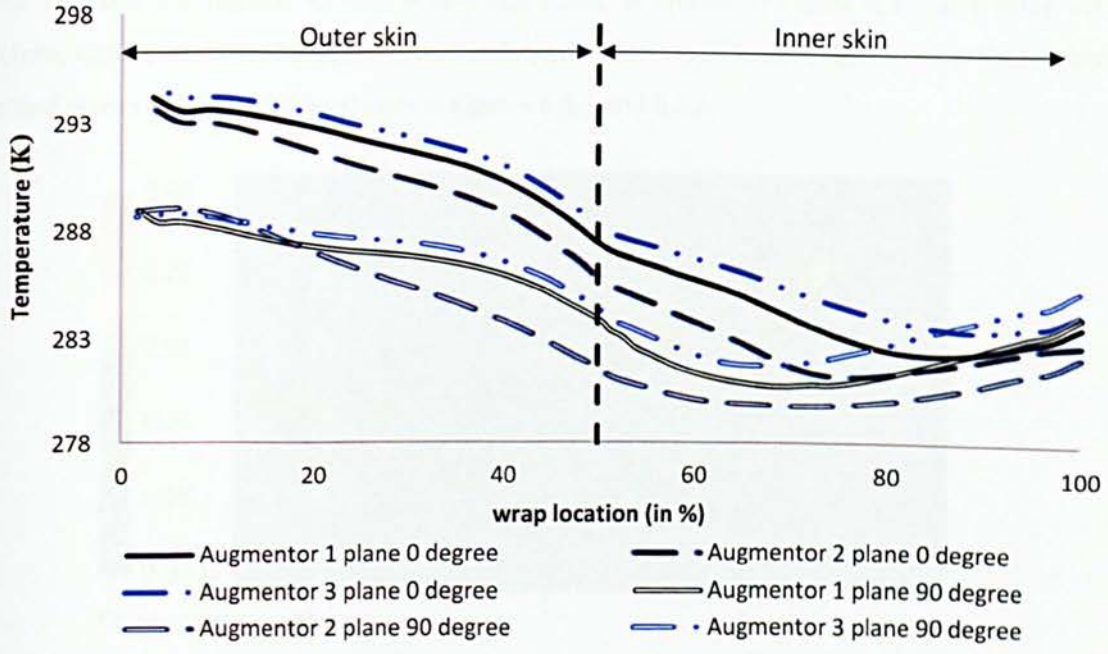

Figure 6.3.6: Local temperature profiles along wrap location in plane 0° and plane 90° for various augmentors

Table 6.3.1: Summary of the thermal performance for SAI with different augmentors

	T_{ave}(K)	$(T_{hi} - T_{lo})$ (K)	σ (K)	$C_{tem\ deviation}$ (%)
Augmentor 1	290.51	47.44	8.82	36.48
Augmentor 2	289.71	57.1	10.01	42.82
Augmentor 3	290.96	44.94	8.52	34.60

Table 6.3.1 shows the summary of the thermal performances of SAI for the three augmentor designs. It shows that Augmentor 3 produces the highest T_{ave} (290.96K) followed by Augmentor 1 (290.51K) and Augmentor 2 (289.71K). The lowest $T_{hi} - T_{lo}$ is shown by Augmentor 3 and the highest

by Augmentor 2. In addition, Augmentor 2 produces the highest σ and $C_{tem\ deviation}$, followed by Augmentor 1 and Augmentor 3.

Figure 6.3.7 shows that the jet from the nozzle hits at the side wall of Augmentor 2 before it flows out. Then, hot air seems to reflect towards the outer skin due to Augmentor 2 having no diffuser section. Therefore, Z of Augmentor 2 is shorter compared to Augmentor 1 and Augmentor 3. As a result, Augmentor 2 produces the highest T_{hi}, and exhibits the worst air mixing process. Thus, the average Mach number of swirling air and Mach number of swirling air in the cold spot plane for Augmentor 2 are the lowest in the present study. Consequently, Augmentor 2 produces the lowest T_{lo} and T_{ave}, and the highest $T_{hi} - T_{lo}$, σ and $C_{tem\ deviation}$ as shown in Figure 6.3.1 and Table 6.3. Therefore, Augmentor 2 produces the worst uniform distribution of local temperature in the hotspot plane and planes of 0° and 90°, as shown in Figures 6.3.5 and 6.3.6.

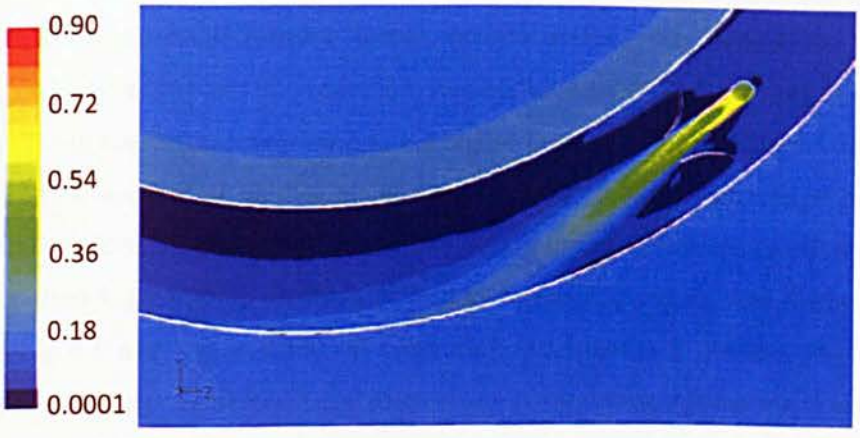

Figure 6.3.7: Mach number contour in Augmentor 2 vicinity

It is worth noting that Augmentor 3 produces lower T_{hi} than that of Augmentor 1 despite both having the same hotspot plane. This is due to hot air Mach number distribution between augmentor outlet and impinging surface being more uniform for Augmentor 3 than for Augmentor 1, as shown in Figure 6.3.8. Thus, Augmentor 3 produces a lower hot air Mach number gradient on the hotspot surface than Augmentor 1 does, resulting lower T_{hi} (Figure 6.3.5).

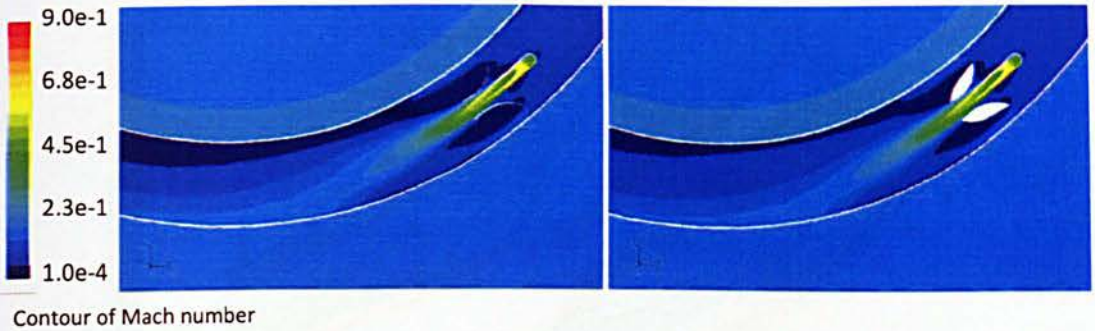

Figure 6.3.8: Air Mach number contour in augmentor and nozzle vicinity

It is well known that airfoil has several advantages compared to other curved shapes. Since it delays flow separation point, the airfoil produces smaller vortex area. Thus, it reduces pressure drop and momentum loss as free stream velocity flows over it [107]. This fact has been demonstrated by - Augmentor 3 which produced smaller vortex volume around the Augmentor compared to Augmentor 1 - (Figures 6.3.9a and b). In addition, Augmentor 3 facilitated relatively better air mixing in D-chamber. These two factors contribute to the higher average Mach number of swirling air in D-Chamber and Mach number of swirling air in the cold spot plane of Augmentor 3 compared to Augmentor 1. Therefore, Augmentor 3 shows the best uniform temperature distribution on the nacelle lip-skin than Augmentor 1, as characterized by higher T_{ave} and T_{lo}, and lowest T_{hi}-T_{lo}, σ and $C_{tem\ deviation}$ (Table 6.3 and Figure 6.3.4). In conclusion, Augmentor 3 provides the best thermal performance, followed by Augmentor 1 and Augmentor 2. Therefore, Augmentor 3 was used in the following study.

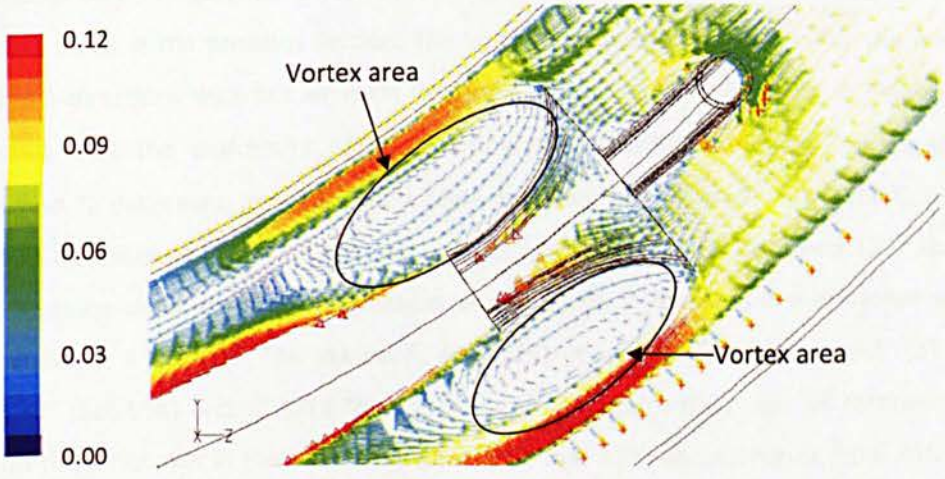

Figure 6.3.9a: Air Mach number vector in Augmentor 1 vicinity

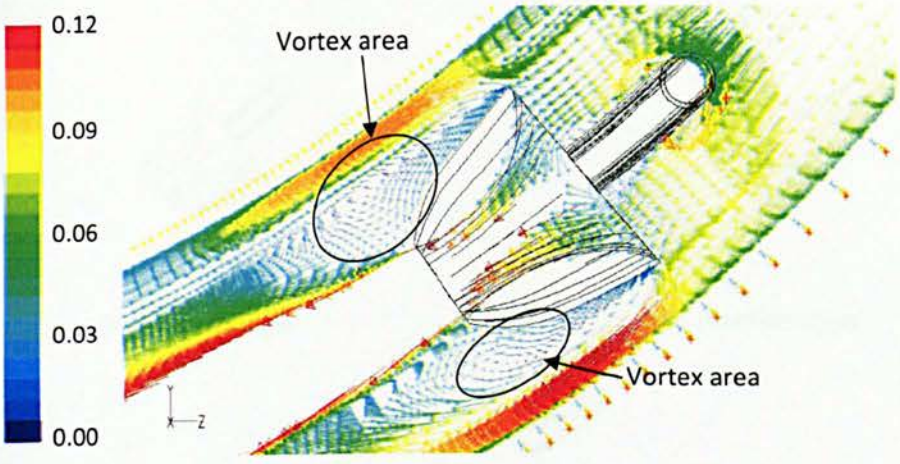

Figure 6.3.9b: Air Mach number vector in Augmentor 3 vicinity

6.4 Effect of Augmentor Rotation Angle to Thermal Performance of SAI Systems

In this part of the study, the directions of both the augmentors and the nozzle were altered towards the inner skin in order to enhance the thermal performance of SAI. Directing the flow towards the inner skin increases Z and hence T_{ave} and T_{lo}, and decreases T_{hi}. Therefore, several rotation angles were investigated. Two different $m_{hot\ air}$, 0.0118kg/s and 0.0236 kg/s, were used in the study, while other operating conditions such as T_{nozzle}, T_{∞} etc., were not changed. The thermal performance of five different augmentor rotation angles such as 0°, 2°, 3°, 4° and 7° were analysed.

Figure 6.4.1 shows the orientation of augmentor rotation angle towards inner skin. The performance characteristics used to study the thermal performance for various augmentor rotation angles were the same as those in the previous section. The lip-skin temperature contours for the five different Augmentor 3 directions with hot air mass flow rate of 0.0118kg/s are shown in Figure 6.4.2. The results show that the uniformity of local temperature distribution along the nacelle lip-skin improves, and T_{hi} decreases, as the rotation angle increases from 0° to 4°; however T_{hi} increases as the rotation increases to 7. For all the cases, T_{hi} occurs in the planes between 173° and 185°. In addition, T_{hi} is on outer surfaces for rotation angles up to 3° whereas it is on inner surface for rotation angles at 4° and 7°. The lowest T_{hi} (312.12K) occurs at 4° followed by 3° (313.11K), 2° (315.18K), 0° (326.05K) and 7° (326.76K), as shown is in Figure 6.4.2. For all rotation angles T_{lo} appears on the inner skin in the planes between 120° and 123° and increases from 281.16K up to 282.64K from 0° to 4°, and then drops to 282.27K as the angle increases to 7°.

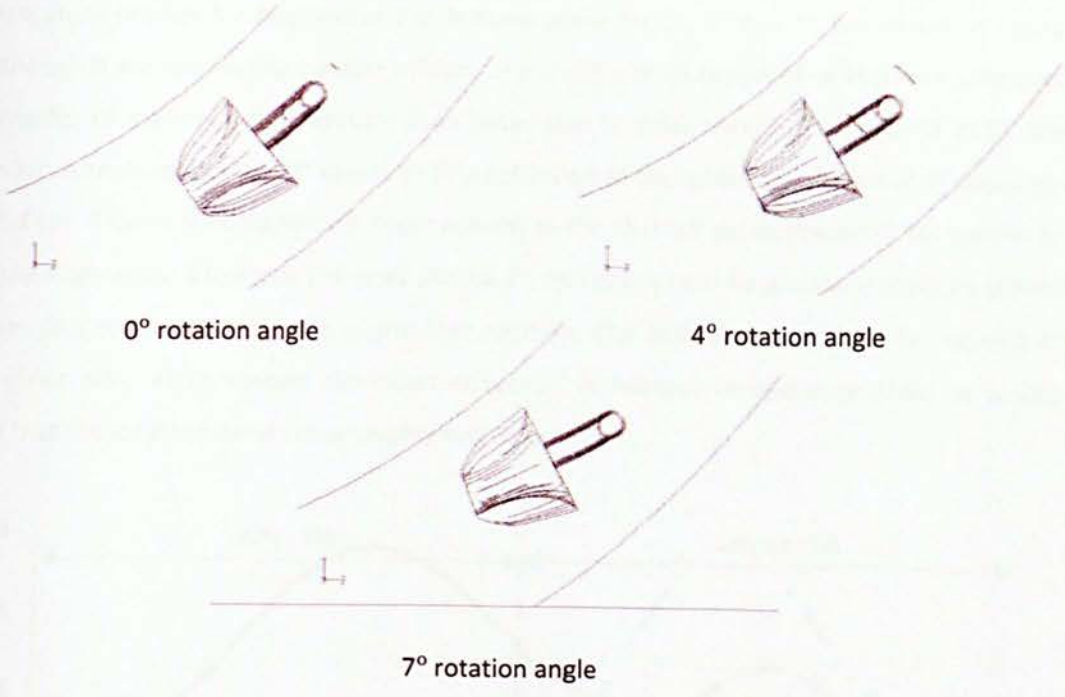

Figure 6.4.1: Orientations of Augmentor 3 at three different rotation angles

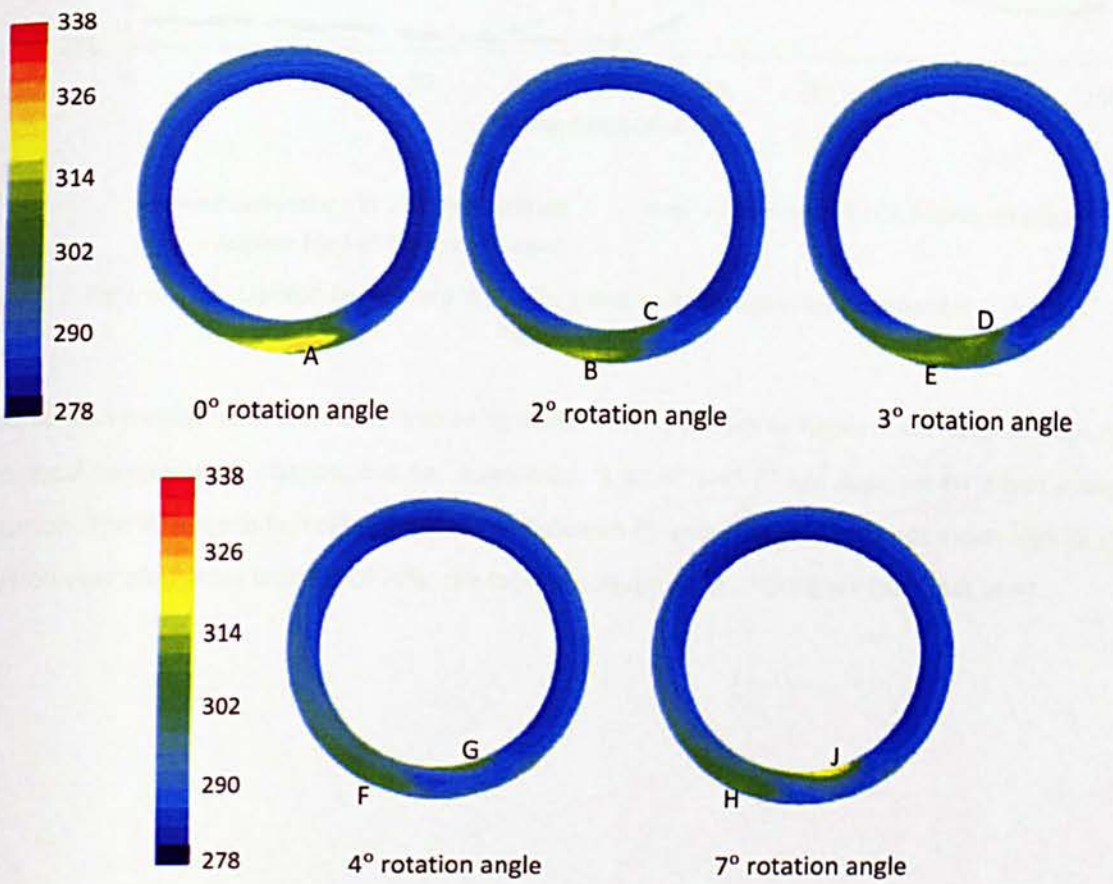

Figure 6.4.2 Lip-skin temperature contour (in K) for different rotation angles of Augmentor 3

The temperature profiles for Augmentor 3 in hotspot plane for 0°, 4° and 7°, are shown in Figure 6.4.3. Although there are two favourable effects, a) a slight overall reduction in local temperatures and b) transfer of maximum temperature from outer skin to inner skin at 7° compared to 0°, the local temperature distribution at 7° seems to be a reflection of the local temperature at 0° about the Highlight. Even if there is no significant improvement to the thermal performance of SAI system by rotating the Augmentor 3 towards the inner skin by 7°, maximum local temperature could be shifted from outer skin to inner skin by the augmentor rotation. This is further confirmed by rotating 4° towards inner skin, which caused significant reduction in hotspot temperature (14K). It is also observed that the local temperature is roughly kept constant.

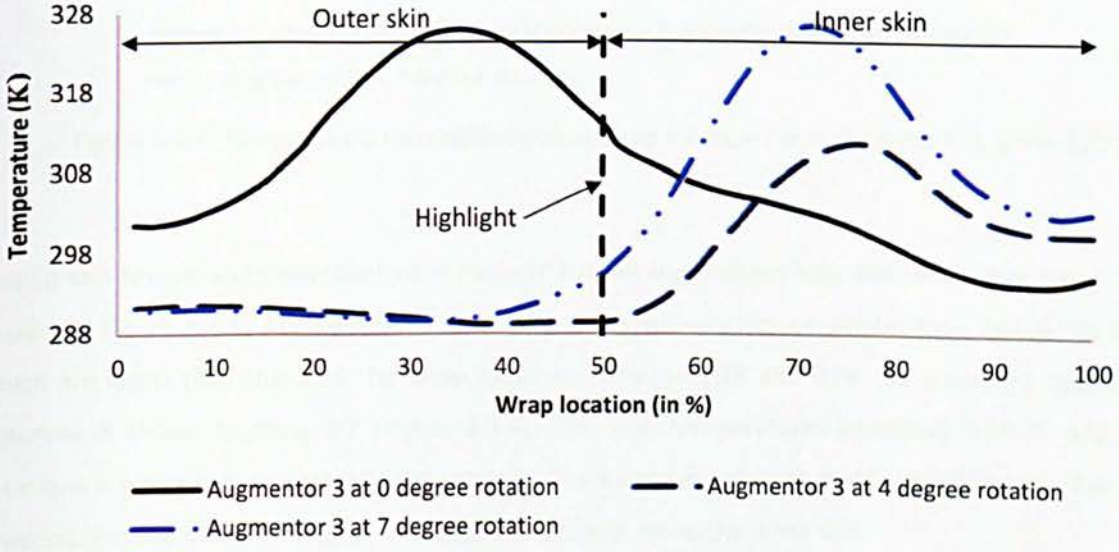

Figure 6.4.3: Lip-skin temperature profile along wrap location for Augmentor 3 in the hotspot plane

The lip-skin local temperature distribution in plane 270° is shown in Figure 6.4.4. It is obvious that the local temperature distributions for Augmentor 3 at 4° and 7° are superior to those without rotation. The difference in local temperatures between 4° and 7° is generally not much high (2 to 3 K); however after wrap location of 70%, the local temperature at 7° is higher than that at 4°.

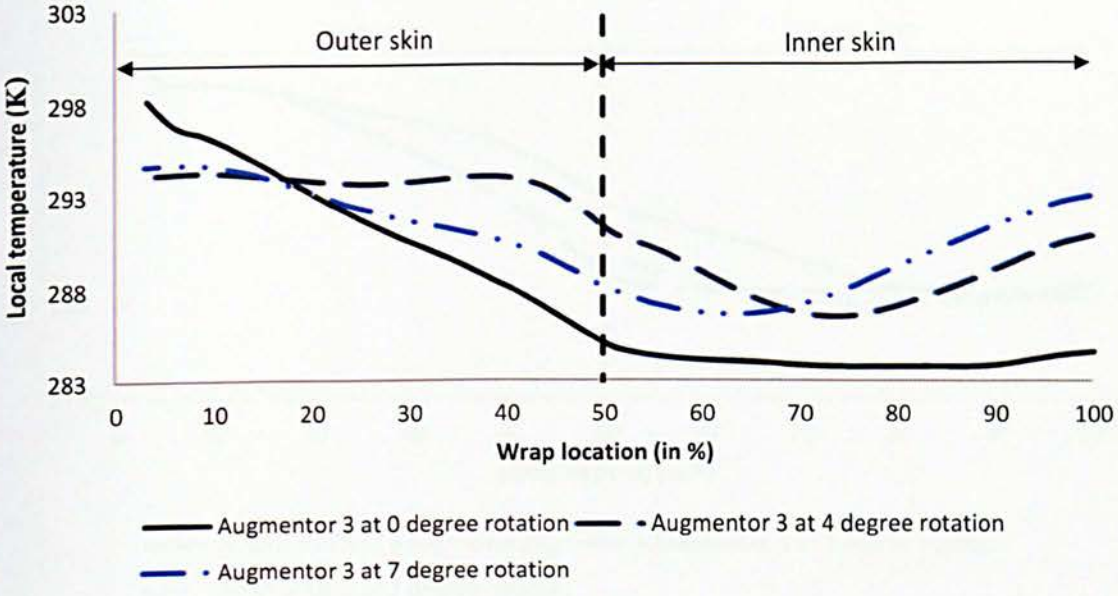

Figure 6.4.4: Temperature distribution across wrap location for Augmentor 3 in plane 270°

The lip-skin temperature distributions in plane 0° for the augmentors 3 for the same three cases are shown in Figure 6.4.5. Augmentors 3 at 4° and 7° rotations produce similar local temperatures, which are lower than that at 0° for wrap locations between 19% and 83%. However, the opposite outcome is shown in plane 90° (Figure 6.4.6). The local temperatures produced with 4° and 7° rotations are higher than that without rotation. The local temperature at 4° should be regarded as *favourable* compared with that at 7° *because* it is higher along the inner skin.

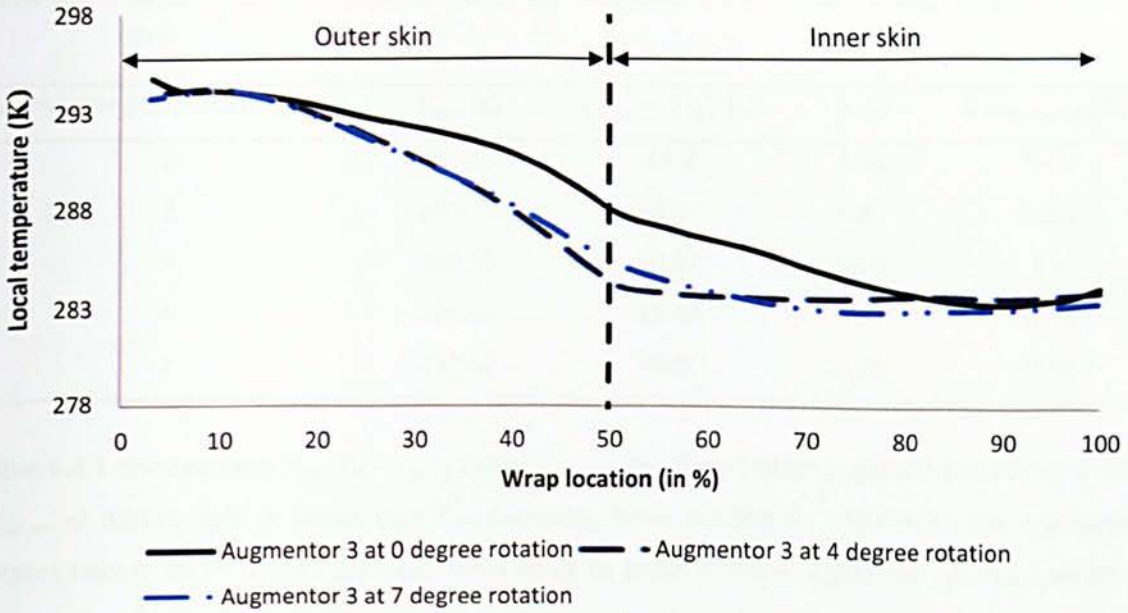

Figure 6.4.5: Lip-skin temperature profile against wrap location in plane 0°

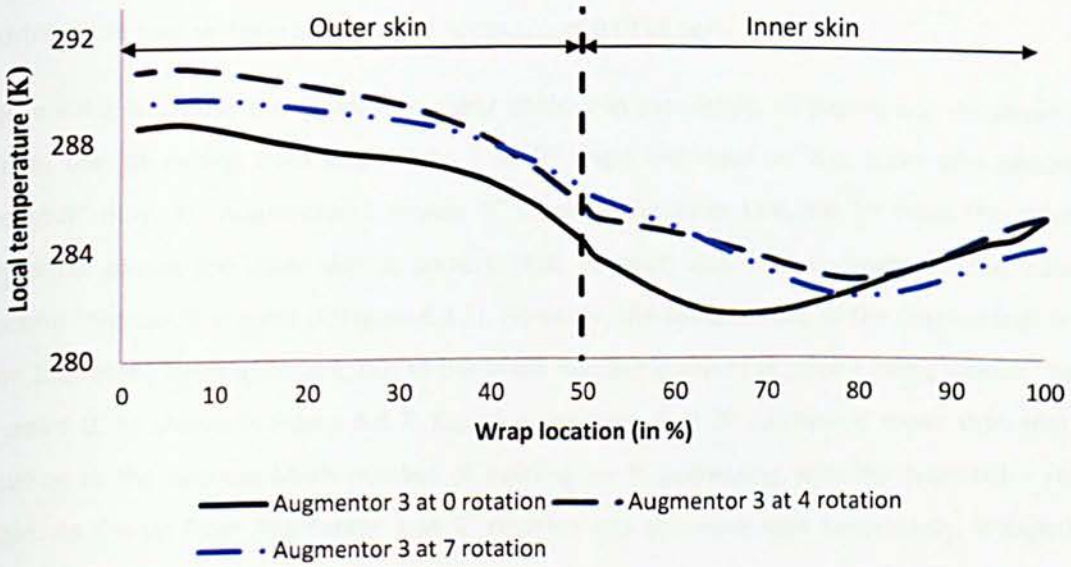

Figure 6.4.6: Temperature profile vs. wrap location for Augmentor 3 in plane 90°

Table 6.4.1: Summary of thermal performance with Augmentor 3 at various rotation angles in Part One

Augmentor 3 Rotation angle (°)	T_{ave}(K)	$(T_{hi} - T_{lo})$ (K)	σ (K)	$C_{tem\ deviation}$ (%)
0	290.96	44.9	8.52	34.6
2	290.74	33.12	6.47	26.51
3	290.65	30.57	6.08	25
4	290.64	29.48	5.72	23.53
7	290.62	44.5	6.72	27.59

Table 6.4.1 demonstrates T_{ave}, $T_{hi} - T_{lo}$, σ and $C_{tem\ deviation}$ for five rotation angles of Augmentor 3 with $m_{hot\ air}$ of 0.0118 kg/s. It shows that T_{ave} decreases from 290.96K to 290.62K as the augmentor rotates from 0° to 7°. $T_{hi} - T_{lo}$ decreases from 44.9K to 29.5K with the augmentor rotates from 0° to 4°, and then increases to 44.5K as the augmentor further rotates from 4° to 7°. σ shows a similar trend with $T_{hi} - T_{lo}$; decreasing from 8.52K to 5.72K, and then increasing to 6.72K. $C_{tem\ deviation}$ decreases from 34.6% to 23.53% as the augmentor rotates from 0° to 4° and then rises up to 27.59% as the augmentor rotates further to 7°. Thus it is concluded that Augmentor 3 at 4° rotation produces the best uniform temperature for $m_{hot\ air}$ of 0.0118 kg/s.

Figure 6.4.7 illustrates the air Mach number contour in the vicinity of augmentor. As shown in the figure, the jet exiting from Augmentor 3 at 0° angle impinges on the outer skin causing one "hotspot" only. As Augmentor 3 rotates 3° towards the inner skin, the jet from the augmentor tangential passes the inner skin at point E (first hotspot) and then impinges on the outer skin (second "hotspot") at point D (Figure 6.4.2). However, the temperature of the first hotspot is lower than that of the second hotspot, due to the Mach number gradient at point E being smaller than that at point D, as shown in Figure 6.4.7. T_{ave} of Augmentor 3 at 3° rotation is lower than that at 0° rotation as the average Mach number of swirling air is decreasing with the augmentor rotation angle. As the jet from Augmentor 3 at 3° rotation hits the inner skin tangentially, it experiences higher momentum loss.

The effect of jet impinging tangentially on the inner skin becomes obvious as the rotation angle increases to 4°. The first hotspot temperature at point G is slightly higher than the second hotspot temperature at point F (Figure 6.4.2). Moreover, T_{ave} of the nacelle lip-skin reduces to 290.64K as the rotation increases to 4°. For 7°, the temperature of the first hotspot is much higher than the second hotspot. T_{ave} of Augmentor 3 at 7° is the lowest as shown in Table 6.4.1.

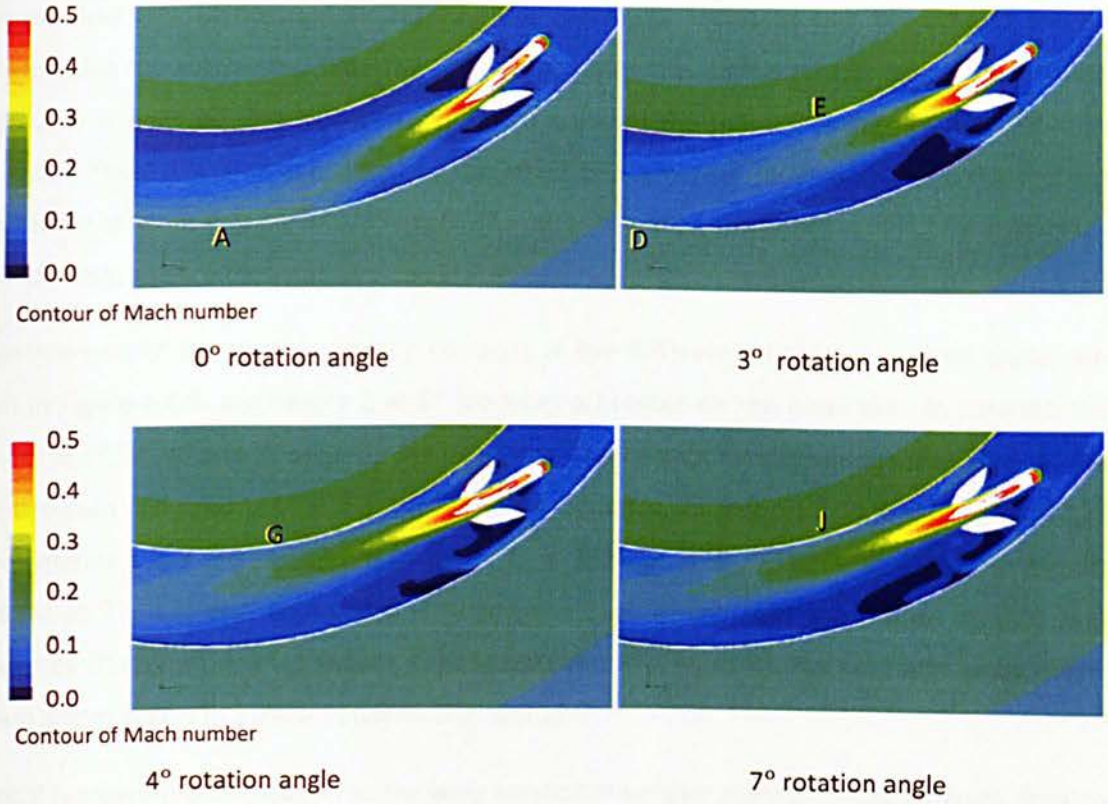

Figure 6.4.7: Air Mach number contour in Augmentor 3 vicinity at four different augmentor rotation angles

The T_{lo} increases from 281.16K to 282.64K as the augmentor rotation increases from 0° to 4°, since the hot air is directed more towards inner skin at 4° rotation. However, T_{lo} slightly drops to 282.27K because the hot air is over-directed towards the inner skin. Therefore, the impingement causes too much momentum loses, which leads to a severe Mach number drop of the swirling air in the cold spot plane as the rotation angle increases to 7°. When the angle is less than 4°, the temperature distribution along the lip-skin is more uniform, which is characterized by the decrease of $T_{hi} - T_{lo}$ with increase of rotation angle. However, $T_{hi} - T_{lo}$ increasing tremendously as the augmentor rotation increases further to 7°, which shows that the uniformity of the temperature distribution along the lip-skin deteriorates.

In Part One ($m_{hot\ air}$ of 0.0118kg/s), it can be concluded that the anti-icing performance increases with the increase of augmentor rotation angle until 4°. This is demonstrated by the phenomena of tangential impingement of jet on the inner skin, the increase of the temperature along the inner skin and the decrease of the temperature difference between the hotspot and cold spot. However, over-rotating the augmentor towards lip-skin to 7° diminishes the thermal performance.

The air pressure inside the augmentor influences the thermal performance of SAI with augmentor. The mass flow rate of the cold air entering the augmentor increases with decrease of the air pressure inside the augmentor. Since the air pressure inside the augmentor decreases with increase of $m_{hot\ air}$, it is believed that higher $m_{hot\ air}$ would enhance the thermal performance of SAI with augmentor. Thus, this is demonstrated by the effect of augmentor rotation angle on the thermal performance of SAI at $m_{hot\ air}$ of 0.02354 kg/s. The other operating conditions in Part 2 i.e. augmentor type and nozzle size are the same as those in Part 1.

The comparison of lip-skin temperature contours at five different augmentor rotation angles are shown in Figure 6.4.8. Augmentor 3 at 0° produces a hotspot on the outer skin. In contrast, the hotspots at 2°, 3°, 4° and 7° occur on the inner skin. The hotspot location moves backwards to the plane between 160° and 165° as the rotation angle increases. T_{hi} reduces from 348.59K to 347.22K as the rotation angle increases from 0° to 2°. T_{hi} is 352.41K at 3°, 353.96K at 4°and the highest (354.93K) at 7°. It is also observed that Augmentor 3 at 2° produces the highest T_{lo} (301.14K) followed by 0° (300.91K), 3° (300.16K), 4° (298.80K) and 7° (298.25°C). The cold spot for all nozzle rotation angles occurs in a plane between 120° and 121°.

The local temperature distribution across wrap location in hotspot plane for three different rotation angles is shown in Figure 6.4.9. All the curves have a similar trend, i.e. increasing to the peak temperature before decreasing gradually with wrap location until 100%. Augmentor 3 at 0° produces the highest temperature on the outer skin, followed by 2° and 7° with maximum temperature differences of 22K. The local temperature of Augmentor 3 at 7° is the highest on the inner skin, followed by 2° and 0° with the maximum temperature differences of 16.2K. However, 2° has the most uniformly distributed temperature in hotspot plane.

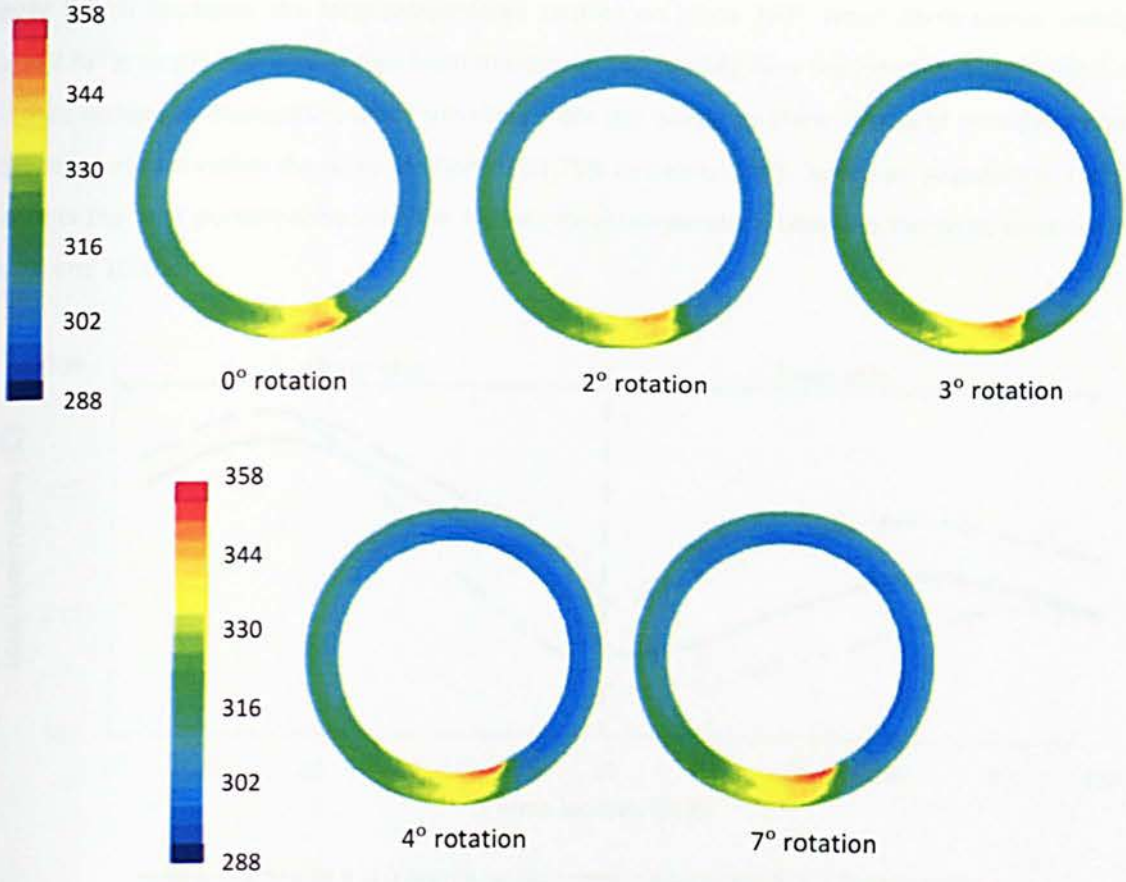

Figure 6.4.8: Lip-skin temperature contour for various Augmentor 3 rotation angles at $m_{hot\ air}$ of 0.02354 kg/s

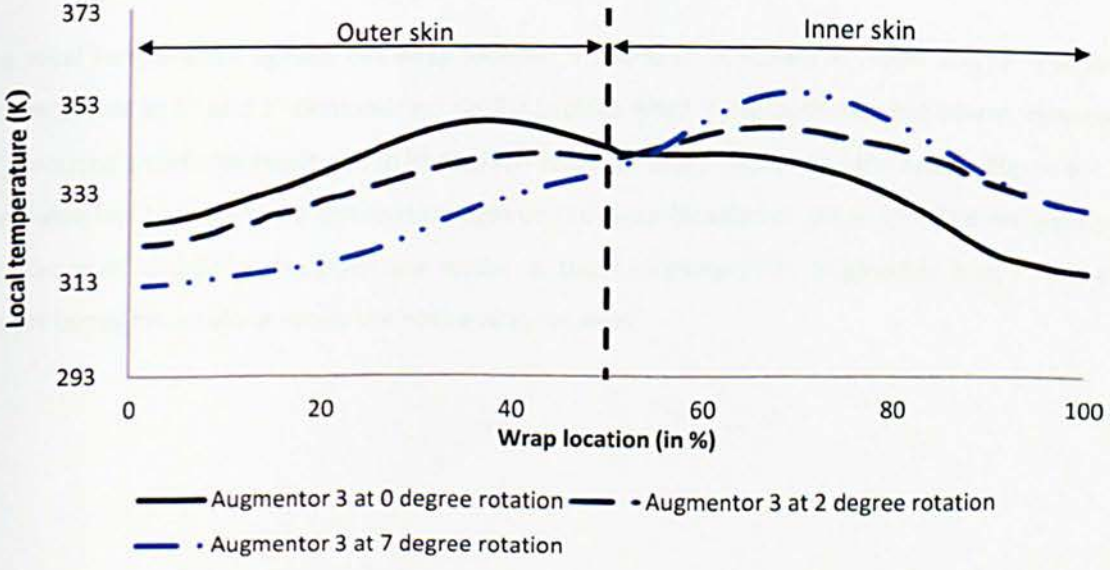

Figure 6.4.9: Temperature distribution along wrap location of Augmentor 3 in hotspot plane

Figure 6.4.10 illustrates the local temperature profiles on plane 270°, which show similar trends. Plane 270° is nearly half way farther from the nozzle; the swirling flow produced by Augmentor 3 at 7° loses maximum momentum while travelling from the nozzle to Plane 270° and provides lowest local temperature within the wrap location of 23.75% to nearly 100%. However, Augmentor 3 at 2° presents the best performance with the highest local temperature between the wrap locations of 19.7% and 100%.

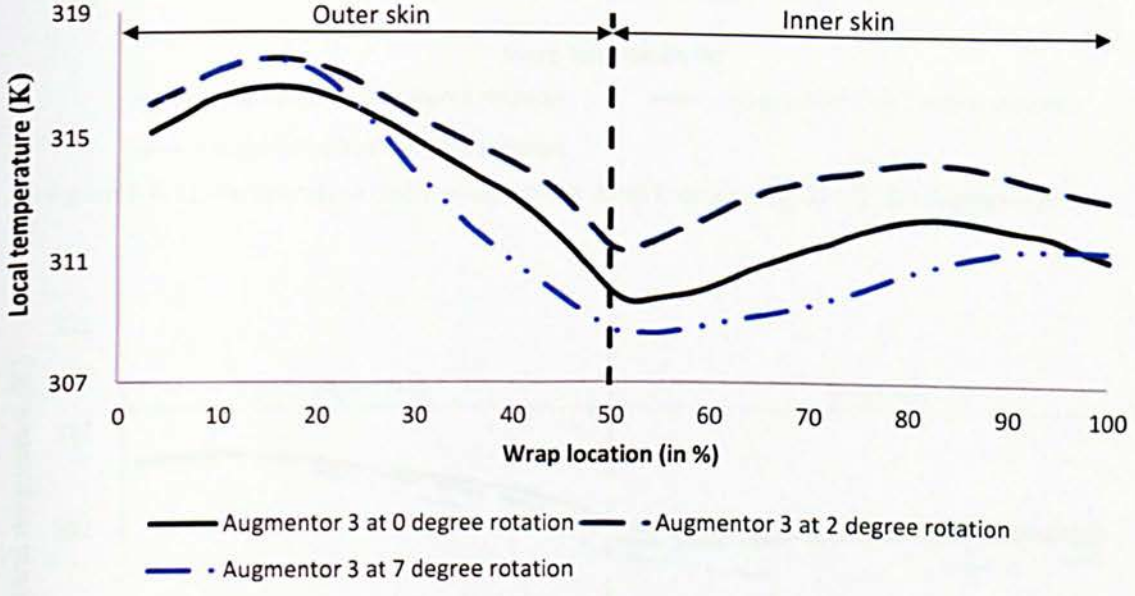

Figure 6.4.10: Local temperature profile against wrap location for Augmentor 3 in plane 270°

The local temperature against the wrap location in plane 0° is shown in Figure 6.4.11. The local temperatures at 0° and 2° demonstrate similar profiles which have both ups and downs. However, 7° produced an inferior result due to its location which is farther away from the nozzle. Figure 6.4.12 illustrates local temperature distribution against the wrap location in plane 90°. The temperature profiles at 0° and 2° in this plane are similar to those in plane 270°. Augmentor 3 at 7° has the lowest temperature along nearly the entire wrap location.

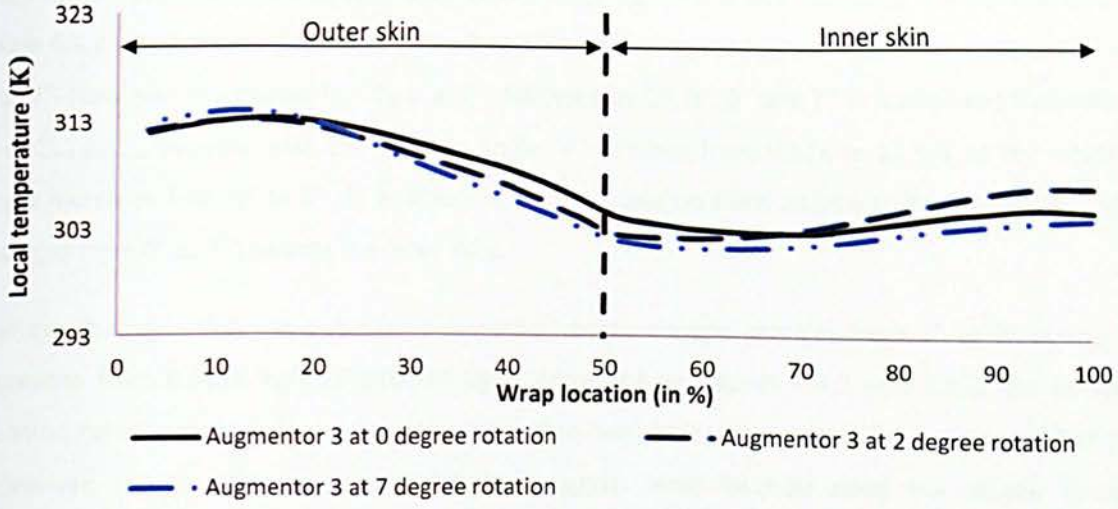

Figure 6.4.11: Temperature distribution across wrap location in plane 0° for Augmentor 3

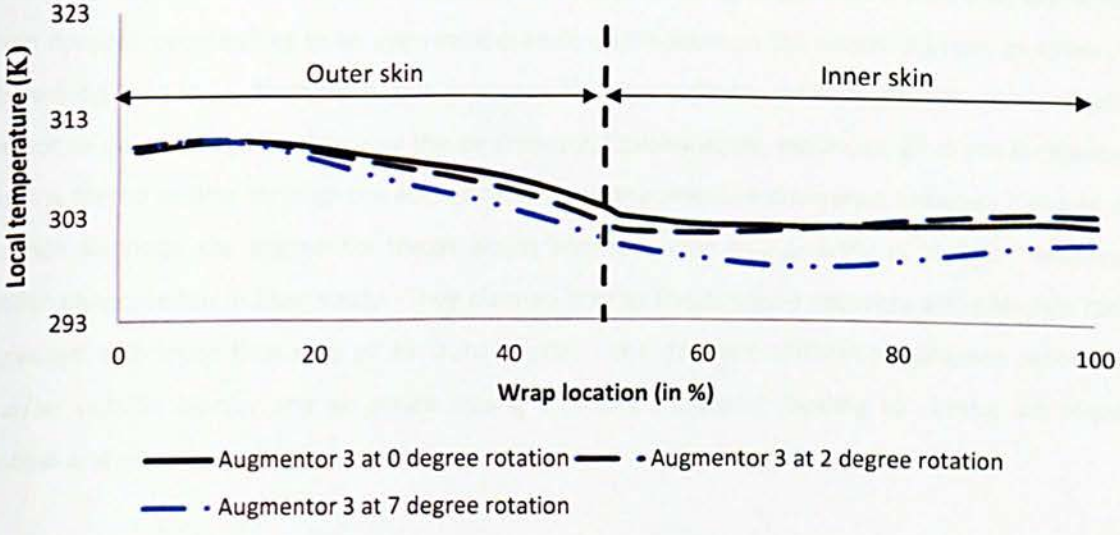

Figure 6.4.12: Temperature distribution along wrap location for Augmentor 3 in plane 90°

Table 6.4.2: Summary of SAI thermal performance with Augmentor 3 at various rotation angles in Part Two

Augmentor 3 rotation angle (°)	T_{ave}(K)	$(T_{hi} - T_{lo})$ (K)	σ (K)	$C_{tem\ deviation}$ (%)
0	312.93	47.68	9.62	20.65
2	313.42	46.07	9.98	21.19
3	313.48	52.24	10.17	21.57
4	312.86	55.16	11.22	24.12
7	312.55	56.68	11.37	24.60

SAI thermal performance characteristics such as T_{ave}, $T_{hi} - T_{lo}$, σ and $C_{tem\ deviation}$, are summarised in Table 6.4.2 which shows that Augmentor 3 at 3° rotation has the highest T_{ave}, followed by 2°, 0°, 4° and 7°. However, the lowest $T_{hi} - T_{lo}$ is at 2°, followed by 0°, 3°, 4° and 7°. It is also seen that both σ and $C_{tem\ deviation}$ increase with the rotation angle. σ increases from 9.62K to 11.37K as the rotation angle increases from 0° to 7°. In addition, $C_{tem\ deviation}$ rises up from 20.65% to 24.60% as the angle changes from 0° to 7° towards the inner skin.

The result shows that the optimum augmentor rotation angle changes from 4° to 2° as $m_{hot\ air}$ increases from 0.0118 kg/s to 0.02534 kg/s. According to Figures 6.4.2 and 6.4.8, the hotspot location completely transforms from the outer skin onto inner skin, except for Augmentor 3 at 0°. Moreover, the local temperature distribution against wrap location along the nacelle lip-skin becomes more uniform as $m_{hot\ air}$ increases from 0.0118 kg/s to 0.02534 kg/s (Figures 6.4.9 to 6.4.12). In addition, at any given rotation angle, $C_{tem\ deviation}$ decreases with $m_{hot\ air}$. This is because the jet with the higher Mach number emerging from the augmentor diverges better than that with lower Mach number, contributing to an even temperature distribution on the nacelle lip-skin, as shown in Figure 6.4.13. As $m_{hot\ air}$ from the nozzle increases, the chock effects at the augmentor throat speeds the hot air up which lead to decrease the air pressure. Consequently, more cold air in the D-chamber is being forced to flow through the augmentor due to the pressure difference between the cold air and hot air inside the augmentor throat which increases with $m_{hot\ air}$. Kong et al. [121] observed similar phenomenon in their study. They claimed that as the pressure recovery and pressure ratio increased with mass flow rate of air from nozzle, - the pressure difference between secondary flow/air outside ejector and air inside mixing chamber increased, leading to better air mixing process and enhanced ejector performance.

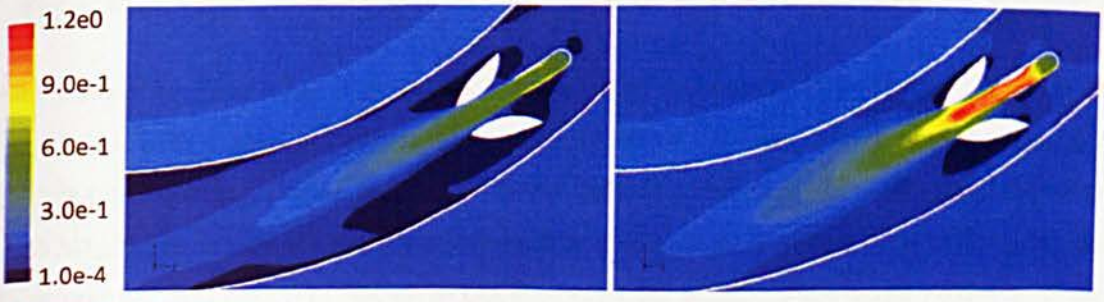

$m_{hot\ air}$ = 0.0118kg/s

$m_{hot\ air}$ = 0.02534kg/s

Figure 6.4.13: Air Mach number contour in Augmentor 3 at 2° rotation for mass flow rates of 0.0118kg/s and 0.02354kg/s

6.5 Comparison between SAI with Augmentor 3 and SAI without Augmentor

The comparison of thermal performance between best nozzle rotation angle (nozzle at 13° rotation) and best augmentor rotation angle is elaborated in this section. Augmentor 3 at 2° is selected because it shows the best thermal performance at $m_{hot\ air}$ of 0.02534 kg/s. In order to simplify the discussion, Model H represents the Circle nozzle at 13° and Augmentor 3 at 2° is denoted by Model J. Four different values of $m_{hot\ air}$ from 0.0118kg/s to 0.04536kg/s at the total temperature of 533K were investigated to compare the thermal performance between Model J and Model H. The parameters used in this comparison were T_{ave}, T_{hi}, T_{lo}, and σ.

Figure 6.5.1 shows the nacelle lip-skin temperature contours for Model J and Model H at $m_{hot\ air}$ of 0.02354kg/s. Model J seems to present a better uniform temperature distribution on the nacelle lip-skin compared to Model H. However, Model H has lower T_{hi} than Model J, but Model J produces higher T_{lo} than Model H at this hot air mass flow rate.

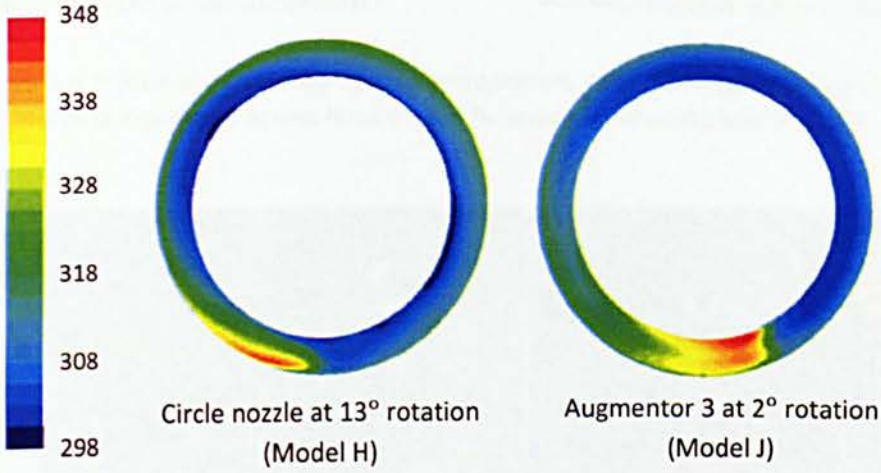

Figure 6.5.1: Lip-skin temperature contour (in K) for Model H and Model J at $m_{hot\ air}$ of 0.02354 kg/s

The trends of T_{lo}, T_{hi} and T_{ave} vs. $m_{hot\ air}$ for Models J and H are compared in Figure 6.5.2 which shows that T_{ave} for both models are almost identical. T_{hi} of Model J is lower than Model H at $m_{hot\ air}$ from 0.0118kg/s to 0.019kg/s while Model J produces higher T_{hi} than Model H at $m_{hot\ air}$ of 0.019kg/s to 0.04536kg/s. The reason for this phenomenon is that the hot air of model J has better and uniform Mach number distribution of hot air in the vicinity of the nozzle compared to model H. Since the hotspot moves from outer skin to inner skin, T_{hi} of Model J is higher than T_{hi} of Model H at $m_{hot\ air}$ of 0.019kg/s and above. Although Model H seems to have lower T_{lo} than Model J until $m_{hot\ air}$ of 0.028kg/s, T_{lo} of Model H is higher than T_{lo} of Model J when $m_{hot\ air}$ exceeds 0.028kg/s. Since hot air exiting from the augmentor diverges excessively at $m_{hot\ air}$ = 0.028kg/s and above, Model J loses a lot of momentum, as shown in Figure 6.5.3. This momentum loss severely affects the Mach number of

swirling air in the cold spot plane, which leads to lower T_{lo} being produced by Model J compare to Model H.

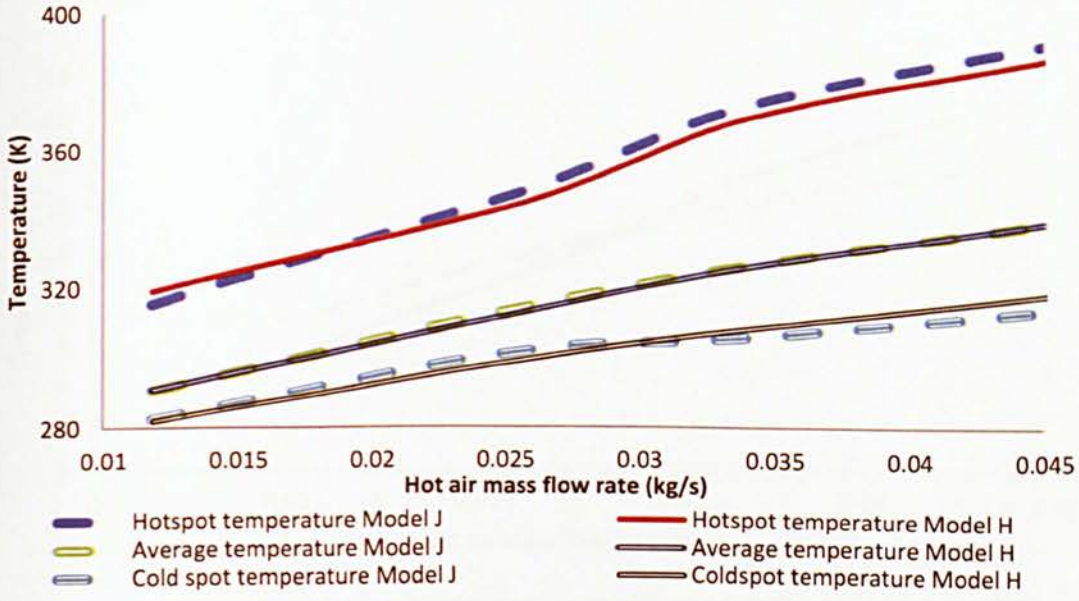

Figure 6.5.2: Profiles of average lip-skin temperature, hotspot temperature and cold spot temperature across hot air mass flow rate for Model J and Model H

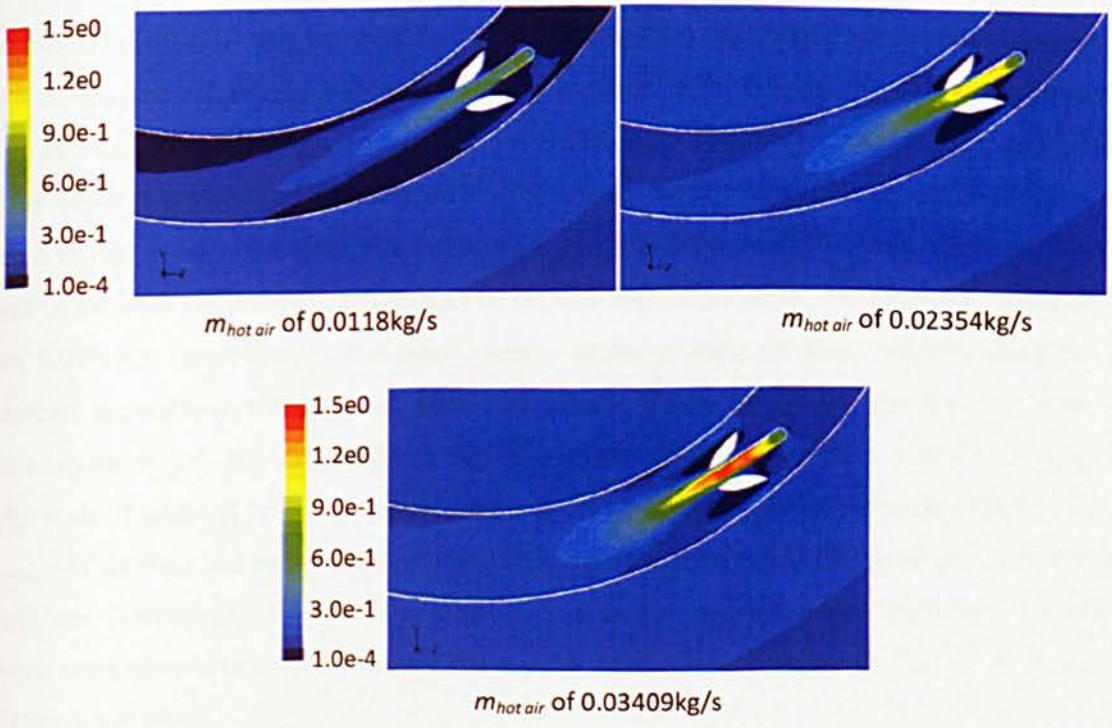

Figure 6.5.3: Air Mach number contour in Augmentor 3 vicinity for three different hot air mass flow rate

Figure 6.5.4 shows σ for Models J and H; Model J has lower σ than Model H between 0.0118kg/s and 0.029kg/s. However, Model J provides higher σ than Model H at $m_{hot\ air}$ in the range of 0.029kg/s to 0.04536kg/s.

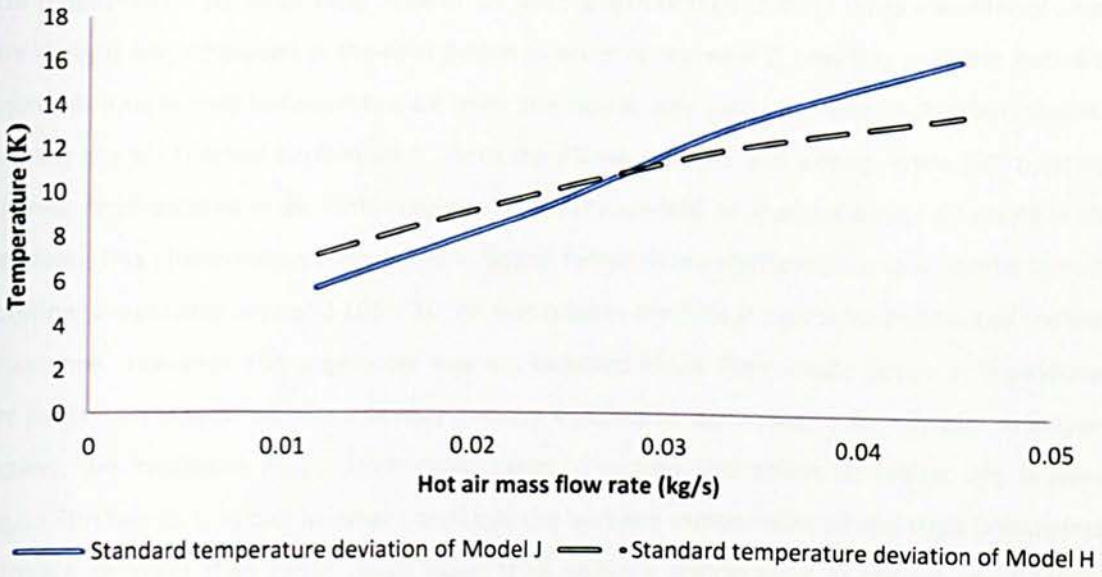

Figure 6.5.4: Curves of standard temperature variation along hot air mass flow rate of for both Model J and Model H

In conclusion, although Augmentor 3 at 4° shows a better thermal performance than Augmentor 3 at 2° at $m_{hot\ air}$ of 0.0118kg/s, Augmentor 3 at 2° has better thermal performance than Augmentor 3 at 4° at $m_{hot\ air}$ of 0.02534kg/s and above. The results also show that the augmentor produces a better uniform temperature distribution on the nacelle lip-skin than SAI without augmentor, as shown in Figure 6.5.1. However, the momentum loss and pressure drop in the augmentor vicinity seem to diminish the thermal performance of SAI with augmentor when the mass flow rate is higher than 0.029kg/s. Consequently, the Mach number of the swirling air drops severely along the D-chamber, especially in the cold spot plane. This means Augmentor 3 at 2° has lower T_{lo} than the Circle nozzle at 13° at $m_{hot\ air}$ of 0.029 kg/s and above. Overall, Augmentor 3 at 2° has a better uniform distribution of lip-skin temperature along the wrap location than the Circle nozzle at 13° at $m_{hot\ air}$ of 0.029kg/s and below as Augmentor 3 has a better uniform distribution of air Mach number inside the D-chamber. However, the Circle nozzle at 13° rotation angle has a better uniform temperature distribution on the entire the nacelle lip-skin than Augmentor 3 at 2° at $m_{hot\ air}$ of 0.029kg/s and above.

6.6 Final Nozzle Design

This section describes the thermal performance of SAI with Final nozzle design. In the present study, Final nozzle design was the combination of best design of nozzle rotation angle (NRA), nozzle length, nozzle shape, nozzle outlet surface. NRA of 13° with length of 0.01829m (2 times diameter of small nozzle design) was employed in the final design in order to increase Z, resulting in better heat and momentum interactions between hot air from the nozzle and cold air inside D-chamber, thereby enhancing the SAI thermal performance. Both the Ellipse nozzle 1 and sloped nozzle (60° opposite side) were -incorporated in the Final nozzle, which was expected to produce earlier air mixing in the SAI system. This phenomenon contributes to better temperature distribution on the nacelle lip-skin. In addition, the exhaust area of $2.105 \times 10^{-3}m^2$ was used in the final design since it produced the best performance. However, the augmentor was not included in the Final nozzle design as it produced lower performance than SAI alone at $m_{hot\ air}$ above 0.029kg/s. According to Bombardier Aerospace Company, the maximum $m_{hot\ air}$ from compressor to nacelle D-chamber of Falcon 20g is about 0.2kg/s. Furthermore, in bad weather condition, the ambient temperature of real flight is extremely low (might be lower than 233K), much lower than ambient temperature of present study (266K). Therefore, the present work decides to select SAI without augmentor which has better performance at high $m_{hot\ air}$. The final nozzle design is illustrated schematically in Figure 6.6.1.

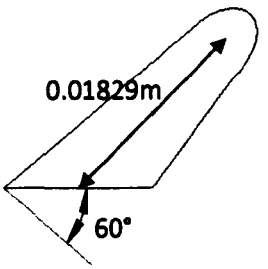

Figure 6.6.1: Illustration of Final nozzle design

The thermal performance of SAI with Final nozzle design was studied and then compared with that of circle and Ellipse nozzles at NRA of 13°, at four different $m_{hot\ air}$ between 0.0118kg/s and 0.04536kg/s. The T_{nozzle}, T_∞ and free stream Mach number were not changed. The thermal performance characteristics analyzed were temperature contours, temperature profiles, T_{hi}, T_{lo}, T_{ave}, σ and $C_{tem\ deviation}$.

Figure 6.6.2 illustrates the temperature contours for three different nozzle designs at $m_{hot\ air}$ of 0.0118kg/s. The result reveals that the T_{hi} for all nozzle designs occur in planes between 195° and 197°, while the T_{lo} for all nozzles develops in plane 120°. The final nozzle design shows the most

uniform temperature, followed by Ellipse nozzle 1 and circle nozzle. Final nozzle produces the lowest hotspot, which is 3.4K and 4.8K lower than that of Ellipse nozzle 1 and Circle nozzle respectively. Meanwhile, the T_{lo} of Final nozzle, Ellipse nozzle 1 and Circle nozzle are 283K, 282.51K and 281.89K respectively.

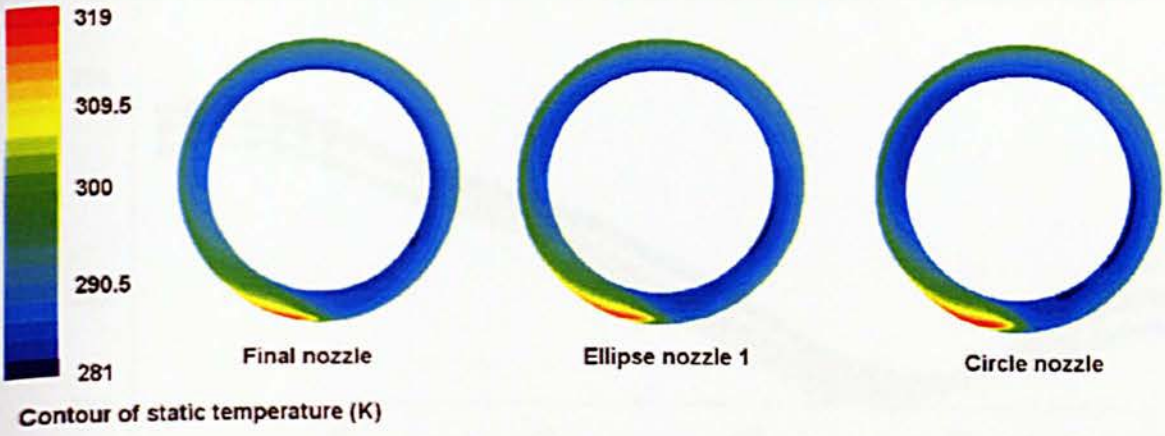

Figure 6.6.2: Lip-skin temperature contour for Final nozzle, Ellipse nozzle 1 and Circle nozzle designs

The temperature distribution along wrap location in the hotspot plane is shown in Figure 6.6.3. At wrap location below 26%, Final nozzle design has the lowest temperature, whereas at wrap location above 26%, Ellipse nozzle 1 has the lowest temperature. Except wrap location of 35% and below, the temperature of Final nozzle design 1 is similar to that of circle nozzle. Further, Final nozzle design provides the most uniform temperature in this plane as it has the lowest temperature difference between peak temperature and lowest temperature (33.5K) followed by Ellipse nozzle 1 (34.5K) and circle nozzle (36.8K).

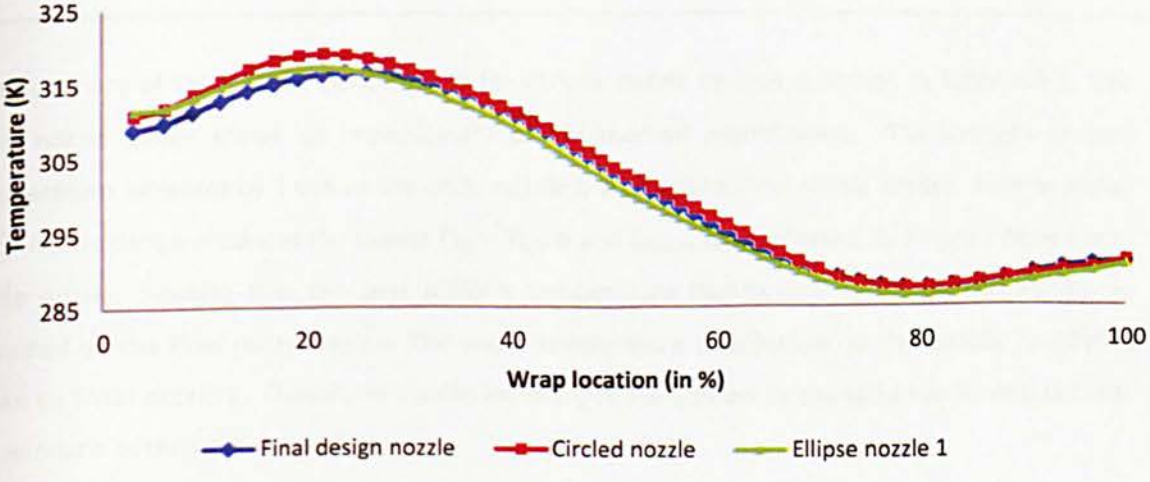

Figure 6.6.3: Temperature distribution in hotspot plane

Figure 6.6.4 describes the comparison of temperature distributions for three different nozzles in cold spot plane. Circle nozzle has the lowest temperature distribution until wrap location of 81%, and thereafter it produces the highest temperature. The temperature distribution of Final nozzle design is higher than that of circle nozzle at wrap location between 28% and 81%. It is also demonstrated that Final nozzle design produces the most uniform temperature distribution in the cold spot plane.

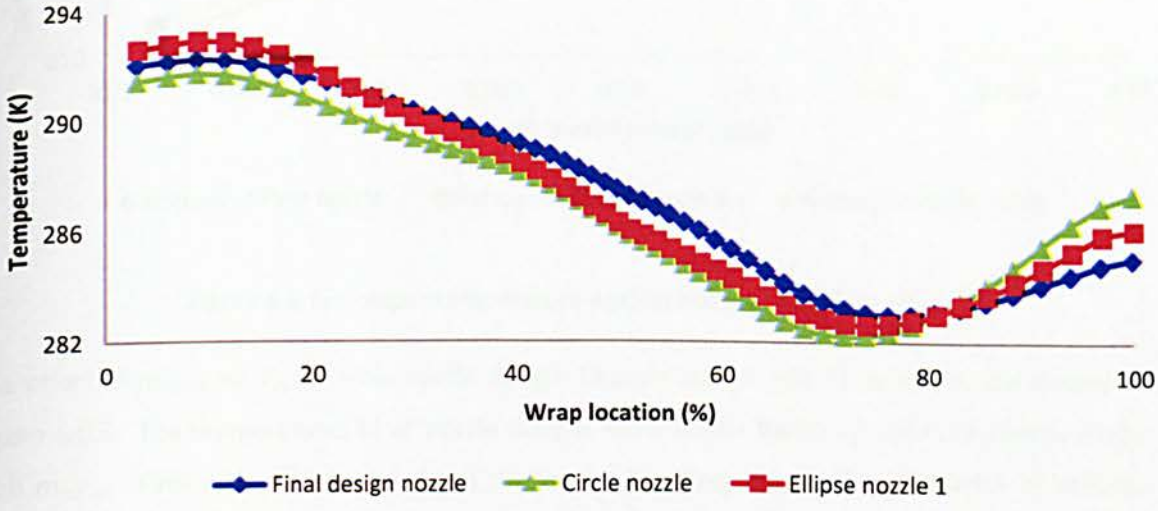

Figure 6.6.4: Temperature distribution against wrap location in cold spot plane

Table 6.6.1: Summary of SAI thermal performance for three nozzle designs

Nozzle type	T_{ave} (K)	$(T_{hi} - T_{lo})$ (K)	σ (K)	$C_{\text{tem deviation}}$ (%)
Circle nozzle	290.98	36.94	7.20	29.21
Ellipse nozzle 1	291.66	34.54	6.81	26.89
Final nozzle design	291.90	33.15	6.53	25.57

The summary of SAI thermal performance for various nozzle designs is shown in Table 6.6.1. The Final nozzle design shows an improvement of SAI thermal performance. The average lip-skin temperature increases by 1.08K as the circle nozzle is changed to Final nozzle design. Furthermore, Final nozzle design produces the lowest $T_{hi} - T_{lo}$, σ and $C_{\text{tem deviation}}$, followed by Ellipse nozzle 1 and circle nozzle, meaning that the best uniform temperature distribution in the nacelle lip-skin is provided by the Final nozzle design. The worst temperature distribution on the nacelle lip-skin is given by Circle nozzle 1. Overall, no significant changes are noticed by changing nozzle design from circle nozzle to the Final nozzle design.

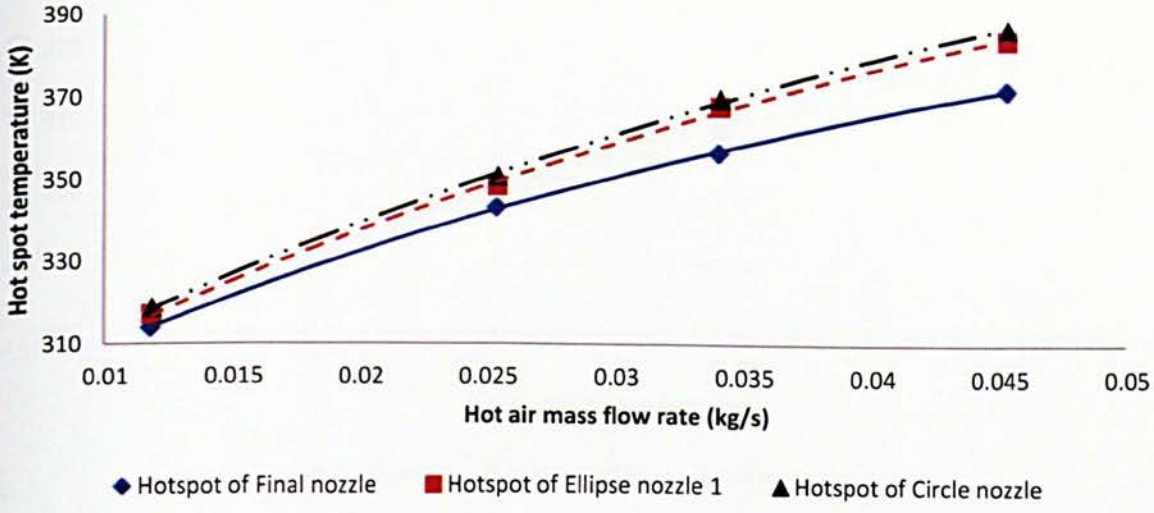

Figure 6.6.5: Hotspot temperature against hot air mass flow rate

The effect of $m_{hot\ air}$ on T_{hi} for Final nozzle design, Ellipse nozzle 1 and Circle nozzle are plotted in Figure 6.6.5. The temperatures of all nozzle designs show similar trend, i.e. increase exponentially with $m_{hot\ air}$. Final nozzle design produces the lowest T_{hi} along $m_{hot\ air}$. The difference in hotspot temperature between Final nozzle design and Ellipse nozzle 1 is increasing with $m_{hot\ air}$, as summarized in Table 6.6.2.

Table 6.6.2: The hotspot temperature difference and cold spot temperature difference between Final nozzle design and Nozzle Ellipse 1

Hot air mass flow rate (kg/s)	0.0118	0.02534	0.03402	0.04356
Hotspot temperature difference (K)	3.16	5.24	11.06	12.29
Cold spot temperature difference (K)	0.49	0.57	1.53	2.69

The influence of $m_{hot\ air}$ on T_{lo} for three different nozzle designs is illustrated in Figure 6.6.6. Similar to the hotspot trend shown in Figure 6.6.5, T_{lo} increases exponentially with $m_{hot\ air}$ for all nozzle designs. T_{lo} of Final nozzle design is the highest, followed by Ellipse nozzle 1 and Circle nozzle. The cold spot temperature difference between Final nozzle design and Ellipse nozzle 1 increases with $m_{hot\ air}$; however, this is much smaller than the hotspot temperature difference, as shown in Table 6.6.2.

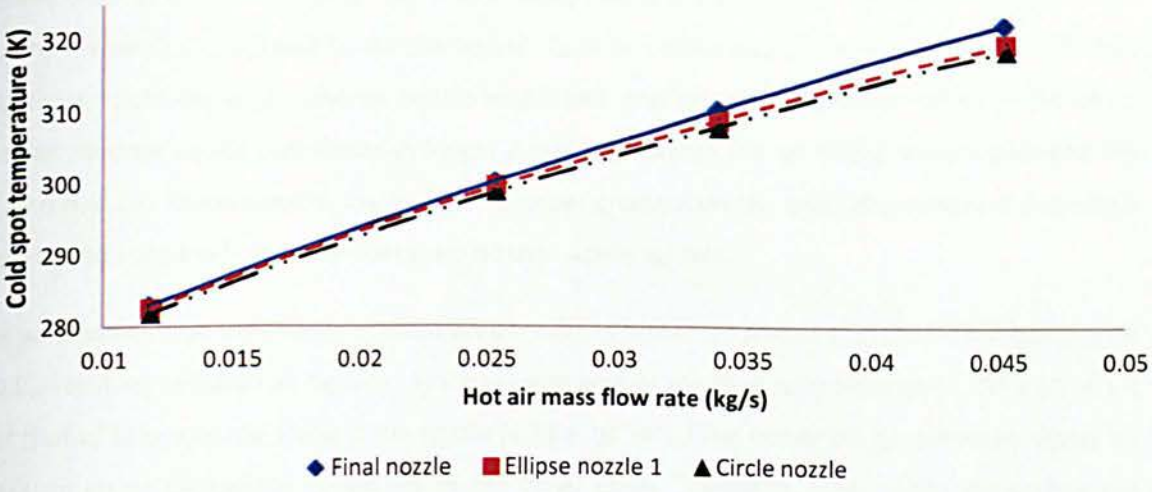

Figure 6.6.6: Cold spot temperature along hot air mass flow rate

Figure 6.6.7 shows the relationship between $C_{tem\ deviation}$ and $m_{hot\ air}$ for three different nozzle shapes. As expected, the $C_{tem\ deviation}$ is inversely related to $m_{hot\ air}$. $C_{tem\ deviation}$ of Circle nozzle reduces by 10.5% as the $m_{hot\ air}$ increases from 0.0118kg/s to 0.04536kg/s. $C_{tem\ deviation}$ of Ellipse nozzle 1 and Final nozzle design decrease by 9% and 12.4% respectively with the same $m_{hot\ air}$ reduction. Final nozzle design produces the lowest $C_{tem\ deviation}$ along $m_{hot\ air}$, followed by Ellipse nozzle 1 and Circle nozzle.

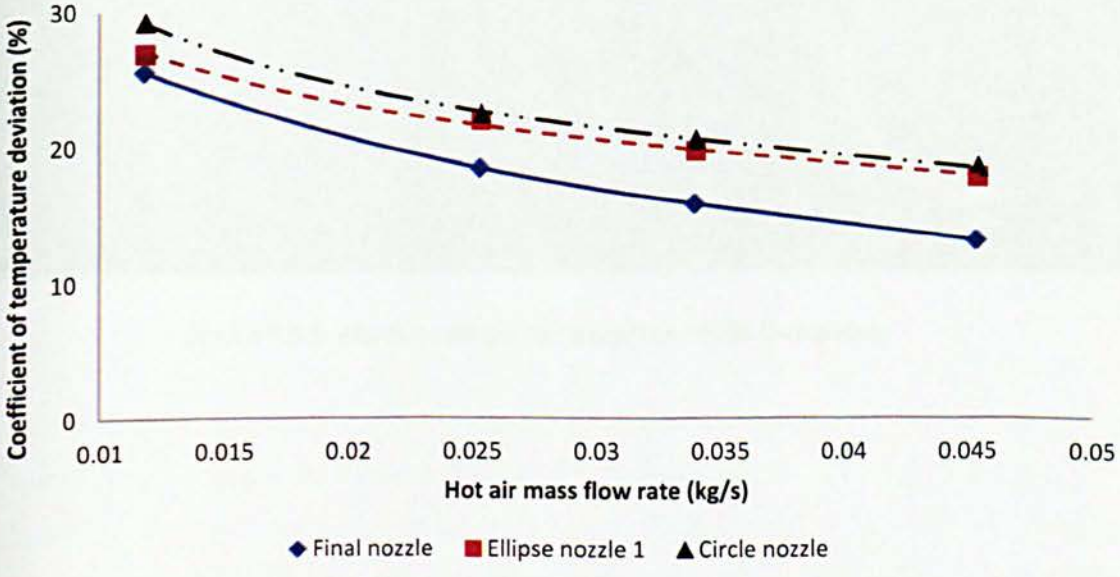

Figure 6.6.7: Relationship between coefficient of temperature deviation and hot air mass flow rate

Figures 6.6.5 to 6.6.7 reveal that Final nozzle design exhibits the best thermal performance, which has the lowest $C_{tem\ deviation}$ and T_{hi} and the highest T_{lo} at any given $m_{hot\ air}$. This is attributed to the fact that Final nozzle design has shorter nozzle-length and smaller exhaust-area compared to the other nozzles. Shorter nozzle contributes in longer Z, which enhances the air mixing process between hot air and cold air. Consequently, the air Mach number gradient on the impinging-surface is decreased thereby reducing the hotspot temperature on the nacelle lip-skin.

It is well known that the smaller exhaust area results in higher air pressure inside D-chamber (Figure 6.6.8), resulting in higher air density. Since exhaust area of the Final nozzle design ($2.105 \times 10^{3}m^{2}$) is half that of Ellipse nozzle 1 and Circle nozzle ($4.21 \times 10^{-3}m^{2}$), Final nozzle design produces higher air pressure inside D-chamber compared to the other cases. Therefore, Final nozzle design has the highest air density at any given $m_{hot\ air}$; consequently its jet experiences the highest air pressure drop inside D-chamber, which leads to the highest air Mach number decay from the nozzle to impinging-surface as shown in Figure 6.6.9a. z/Z is the ratio of distance between local point and the nozzle to distance between nozzle outlet and impinging-surface. The positions of z, Z and nozzle inside D-chamber is illustrated in Figure 6.6.9b.

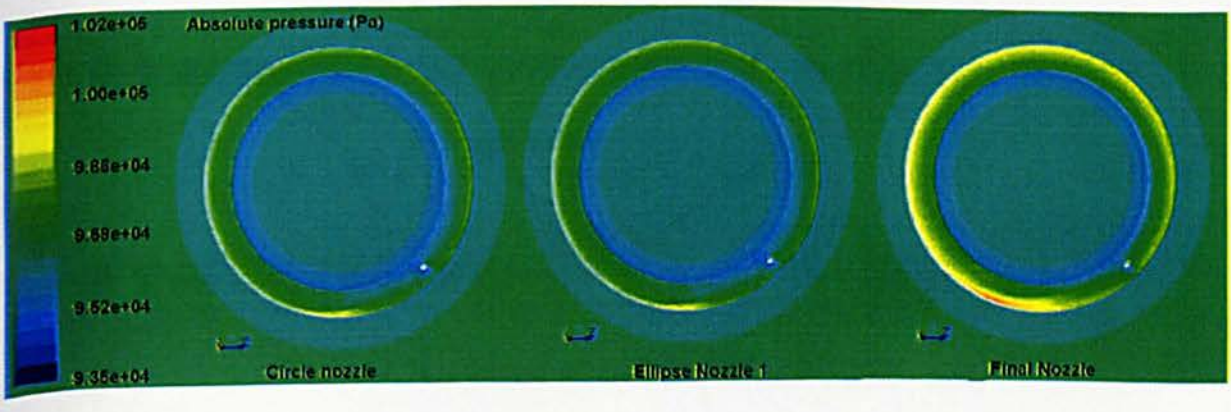

Figure 6.6.8: Absolute air pressure contour inside D-chamber

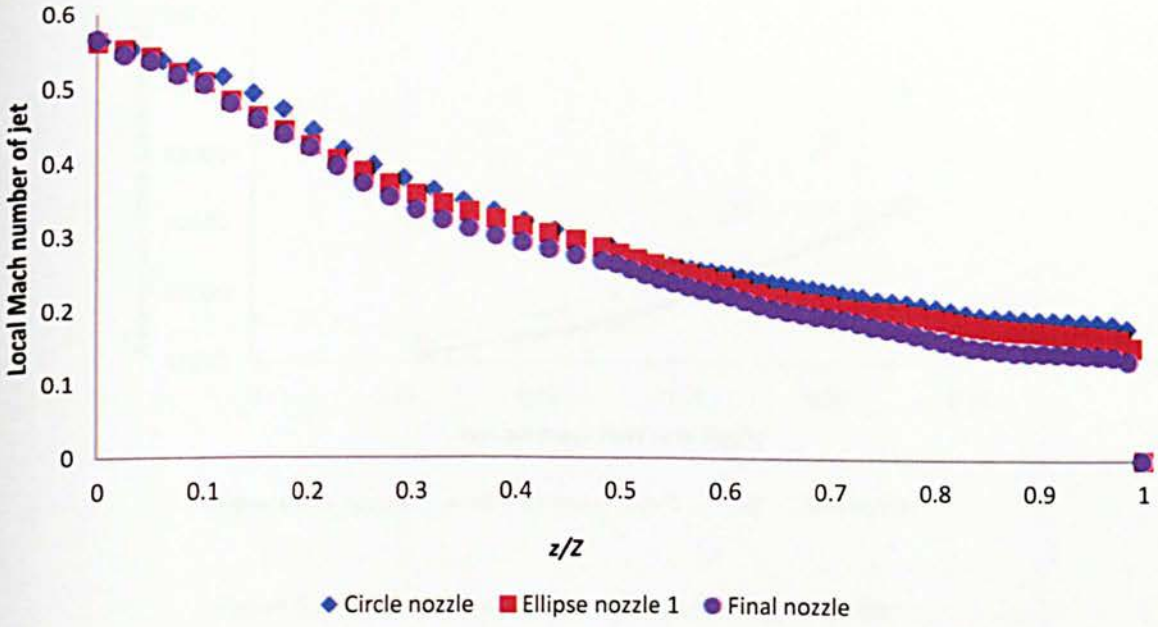

Figure 6.6.9a: Mach number profile of jet between nozzle and impinging-surface

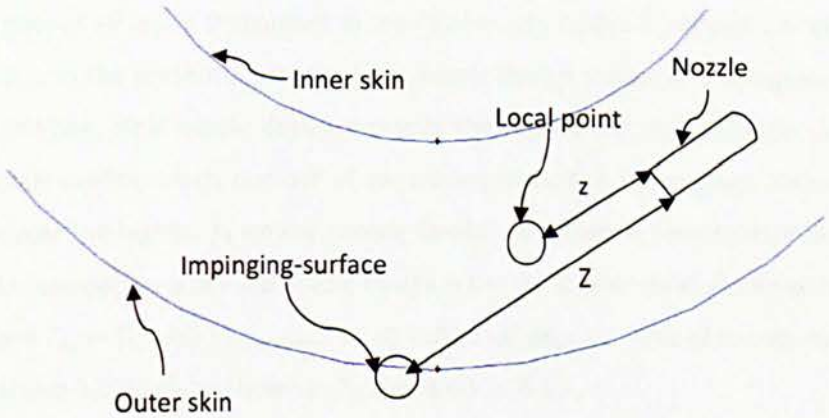

Figure 6.6.9b: Positions of nozzle, z and Z in SAI system

Figure 6.6.10 reveals that the effect of $m_{hot\ air}$ on the average absolute pressure of air inside D-chamber for the three different nozzles; the absolute pressure increases with $m_{hot\ air}$ in all cases. Final nozzle design produces the highest absolute pressure since it has the smallest exhaust area; the other nozzles have equal absolute pressures due to the same exhaust area. The difference in absolute pressures, between Final nozzle design and Ellipse nozzle 1, increases with $m_{hot\ air}$, which contributes to higher air density and pressure drop. As a result, the difference in T_{hi} between Final nozzle design and Ellipse nozzle increases with $m_{hot\ air}$, as shown in Table 6.6.2.

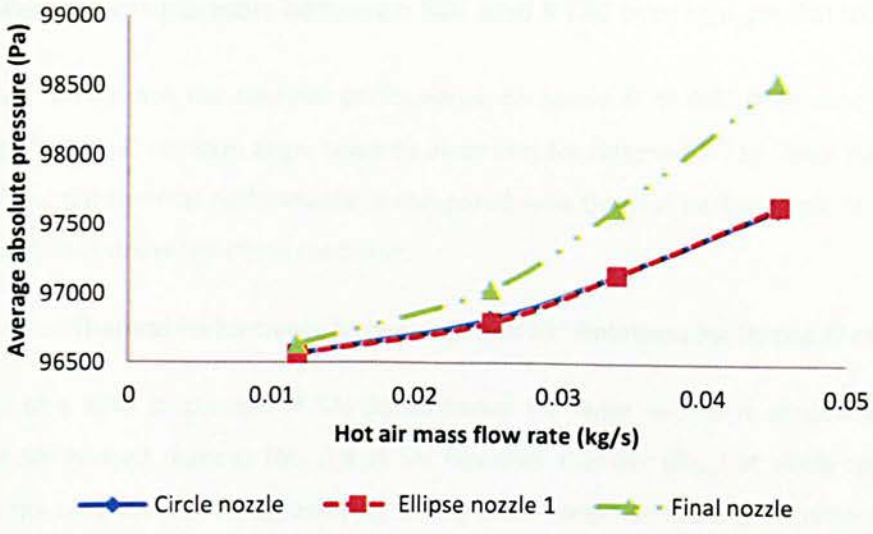

Figure 6.6.10: Average absolute pressure inside D-chamber

As the jet exit from Final nozzle design experiences higher Mach number decay as shown in Figure 6.6.9, it transfers higher momentum and heat to cold air inside D-chamber. Thus, the average swirling Mach number of air inside D-chamber of the Final nozzle design is highest. Consequently, as shown in Table 6.6.1, in the present work, the Final nozzle design produces the highest T_{ave} at the given $m_{hot\ air}$. In addition, Final nozzle design provides the highest air Mach number in cold spot plane as the average swirling Mach number of air exiting from it is the highest. Therefore, Final nozzle design produces the highest T_{lo} on the nacelle lip-skin as shown in Figures 6.6.4 and 6.6.6. In addition, the lip-skin temperature of Final nozzle design is the most uniform in the present work as it produces the lowest $T_{hi} - T_{lo}$ and $C_{tem\ deviation}$ at all values of $m_{hot\ air}$. This phenomenon becomes obvious at $m_{hot\ air}$ above 0.026kg/s as shown in Figures 6.6.5 to 6.6.7.

In conclusion, Final nozzle design produces the best thermal performance in the present work since it has the most uniform temperature, the lowest T_{hi} and the highest T_{lo} as shown in Figures 6.6.2 to 6.6.7 at any given $m_{hot\ air}$.

Chapter 7: Comparison between SAI and PTAI thermal performance

Chapter 7 look briefly into the thermal performance of nozzle $\check{D}$ of 0.0108 (Nozzle diameter of 0.01707m) at 0° and 13° rotation angle towards inner skin for Nacelle BR 710 (large nacelle) at the climb case. Then, SAI thermal performance is compared with thermal performance of PTAI for the large nacelle (BR 710) under the climb condition.

7.1 Comparison of Thermal Performance between 0° and 13° Rotations for Nozzle $\check{D}$ of 0.0108

The objective of a brief discussion of SAI performance for large nacelle is to develop empirical correlation of SAI Nusselt number (Nu_{sw}) and SAI Reynolds number (Re_{sw}) at climb condition. It is believed that the coefficients of Nu_{sw} and Re_{sw} at the climb condition are slightly different from the ground condition since the ambient pressure and temperature at the climb condition are lower comparing to the ground condition due to different altitudes. Therefore, the altitude affects air properties especially air thermal conductivity.

Figure 7.1.1 shows the comparison of temperature contour of SAI at 0° and 13° nozzle rotations. T_{nozzle} and $m_{hot\ air}$ in Figure 7.1.1 are 545K and 0.09234kg/s respectively. According to the result, T_{hi} drops from 365.5K to 341.9K as the nozzle rotates from 0° to 13° towards the inner skin. Moreover, SAI at 13° produces better uniformity of temperature distribution on nacelle lip-skin than SAI at 0°. The result also reveals that T_{lo} increases from 297.6K for 0° rotation to 302.6K for 13° rotation, although the T_{ave} almost does not show any significant changes with the nozzle rotation angle. As shown in Table 7.1.1, σ of SAI at 13° is 6.23K, which is 5.08K lower than SAI at 0°. Thus, SAI at 13° produces lower $C_{tem\ deviation}$ than SAI does at 0° for the same $m_{hot\ air}$ as shown in Table 7.1.1.

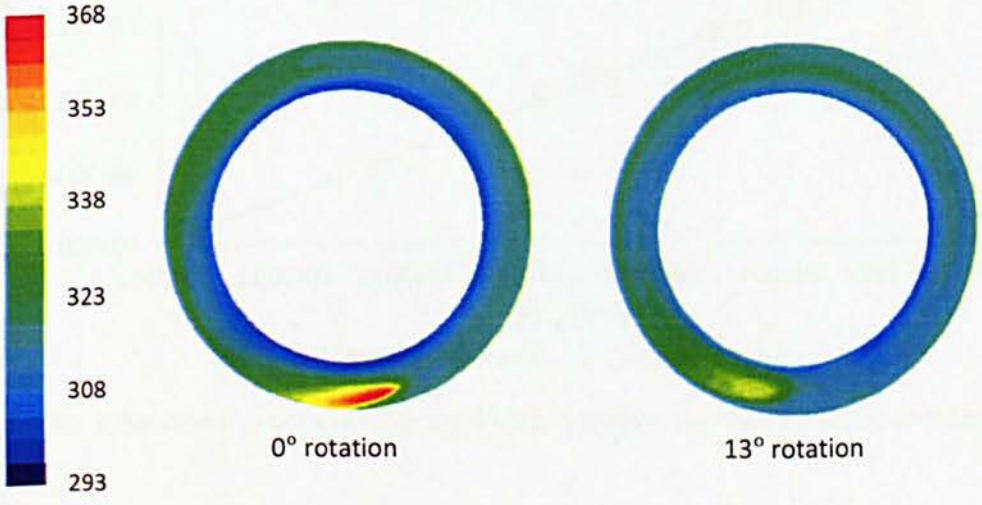

Figure 7.1.1: Temperature contour (in K) along the nacelle lip-skin for nozzle rotation at 0° and 13°

Table 7.1.1: Summary of SAI thermal performance for nacelle lip-skin BR710

Nozzle rotation angle	$m_{hot\ air}$ (kg/s)	T_{ave} (K)	σ (J)	$C_{tem\ deviation}$ (%)
0	0.0924	315.08	11.31	28.95
13	0.0924	315.35	6.23	15.90

The h_{sw} against Re_{sw} for both nozzle rotation angles is shown in Figure 7.1.2. As expected, h_{sw} increases with Re_{sw} for both nozzle rotation angles, which is not affected by nozzle rotation. Figure 7.1.3 illustrates the relationship of Nu_{sw} vs. Re_{sw}. As shown in the figure, Nu_{sw} is directly proportional to $Re_{sw}^{0.975}Pr^{0.3}$, which is independent of nozzle rotation angle. From the figure, the correlation between Nu_{sw}, Re_{sw} and Pr can be obtained as:

$$Nu_{sw} = 0.0032Re_{sw}^{0.975}Pr^{0.3} \tag{7.1}$$

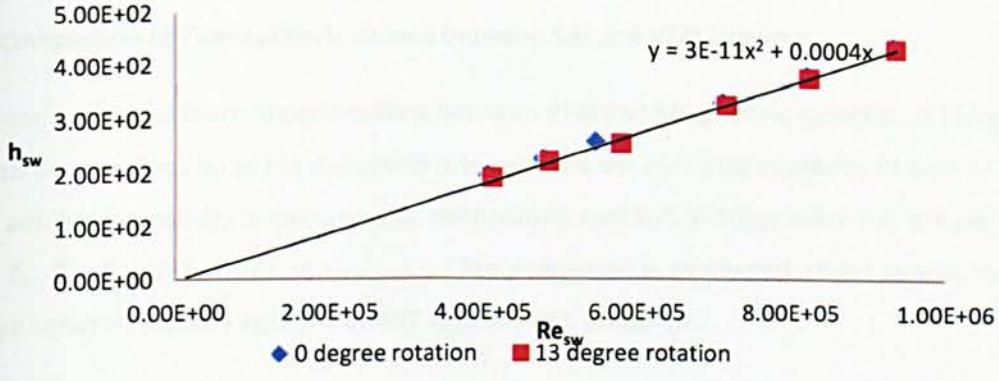

Figure 7.1.2: SAI average heat transfer coefficient vs. SAI Reynolds number for large nacelle (BR710)

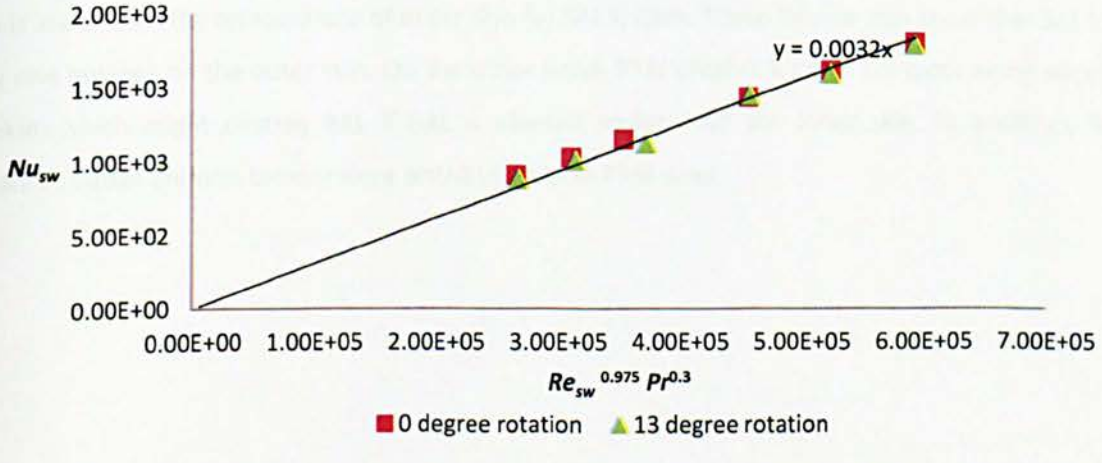

Figure 7.1.3: Relationship between average Nusselt number and Reynolds number for SAI system

From the comparison between equations 7.1, 5.10 and 5.13, it is evident that air pressure in D-chamber affects coefficient between Nu_{sw} and $Re_{sw}^{0.975}Pr^{0.3}$ at a given m_{sw}. This coefficient increases with air pressure inside D-chamber, although the influence of the pressure inside the D-chamber is small. At the given $m_{hot\ air}$, the swirling air temperature increases with air pressure, which leads to change of air properties especially air conductivity. Therefore, the coefficient between Nu_{sw} and $Re_{sw}^{0.975}Pr^{0.3}$ is related to swirling air pressure inside D-chamber as shown in Equations 7.1, 5.10 and 5.13.

$$Nu_{sw} = 0.0036Re_{sw}^{0.975}Pr^{0.3} \quad (5.10)$$

$$Nu_{sw} = 0.0041Re_{sw}^{0.975}Pr^{0.3} \quad (5.13)$$

7.2 Comparison of Thermal Performance between SAI and PTAI Systems

The comparison of thermal performance between PTAI and SAI at climb condition is being discussed in this section. The aim of the discussion is to evaluate the anti-icing capability of both PTAI and SAI. The anti-icing capability is measured by temperature contour, average inner skin temperature ($T_{inner\ ave}$), T_{hi}, T_{lo}, T_{ave}, EFF, T_{hi}-T_{lo}, σ, $C_{tem\ deviation}$. The evaluation is conducted under several $m_{hot\ air}$ in the range between 0.09234 kg/s and 0.3692 kg/s at climb condition.

Figures 7.2.1 and 7.2.2 illustrate the nacelle lip-skin temperature contours of PTAI and SAI at 13° respectively. $m_{hot\ air}$ and T_{nozzle} at the inlet are 0.159 kg/s and 545K respectively. In PTAI system, the inner skin shows much higher temperature than outer skin does. However, the temperature of inner skin is lower than the temperature of outer skin for SAI system. These figures also show that SAI has only one hotspot on the outer skin. On the other hand, PTAI creates a lot of hotspots along nacelle lip-skin; which might destroy BAL if BAL is planted underneath the inner skin. In addition, SAI produces better uniform temperature distribution than PTAI does.

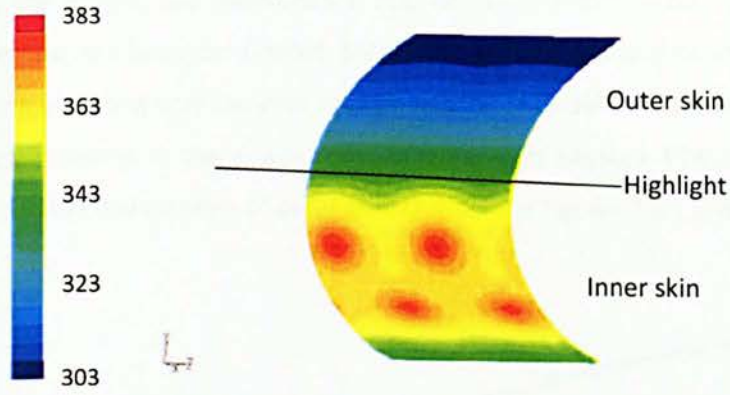

Figure 7.2.1: Lip-skin temperature contour of PTAI system

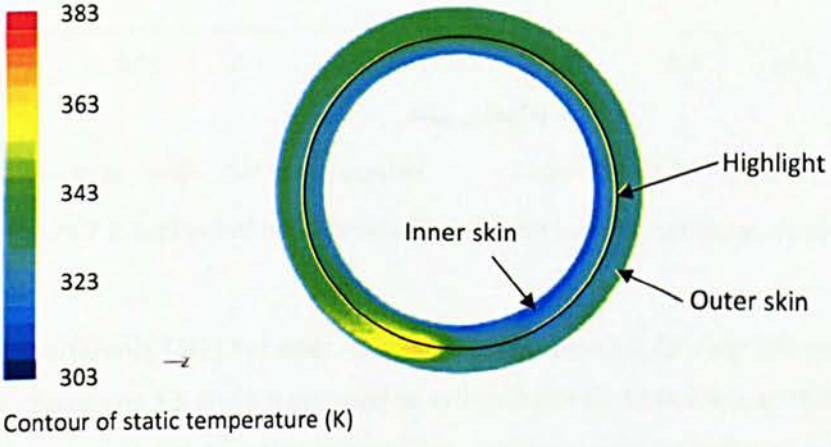

Figure 7.2.2: Lip-skin temperature contour of SAI for nozzle at 13° rotation

Protecting inner skin from ice accumulation is a priority of an anti-icing system in order to prevent ice from being digested by compressor/engine. That is the main reason why PTAI produces the higher inner skin temperature compare to outer skin temperature. Although SAI is unable to produce the same result as mentioned above, it is able to provide adequate temperature that enough to prevent ice accumulation on inner skin. Average inner skin temperature ($T_{inner\ ave}$) against $m_{hot\ air}$ is displayed in Figure 7.2.3 to elaborate the capability of SAI and PTAI systems to protect inner skin from ice accumulation. The figure shows that $T_{inner\ ave}$ is increases with $m_{hot\ air}$ for both SAI and PTAI systems. The figure also shows that PTAI produces the highest $T_{inner\ ave}$ at any given $m_{hot\ air}$, which is followed by SAI at 13° and then SAI at 0°. Therefore, PTAI seems to be the better system in preventing ice accumulation on the inner skin than SAI is. However, when other factors, such as

complexity, the weight, the maintenance cost of the system, the future implementation of bias acoustic liner etc., are being considered, SAI system will demonstrate its advantages, bearing in mind that achieving anti-icing only requires enough degree of lip-skin temperature. Besides, the runback icing possibly happens in the downstream of outer skin because PTAI is unable to provide high temperature in the downstream of outer skin as shown in Figures 7.2.1 and 7.2.2.

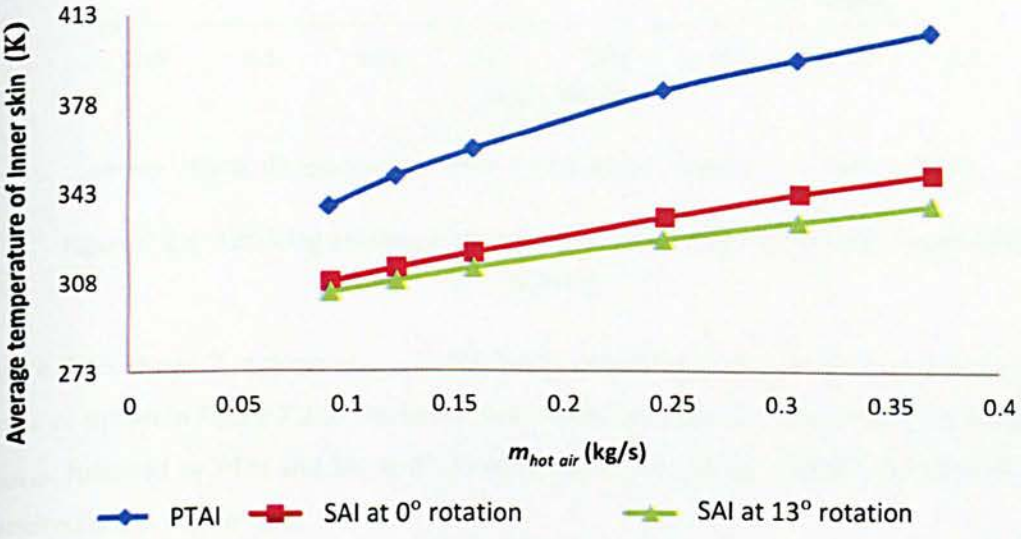

Figure 7.2.3: Effect of hot air mass flow rate on average temperature of inner skin

The anti-icing efficiency (*EFF*) has been calculated and presented for both SAI and PTAI systems in Figure 7.2.4. Equations 3.5 and 3.6 are used to estimate *EFF* for both SAI and PTAI. The discussion is based on $m_{hot\ air}$ instead of Reynolds number since SAI (conventional convection heat transfer) and PTAI (Impinging heat transfer) are based on different heat transfer mechanisms which would lead to different formula of Reynolds number for SAI and PTAI. The figure shows that *EFF* for both anti-icing systems are decreasing while $m_{hot\ air}$ increases and *EFF* of PTAI is slightly lower than that of SAI for $m_{hot\ air}$ from 0.0924 kg/s to 0.369 kg/s. The figure also shows that *EFF* is not affected by nozzle rotation angle.

$$EFF = \frac{T_{piccolo} - T_{exh}}{T_{piccolo} - T_{adiabatic\ wall}} \tag{3.5}$$

$$T_{adiabatic\ wall} = T_{\infty}\left(1 + R_f\left(\frac{\gamma-1}{2}\right)M_n^2\right) \tag{3.6}$$

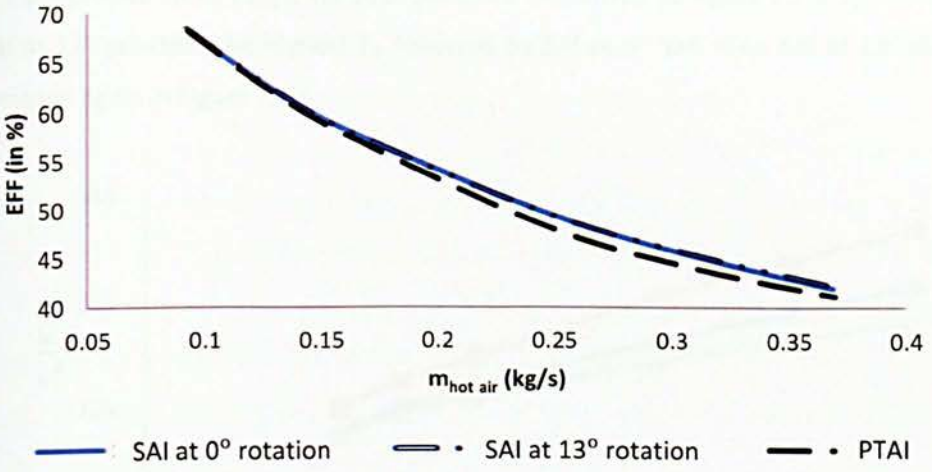

Figure 7.2.4: Anti-icing efficiency against hot air mass flow rate for both SAI and PTAI systems

Figure 7.2.5 shows T_{hi} against $m_{hot\ air}$ for SAI at 0° and 13° and PTAI. T_{hi} increases with $m_{hot\ air}$ for all cases as shown in Figure 7.2.5. The figure also reveals that SAI at 13° produces the lowest T_{hi} along $m_{hot\ air}$, followed by PTAI and SAI at 0°. In other words, SAI at 13° rotation demonstrates the best performance in Figure 7.2.5.

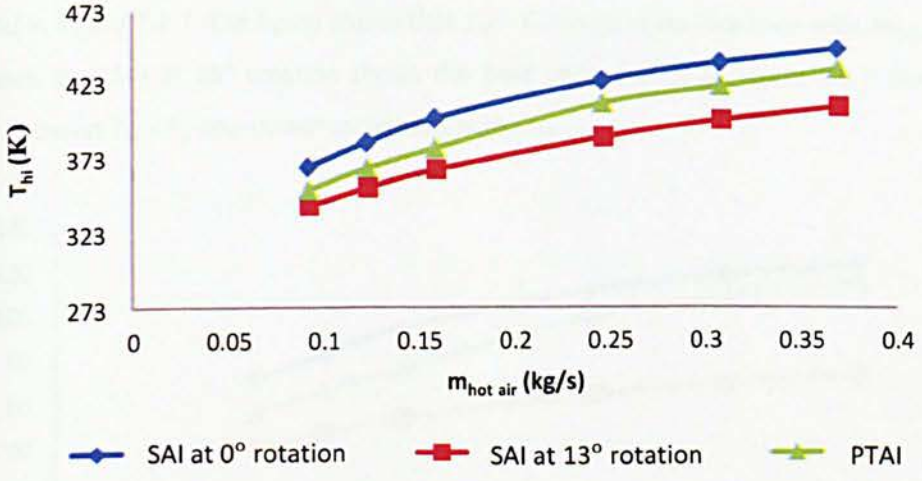

Figure 7.2.5: Relationship between hotspot temperature and hot air mass flow rate for both SAI and PTAI systems

Figure 7.2.6 plotted T_{lo} vs. $m_{hot\ air}$ for both SAI and PTAI. Similar to Figure 7.2.5, T_{lo} is related to $m_{hot\ air}$ and SAI at 13° provides the highest T_{lo} followed by SAI at 0° and PTAI. SAI at 13° shows the best performance again in Figure 7.2.6.

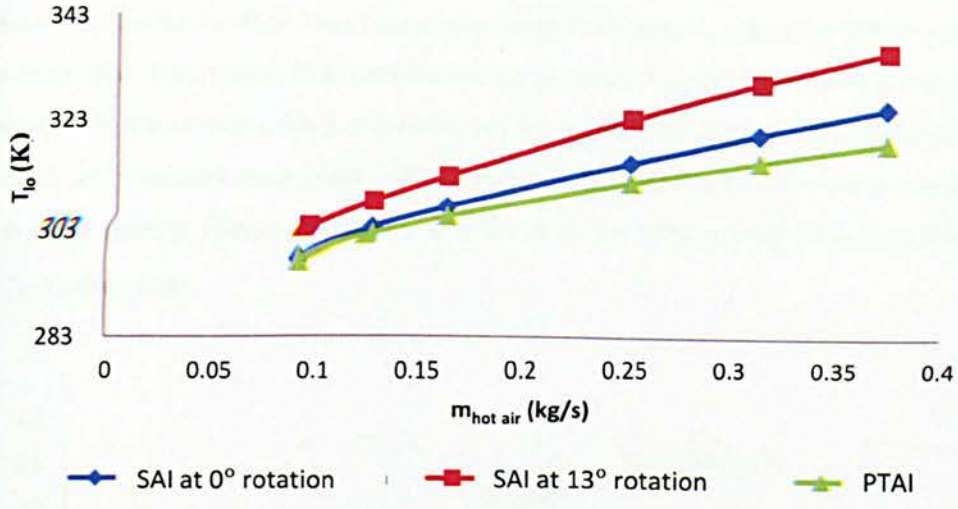

Figure 7.2.6: Cold spot temperature against hot air mass flow rate for both SAI and PTAI systems

The temperature differences between hotspot and cold spot for SAI at 0°, 13° and PTAI are illustrated in Figure 7.2.7. The figure shows that $T_{hi} - T_{lo}$ for all cases increases with $m_{hot\ air}$. The figure also reveals that SAI at 13° rotation shows the best performance in Figure 7.2.7 because that it shows the lowest $T_{hi} - T_{lo}$ and slower increment with $m_{hot\ air}$.

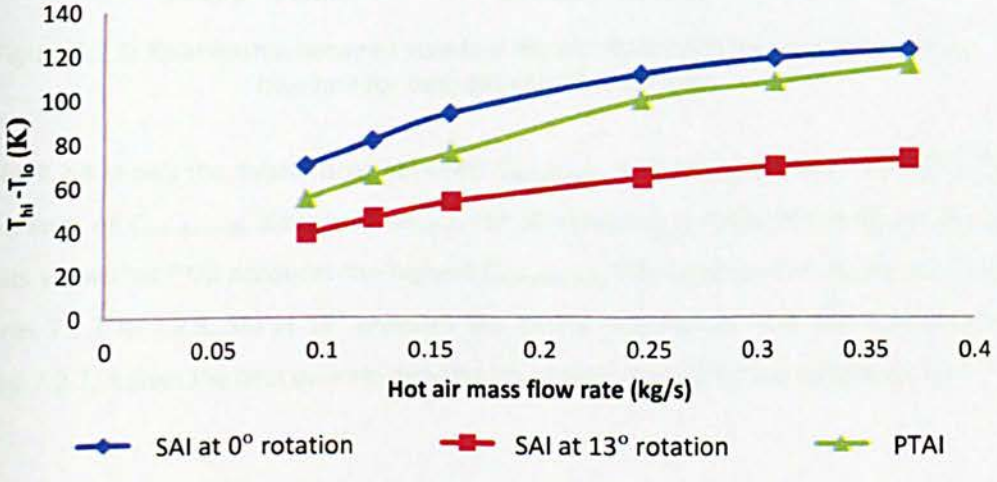

Figure 7.2.7: Effect of hot air mass flow rare on hotspot and cold spot temperature difference for both SAI and PTAI systems

Standard temperature deviation and $C_{tem\ deviation}$ are used to measure uniformity of whole nacelle lip-skin. Figure 7.2.8 shows σ against $m_{hot\ air}$ for SAI at 0°, 13° and PTAI. As shown in the figure, σ increases as $m_{hot\ air}$ increases. Although PTAI demonstrate lower T_{hi}-T_{lo} than SAI at 0° does (Figure 7.2.7), it shows the highest σ within the three cases which reveals the least uniformity of temperature distribution for PTAI. That happens because PTAI gives T_{hi} values for almost everywhere along the inner skin. That means PTAI inherits the highest temperature differences along the whole nacelle lip-skin. On the contrary, SAI just creates one hotspot on the outer lip-skin as shown in Figure 7.2.2. Overall, SAI produces quite good uniform distribution of temperature on the nacelle lip-skin except in hotspot vicinity. That is the reason why SAI at 0° has lower σ than PTAI even it has higher values for T_{hi}-T_{lo} than PTAI.

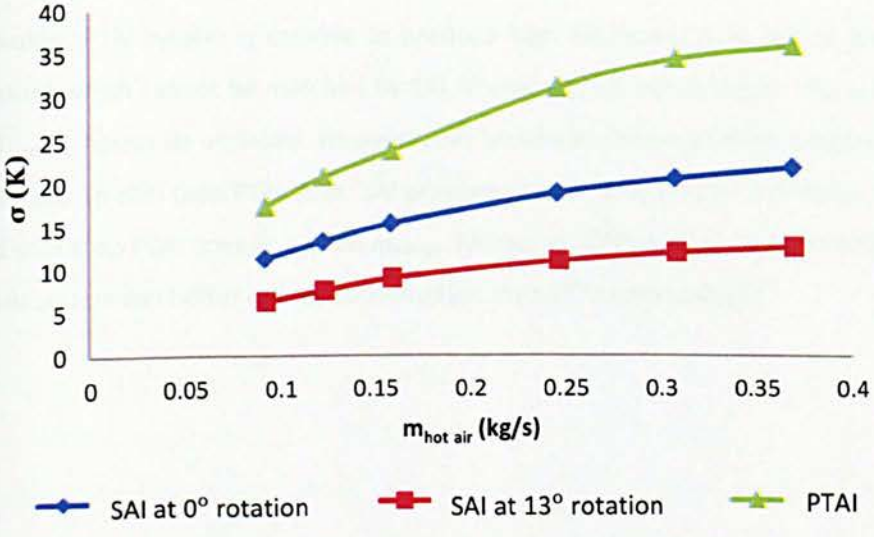

Figure 7.2.8: Relationship between standard temperature deviation and hot air mass flow rate for both SAI and PTAI systems

Figure 7.2.9 shows the relationship between $C_{tem\ deviation}$ and $m_{hot\ air}$ for both SAI and PTAI systems. The trends of $C_{tem\ deviation}$ along with $m_{hot\ air}$ for all anti-icing systems in the figure are similar. The results show that PTAI produces the highest $C_{tem\ deviation}$, the worst case in Figure 7.2.9. As shown in Figures 7.2.7 to 7.2.9, SAI at 13° provides the lowest σ in Figure 7.2.8 and the lowest $T_{hi} - T_{lo}$ in Figure 7.2.7, it gives the best uniform distribution of temperature on the nacelle lip-skin.

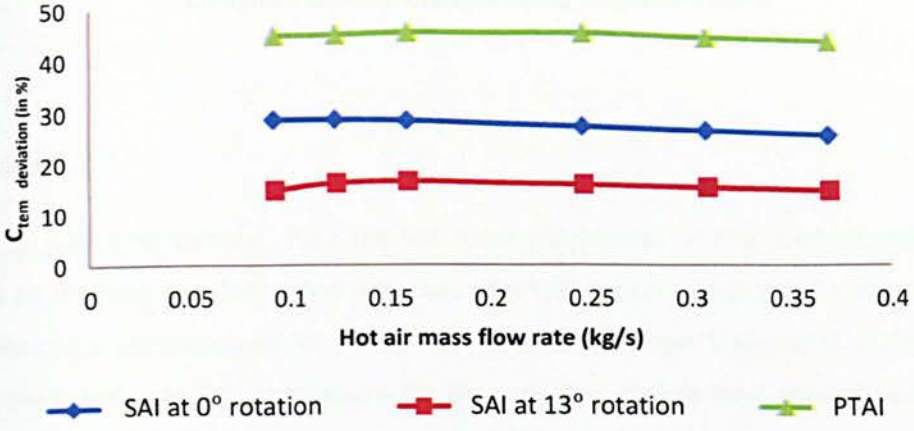

Figure 7.2.9: Coefficient of temperature deviation along hot air mass flow rate for both SAI and PTAI systems

In conclusion, PTAI system is capable to produce high temperature in critical area i.e. inner skin temperature which cannot be matched by SAI. Therefore, SAI needs higher $m_{hot\ air}$ than PTAI does if similar $T_{inner\ ave}$ has to be achieved. However, SAI possesses better uniform temperature distribution on the nacelle lip-skin than PTAI does. SAI produces lower temperature difference between hotspot and cold spot than PTAI does at a given $m_{hot\ air}$. Moreover, *EFF* of SAI is higher than *EFF* PTAI is, which means SAI system has better energy consumption than PTAI system does.

Chapter 8: Conclusion and Future Work

Introduction

Two hot air anti icing systems, PTAI and SAI, were investigated in this research, with particular emphasis on the heat transfer performance and potential improvement of SAI system. In addition, the PTAI empirical correlation among Nu_{PTAI}, Re_G, Pr, T_∞, C_x and d from Brown et al. [41] was modified and improved, and new SAI correlations for Nu_{SW} vs. Re_{SW} and Pr have been developed. In this chapter, the main findings of the current study, the conclusions drawn and the suggestions for potential future work, are summarized.

8.1 Conclusion

The investigation was started with modelling the PTAI system. In the PTAI system, hot air from the compressor was directed to inner skin in order to prevent ice accumulation on the inner skin and its consequence that the broken-off ice is digested by the compressor. Thus, hotspots were occurred at points where the high Mach number jets from the nozzles impinged on the surface along inner skin. The results showed that the temperature of the lip-skin increased with Re_{PTAI} since the heat and hot jet Mach number increased with Re_{PTAI} and $m_{hot\ air}$. However, EFF decreased exponentially with Re_{PTAI}. The simulation results also showed good agreement with experimental results from Bombardier Aerospace [100]. In addition, the numerical results demonstrated that T_∞ affected the coefficient of Nu_{PTAI} against Re_G. Therefore, a modified Brown's correlation (Equation 3.11) was proposed in this study in order to make it more accurate and suitable for all of the conditions analysed.

$$Nu_{PPAI} = (0.0152T_\infty - 4.028)Re_G^{0.922}\left(\frac{C_x}{d}\right)^{0.064}Pr^{\frac{1}{3}} \qquad (3.11)$$

It could be concluded that FLUENT CFD code has the ability to predict the thermal performance of an anti-icing system in turbulent flow regime.

Then, the verified modelling techniques were applied to SAI system. The purpose of introducing SAI was to reduce the number of hotspots and enhance the uniformity of temperature distribution along the nacelle lip-skin. A single hotspot of SAI occurred on the outer skin as the hot jet from the nozzle directly impinged on the outer skin surface. The SAI system produced only one hotspot compared to PTAI system which produced a lot of hotspots along the inner skin. The outer skin had a higher temperature than inner skin since swirling air Mach number and temperature in the D-chamber close to the outer skin were higher than those close to the inner skin. In the study of small nozzles,

some alternative designs of nozzle including sloped nozzle, rotate nozzle angle, length of nozzle and various nozzle outlet profiles, were investigated in order to enhance the thermal performance of SAI anti-icing. The result showed that T_{ave} for all nozzle types and rotation angles were similar. Rotating nozzle angle towards inner skin showed the best improvement in thermal performance of SAI. T_{hi} decreased by 18.5K, T_{lo} increased by 2.5K and $C_{tem\ deviation}$ decreased by 13.7% respectively as the nozzle direction changed from 0° to 13° towards inner skin. Nozzle length showed an improvement in SAI thermal performance. T_{lo} increased by 1.1K and $C_{tem\ deviation}$ decreased by 2.18% respectively as the nozzle length decreased from 3d to 1d. Nozzle type also enhanced the thermal performance of SAI even through it was less significant than rotating nozzle towards inner skin. T_{lo} increased from 8.95K to 9.51K, T_{hi} and $C_{tem\ deviation}$ decreased by 1.86K and 2.32% respectively as the nozzle type changed from circle nozzle to ellipse nozzle 1. Finally, sloped nozzle had potential to enhance SAI thermal performance even it was not as significant as changing nozzle direction. T_{lo} increased by 0.72K, even though T_{hi} decreased by 2.47K as the original nozzle was changed to sloped nozzle with -60° cut. Rotating nozzle direction towards inner skin showed the best improvement in SAI thermal performance followed by varying nozzle length, implementing different nozzle types and sloped nozzle.

To investigate the effects of mass flow rate ($m_{hot\ air}$ and m_{sw}) on anti-icing performance, large nozzles (nozzle diameters from 0.0127m to 0.0254m) were studied as the simulation of small nozzle crashed at high $m_{hot\ air}$. The results showed that the nozzle diameter had a significant effect on SAI thermal performance. At the given $m_{hot\ air}$ of 0.0464kg/s, T_{lo} and T_{ave} decreased by 22.41K and 6.67K respectively as the nozzle diameter increased from 0.0127m to 0.0254m. In addition, T_{hi} and $C_{tem\ deviation}$ increased by 9.1K and 7.91% respectively with a same nozzle diameter increment. Exhausts area showed a small effect on SAI thermal performance due to the fact that air pressure increases as the exhaust area decreases. At the given $m_{hot\ air}$ of 0.059kg/s and nozzle diameter of 0.01905m, T_{hi} decreased by 3.2K as the exhaust area decreased from $4.210 \times 10^{-3}m^2$ to $1.263 \times 10^{-3}m^2$. First, T_{ave} increased by 0.9K; T_{lo} increased by 3.1K and $C_{tem\ deviation}$ decreased by 1% as the exhaust decreased from $4.210 \times 10^{-3}m^2$ to $2.105 \times 10^{-3}m^2$. However, T_{ave} decreased by 0.5K; T_{lo} decreased by 1.0K and $C_{tem\ deviation}$ increased by 0.7% when the exhaust area was decreased further to $1.263 \times 10^{-3}m^2$. The change of the heat transfer performance with number of exhaust from low to high before lowering down means there might be a maximum value within the trend. Based on the numeric results, the empirical correlations for small nozzle with exhaust area of $4.210 \times 10^{-3}m^2$ and large nozzle with exhaust area of $2.105 \times 10^{-3}m^2$ were formulated as presented in Equations 5.10 and 5.13 respectively.

$$Nu_{sw} = 0.0036 Re_{sw}^{0.975} Pr^{0.3} \quad (5.10)$$

$$Nu_{sw} = 0.0041 Re_{sw}^{0.975} Pr^{0.3} \quad (5.13)$$

The gradient of Nu_{sw} against $Re_{sw}^{0.975} Pr^{0.3}$ for small nozzle was slightly lower than the coefficient for large nozzle because the exhaust area of small nozzle was larger than that of large nozzle. At any given $m_{hot\ air}$, smaller nozzle showed better performance than larger nozzle.

Next, the augmentor was developed and employed in the SAI system in order to enhance SAI thermal performance. The application of the augmentor in SAI system improved mixing between hot air and cold air, thus enhancing uniformity of temperature distribution along the nacelle lip-skin. However, the swirling air Mach number and air pressure dropped as the swirling air passing through the augmentor has been identified as the main disadvantage of augmentor. Therefore, the aerofoil shape of augmentor section (Augmentor 3) was developed and studied in order to reduce air velocity and pressure drop in augmentor vicinity. However, the average swirling air velocity of SAI with augmentor 3 was still relatively lower than that without augmentor. Therefore, augmentor 3 rotating towards the inner skin was investigated. The results showed that the thermal performance of augmentor 3 with 2° rotation produced better performance than SAI with 13° rotation. However, at the high $m_{hot\ air}$ (approximately above 0.028kg/s), SAI with 13° rotation showed better performance than SAI with augmentor at 2° rotation. Afterwards, the Final nozzle (the combination of best design of NRA, nozzle length, nozzle outlet surface) has been developed and studied. As expected, the Final nozzle provided the best thermal performance at all values of $m_{hot\ air}$. The high performance of Final nozzle became obvious at high $m_{hot\ air}$. At $m_{hot\ air}$ of 0.04536 kg/s, T_{hi}, T_{lo} and $C_{tem\ deviation}$ of Final nozzle were 371.4K, 332.0K and 13.2% respectively; this was the best performance found in the present work.

Finally, the performances of SAI and PTAI were compared. The results showed that air pressure affected the coefficient of Nu_{sw} vs. $Re_{sw}^{0.975} Pr^{0.3}$. Although PTAI was capable to produce higher temperature in critical areas, SAI possessed better uniform temperature distribution and *EFF*. In addition, SAI with 13° rotation showed much lower T_{hi} and higher T_{lo} than PTAI did. Moreover, SAI had only one hotspot on the outer skin while PTAI produced a lot of hotspots on the inner skin along nacelle lip-skin. In addition, with the suitable mass flow rate, SAI would provide sufficient level of temperature to achieve the required anti-icing functionality. Therefore, SAI is applicable if BAL is implanted at the inner skin. In addition, SAI has fewer components, simple plumbing, and is light and inexpensive compared to PTAI.

8.2 Future Work

The following future works are recommended based on the current research:

- To investigate the thermal performance of integration of BAL and PTAI. The study should include temperature profile, anti-icing efficiency and uniformity of temperature distribution on the nacelle lip-skin, exploring the relationship between BAL area and the thermal performance of PTAI, and developing a new correlation for PTAI with BAL system.
- The present study has emphasised the augmentor design only for small nozzle. Therefore, study of augmentor design for large nozzle is essential in order to enhance thermal performance of SAI for large nozzle.
- To study the thermal performance of integration of BAL and SAI, and develop a correlation for SAI with the presence of BAL. The study also needs to include air pressure inside the D-chamber. It is believed that the porosity of front face and back face sheets of BAL will affect the air pressure in the D-chamber and hence the SAI thermal performance.

References

[1] W.G. Habashi "Recent Advances in CFD for In-Flight Icing Simulation" *Journal of Japan Society of Fluid Mechanics,* Vol. 28 no.2, pp. 99-118, 2009

[2] A. Zamora "Numerical Investigation of Wing Hot Air Ice Protection System", Master of Science thesis, *Wichita State University*, 2007.

[3] National Transportation Safety Board, http://www.ntsb.gov/aviation.html June 2008

[4] National Transportation Safety Board, Crash During Approach to Landing, Circuit City Stores, Inc., Cessna Citation 560, N500AT, Pueblo, Colorado, February 16, 2005, Aircraft Accident Report NTSB/AAR-07/02,PB2007-910403,Washington, D.C. 2007.

[5] *"The jet engine"* Rolls-Royce 5th edition pp. 147-151, 1996.

[6] A.O. Ives "Perforated Honeycomb Acoustic Liner Heat Transfer" PhD Thesis, *Queen University Belfast*, 2009

[7] S.K. Thomas and R.P. Cassoni, "Aircraft Anti-Icing and De-Icing Techniques and Modelling", *Journal of Aircraft*, Vol. 33, No. 5, pp. 841-854, 1996.

[8] M.K. Politovich, "Predicting In-Flight Aircraft Icing Intensity", *Journal of Aircraft*, Vol. 40, No. 4, pp. 639-644, 2003.

[9] S.K. Thomas, R.P. Cassoni, "Aircraft Anti-Icing and De-Icing Techniques and Modeling", *Journal of Aircraft*, Vol. 33, No. 5, pp. 841-854, 1996.

[10] G.A. Ruff and B.M. Berkowitz, "User's Guide for the NASA Lewis Ice Accretion Prediction Code (LEWICE)", *Sevrdrup Tech., Inc., LeRC Group*, 1986

[11] J.C. Tsao and A.P. Rothmayer "Application of Triple-Deck Theory to the Prediction of Glaze Ice Roughness Formation on an Airfoil Leading Edge", *Journal of Computer and Fluids*, Vol. 31, No.8, pp. 977-1014, 2002

[12] M.B. Brag, G.M. Gregorek and J.D. Lee "Airfoil aerodynamic in Icing Condition", *Journal of Aircraft*, Vol. 23, No. 1, pp. 76-81, 1986.

[13] R.C. Griffiths and K.D. Korkan "Study of Theoretical and Wind Tunnel Results on the Flight Performance Degradation due to Leading Edge Rime Ice Accretion", *29th Aerospace Science Meeting*, Reno, NV, USA, 6-9 January, AIAA, pp. 92-0038, 1992, 92-0134.

[14] F.L. Boeke and R.A. Paselk "Icing Problems and the Thermal Anti-Icing System", *Journal of the Aeronautical Science*, Vol.13, No. 9, pp. 485- 497, 1946

[15] R.J. Hansman Jr., K. Yamaguchi, B. Berkowitz and M. Potapczuk "Modelling of Surface Roughness Effect on Glaze Ice Accretion", *27th Aerospace Science Meeting*, Reno, NV, USA, 9-12 January, pp. 35-42, 1989, 89-0734.

[16] M. Papadakis, M. Breer, N. Craig and X. Liu "Experimental Water Droplet Impingement Data on Airfoils, Simulated Ice Shapes, an Engine Inlet and a Finite Wing", *NASA Contractor Report,* Vol. 4636, 1994.

[17] C.S. Bidwell, S.R. Mohler Jr. "Collection Efficiency and Ice Accretion Calculation for a Sphere, a Swept MS(1)-317 Wing, a Swept NACA-0012 Wing Tip, an Axisymmetric Inlet and Boeing 737-300 Inlet", *33rd Aerospace Science Meeting and Exhibit sponsored by the AIAA*, Reno, NV, USA, 9-12 January, AIAA, 1995, 95-0755.

[18] J.T. Riley, "Mixed-Phase Icing Conditions: A Review", *U.S Department of Transportation and Federal Aviation Administration report*, 1998.

[19] R.J. Ronaudo, J.G. Batterson, A.L. Reehors, T.H. Bonds and T.M. O'Mara "Effect of Tail Ice on Longitudinal Aerodynamic Derivatives", *Journal of Aircraft*, Vol. 28, No. 3, pp. 193-199, 1991

[20] R.J. Ronaudo, J.G. Batterson, A.L.Reehors, T.H. Bonds and T.M.O'Mara, "Effect of Tail Ice on Longitudinal Aerodynamic Derivatives", *Journal of Aircraft*, Vol. 28, No. 3, pp. 193-199, 1991.

[21] S. Ramamurthy, T.G. Keith Jr., K.J. De Witt, J.C. Putt, C.A. Martin and K.L Leffel "Numerical Modelling of an Advanced Pneumatic Impulse Ice Protection System (PIIP) for Aircraft", *AIAA 29th Aerospace and Science Meeting*, Rena, NV, USA, 7-10 January, AIAA, 1991, 91-0555.

[22] C.A. Martin and J.C. Putt "An Advanced Pneumatic Impulse Ice Protection System (PIIP) for Aircraft", *AIAA 28th Aerospace Science Meeting*, Rena, NV, USA, 8-11 January, AIAA, 1990, 90-0492.

[23] D.L. Kohlman and W.G. Schweikhard "Icing-Tunnel Test of a Glycol-Exuding, Porous Leading-Edge Ice Protection System", *Journal of Aircraft*, Vol. 19, No. 8, pp. 647-654, 1982.

[24] G.W. Zumwalt "Electromagnetic Impulse De-Icing Applied to a Nacelle Nose Lip", *21st Joint Propulsion Conference*, Monterey, California, USA, 8-10 July, AIAA, 1985, 85-1118

[25] G.N. Labeas, I.D. Diamantakos and M.M. Sunaric "Simulation of Electroimpulse De-Icing Process of Aircraft Wings", *Journal of Aircraft*, Vol. 43, No. 6, pp. 1876-1885, 2006.

[26] R.I. Egbert, R.L. Schrag, W.D. Bernhart, G.W. Zumwalt and T.J. Kendrew "An Investigation of Power Line De-Icing by Electro-Impulse Methods", *Journal of IEEE Transactions on Power Delivery*, Vol. 4 No. 3, pp. 1855-1861, 1989.

[27] D.O. Nelepovitz, H.A. Rosenthal and H.M. Rockholt. "Test and Analysis of Electro-Impulse De-Icing System in Turbine Engine Inlets", *26th Aerospace Sciences Meeting*, Reno, NV, USA, 11-14 January, AIAA, 1988, 88-0020.

[28] J.J.G. Dryden and R.B.I. Aurora "Electro-magnetic Expulsion De-icing System", *US Pattern 6102333A*.

[29] K. Al-Khalil, T. Ferguson and D. Philips "A Hybrid Anti-Icing Ice Protection System", *35th Aerospace Sciences Meeting and Exhibit*, Reno, NV, USA, 6-9 January, AIAA, 1997, 97-0302.

[30] G.C. Botura, M.S. Dave Sweet and D. Flosdroft "Development and Demonstration of Low Power Electrothermal De-icing System", *43rd AIAA Aerospace Science and Exhibit*, Reno, NV, USA, 10-13 January, AIAA, 2005, 2005-1460.

[31] K. Al-Khalid," Thermo-Mechanical Expulsive De-icing System – TMEDS", *AIAA 45th Aerospace Science Meeting and Exhibit*, 8-11 January, 2007, AIAA, 2007-692.

[32] K. Al-Khalil, T. Ferguson and D. Philips "A Hybrid Anti-Icing Ice Protection System", *35th Aerospace Sciences Meeting and Exhibit*, Reno, NV, USA, 6-9 January, AIAA, 1997, 97-0302.

[33] J.F. Ross and J.T. Connolly "Contrasting Requirements for Type II De/Anti-Icing Fluids", *Journal of Aircraft*, Vol. 30, No.1, pp. 10-13, 1993.

[34] P.R.Louchez, S. Bernardin and J.L. Laforte "Physical Properties of Aircraft De-Icing and Anti-Icing Fluids", *36th Aerospace Science Meeting and Exhibit*, Reno, NV, USA, 12-15 January, AIAA, 1998, 98-0575.

[35] A. Albright "A summary of NASA research on the fluid ice protection research", *23rd Aerospace Science Meeting*, Reno, NV, USA, 14-17 January, AIAA, 1985, 85-0467.

[36] S. Thomas, R. Cassoni and C. MacAuthur "Aircraft anti-icing and De-icing Techniques and Modelling," *Journal of Aircraft*, Vol. 33, No.5, pp. 841-854, 1996.

[37] W.B. Wright "An Evaluation of Jet Impingement Heat Transfer Correlation for Piccolo Tube Application", 42nd AIAA Aerospace Science Meeting and Exhibit, 2004.

[38] K.A. Khalil, E. Irani and D.Miller "Mixed Phase Icing Simulation and Testing at the Cox Icing Wind Tunnel", *41st Aerospace Science Meeting and Exhibit*, Reno, NV, USA, 5-8 January, AIAA, 2003, 2004-62.

[39] S. Raghunathan, E. Benard, J.K. Watterson, R.K. Cooper, R. Curran, M. Price, H. Yao, R. Devine, B. Crawford, D. Riordan, A. Linton, J. Richardson and J. Tweedle "Key aerodynamic technologies for aircraft engine nacelles", *The Aeronautical Journal*, Vol.110, no.17, pp.265-288, 2006.

[40] J.M. Brown, S. Raghunathan and J.K. Watterson "Heat Transfer Correlation for Anti-icing System", *Journal of Aircraft*, Vol. 39, No.1, pp. 65-70, 2002.

[41] J.M. Brown "Investigation of Heat Transfer between a Staggered Array of Hot Air Jets and a Jet Engine Nacelle Lipskin Surface", PhD Thesis, *Queens University Belfast*, 1999.

[42] R.Herman "Swirl anti-icing system", *US Pattern 4688745*, 1987.

[43] M.S. Vest "Hot Air Injection for Swirling Rotational Anti-Icing System", *US Pattern 6267328 B1*, 2001.

[44] H.A. Rosenthal and D.O. Nevepovitz "Performance of a New Nose-Lip Hot-air Anti-Icing system", *21st Joint Propulsion Conference*, Monterey, California, USA, AIAA, 1985, 85-1117.

[45] F. Birbragher "Nacelle anti-icing system", *US Pattern 4738416*, 1988.

[46] M.A. Gilan and R.Farren "Optimal Design of Nacelle Thermal Anti-Icing Exhaust Grills for Enhanced Mixing", *Journal of Aircraft*, Vol.36, No.6, pp. 669-674, 1996.

[47] A. Porte "Protection Device for a Jet Engine Air Inlet Cowl Equipp.ed with a Deicing System", *US Pattern 6241189 B1*,2001

[48] F. P. Incropera and D. P. Dewitt "*Fundamental of Heat and Mass Transfer, fourth edition*", s.l.:John Willey & Sons, pp. 347-389, 1994.

[49] K.P. Perry "Heat Transfer by Convection from a Hot Gas Jet to a Plane Surface", *Proceeding of the Institution of Mechanical Engineers*, Vol. 168 no.1, pp. 775-784, 1954 .

[50] S. Roy and P. Patel "Study of Heat Transfer for Pair of Rectangular Jets Impinging on an Inclined Surface", *International Journal of Heat and Mass Transfer*, Vol. 46, No.3, pp. 411-425, 2003.

[51] K. Choo, T.Y. Kang and S.J. Kim "The Effect of Inclination on Impingement jet at small-to-plate Spacing", *International Journal of Heat and Mass Transfer*, Vol. 55, No. 13, pp. 3327-3334, 2012.

[52] N. Souris, H. Liakos and M. Founti "Impinging Jet Cooling on Concave Surface", *AIChe Journal*, Vol. 50. No. 8, pp. 1672-1683, 2004.

[53] C.H. Lee, K.B. Lim, S.H. Lee, Y.J. Yoon and N.W. Sung "A study of the heat transfer characteristics of Turbulent Round Jet on the Inclined Concave Surface Using Liquid Cristal Transient Method", *Experimental Thermal and Fluid Science*, Vol. 31 No. 6, pp. 559-565, 2007.

[54] G. Yang, M. Choi and J.S. Lee "An Experimental Study of Slot Jet Impingement Cooling on Convace Surface: Effect of Nozzle Configuration and Curvature", *International Journal of Heat and Mass Transfer*, Vol. 42, No.12, pp. 2199-2209, 1999.

[55] T.L. Chan, C.W. Leung, K. Jambunathan, S. Ashforth-Frost, Y. Zhou and M.H. Liu "Heat Transfer Characteristic of a Slot Jet Impinging on a Semi-Circular Convex Surface" *International Journal of Heat and Mass Transfer*, Vol. 45, No. 5, pp. 993-1006, 2002.

[56] D.H.Lee, Y.S.Chung and M.G.Kim "Technical Note Turbulent Heat Transfer from a Convex Hemispherical Surface to a Round Impinging Jet" *International Journal of Heat and Mass Transfer*, Vol. 42, No. 3, pp. 1147-1156, 1999.

[57] K.B.Lim, C.H.Lee, N.W.Sung and S.H.Lee "An Experimental Study on the Characteristic of Heat Transfer on the Turbulent Round Impingement Jet According to the Inclined Angle of Vortex Surface Using the Liquid Cristal Transient Method" *Experimental Thermal and Fluid Science*, Vol. 31, No. 2, pp. 711-719, 2007.

[58] C. Cornaro, A.S. Fleischer and R.J. Goldstein "Flow Visualization of a Round Jet Impinging on Cylindrical Surface" *Experimental Thermal and Fluid Science*, Vol. 20, No. 2, pp. 66-78, 1999.

[59] W.M. El-Maghlany, A.A. Hanafy, K.M. Abdou and M.A. Teamah "Numerical Simulation for Confined Rectangular Slot Jets Impingement on Isothermal Horizontal Plate", *European Journal of Scientific Research*, Vol. 76 No. 4 pp. 553-566, 2012.

[60] J. Badra, A.R. Masri, M. Freeman and M. Fitch "Enhanced Heat Transfer from Arrays of Jets Impinging on Plates" *16th Australian Fluid Mechanics Conference*, Crown Plaza, Gold Coast, Australia, AFMC, pp. 1187-1192, 2007.

[61] J. Lee and S.J. Lee "Stagnation Region Heat Transfer of a Turbulent Axisymmetric Jet Impingement" *Experimental Heat Transfer*, Vol. 12, No. 2, pp. 137-156, 1999.

[62] N.K. Chougule, G.V. Parishwad, P.R. Gore, S. Pagnis and S.N. Sapali "CFD Analysis of Multi-jet Air Impingement on Flat Plate" *Proceeding of the world congress on engineering Vol. III*, London, UK, 6-8 July, WCE, pp.2431-2435, 2011.

[63] M. Fregeau, F. Saeed and I. Paraschivoiu "Numerical Heat Transfer Correlation for Array of Hot-Air Jets Impinging on 3-Dimensional Concave Surface, *Journal of Aircraft*, Vol. 42 No. 3, pp. 665-670, 2005.

[64] R. Gardon and J. Cobonpue "Heat Transfer between a Flat Plate and Jets of Air Impinging on It" *International Development in Heat Transfer ASME*, pt 2, pp. 454-460, 1961.

[65] K.M. Al-Khalil, T.G. Keith Jr. and K.J. DeWitt "Thermal Analysis of Engine Inlet Anti-Icing", *Journal of Propulsion and Power*, Vol. 6, No. 5 pp. 628-634, 1990.

[66] A.G. Smith and K. Taylor, "The Simulation of an Aircraft Engine Intake Anti-Icing System" *PHEONICS Journal of CFD and its Application*, Vol. 10, No. 2, pp. 150-166, 1997.

[67] G. Croce, W.G. Habasi, G. Guevroment and F. Tezok, "3D Thermal Analysis of an Anti-Icing Device Using FENSAP-ICE" *36th Aerospace Sciences Meeting and Exhibit*, Reno, NV, USA, 12-15 January, AIAA, 1998, 98-0193.

[68] F. Morency, M.T. Brahimi, F. Tezok and I. Paraschiviou "Hot Air Anti-Icing System Modelization in the Ice Prediction Code Canice", *36th Aerospace Sciences Meeting and Exhibit*, Reno, NV, USA, 12-15 January, AIAA, 1998, 98-0192.

[69] B. deMattos and G. Olivera "Three Dimensional Thermal Coupled Analysis of a Wing Slice Slat with a Piccolo Tube", *18th Applied Aerodynamics Conference*, Denver, Colorado, 14-17 January, AIAA, 2000, 2000-3921.

[70] F. Morency, F. Tezok and I. Paraschiviou "Heat and Mass Transfer in the Case of Anti-Icing System Simulation", *Journal of Aircraft*, Vol. 37 no. 2, pp. 245-252, 2000.

[71] J. Hua and H.T Liu "Fluid Flow and Thermodynamic Analysis of a Wing Anti-Icing system", *Canadian Aeronautics and Space Journal*, Vol. 51 no. 1, pp. 35-40, 2005.

[72] P. Planquart, G.V. Borre and J.M. Buchlin "Experimental and Numerical Optimization of a Wing Leading Edge Hot Air Anti-Icing", *43th Aerospace Sciences Meeting and Exhibit*, Reno, NV, USA, 10-13 January, AIAA, 2005, 2005-1277.

[73] D. Rigby "Numerical Investigation of Hole Pattern Effect on Piccolo Tube Anti-Icing", *44th Aerospace Sciences Meeting and Exhibit*, Reno, NV, USA, 9-12 January, AIAA, 2006, 2006-1012.

[74] M. Papadakis and S.J. Wong "Parametric Investigation of a Bleed Air Ice Protection System", *44th Aerospace Science Meeting and Exhibit*, Reno, NV, USA, 9-12 January, AIAA, 2006, 2006-1013.

[75] F. Saeed and A.Z. Al-Garni "Numerical Simulation of Surface Heat Transfer from an Array of Hot Air Jets", *25thApplied Aerodynamics Conference*, Miami, FL, 25-28 June, AIAA, 2007, 2007-4287.

[76] J. Hua, F. Kong and H.T. Liu, "Unsteady Thermodynamic CFD Simulation of Aircraft Wing Anti-Icing Operation", *Journal of Aircraft*, Vol. 44, no. 4, pp. 1113-1117, 2007.

[77] H. Wang, P. Tran, W.G. Habashi, Y. Chen, M. Zhang and L. Feng "Anti-Icing Simulation in Wet Air of a Piccolo System using FENSAP-ICE", *SAE Aircraft and Engine Icing International Conference, 24 September, SAE* , 2007, 2007-01-3357.

[78] R. Elangton and K.E. Hung "Minimum Heating Energy Requirement of Piccolo Tube Jet Impingement Anti-Icing System", *Proceeding of HT 2007,Thermal Engineering Summer Heat Transfer Conference*, Vancouver, British Colombia, Canada, 8-12 July, ASME-JSME, 2007, HT2007-32080.

[79] S.H. Wong, M. Papadakis and A. Zamora "Computational Investigation of Bleed Air Ice Protection System", *1st Atmospheric and Space Environments Conference*, San Antonio, Texas, 22-25 June, AIAA, 2009, 2009-3966.

[80] R.H. Domingos, M. Papadakis and A. Zamora "Computational Methodology for Bleed Air Ice Protection System Parametric Analysis", *Atmospheric and Space Environments Conference*, Toronto, Ontario Canada, 2-5 August, AIAA, 2010, 2010-7834.

[81] N.L. Efremov and A.N. Karaiko "Theory of an Ideal Jet Thrust Augmentor", *Fluid Dynamic*, Vol. 39 No. 4, pp. 621-632, 2004.

[82] W.M. Presz and G. Reynolds "Thrust Augmentation with Mixer/Ejector Systems", *40th AIAA Aerospace Sciences Meeting and Exhibit*, Reno, NV, USA, 14-17 January, AIAA, 2002, 2002-0230.

[83] S.K. Chou, P.R. Yang and C. Yap "Maximum mass flow ratio due to secondary flow chocking in an ejector refrigeration system", *International Journal of Refrigeration*, Vol. 24, No.6, pp. 486-499, 2001.

[84] A. Levy, M. Jelinek and I. Borde "Numerical study on the design parameter of a jet ejector for absorption system", *Applied energy*, Vol. 72, No. 2, pp. 467-478, 2002.

[85] E. Rusly, L. Aye, W.W.S. Charters and A. Ooi "CFD analysis of ejector in a combined ejector cooling system", *International journal of refrigeration*, Vol. 28, No. 7, pp. 1092-1101, 2005.

[86] J.A. Scroggins, F. Zheng, J.S. Sayres, N.L. Cousineau, T.L. Turner and W.L. Robert "Experimental and Numerical Investigation of Thrust Augmentor on a Micro Valve less Pulsejet", Washington DC, 1-4 December, *PowerMEMS*, 2009, 9746311.

[87] M.R. Seiler and E.F. Schum "Analytical and Experimental Investigation of Diffusers for VSTOL Thrust-Augmenting Ejector", *Journal of Aircraft*, Vol. 16 No. 10, pp. 634-644, 1979.

[88] D.A. Hoffman "Experimental Investigation of Turbojet Thrust Augmentation using an Ejector" Thesis, Degree of Master of Science in Aeronautical Engineering, Department of the Air Force Air University, 2007.

[89] Amin, M. Sameh and C.A. Garris, Jr. "An Experimental Investigation of a Non-Steady Flow Thrust Augmenter", *Proceedings of the 31st Joint Propulsion Conference*, San Diego, CA, 10-12 July, AIAA, 1995, 95-2802.

[90] G.B. Gilbert and P.G. Hill "Analysis and Testing of Two-Dimensional Slot Nozzle Ejector with Variable Area Mixing Section", *NASA CR-2251*, 1973.

[91] K. Hunecke, "Jet Engine: Fundamentals of Theory, Design and Operation", *Airlife Publishing Ltd.*, pp. 45-54, 1997.

[92] T.S. Lund, D.A. Tavella and L.Robert "A Zonal Computational Approach to Thrust Augmentor Optimization", *23rd Aerospace Science Meeting*, Stanford, CA, 14-17 January, AIAA, 1985, 85-0110.

[93] W.M. Presz Jr. and M. Werle "Multi-Stage Mixer/Ejector System", *38th Joint Propulsion Conference Exhibit*, Indianapolis, Indiana, 7-10 July, AIAA, 2002, 2002-4064.

[94] R. Ramesh, S. Pradeep, T.M. Muruganandam and R.I Sujith "Studies on Free jet from Nozzle for High-Speed Mixing Application", *Experiments in Fluids*, Vol. 29, No.4, pp. 359-368, 2000.

[95] S. Kadirvel, F. Liu, S. Horowitz, T. Nishida, K. Ngo, L. Cattafesta and M. Sheplak "A Self-Powered Wireless Active Acoustic Liner", *12th Aero-acoustic Conference*, Cambridge, Massachusetts, 8-10 May, AIAA, 2006, 2006-2400.

[96] A.B. Bauer "Impedance Theory and Measurement on Porous Acoustic Liners", *Journal of Aircraft*, Vol. 14, No. 8, pp. 720-728, 1977.

[97] A.O.Ives, J.Wang, S.Raghunathan, E.Benard and P.Sloan "Three Dimensional Numerical Solution of Heat Transfer in a Honeycomb Cell", *7th Aviation Tech., Integration and Operation Conference*, Belfast, Northern Ireland, 18-20 September, AIAA, 2007, 2007-7825.

[98] M.W. Jeffrey, Wunsch, J.J. Sperling, S. Micheal "Method and Apparatus for Noise Abatement and Ice Protection of an Aircraft Engine Nacelle Inlet Lip, *European Patent 1495963A2*, 2005.

[99] M.D. Breer, R.F. Olsen, R.K. Kunze, Jr., B.L. Riedel "Method and Apparatus for Aircraft Inlet Ice Protection", *US Patent 6371411B1*, 2002.

[100] Short Bombardier Report "*Nacelle Anti-Icing System Dry Flight Test Report* ", 1999.

[101] J. Curwin and R. Slater "*Quantitative Methods for Business Decisions*" s.l.:Chapman and Hall, pp. 5-30, 1991.

[102] S. Kalpakjian and S.R. Schmid "*Manufacturing Engineering and Technology 4th edition*", s.l.:Prentice-Hall, Inc., pp. 982-989, 2001.

[103] Fluent Incorporated, FLUENT 6.3 User Guide, Lebanon, NH, 2007.

[104] Fluent Incorporated, GAMBIT 2.4 User Guide, Lebanon, NH, 2002.

[105] E.L. Houghton and P.W. Carpenter "*Aerodynamic for Engineering Student*", Butterworth Heinemann, pp. 274-279.

[106] P.H. Oosthuizen and W.E. Carscallen "*Compressible Fluid Flow*", McGraw-Hill International Edition, pp. 40-46.

[107] W. Pfenniger [book auth.] G.V. Lachman "Boundary layer and flow control", s.l.: Pergamon, 1963.

[108] S.A. Berger, L. Talbot and L.S. Yoa "Flow in Curved Pipes", *Ann. Rev. Fluid Mech*, Vol. 15, No. 1, pp. 46-512.

[109] D. Doorly and S. Sherwin "Geometry and Flow", *Cardiovascular Mathematics MS&A*, Vol. 1, No.5, pp. 177-209, 2009.

[110] C. Nuntadusit, M. Wae-Hayee, A. Bunyajitradulya, S. Eiamsa-ard "Visualization of Flow and Heat Transfer Characteristics for Swirling Impinging Jet", *International Communications in Heat and Mass Transfer*, Vol. 39, No.5, pp. 640-648, 2012.

[111] J. Ortega-Casanova "CFD and Correlation of the Heat Transfer from a Wall at Constant Temperature to an Impinging Swirling Jet", *International Journal of Heat and Mass Transfer*, Vol. 55, No.21-22, pp. 5836-5845, 2012.

[112] http://www.lxcad.net/STAR-CCM/online/134-using TurbulenceModels-05.html

[113] B. Bell "Turbulent Flow Case Study", *Fluent Software Training*, UGM, 2003.

[114] Prediction of Separated Flow in a Two-Dimensional Diffuser" Computational Fluid Dynamics 3, 105AER306 Laboratory 3, 2009, Queen University Belfast.

[115] J.P. Holman "*Heat Transfer 8th Edition*", s.l.:McGraw-Hill, inc. pp. 218-321, 2002.

[116] Y. Nakayama and R.F. Boucher "*Introduction to Fluid Mechanics*", s.l.: Arnold, pp. 74-90

[117] M.C. Smith and A.M. Kuethe "Effect of Turbulent on Laminar Skin Friction and Heat Transfer", *The physics of fluid*, Vol. 9, no. 12, pp. 2337-2344, 1966

[118] A. Kondyogan and J.D. Daudin "Effect of Free Stream Turbulent Intensity on Heat and Mass Transfer at the surface of Circular Cylinder and an Elliptical Cylinder, Axis Ratio 4", *Int. J. Heat Mass Transfer*, Vol. 38 no. 10, pp. 1735-1749, 1995.

[119] C.A. Parente and C.J. Weizenecker "Method of Fabricating an Acoustic Liner" *US Patent 617696481*, 2001

[120] Jun-Yang San and Wen-Zheng Shiao "Effect of Jet Plate Size and Plate spacing on the Stagnation Nusselt Number for a Confined Circular Air Jet Impinging on a Flat Surface" *Int. J. Heat Mass Transfer*, Vol. 49 no. 10, pp. 3477-3486, 2006.

[121] Fan Shi Kong, Heuy Dong Kim, Yingzi Jin, Toshiaki Setoguchi "Application of Chevron Nozzle to a Supersonic Ejector-Diffuser System" Procedia Engineering Vol. 56 no. 5, pp. 193-200, 2013.